



HAL
open science

Non-linear physics associated to chiral symmetry in driven dissipative polariton lattices

Nicolas Pernet

► **To cite this version:**

Nicolas Pernet. Non-linear physics associated to chiral symmetry in driven dissipative polariton lattices. Pattern Formation and Solitons [nlin.PS]. Université Paris-Saclay, 2022. English. NNT : 2022UPASP054 . tel-03917551

HAL Id: tel-03917551

<https://theses.hal.science/tel-03917551v1>

Submitted on 2 Jan 2023

HAL is a multi-disciplinary open access archive for the deposit and dissemination of scientific research documents, whether they are published or not. The documents may come from teaching and research institutions in France or abroad, or from public or private research centers.

L'archive ouverte pluridisciplinaire **HAL**, est destinée au dépôt et à la diffusion de documents scientifiques de niveau recherche, publiés ou non, émanant des établissements d'enseignement et de recherche français ou étrangers, des laboratoires publics ou privés.

Non-linear physics associated to chiral symmetry in driven dissipative polariton lattices

*Physique non-linéaire associée à la symétrie chirale de
réseaux de microcavités à polaritons*

Thèse de doctorat de l'université Paris-Saclay

École doctorale n°572, Ecole Doctorale Ondes et Matière (EDOM)
Spécialité de doctorat: Physique
Graduate School : Physique. Référent : Faculté des sciences d'Orsay

Thèse préparée dans l'unité de recherche **Centre de Nanosciences et de
Nanotechnologies** (Université Paris-Saclay, CNRS),
sous la direction de **Jacqueline BLOCH**, Directrice de recherche
et le co-encadrement de **Sylvain RAVETS**, Chargé de recherche

Thèse soutenue à Paris-Saclay, le 20 Juin 2022, par

Nicolas PERNET

Composition du jury

Emmanuelle DELEPORTE Directrice de recherche, ENS Paris-Saclay, CNRS	Présidente
Anna MINGUZZI Directrice de recherche, Université Grenoble-Alpes, CNRS	Rapporteuse & Examinatrice
Christian SCHNEIDER Professeur, Oldenburg Universität, Germany	Rapporteur & Examineur
Iacopo CARUSOTTO Professeur, Università di Trento, CNR, Italy	Examineur
Sylvain NASCIBENE Maître de conférences, Sorbonne Université, CNRS	Examineur
Jacqueline BLOCH Directrice de recherche, Université Paris-Saclay, CNRS	Directrice de thèse

Titre: Physique non-linéaire associée à la symétrie chirale de réseaux de microcavités à polaritons.

Mots clés: Polaritons de cavité, Fluides de lumière, Optique non-linéaire, Microstructures, Spectroscopie optique

Résumé: Les polaritons d'excitons sont des particules mixtes lumière-matière émergeant du couplage fort entre photons de cavité et excitations électroniques dans des microcavités semi-conductrices. Ces quasi-particules héritent des propriétés de leurs deux constituants élémentaires : la composante électronique leur confère une non-linéarité Kerr géante, tandis que la partie photonique rend le système intrinsèquement dissipatif et permet de confiner les polaritons dans des microstructures obtenues en gravant la cavité. Cette thèse présente l'étude des propriétés non-linéaires de réseaux de microcavités optiques présentant la symétrie chirale. La première partie de l'étude est consacrée à des chaînes topologiques unidimensionnelles émulant le modèle de Su-Schrieffer-Heeger. Dans le régime non-linéaire, le pompage cohérent du système en utilisant un laser conduit à la formation de solitons de gap dans le réseau massif ainsi qu'aux bords du réseau. Ces solitons possèdent des propriétés de symétrie qui les rendent robustes face à certains types défauts. D'autre part, en structurant la phase du laser de pompe, de nouvelles solutions non-linéaires apparaissent,

qui sont spécifiques à la physique des systèmes ouverts. En présence d'un tel état stationnaire, l'analyse détaillée du spectre des excitations permet de mettre en évidence une transition de phase topologique induite par les interactions. Dans un second temps, l'étude de l'interaction entre deux solitons a permis de montrer que le signe de cette interaction est étroitement lié à la structure du réseau sous-jacent. Ces travaux ont mis en évidence la présence d'une brisure spontanée de symétrie entre les deux solitons. Au voisinage de cette phase, un nouvel effet de multi-stabilité a été découvert, qui permet d'induire de la chiralité dans la réponse du système en fonction du protocole de pompage. Nous dénomons cet effet "bistabilité hélicoïdale". Cet effet très général peut être obtenu dans un simple système de deux résonateurs non-linéaires couplés, et relié ainsi à la physique d'une particule de spin demi-entier. Ces résultats sont étayés à la fois par des simulations numériques détaillées ainsi que par des expériences. Cette thèse illustre ainsi comment symétries et non-linéarités permettent d'enrichir considérablement la physique des systèmes photoniques.

Title: Non-linear physics associated to chiral symmetry in driven dissipative polariton lattices.

Keywords: Cavity polaritons, Fluids of light, Nonlinear optics, Microstructures, Optical spectroscopy

Abstract: Microcavity polaritons originate from the strong coupling between cavity photons and electronic excitations of a semiconductor microcavity. These quasi-particles inherit properties from both constituents: the electronic component is responsible for giant Kerr nonlinearities while the photonic part makes the system inherently dissipative and allows confining polaritons in microstructures obtained via etching of the cavity. This thesis presents the study of the non-linear properties of microcavity arrays with chiral symmetry. The first part of the work is dedicated to one-dimensional topological lattices emulating the Su-Schrieffer-Heeger model. In the non-linear regime, driving the system coherently using a laser leads to the formation of gap solitons at the edges and in the bulk of the structure. We evidenced that such solitons present symmetry properties making them robust against certain types of defects. In addition, we unveiled that a careful engineering of the drive allows observing novel non-

linear solutions which are specific to open systems. We analyzed the systems excitations spectrum in presence of such stationary state and demonstrate the possibility to realize a topological phase transition induce by the interactions. In the second part, we explored the properties of the interaction between two gap solitons and showed that the interaction sign is strongly linked to the underlying structure of the lattice. This work showed the presence of a spontaneous symmetry breaking. The study of the systems non-linear response in the vicinity of such phase allows us to discover a novel effect of bistability allowing to induce chirality in the system depending on the drive protocol. We called this effect "helical bistability". The helical bistability is a very general effect that can be observed in a simple set of two coupled Kerr resonators and is linked to the physics of a particle with spin one half. These results are supported both by numerical simulations and experiments. This thesis illustrates how symmetries and non-linearities enriches the physics of photonic systems in a driven-dissipative context.

Résumé

Les polaritons d'excitons sont des particules mixtes lumière-matière émergeant du couplage fort entre photons de cavité et excitations électroniques dans des microcavités semi-conductrices. Ces quasi-particules héritent des propriétés de leurs deux constituants élémentaires : la composante électronique leur confère une non-linéarité Kerr géante, tandis que la partie photonique rend le système intrinsèquement dissipatif et permet de confiner les polaritons dans des microstructures obtenues en gravant la cavité. Cette thèse présente l'étude des propriétés non-linéaires de réseaux de microcavités optiques présentant la symétrie chirale.

Les deux premiers chapitres de cette thèse constituent une introduction à la physique des polaritons de microcavités à semi-conducteur. Le premier chapitre aborde la physique linéaire et non-linéaire des polaritons dans une cavité planaire en commençant par la description des deux constituants élémentaires du polariton: l'exciton de puit quantique et le photon piégé dans une cavité de miroirs multicouches. Ce chapitre introduit également les méthodes expérimentales permettant d'étudier les polaritons en collectant les photons émis par l'échantillon. Le second chapitre présente la physique des polaritons dans les réseaux de microcavités. Nous commençons par introduire les différentes méthodes utilisées pour confiner les polaritons dans les réseaux puis présentons deux approches considérées pour décrire et modéliser la physique des polaritons dans ces réseaux. Nous présentons notamment les méthodes numériques utilisées dans le reste du manuscrit pour simuler et comprendre la physique non-linéaire des réseaux à polaritons.

Le troisième chapitre est dédié à l'exploration des propriétés non-linéaire d'un réseau SSH, qui est un précurseur à l'étude de réseaux non-linéaires présentant des propriétés de topologie. Nous détaillons la formation de solitons de gap (bande interdite) dans le gap topologique du réseaux SSH et analysons leur profile de densité en terme de pseudo-spin de sous-réseau. Nous commençons par créer un soliton au niveau d'un défaut d'interface topologique et explorons ensuite la réponse du matériau massif. Nous montrons ainsi que les solitons créés dans le massif présentent des propriétés liées à la symétrie chirale du réseau SSH, qui ont d'importantes conséquences sur l'interaction d'un soliton avec un défaut. La texture de pseudo-spin des queues exponentielles du soliton est associée à une robustesse du soliton face à des défauts localisés sur un sous-réseau.

Enfin, en réalisant une ingénierie du champ d'excitation, nous démontrons l'existence de nouvelles solutions solitoniques qui n'existent pas dans les systèmes conservatifs. Nous créons des solitons avec un pseudo-spin total non nul et analysons l'effet d'un tel soliton sur le réseau. Nous prédisons que cette nouvelle solution se comporte comme une interface non-triviale pour le spectre des excitations.

Le quatrième chapitre présente l'étude de l'interaction entre deux solitons générés dans le gap topologique du réseau SSH. Nous mettons en évidence la présence d'une brisure de symétrie et explorons la réponse non-linéaire du système au voisinage de ce régime critique.

En réalisant une ingénierie du protocole d'excitation, nous avons découvert un nouvel effet de multi-stabilité en phase qui permet d'obtenir une réponse chirale du système. D'autre part, le système n'explore pas les mêmes solutions non-linéaires dépendamment du sens de scan de la phase (horaire ou trigonométrique). Nous appelons ce nouvel effet "bistabilité hélicoïdale" et montrons que l'addition de degrés de liberté permet d'enrichir la physique observées. Nous comparons nos résultats expérimentaux à des simulations numériques qui mettent en évidence un possible lien entre la symétrie chirale du réseau et la bistabilité hélicoïdale.

Enfin, dans le cinquième chapitre, nous explorons numériquement la bistabilité hélicoïdale en se concentrant sur l'un des systèmes les plus simples présentant la symétrie chirale: deux résonateurs Kerr couplés. Nous démontrons numériquement que ce système élémentaire, qui est aussi sujet à une brisure de symétrie, peut faire apparaître le phénomène de bistabilité hélicoïdale. En faisant une analogie entre ce système est un spin demi-entier, nous représentons les trajectoires du système sur la sphère de Poincaré et détaillons les différents régimes observés. Nous confirmons expérimentalement ces résultats en utilisant deux solitons dans le réseau SSH. Par des méthodes interférométriques, nous sommes capables de réaliser la tomographie du champ de polaritons et de représenter les trajectoires expérimentales sur la sphère de Poincaré. Ces résultats constituent la première observation numérique et expérimentale de la bistabilité hélicoïdale dans sa forme la plus simple.

Les résultats présentés dans ce manuscrit démontrent que l'ingénierie du champ d'excitation est une ressource particulièrement importante pour stabiliser de nouvelles solutions non-linéaires qui ont le potentiel de modifier la topologie du système. Nous démontrons également l'importance de cette méthode pour induire une réponse chirale dans les systèmes non-linéaires. Dans la dernière partie du manuscrit, nous proposons différentes perspectives à cette thèse pour l'extension de ces idées aux réseaux bidimensionnels ou pour la réalisation de pompes topologiques à solitons.

Acknowledgment

This adventure started back in 2018 when I asked Jacqueline about the possibility to do an internship in her group. I had followed her Master 2 courses about light matter-interaction in semiconductor structures and, as a novice in condensed matter physics, I was amazed by all the possibilities offered by the polariton platform: superfluidity of light, polariton condensation or polariton lasing, the emulation of quasi-crystalline structures or of molecular orbitals with photons to cite a few. Jacqueline answered positively and welcomed me at the Center for Nanosciences and Nanotechnologies (C2N) in Marcoussis, which would soon be moved to the campus of Saclay. What I found at C2N was a particularly dynamical yet humane environment and I think this atmosphere has been particularly important for the well-being of my development during these four years. Here, I would like to thank all people who contributed to my work or helped me to face the difficulties associated to the move and contingencies that occurred during this period (helium shortage and covid among others).

First, I would like to thank my jury members for having taken the time to read and review my manuscript and for their interesting and pertinent questions during the PhD defense.

I want to thank Jacqueline Bloch, my PhD advisor, for all the things she taught me during those years and for the freedom and time she gave me to explore the system, even in directions which did not seemed particularly interesting at first glance. I am extremely thankful for all the time I was granted to fail in the first observation of the Helical bistability. After a few months of failure, even though this effect looked more and more like a numerical error, Jacqueline expressed her concerns but let me persevere. The success of this experiment is barely due to my perseverance and mostly a consequence of the support and trust you gave me even when I started to doubt my own results. I will always remember that when Quentin and I first observed the effect with gap solitons, you were with us very late in the lab and you pushed us to perform the scans that revealed the Helical bistability. Beside everything I gained from the scientific point of view, I also want to thank you for allowing me to join this polariton family that you built and which keeps growing.

I am particularly grateful to Sylvain Ravets, my co-supervisor. Your numerous tips and your technical expertise have proven to be extremely efficient in shortening the time it takes to correctly align the setup. Your presence in the labs is precious to everyone. In addition to your incredibly valuable help with the realization of experiments, you always gave me on point feedback on my work. Above all, what I will remember most is your natural kindness. This quality of yours is recognized by everyone you met and it has been of great importance in difficult moments. Finally,

I think that your kind heart is, and will remain, at the origin of most of these hectic and fantastic stories that you happily share with us during breaks.

During those four years I had the chance to meet wonderful people. I want to thank Valentin Goblot for taking care of me during my internship, for all he taught me about polariton physics and for his tips on how to proceed with nonlinear experiments. Many thanks to Philippe St-Jean for his support during the two first years of my PhD, you were always there when I had a question or problem, scientific or not. Especially, you taught me all I know about topology and the SSH model. Big thanks to Titta, you have been an example of scientific curiosity and I will never be able to say how much I owe you for the time we spent together in the Montana lab trying to work on the Helical bistability of the dimer and with polarization. Not only you proved that my calculations were right by reproducing them but you also decided to spend a lot of your time working with me and supporting me when the experiments were not working as expected. You were also an example of determination, you proved me several time that you could obtain what you wanted from administrative or IT services if you bored them long enough, I still did not master this skill. Many thanks also to Quentin Fontaine, your presence and kindness have been of great support to Ateeb and then to me. I can't thank you enough for enduring my little eccentricities and craziness when we started to stay a bit too long in the lab. I wish our bonds of friendship remain as tight as the screws you mechanically soldered to the breadboard. I want to thank Martin Guillot for being an endless source of jokes and for withstanding mine.

I want to thank Alberto Amo for his enthusiasm and for his constructive criticism on my work, you have a particular talent in thinking out of the box and revealing other possible point of views. I also want to thank the rest of polariton group working at the PhLAM in Lille. The interactions between our group and Alberto's one have been of particular importance in my scientific development.

I want to acknowledge all the interns that I had the pleasure to interact with: Tom Guillemot, Carelle Keyrouz, Yasmine Asselah. I have a special thought to Yiannis Georgakilas who kept me awake at 4:00 a.m. a certain night before a group meeting, the simulations I did while you were preparing yours slides changed the direction of my whole PhD. I want to thank Ateeb Toor for the time shared in the labs, as Quentin is saying, you are an hard-worker and an example of abnegation. I wish all the best to Daniela Pinto-Dias who will soon start a PhD in the group which, I al sure, will be full of success.

I also want to thank the rest of the GOSS group and particularly Anne, Marie and Florian who shared a lot of coffee breaks and time with me in the office.

Thanks also to the IT service, the workshop and the administration of the C2N for their help in these complicated times mixed between the move of the lab and the covid crisis.

All the experiments presented in this manuscript where only made possible by the precious work of Luc Le Gratiet, Abdou Harouri, Isabelle Sagnes who take care of the etching of the exquisite samples grown by Martina Morassi and Aristide Lemaître. Thank you also Aristide for being another source of jokes, I am still waiting for your famous Tuna quiche recipe.

I also want to acknowledge the precious contributions of the different theoreticians I interacted and collaborated with during my PhD. Especially Dmitry D.

Solnyshkov and Guillaume Malpuech from Institut Pascal, for the important work they have done on the physics of gap solitons in the driven-dissipative SSH model. I also thank Oded Zilberberg from ETH Zurich and the rest of his group for the insight brought on what used to be called "The Ratchet". I want to acknowledge the enriching discussions I had with Iacopo Carusoto and I also want to thank you for your exceptional enthusiasm whatever which topic is discussed.

Finalemment je voudrais remercier mes parents, toute ma famille et mes amis. Leur soutien inconditionnel a été d'un grand secours durant les moments difficiles. Un merci tout particulier au groupe de rôlistes qui a su égayer tant de soirées, à tel point qu'Émilie venait me disputer "ris moins fort tu vas réveiller les voisins".

Contents

Introduction	1
1 Introduction to micro-cavity exciton-polaritons	5
1.1 Quantum well excitons	6
1.1.1 Excitons in the bulk	6
1.1.2 Excitons in quantum wells	7
1.1.3 Exciton radiative recombination	8
1.2 The optical cavity	10
1.2.1 The Fabry-Pérot cavity	10
1.2.2 The distributed Bragg reflector	12
1.2.3 The Bragg mirror cavity	13
1.3 Exciton-photon hybrid quasi-particles	14
1.3.1 Light-matter strong coupling	14
1.3.2 Quantum description of polaritons	15
1.3.3 Polaritons characteristics	18
1.4 Experimental observation	19
1.4.1 Sample structure	19
1.4.2 Experimental setup	20
1.4.3 Characterization of a planar sample	22
1.5 Polariton fluids	23
1.5.1 The polariton-polariton interaction	24
1.5.2 Non-resonant excitation	27
1.5.3 Resonant excitation	29
1.5.4 Solitons in polariton fluids	34
1.6 Summary	37
2 Polaritons in lattices	39
2.1 Engineering an energy landscape for Polaritons	40
2.1.1 Potential acting on the excitonic component	40
2.1.2 Potential acting on the photonic component	42
2.1.3 Etching the planar cavity	43
2.2 Modeling polaritons in deeply etched lattices	44
2.2.1 The nearly-free model to describe 1D and 2D structures	45
2.2.2 Micropillars as artificial atoms	47
2.2.3 Coupling micropillars to build photonic molecules	48
2.3 Interacting non-linear polariton fluids in lattices	51
2.3.1 Experimental realizations	51

2.3.2	The discrete Gross-Pitaevskii equation	54
2.3.3	Bogoliubov theory	58
2.4	Summary	62
3	Gap solitons in a 1D topological lattice	65
3.1	Introduction to topology	67
3.1.1	The mathematical field of topology	67
3.1.2	A new phase of matter: topological insulators	68
3.1.3	Experimental realizations of topological phases with photonic platforms	70
3.1.4	The SSH model: notion of chiral symmetry	72
3.2	An emerging field: non-linear topological photonics	78
3.2.1	Topological lasers	79
3.2.2	Non-linear phase transitions and wave-mixing	80
3.2.3	Topological solitons	83
3.3	Non-linearities in the topological gap of SSH: formation of topological gap solitons	83
3.3.1	Emulating the SSH model with “s” modes	84
3.3.2	Bistability of a topological interface state: a topological soliton	88
3.3.3	Generation of gap solitons in the bulk	91
3.3.4	Numerical simulations: Gap solitons as Truncated Bloch Waves	94
3.3.5	Spin polarized tails, a specificity of the topological gap	96
3.4	Robustness of a topological gap solitons	99
3.4.1	The case of conservative systems	99
3.4.2	All optical engineering of a non-Hermitian defect	101
3.4.3	Sub-lattice robustness of a driven-dissipative soliton	103
3.5	Novel solutions: spin-polarized topological gap solitons	107
3.5.1	Experimental setup	107
3.5.2	A soliton with spin-polarized core	108
3.5.3	The spin-polarized bulk soliton, a solution stabilized by the drive	109
3.5.4	Bogoliubov spectrum in presence of a spin-polarized soliton	111
3.6	Perspectives	116
4	Interaction between gap solitons on a driven-dissipative SSH lattice	119
4.1	Introduction	120
4.1.1	General overview	120
4.1.2	Interaction between gap solitons on a lattice: role of the band symmetry	121
4.2	A symmetry breaking revealed in the interaction phase diagram	123
4.2.1	Phase frustration in the solitons tails	123
4.2.2	A symmetry breaking induced by a phase frustration between the driving field and renormalized states	128
4.2.3	Phase diagram of coupled solitons formation for $D = 2a$	132
4.3	Helical bistability	135
4.3.1	Scanning the phase to navigate through the stability diagram	135
4.3.2	Chiral response to the phase gradient	138

4.3.3	Power dependence of the helical bistability	142
4.3.4	Soliton trapping	145
4.3.5	The helical bistability: an effect specific from lattices with chiral symmetry	148
4.4	Conclusion and perspectives	150
5	Chiral symmetry breaking at the heart of the Helical bistability	153
5.1	Helical bistability in two coupled Kerr resonators	154
5.1.1	Phase bistability of two coupled Kerr resonators	154
5.1.2	Representation on the Bloch Sphere	156
5.2	Observation with gap solitons	159
5.2.1	The SSH unit cell as a single Kerr resonator	159
5.2.2	Phase diagrams and symmetry breaking	160
5.2.3	Experimental Helical bistability, representation on the Bloch sphere	162
5.2.4	Phase diagrams associated to phase scans	164
5.3	Conclusion and perspectives	165
	Conclusion and outlook	167
	Publications	171
A	Interaction between gap solitons: SSH versus AB lattice	173
A.1	The AB lattice: gap solitons in a trivial gap	173
A.2	Numerical comparison	174
A.2.1	Power scans	174
A.2.2	Phase scans	175
B	Helical bistability of two coupled Kerr resonators	181
B.1	Numerical results: particle density versus $\Delta\varphi$	181
B.2	Experimental results	182
B.2.1	Density diagrams	182
B.2.2	Evolution of S_Z versus $\Delta\varphi$	183
B.2.3	Bloch sphere representation of the helical bistability and soli- ton trapping for solitons interacting <i>via</i> chiral tails	184
	Bibliography	187

Introduction

Topology is a field of mathematics which aims at the classification of geometrical objects based on global properties that are unaffected under continuous deformations. The quantities that characterize the topology of an object are called topological invariants. The mathematical field of topology was recently found to be useful to get deeper insight into fundamental physical effects. For instance, in the Quantum Hall Effect [1], the fact that the Hall conductance is a multiple of e^2/h can be explained by the existence of a topological invariant associated to each Landau level [2].

Topological photonics is a research field which aims at the implementation of topological phases (discovered in condensed matter) with photons [3,4]. The idea is to endow light states with novel properties which can for example lead to symmetry protection. It appears very promising in view of developing devices protected from fabrication defects or unaffected by environmental perturbations. Photonic platforms have allowed pushing the exploration of topological phases of matter beyond the realm accessible to conservative systems, for example through the engineering of \mathcal{P} - \mathcal{T} symmetric phases [5,6]. Nowadays, particular attention is devoted to the exploration of non-linear topological photonics [7]. Reaching regimes where inter-particle interactions play a significant role is expected, for instance, to trigger topological phase transitions. Extending the fascinating properties of linear topological phases, it is also expected to induce symmetry protection and robustness properties for the many-body system.

A plethora of different platforms can be considered to explore topological phases of matter in presence of non-linearities: superconducting circuits, cold atoms, trapped ions, vacancy defects, photonic systems, opto-mechanical and mechanical resonators or gyromagnetic materials to cite a few. Each system, depending on its nature, has specificities that makes it useful to address peculiar problems: for example, the dissipative nature of certain photonic platforms allows to address problems whose resolution is inaccessible to closed systems. However, since photons show particularly weak inter-particle interactions in vacuum, the emulation of non-linear sets of equations using photons requires to use hybrid platforms where they are forced to interact *via* light-matter interaction.

Micro-cavity exciton polaritons have recently emerged as a powerful platform to study non-linear photonics. The strong coupling between cavity photons and excitons in a semiconductor quantum well leads to the formation of mixed states of light and matter. These composite quasi-particles inherit properties from both components: for example, the excitonic part is responsible for a significant inter-particle interaction and the photonic component endow polaritons with a low effective mass

which allows to observe the discretization of polaritons modes in microscopic structures. Driven-dissipative platforms such as polariton are particularly suited to explore regimes where non-Hermiticity, non-linearities and topology are combined. By playing with gain and loss of the system, the non-Hermiticity enables the exploration of non-linear $\mathcal{P}\mathcal{T}$ symmetric phases but, in addition, the engineering of the drive can be used to stabilize novel non-linear solutions, and to modify the topology of the underlying excitation spectrum [8].

This thesis work fits in the context of the emerging field of non-linear topological photonics. The works described in this manuscript contribute to the exploration of the interplay between symmetries and non-linearities in a driven-dissipative context. In particular, we study the properties of a one-dimensional polariton lattice emulating the Su-Schrieffer-Heeger model which is a toy model to start exploring topological phases of matter. We probe the non-linear response of the system and investigate the physics of gap solitons. Taking advantage of the versatility of our photonic platform, we show that engineering of the drive enables acting on the physics of the system to induce novel physical effects.

The present manuscript is organized as follows.

In the **first chapter**, we introduce the key ingredient at the basis of experiments with polaritons. We present the two basic constituents of a polariton, the photon trapped in a cavity and the exciton in a semiconductor quantum well. We discuss the conditions for strong coupling between them. This strong coupling leads to the formation of mixed particles of light and matter: exciton-polaritons. We discuss the linear physics of polaritons in planar samples, we provide information about sample structures and present the experimental setup and methods employed for their characterization. We finally introduce the polariton-polariton interaction and the current state of the art of experiments involving non-linear fluids of polaritons in planar cavities.

In the **second chapter**, we describe the physics of polariton lattices. We present the different methods used to confine polaritons and especially focus on the etching technique used at C2N to process samples and obtain polariton cavities with a patterned geometry. We introduce the models we use to describe and numerically simulate the physics of polariton in tailored structures. We present two approaches considered to design samples and interpret experimental results: the continuous or nearly-free model and the tight-binding approach. We finally discuss experimental realizations involving polariton-polariton interactions in lattices and low dimensional structures and we introduce the numerical tools we use to simulate and understand the physics of non-linear polariton fluids.

The **third chapter** is dedicated to the exploration of non-linear optics in a SSH lattice, which is a precursor to start the exploration between topology and non-linearities in a driven-dissipative context. We detail the formation of solitons in the topological gap of the SSH lattice and analyze their density profile in terms of sub-lattice pseudo-spin. We first create a soliton at a non-trivial interface of the SSH model and we then explore the lattice bulk. We show that gap solitons created far from lattice edges show signatures of the underlying chiral symmetry. Solitons created in the bulk of the lattice present exponentially decaying tails with opposite non-zero pseudo-spin, such that the overall soliton spin remains equal to zero. We then study the interaction of a soliton with a defect. We demonstrate that their

spin-texture is responsible for robustness of the solitons against defects located on one sub-lattice. Finally, engineering the drive enables us to access a new family of gap solitons which has no counterpart in conservative systems. We generate fully spin-polarized solitons in the bulk of the lattice and analyze their effect on the underlying excitation spectrum. We predict that they effectively create a non-trivial interface in the lattice thus inducing an interface state in the gap of the excitation spectrum.

The **fourth chapter** is dedicated to the interaction between two gap solitons with spin-polarized tails. We show that the interaction between gap solitons strongly depends on the lattice structure. We evidence the presence of a symmetry breaking and explore the non-linear behavior of the system in the vicinity of this critical regime. By engineering of the drive protocol, we discover a new kind of phase multistability which allows inducing chirality in the system response. The system does not explore the same non-linear solutions whether we scan clockwise or anticlockwise a phase difference in the driving field. We call this effect “Helical bistability” and show that additional degrees of freedom can be used to enrich its physics. We compare our experimental results to numerical simulations and evidence a possible link between the chiral symmetry of the lattice and the helical bistability.

In the **fifth chapter**, we numerically explore the Helical bistability effect by concentrating on one of the simplest systems presenting the chiral symmetry: two coupled Kerr resonators. We numerically demonstrate that this elementary system, also subjected to a symmetry breaking, can exhibit helical bistability. Mapping the two coupled resonators to a classical spin $\frac{1}{2}$, we represent the system trajectory on the Bloch sphere and present the different non-linear regimes we observe. We experimentally confirm our numerical predictions using gap solitons in the SSH lattice. We show that a system of two interacting solitons can be mapped to two coupled resonators. Using interferometry, we are able to perform the polariton field tomography and to represent experimental trajectories on the Bloch sphere. These results constitute the first numerical and experimental observations of helical bistability in its simplest form.

Our results demonstrate that drive engineering is a powerful tool to stabilize novel non-linear solutions that can potentially modify the topology of the system. We also demonstrate that chiral or helical driving protocols can induce a chiral response of the systems. This novel approach to non-linear topological photonics, that we name driven topology, is just at its infancy. In the last part of the manuscript we describe some perspectives extending these ideas to 2D lattices or to topological pump protocols.

Chapter 1

Introduction to micro-cavity exciton-polaritons

In the first chapter we introduce the physics of micro-cavity exciton-polaritons. Polaritons are bosonic quasi-particles arising from the strong coupling between photons confined in a cavity and excitons trapped in a quantum well. These hybrid light-matter particles inherit physical properties from both photonic and excitonic components. Their photonic nature allows confining them at micron scale *via* tailoring of the cavity and endows them with a relatively low effective mass. Their excitonic nature allows polaritons to interact *via* a Kerr-like term, which is much stronger than the one conventionally obtained with most non-linear crystals. We start by separately introducing the two key ingredients of the formation of polaritons, describing first the exciton (Sect. 1.1). Second, we show how to confine light in a cavity composed of distributed Bragg reflectors (Sect. 1.2). We then proceed with the description of light-matter strong coupling between those two elements resulting in the creation of exciton-polaritons (Sect. 1.3). Section 1.4 is dedicated to the description of linear physics with 2D cavity polaritons. We will also present the experimental setup and the methods used to characterize polariton planar micro-cavities. Finally, the non-linear and collective behaviors of polaritons will be discussed in Sec. 1.5.

1.1 Quantum well excitons

Semiconductor materials are crystalline materials whose ground state consists in a completely occupied valence band and an empty conduction band separated by a gap. In the general case, the first excited state of a semiconductor is obtained by promoting an electron from the top of the valence band to the bottom of the conduction band. To describe the dynamics of electrons in the system, it is convenient to describe the valence band lacking a single negative charge as a positively charged quasi-particle that is called a hole. The electron and the hole are delocalized over the crystal and the two carrier wavefunctions are usually uncorrelated: the probability of presence of the electron at a given position is independent of the position of the hole. This excited state is called an electron-hole pair. Yet, it does not constitute the lowest possible excited state of the semiconductor: the Coulomb interaction between the electron and the hole can lead to the formation of a bound state. This quasi-particle is called an exciton [9].

1.1.1 Excitons in the bulk

To describe the exciton, we consider the system composed of two charged massive particles, an electron and a hole respectively of effective masses m_e^* and m_h^* . They carry opposite charges $q_e = -e$ and $q_h = +e$. In the vicinity of $\mathbf{k} = 0$, the conduction and valence bands of a direct gap semiconductor can be approximated by parabolas. The conduction band electron is therefore described as a free particle with a positive effective mass and, the electrons in the valence band having a negative effective mass, the hole is also described as a free particle of positive effective mass. Their energy dispersions read:

$$\begin{aligned} E_e(\mathbf{k}) &= E_g + \frac{\hbar^2 k^2}{2m_e^*} \\ E_h(\mathbf{k}) &= -\frac{\hbar^2 k^2}{2m_h^*} \end{aligned} \quad (1.1)$$

where E_g represents the amplitude of the energy gap of the material and k is the norm of wavevector \mathbf{k} . Electron and hole wavefunctions are described by Bloch functions, respectively:

$$\phi_e^{\mathbf{k}}(\mathbf{r}) = e^{i\mathbf{k}\cdot\mathbf{r}} u_e(\mathbf{r}) \quad \text{and} \quad \phi_h^{\mathbf{k}}(\mathbf{r}) = e^{i\mathbf{k}\cdot\mathbf{r}} u_h(\mathbf{r}) \quad (1.2)$$

where u_e and u_h are periodic functions over the crystalline lattice. This description is not anymore valid if we consider the electron-hole Coulomb interaction. In this case the system is governed by the following Hamiltonian:

$$\mathcal{H}_{eh} = E_g + \frac{p_e^2}{2m_e^*} + \frac{p_h^2}{2m_h^*} - \frac{e^2}{4\pi\kappa\|\mathbf{r}_e - \mathbf{r}_h\|} \quad (1.3)$$

with \mathbf{r}_e and \mathbf{p}_e (respectively \mathbf{r}_h and \mathbf{p}_h) being the position and momentum of the electron (the hole). κ is the dielectric constant of the medium. The interaction term couples the electron and hole positions which are therefore not independent. It is more convenient to describe the resulting quasi-particle, called an exciton, in the center of mass frame.

We consider the coordinates $\boldsymbol{\rho} = \mathbf{r}_e - \mathbf{r}_h$ and $\mathbf{R} = \frac{m_e^* \mathbf{r}_e + m_h^* \mathbf{r}_h}{M}$, which corresponds to the relative and center of mass position of the coupled system, as well as the reduced and total masses $\mu = \frac{m_e^* m_h^*}{M}$ and $M = m_e^* + m_h^*$. The associated momenta read $\mathbf{p} = -i\hbar\nabla_{\boldsymbol{\rho}}$ and $\mathbf{P} = -i\hbar\nabla_{\mathbf{R}}$. Under this formalism, the Hamiltonian is separable:

$$\begin{aligned} \mathcal{H}_X &= \mathcal{H}_{\text{CM}} + \mathcal{H}_{\text{Rel}} \\ \mathcal{H}_{\text{CM}} &= E_g + \frac{P^2}{2M^*} \quad \text{and} \quad \mathcal{H}_{\text{Rel}} = \frac{p^2}{2\mu} - \frac{e^2}{\kappa\rho} \end{aligned} \quad (1.4)$$

highlighting the internal and external dynamics of the exciton which are respectively described by \mathcal{H}_{Rel} and \mathcal{H}_{CM} . As these two Hamiltonians commute, the corresponding dynamics are independent and one can search for eigenstate that are product of solution of \mathcal{H}_{Rel} and \mathcal{H}_{CM} . \mathcal{H}_{Rel} is an hydrogenoid Hamiltonian, its eigenstates are the well-known orbitals of an hydrogenoid atom (labeled ϕ_n with $n = \{1s, 2s, 2p_x, \dots\}$ the principal quantum number) whereas \mathcal{H}_{CM} describes the motion of a free particle and its solution is given by plane waves. The general expression of the solutions of \mathcal{H}_X reads:

$$\Psi_{\mathbf{K},n}^X(\mathbf{R}, \boldsymbol{\rho}) = e^{i\mathbf{K}\cdot\mathbf{R}} \phi_n(\boldsymbol{\rho}) \quad (1.5)$$

and the energy dispersion for a bulk exciton with principal quantum number n yields:

$$E_{X,n}(\mathbf{K}) = E_g + \frac{\hbar^2 K^2}{2M} - \frac{R^*}{n^2} \quad (1.6)$$

where $R^* = \hbar^2/2\mu a_B^2$ is the Rydberg energy of the exciton, which corresponds to its binding energy. a_B is the Bohr-radius of the exciton which is given by $a_B = 4\pi\kappa\hbar^2/\mu e^2$.

1.1.2 Excitons in quantum wells

We now consider a semiconductor quantum well, a hetero-structure consisting in a quasi-2D semiconductor layer of size $L_x \times L_y \times L_z$ with $L_z \sim a_B$, embedded between layers of semiconductor materials possessing a higher energy gap. These surrounding layers therefore act as a potential barrier. In this hetero-structure, illustrated in Fig. 1.1, the excitons are confined along the z spatial direction and are free to propagate in the (Oxy) plane. The potential barriers induce a modification of the Hamiltonian given in equation 1.3 which consists in additional terms acting on z_e and z_h , the electron and hole position along the z direction. It yields:

$$\mathcal{H}_{eh} = E_g + \frac{p_e^2}{2m_e^*} + \frac{p_h^2}{2m_h^*} - \frac{e^2}{\kappa|\mathbf{r}_e - \mathbf{r}_h|} + V_e(z_e) + V_h(z_h) \quad (1.7)$$

where V_e (V_h) is the amplitude of the potential barriers acting on the electron (the hole).

This Hamiltonian cannot be separated in center of mass and relative motion, it is only possible when the in plane motion can be decoupled from the motion along the z direction i.e. when the Coulomb interaction depends only on the in plane position. This is valid when the electron and hole wavefunctions are confined in a quantum well whose thickness is on the order of the Bohr radius a_B [9]. In that case the wavefunction of the exciton can be searched in the form:

$$\Psi_{\mathbf{K},n}^X(\mathbf{R}, \boldsymbol{\rho}, z) = e^{i\mathbf{K}\cdot\mathbf{R}} \chi_h(z) \chi_e(z) \phi_n(\boldsymbol{\rho}) \quad (1.8)$$

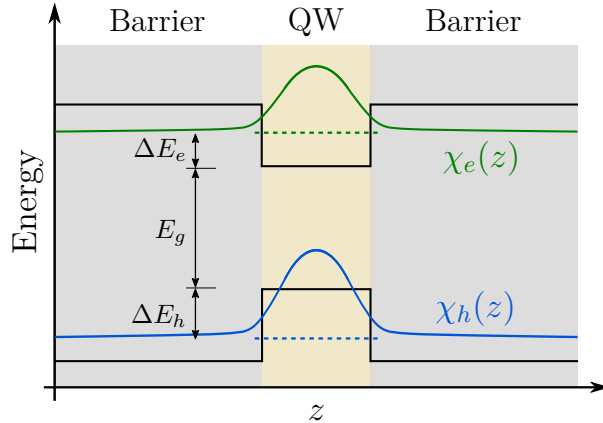


Figure 1.1: Scheme of the quantum well embedded between two higher energy gap semiconductors. Electron and hole envelope wavefunctions χ_e and χ_h are depicted, as well as potential barriers represented by black solid lines.

where \mathbf{K} , \mathbf{R} and $\boldsymbol{\rho}$ now represent the wave vector and position of the center of mass and relative position of the electron hole pair in the (Oxy) plane. ϕ_n is a the solution of the 2D hydrogenoid equation. $\chi_e(z)$ ($\chi_h(z)$) is the ground-state solution of the 1D Schrödinger equation for an electron (a hole) in a potential $V_e(z)$ ($V_h(z)$) with an associated energy noted ΔE_e (ΔE_h). The energy dispersion of the exciton reads:

$$E_{X,n}(\mathbf{K}) = E_g + \Delta E_e + \Delta E_h + \frac{\hbar^2 K^2}{2M} - \frac{R^*}{(n - \frac{1}{2})^2} \quad (1.9)$$

In addition to an increase of the energy due to the electron and hole confinement, the main evolution with respect to the bulk dispersion is the modification of the binding energy which now depends on $n - \frac{1}{2}$ due to the reduced dimensionality of the exciton. In a purely 2D case, the binding energy of the $n = 1s$ exciton is therefore four times bigger than its bulk binding energy. A theoretical prediction of the dependence of the binding energy as a function of the size of the quantum well can be found in Ref. [10].

In the works reported in this manuscript, we will consider shallow $\text{In}_x\text{Ga}_{1-x}\text{As}$ quantum wells in which the electron and hole wavefunctions spread outside of the quantum well. The binding energy of the exciton is thus close to the bulk one: it is on the order of a few milli-electronvolts ($R_{\text{eff}}^* \sim 5 \text{ meV}$). These excitons can therefore only be observed at cryogenic temperature (in the limit $R^* \gg k_B T$).

1.1.3 Exciton radiative recombination

Let us now describe the coupling between an exciton and the electromagnetic field: the absorption of a photon can lead to the formation of a bound electron-hole pair and this pair can radiatively recombine. To describe the radiative recombination of the exciton, we consider the interaction of the electron with the electromagnetic field. In the dipolar approximation and under the Coulomb gauge, it is approximated to:

$$\mathcal{H}_{\text{int}} \approx -\frac{e}{m_e^*} \mathbf{p} \cdot \mathbf{A} \quad (1.10)$$

where \mathbf{A} is the vector potential associated to the electromagnetic field and \mathbf{p} is the momentum of an electron of charge $-e$ and mass m_e^* .

The exciton can couple to a continuum of photon states, the probability to absorb a photon to form an exciton is thus given by the Fermi golden rule and is proportional to the matrix element $\langle \mathbf{K} | \mathbf{p} \cdot \mathbf{A} | 0 \rangle$ where $|0\rangle$ is the ground state of the quantum well and $|\mathbf{K}\rangle$ is the excitonic state of wave vector \mathbf{K} . Radiative excitonic transitions are characterized by an oscillator strength f_{osc} associated to the exciton radiative lifetime Γ_0 :

$$f_{\text{osc}} = \frac{2}{m_e^* \Delta E} |\langle \mathbf{K} | \mathbf{p} \cdot \mathbf{A} | 0 \rangle|^2 \quad \text{and} \quad \Gamma_0 = \frac{e^2}{2\varepsilon_l m_e^* c} \frac{f_{\text{osc}}}{S} \quad (1.11)$$

with ΔE the energy associated to the transition and ε_l is the dielectric constant. f_{osc}/S is the oscillator strength per unit surface [11]:

$$\frac{f_{\text{osc}}}{S} = \frac{2}{m_e^* \Delta E} |\phi(\mathbf{0})|^2 |\langle u_e | \epsilon \cdot \mathbf{p} | u_h \rangle|^2 \left| \int \chi_h(z) \chi_e^*(z) dz \right|^2 \quad (1.12)$$

with $\phi(\mathbf{0})$ the Fourier transform of the envelope function of the exciton, $\langle u_e | \epsilon \cdot \mathbf{p} | u_h \rangle$ is an element of the Kane matrix characteristic of the material where ϵ represents the polarization of the electromagnetic field and $\left| \int \chi_h(z) \chi_e^*(z) dz \right|^2$ is the overlap integral between the electron and hole envelope functions along z .

The matrix element $\langle \mathbf{K} | \mathbf{p} \cdot \mathbf{A} | 0 \rangle$ is non-zero in specific cases, corresponding to several selection rules to be satisfied for an allowed optical transition. Firstly, the transition must satisfy the angular momentum conservation. As a consequence, only excitons with angular momentum $J_{z,X} = \pm 1$ or $J_{z,X} = 0$ can couple to the electromagnetic field. The excitonic angular momentum is given by the sum of electron and hole angular momenta, in the conduction band the electron angular momentum projection along z is $J_{z,e} = \pm \frac{1}{2}$ while the case of a hole in the valence band is a bit more subtle: there exist two types of holes called heavy-holes (hh) and light-hole (lh) in reference to their respective masses ($m_{hh} > m_{lh}$). They possess angular momentum projections $J_{z,hh} = \pm \frac{3}{2}$ and $J_{z,lh} = \pm \frac{1}{2}$. Light-holes are less confined in the structure due to their lower effective mass and in the following we will consider the heavy-hole excitons only. There exists two types of heavy-hole excitons, those with total angular momentum projection $J_{z,X} = \pm 1$ which can couple to light and those with $J_{z,X} = \pm 2$ that do not radiate and are thus called dark excitons.

Secondly, due to the translation invariance along x and y , the projection of the wave vector in the (Oxy) plane must be conserved: $\mathbf{k}_{\parallel} = \mathbf{K}$, where \mathbf{k} is the electromagnetic field wavevector. Note that no conservation rule applies to k_z as the translation invariance of the semiconductor material is broken, which is not the case when considering bulk excitons. Neglecting the radiative linewidth and equating the energy of a photon propagating inside the quantum well ($E_{\text{ph}} = \hbar ck/n$, defining the so-called light-cone) to the one of the exciton with the same in-plane momentum sets an upper bound to \mathbf{K} that we label k_{rad} . k_{rad} is given by the following relation:

$$\frac{\hbar ck_{\text{rad}}}{n_s} = E_X(\mathbf{K} = \vec{0}) + \frac{\hbar^2 k_{\text{rad}}^2}{2M} \quad (1.13)$$

Exciton states with in-plane momentum $K > k_{\text{rad}}$ are therefore non-radiative. This model accounts for the spontaneous emission of the QW which is coupled to a continuum and radiates in all directions.

from an interference process involving the multiple reflections of the incident field between the two mirrors. The total transmitted field reads:

$$E_t = E_i t_1 t_2 e^{i\phi_c/2} \sum_{\ell=0}^{\infty} (r_1 r_2 e^{i\phi_c})^{\ell} = \frac{E_i t_1 t_2 e^{i\phi_c/2}}{1 - r_1 r_2 e^{i\phi_c}} \quad \text{with} \quad \phi_c = 2\pi \frac{2L_{\text{cav}} \cos(\theta_c) n_{\text{cav}}}{\lambda_0} \quad (1.14)$$

where ϕ_c is the phase accumulated per round-trip in the cavity.

Neglecting absorption, the intensity transmission and reflection coefficients are given by:

$$T_c(\lambda_0) = \left| \frac{E_t}{E_i} \right|^2 = \frac{(t_1 t_2)^2}{1 + (r_1 r_2)^2 - 2r_1 r_2 \cos(\phi_c)} \quad \text{and} \quad R_c = 1 - T_c \quad (1.15)$$

Transmission maxima are obtained when the multiply reflected fields interfere constructively: in this case the phase accumulated over a round-trip in the cavity is a multiple of 2π . In spectral regions where the cavity components can be approximated as non-dispersive ($\frac{\partial n_{\text{cav}}}{\partial \lambda_0} \approx 0$, $\frac{\partial r_i}{\partial \lambda_0} \approx 0$, ...) one can observe equally spaced resonances in the reflection and transmission energy spectra: the field is confined in the z direction and discrete modes appear inside the cavity. The frequency difference between each of these resonances defines the free spectral range (FSR) of the cavity which is the inverse of the time per round-trip τ_{RT} . It yields:

$$\Delta\nu_{\text{FSR}} = \frac{1}{\tau_{RT}} = \frac{c}{2n_{\text{cav}}L_{\text{cav}}} \quad (1.16)$$

Resonant frequencies can thus be written as $\nu_q = q\Delta\nu_{\text{FSR}}$, $q \in \mathbb{N}$. We can thus write the energy dispersion of a photon in the cavity. Writing \mathbf{k} its wave vector whose norm is given by $k = \sqrt{k_z^2 + k_{\parallel}^2}$ with $k_z = 2\pi c n_{\text{cav}} \nu_q = \frac{q\pi}{L_{\text{cav}}}$, it yields:

$$E_{C,q}(\mathbf{k}) = \frac{\hbar c}{n_{\text{cav}}} \sqrt{\left(\frac{q\pi}{L_{\text{cav}}}\right)^2 + k_{\parallel}^2} \quad k_z \gg k_{\parallel} \approx E_{C,q}(0) + \frac{\hbar^2 k_{\parallel}^2}{2m_{\text{ph}}} \quad (1.17)$$

where $E_{C,q}(0) = q\hbar\pi c/n_{\text{cav}}L_{\text{cav}}$ and m_{ph} is the effective mass of the photon in the cavity, with

$$m_{\text{ph}} = q \frac{\hbar\pi n_{\text{cav}}}{cL_{\text{cav}}} \quad (1.18)$$

In absence of loss, we obtain Lorentzian resonances with full width at half maximum (FWHM) given by [12]:

$$\Delta\nu_q = \frac{2}{\pi} \Delta\nu_{\text{FSR}} \sin^{-1} \left(\frac{1 - \sqrt{R_1 R_2}}{2\sqrt[4]{R_1 R_2}} \right) \quad \{R_1, R_2\} \sim 1 \approx \frac{\Delta\nu_{\text{FSR}}}{\pi} \frac{1 - \sqrt{R_1 R_2}}{\sqrt[4]{R_1 R_2}} \quad (1.19)$$

The ratio between the FSR and FWHM is called the finesse \mathcal{F} of the cavity, which represents the average number of round-trips traveled by a photon before it escapes the cavity:

$$\mathcal{F} = \frac{\Delta\nu_{\text{FSR}}}{\Delta\nu_q} \approx \pi \frac{\sqrt[4]{R_1 R_2}}{1 - \sqrt{R_1 R_2}} \quad (1.20)$$

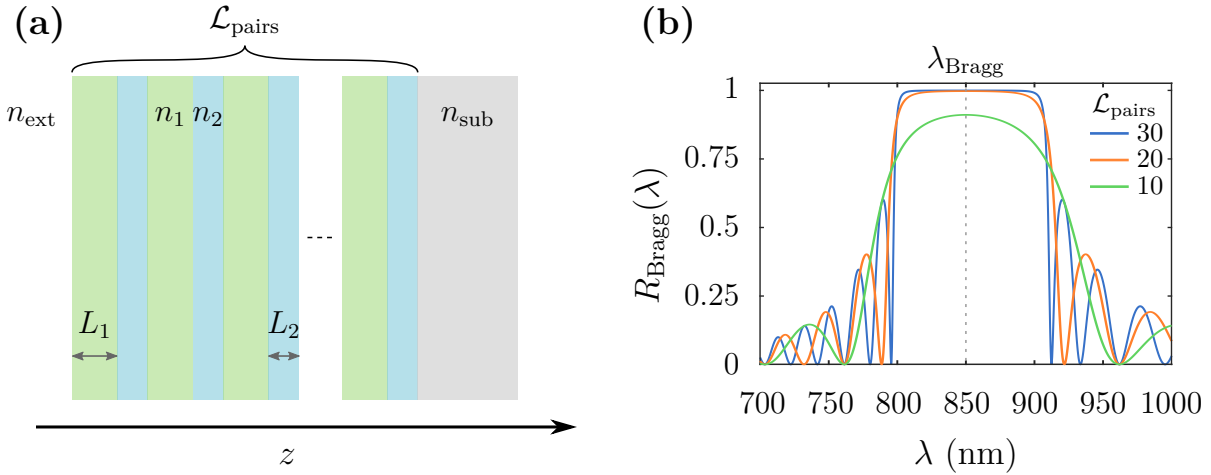


Figure 1.3: **a**, Scheme of the Bragg mirror structure. **b** Reflectivity spectrum of the DBR as a function of wavelength for various number of layer pairs with $\lambda_{\text{Bragg}} = 850$ nm, $n_1 = 2.9$ and $n_2 = 3.5$.

1.2.2 The distributed Bragg reflector

Multi-layer mirrors constitute an solution to obtain high reflectivities: if one designs a set of \mathcal{L} layers such that the field reflected on layer $\ell + 1$ destructively interferes with the field transmitted from layer $\ell - 1$ to layer ℓ , one can obtained a multi-layer mirror whose reflectivity is $R_{ML} = 1 - \varepsilon$ with $\lim_{\mathcal{L} \rightarrow \infty} \varepsilon = 0$.

A distributed Bragg reflector (DBR) is a periodic multi-layered structure (see Fig.1.3) composed of two different media of refractive indices n_1 and n_2 . The thickness of each layer is defined such that the optical paths are equal: $n_1 L_1 = n_2 L_2 = \lambda_{\text{Bragg}}/4$ with λ_{Bragg} the central wavelength at which we desire a high reflectivity. In this condition, interferences are destructive for multi-reflected waves while they are constructive for transmitted ones. Under normal incidence the DBR reflectivity at λ_{Bragg} can be obtained *via* transfer matrix computation [13] which consists in a matrix representation of Fresnel law of refraction. The propagating and contra-propagating electric fields after the interface between layers ℓ and $\ell + 1$ are related to those after the interface between layers $\ell - 1$ and ℓ *via* the matrix M_ℓ :

$$M_\ell(\lambda) = \begin{bmatrix} \exp(i2\pi L_\ell/\lambda) & r_{\ell,\ell+1} \exp(i2\pi L_\ell/\lambda) \\ r_{\ell,\ell+1} \exp(-i2\pi L_\ell/\lambda) & \exp(-i2\pi L_\ell/\lambda) \end{bmatrix} \quad \text{with} \quad r_{\ell,\ell+1} = \frac{n_\ell - n_{\ell+1}}{n_\ell + n_{\ell+1}} \quad (1.21)$$

The matrices associated to each layer can then be composed to relate the field at the surface of the mirror to the one at its output and the obtain the mirror reflectivity:

$$M_{\text{mirror}} = \dots M_{\ell+1,\ell+2} M_{\ell,\ell+1} \dots M_{1,2} M_{\text{ext},1}.$$

Applying this method to the case of a DBR yields:

$$R_{\text{DBR}}(\lambda_{\text{Bragg}}) = \left(\frac{1 - \frac{n_{\text{sub}}}{n_{\text{ext}}} \left(\frac{n_1}{n_2} \right)^{2\mathcal{L}_{\text{pairs}}}}{1 + \frac{n_{\text{sub}}}{n_{\text{ext}}} \left(\frac{n_1}{n_2} \right)^{2\mathcal{L}_{\text{pairs}}}} \right)^2 \stackrel{\mathcal{L}_{\text{pairs}} \gg 1}{\approx} 1 - 4 \frac{n_{\text{sub}}}{n_{\text{ext}}} \left(\frac{n_1}{n_2} \right)^{2\mathcal{L}_{\text{pairs}}} \quad (1.22)$$

where n_{sub} is the refractive index of the substrate on which the mirror is placed and $n_1 < n_2$. The reflectivity bandwidth of the DBR, also called the stop-band, is given

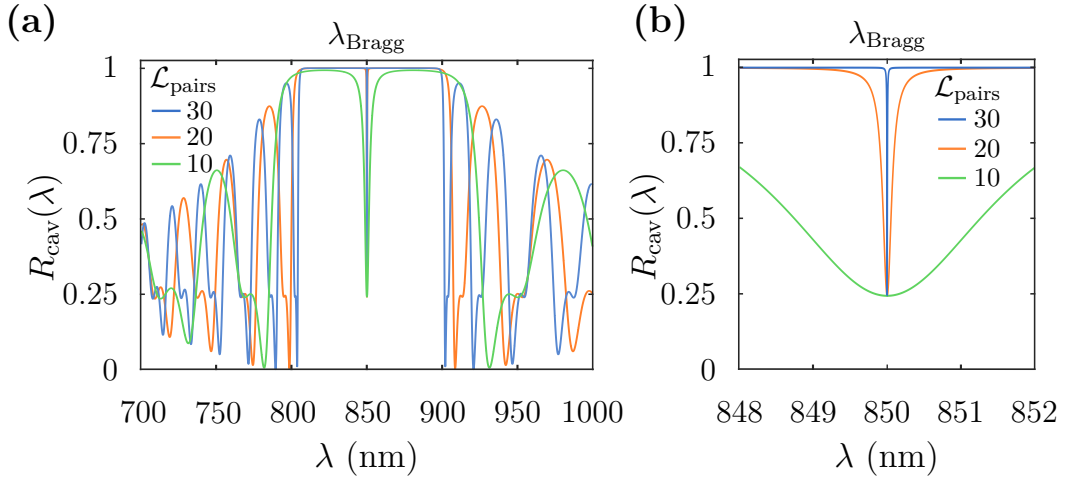


Figure 1.4: **a**, Reflectivity spectrum of a cavity composed of two DBRs. DBR parameters correspond to those used in fig. 1.3, L_{cav} is adjusted for the first cavity resonance to match λ_{Bragg} . **b**, Zoom of **(a)** around the cavity resonance.

by:

$$\frac{\Delta\nu_{\text{Bragg}}}{\nu_{\text{Bragg}}} = \frac{4}{\pi} \sin^{-1} \left(\frac{n_2 - n_1}{n_2 + n_1} \right) \quad n_2 \approx n_1 \quad \frac{4}{\pi} \left(\frac{n_2 - n_1}{n_2 + n_1} \right) \quad (1.23)$$

Increasing the number of pairs thus increases the reflectivity of the mirror but leaves its stop-band unchanged (see Fig.1.3).

1.2.3 The Bragg mirror cavity

To form a Fabry-Pérot cavity with two DBRs we need to approximate each DBR to a thin layer. To do so we consider the characteristic penetration depth of the field in the mirror L_{Bragg} and compute the associated dephasing, ϕ_r , undergone by the field at each reflection on the mirror:

$$\phi_{\text{Bragg}}(\nu) = \frac{2\pi n_{\text{ext}}}{c} L_{\text{Bragg}} (\nu - \nu_{\text{Bragg}}) \quad \text{with} \quad L_{\text{Bragg}} = \frac{c}{2\nu_{\text{Bragg}} n_{\text{ext}}} \frac{n_1}{(n_2 - n_1)} \quad (1.24)$$

Note that L_{Bragg} is defined as the photon path length inside the mirror, the field thus only penetrates up to $L_{\text{Bragg}}/2$.

We now consider a Fabry-Pérot cavity formed of two DBRs, the cavity length is selected such that the cavity resonance is matched to the mirror central wavelength $L_{\text{cav},q} = q\lambda_{\text{Bragg}}/2n_{\text{cav}}$. The photon energy dispersion in the cavity yields:

$$E_{C,q}(k_{\parallel}) = \sqrt{E_{C,q}(k_{\parallel} = 0)^2 + \left(\frac{\hbar c}{n_{\text{eff}}} k_{\parallel} \right)^2} \quad \text{with} \quad n_{\text{eff}}^2 = \int \varphi(z)^* \varepsilon_l(z) \varphi(z) dz \quad (1.25)$$

n_{eff} being the effective index of the cavity [14], ε_l the dielectric constant that now varies over the structure and φ is a longitudinal mode of the cavity, normalized such that $\int |\varphi|^2 dz = 1$.

In the vicinity of $\lambda = \lambda_{\text{Bragg}}$, the cavity transmission coefficient can be approximated by a modified version of equation 1.15 where ϕ_c as to be replaced by a dephasing ϕ_t taking the mirror dephasing into account: $\phi_t = \phi_c + 2\phi_{\text{Bragg}}$. In other words, it means that the cavity length is modified due to the field penetration inside

de mirrors resulting in an effective cavity length $L_{\text{eff}} = L_{\text{cav},q} + L_{\text{Bragg}}$. Figure 1.4 shows the reflection spectrum obtained for such a cavity calculated using transfer matrices. One can observe a reflectivity dip centered on $\lambda_{\text{Bragg}} = \lambda_{q=2}$. A zoom around the cavity resonance is presented in Fig. 1.4 (b), showing how the number of pairs affects the spectral linewidth: the more we add pairs, the smaller is the mode linewidth. Note that, as the FSR is bigger than the mirror stop-band, a single cavity resonance is observed over the cavity stop-band¹.

1.3 Exciton-photon hybrid quasi-particles

Now that we introduced the two building blocks of polariton micro-cavities, we can turn to the description of the strong coupling regime between quantum well excitons and cavity photons obtained by embedding the quantum well inside a high finesse cavity. This strong light-matter coupling leads to the emergence of hybrid eigenstates that are mixed states of photons and excitons called polaritons. Polaritons will be shown to inherit physical properties from both components, which makes the polaritonic platform particularly appealing for the exploration of a plethora of physical effects: polaritons exhibiting a low mass compared to the one of the electron, they are able to propagate on long distances while their excitonic nature is responsible for a strong polariton-polariton interaction enabling the observation of highly non-linear phenomena such as superfluidity.

1.3.1 Light-matter strong coupling

Let us now consider the case where the quantum well is inserted inside a photonic cavity. Upon recombination of the exciton, a photon is emitted inside the cavity. If the cavity resonance is matched to the photon energy, this photon will remain inside the cavity for a time equal to $Q/2\pi$ optical periods, with Q the quality factor of the considered mode. The photon can thus be reabsorbed inside the QW to re-excite the exciton. Considering a high finesse cavity, this absorption-remission process occurs multiple times before the photon escapes the cavity. This coherent transfer of an excitation between two coupled harmonic oscillators is called Rabi oscillation and leads to the redefinition of the system's eigenstates due to the Rabi splitting. In this strong coupling regime, the excitation can neither be considered as a cavity photon nor as a quantum well exciton, it is a superposition called a polariton and which has an energy dispersion differing from the bare exciton and cavity ones.

As a first approach to describe the transition between weak and strong light-matter coupling, one can use a semi-classical representation of the excitonic and photonic transitions as two coupled Lorentz oscillators [11, 16] with same bare energies $E_X = E_C = E_0$ and different damping rates γ_X and γ_{ph} . γ_X represents the non-radiative decay channels of the excitonic states and $\gamma_{\text{ph}} = h\Delta\nu_q$ the cavity

¹**Note concerning the polarization of light:** the model presented above is scalar and does not consider the vectorial nature of light. Yet multi-layered mirrors reflections are often subject to birefringence and the cavity characteristics may therefore depend on polarization. In the case of a centered cavity ($\lambda_{\text{Bragg}} = \lambda_q$) these effects are negligible [15]

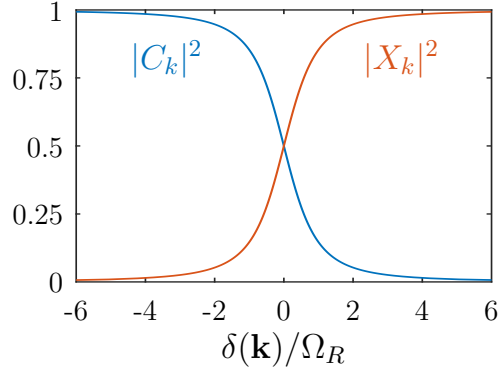


Figure 1.5: Evolution of the Hopfield coefficient amplitudes as a function of the cavity-exciton detuning $\delta(\mathbf{k})$ normalized to the Rabi splitting Ω_R .

losses. The coherent coupling between the two oscillators reads:

$$g_0 = \sqrt{\frac{2c\Gamma_0}{n_{\text{cav}}L_{\text{eff}}}} \propto \sqrt{\frac{f_{\text{osc}}}{L_{\text{eff}}}} \quad (1.26)$$

where Γ_0 is the bare exciton radiative decay rate. To maximize the coupling amplitude, one has to maximize the overlap between the photon and exciton wavefunctions: the quantum well is thus centered on a maximum of the intra-cavity electric field distribution. Note that the coupling can be further increased by inserting more than a single quantum well inside the cavity (g_0 scaling as \sqrt{N} with N the number of QWs). On the other hand, one has to minimize the electric-field mode volume, $L_{\text{cav},q}$ is thus chosen to be the smallest value verifying the resonance condition with a maximum of the field in the cavity center ($q = 2$). The eigenenergies of the coupled system read:

$$E_{\pm} = E_0 \pm \Omega_R/2 = E_0 \pm \sqrt{g_0^2 - \frac{(\gamma_X - \gamma_{\text{ph}})^2}{4}} \quad (1.27)$$

for $g_0 < |\gamma_X - \gamma_{\text{ph}}|/4$, Ω_R is purely imaginary and the real part of the eigenenergies stay degenerate while the decay rates of each modes are modified. It corresponds to the weak coupling regime where a excitation in the system is rapidly dissipated and no coherence is built between the exciton and the cavity field. On the contrary, in the case $g_0 > |\gamma_X - \gamma_{\text{ph}}|/4$, Ω_R is real and thus the real part of the eigenenergies are splitted. In the experimental results discussed in this manuscript, the energy splitting is bigger than both exciton and photon linewidth ($g_0 > \{\gamma_X, \gamma_{\text{ph}}\}$) and the Rabi splitting is approximated to $\Omega_R \approx 2g_0$.

In solid state systems the first theoretical discussion of the strong coupling regime was realized by John Joseph Hopfield in 1958 [17]. Its first observation in 2D semiconductor micro-cavities with embedded QW was done by the group of Claude Weisbuch and Yasuhiko Arakawa in 1992 [18].

1.3.2 Quantum description of polaritons

The description of polaritons can be done under the second quantization formalism where creation and annihilation operators for photons and excitons are respectively written $a_{\mathbf{k}}^{\dagger}, a_{\mathbf{k}}$ and $b_{\mathbf{k}}^{\dagger}, b_{\mathbf{k}}$ with \mathbf{k} the in-plane wave-vector of the considered particle.

Those operators obey bosonic commutation relations: $[a_{\mathbf{k}}, a_{\mathbf{k}'}^\dagger] = \delta_{\mathbf{k}, \mathbf{k}'}$ and $[b_{\mathbf{k}}, b_{\mathbf{k}'}^\dagger] = \delta_{\mathbf{k}, \mathbf{k}'}$. The Hamiltonian describing the coupled system reads:

$$\mathcal{H} = \sum_{\mathbf{k}} \mathcal{H}_{\mathbf{k}} = \sum_{\mathbf{k}} E_C(k) a_{\mathbf{k}}^\dagger a_{\mathbf{k}} + E_X(k) b_{\mathbf{k}}^\dagger b_{\mathbf{k}} + \frac{\Omega_R}{2} (a_{\mathbf{k}}^\dagger b_{\mathbf{k}} + b_{\mathbf{k}}^\dagger a_{\mathbf{k}}) \quad (1.28)$$

This system can be diagonalized by introducing the polaritonic operators $p_{\mathbf{k}}^\dagger, q_{\mathbf{k}}^\dagger$ obtained from photonic and excitonic operators *via* the Hopfield coefficients C_k and X_k through the unitary transformation:

$$\begin{bmatrix} p_{\mathbf{k}}^\dagger \\ q_{\mathbf{k}}^\dagger \end{bmatrix} = \begin{bmatrix} C_k & X_k \\ -X_k & C_k \end{bmatrix} \begin{bmatrix} a_{\mathbf{k}}^\dagger \\ b_{\mathbf{k}}^\dagger \end{bmatrix} \quad (1.29)$$

C_k and X_k are real and positive that verify $|C_k|^2 + |X_k|^2 = 1$ and their respective amplitudes are given by:

$$\begin{aligned} |C_k|^2 &= \frac{1}{2} \left(1 - \frac{\delta(k)}{\sqrt{\delta(k)^2 + \Omega_R^2}} \right) \\ |X_k|^2 &= \frac{1}{2} \left(1 + \frac{\delta(k)}{\sqrt{\delta(k)^2 + \Omega_R^2}} \right) \end{aligned} \quad (1.30)$$

where $\delta(k) = E_C(k) - E_X(k)$ is the detuning between the photon and the exciton. $|C_k|^2$ and $|X_k|^2$ respectively correspond to the photonic and excitonic (respectively excitonic and photonic) fractions of the eigenstate associated to $p_{\mathbf{k}}$ and $p_{\mathbf{k}}^\dagger$ (respectively $q_{\mathbf{k}}$ and $q_{\mathbf{k}}^\dagger$). The evolution of the Hopfield coefficients as a function of the detuning is presented in Fig. 1.5. For $\delta(k)/\Omega_R \ll 0$ the eigenstate associated to $p_{\mathbf{k}}, p_{\mathbf{k}}^\dagger$ ($q_{\mathbf{k}}, q_{\mathbf{k}}^\dagger$) can be considered as purely photonic (excitonic) whereas it can be considered as purely excitonic (photonic) in the limit $\delta(k)/\Omega_R \gg 0$. In the regime where $\delta(k) \sim \Omega_R$ the eigenstates are mixed states of photons and excitons, the excitonic and photonic fractions being equal for $\delta(k) = 0$.

In the new basis described by $p_{\mathbf{k}}^\dagger, q_{\mathbf{k}}^\dagger$, the Hamiltonian writes:

$$\mathcal{H} = \sum_{\mathbf{k}} E_{LP}(k) p_{\mathbf{k}}^\dagger p_{\mathbf{k}} + E_{UP}(k) q_{\mathbf{k}}^\dagger q_{\mathbf{k}} \quad (1.31)$$

where E_{LP} and E_{UP} are the dispersion relations for the lower and upper polariton branches, respectively, which read:

$$E_{LP}^{UP}(k) = \frac{1}{2} \left(E_C(k) + E_X(k) \pm \sqrt{\delta(k)^2 + \Omega_R^2} \right) \quad (1.32)$$

the terminology ‘‘upper’’ and ‘‘lower’’ referring to the energy hierarchy between the two branches ($E_{UP}(k) > E_{LP}(k)$).

In practice the exciton effective mass is much bigger than the photon one and can be assumed as infinite ($E_X(k) = E_X$). A calculation of the polariton dispersion under this assumption for different values of $\delta(k=0)$ is presented in Fig. 1.6, together with the corresponding photonic and excitonic fractions given by $|C_k|^2$ and $|X_k|^2$ for the lower polariton branch. An avoided crossing is observed in the vicinity of $\delta(k) = 0$, associated with a minimum of the energy splitting between the two branches corresponding to $\Delta E_{UP-LP} = \Omega_R$. This avoided crossing is characteristic of the strong coupling regime.

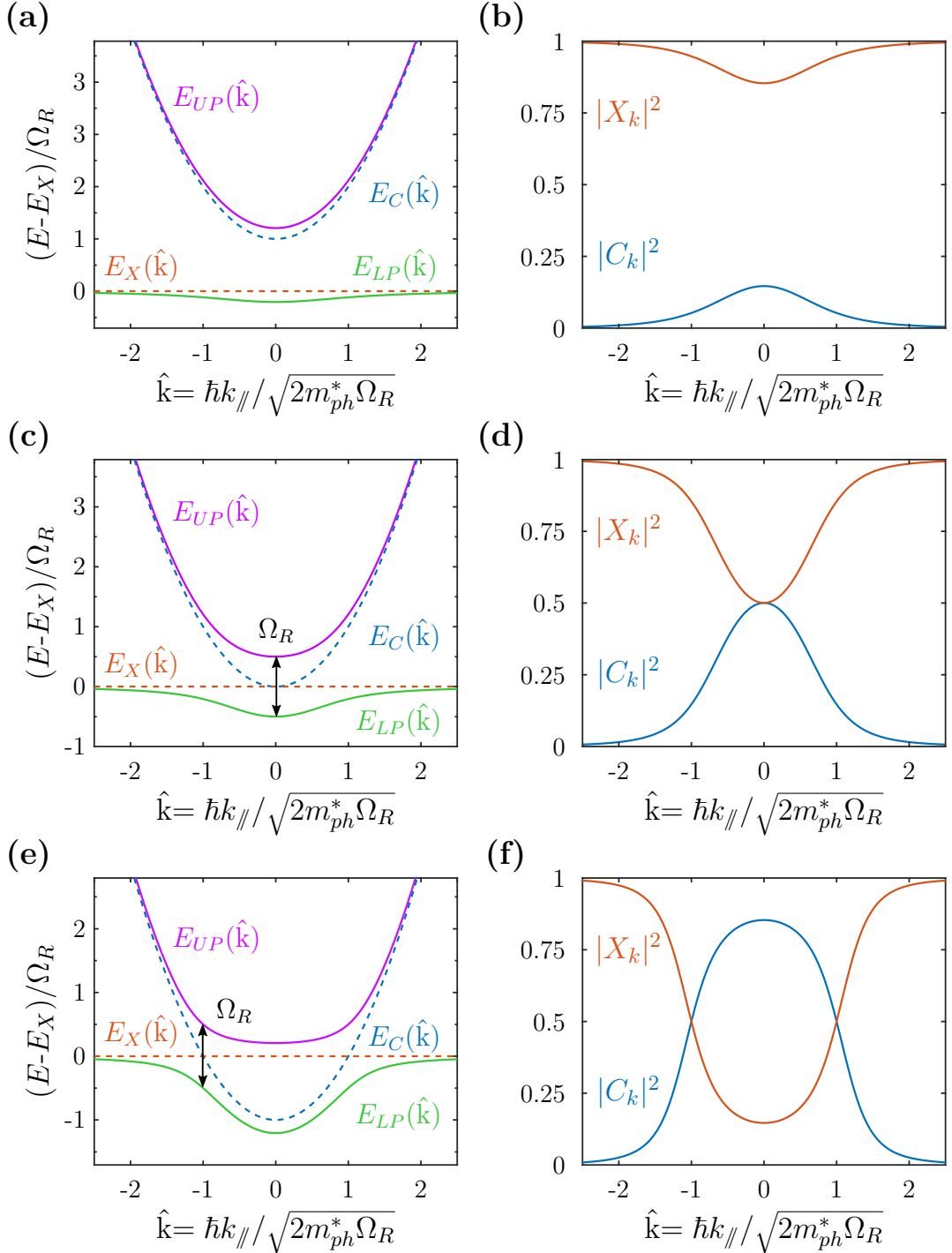


Figure 1.6: Left panels: Simulated dispersions for upper and lower polariton branches (solid lines) as well as for the cavity photon and quantum well exciton (dashed lines). Right panels: Amplitudes of the Hopfield coefficients associated to left. The three sets of figures correspond to different values of the cavity-exciton detuning:

(a)-(b) $\delta(0) = +\Omega_R$, (c)-(d) $\delta(0) = 0$ and (e)-(f) $\delta(0) = -\Omega_R$

1.3.3 Polaritons characteristics

Polaritons being a weighted superposition of photons and excitons, they inherit characteristics from these two constituents. In the following paragraphs, we discuss the single particle polariton properties. We address the non-linear properties, induced by polariton-polariton interaction mediated *via* the excitonic part, later on in Sec. 1.5.

Firstly, quantum well excitons and cavity photons were both previously described as massive free particles, their dispersion being thus approximately parabolic. To some extent this approximation can also be done for polaritons: in the vicinity of $k = 0$, the polariton dispersions can be approximated by parabolic branches with effective masses:

$$\begin{aligned} \frac{1}{m_{\text{LP}}^*} &= \frac{|X_k|^2}{M} + \frac{|C_k|^2}{m_{\text{ph}}^*} \stackrel{M \gg m_{\text{ph}}^*}{\approx} \frac{|C_k|^2}{m_{\text{ph}}^*} \\ \frac{1}{m_{\text{UP}}^*} &= \frac{|C_k|^2}{M} + \frac{|X_k|^2}{m_{\text{ph}}^*} \stackrel{M \gg m_{\text{ph}}^*}{\approx} \frac{|X_k|^2}{m_{\text{ph}}^*} \end{aligned} \quad (1.33)$$

In all cases discussed in this manuscript, we focus on the lower polariton branch with negative cavity-exciton detuning. The considered polaritons thus present an effective mass relatively close to the one of cavity photons $m_{\text{LP}}^* \sim 10^{-5}m_e$, m_e being the electron mass. These polaritons can thus propagate on long distances typically of the order $D \sim 200 \mu\text{m}$ [19].

Secondly, even though the Rabi splitting can be approximated to $\Omega_R \approx 2g_0$ by neglecting contributions from exciton and photon linewidths, polaritonic states remains inherently dissipative. To account for their finite lifetime we can consider complex energies for the photon and the exciton $E_X^*(\mathbf{k}) = E_X(\mathbf{k}) - i\gamma_X$ and $E_{\text{ph}}^*(\mathbf{k}) = E_{\text{ph}}(\mathbf{k}) - i\gamma_{\text{ph}}$, the polariton eigenenergies thus become complex. Their real parts correspond to the previously calculated energy dispersions, E_{LP} and E_{UP} , while their imaginary parts correspond to the polariton linewidth, γ_{LP} and γ_{UP} . It yields:

$$\begin{aligned} \gamma_{\text{UP}} &= |C_k|^2\gamma_X + |X_k|^2\gamma_{\text{ph}} \\ \gamma_{\text{LP}} &= |X_k|^2\gamma_X + |C_k|^2\gamma_{\text{ph}} \end{aligned} \quad (1.34)$$

Note that the \mathbf{k} dependence of γ_{ph} is *a priori* non-trivial as it accounts for cavity losses due to its finite finesse \mathcal{F} but also to the residual absorption of light in the cavity. Same goes for γ_X which accounts for all possible non-radiative decay channels of the exciton (phonon and trap mediated recombination, Auger process,...). In our samples, an important contribution to the exciton linewidth comes from the inhomogeneous broadening which is known to also impact the polariton linewidth [20]. Photo-luminescence measurements of 17nm $\text{In}_{0.04}\text{Ga}_{0.96}\text{As}$ QWs lead to measured values $\gamma_X \sim 0.4\text{-}0.7 \text{ meV}$ which is much larger than the expected exciton radiative lifetime $\gamma_{X,\text{rad}} \approx 0.04 \text{ meV}$.

Finally, we previously established that a radiative recombination event is only accessible to excitons with angular momentum projection $J_z = \pm 1$, resulting into the emission of a circularly polarized photon. As a consequence, the angular momentum projection of polaritons is also bound to $J_z = \pm 1$ and, in absence of any mechanism coupling these two pseudo-spin states, the associated dispersions are degenerate. The polaritons behave as particles with 1/2 pseudo-spin which can be represented

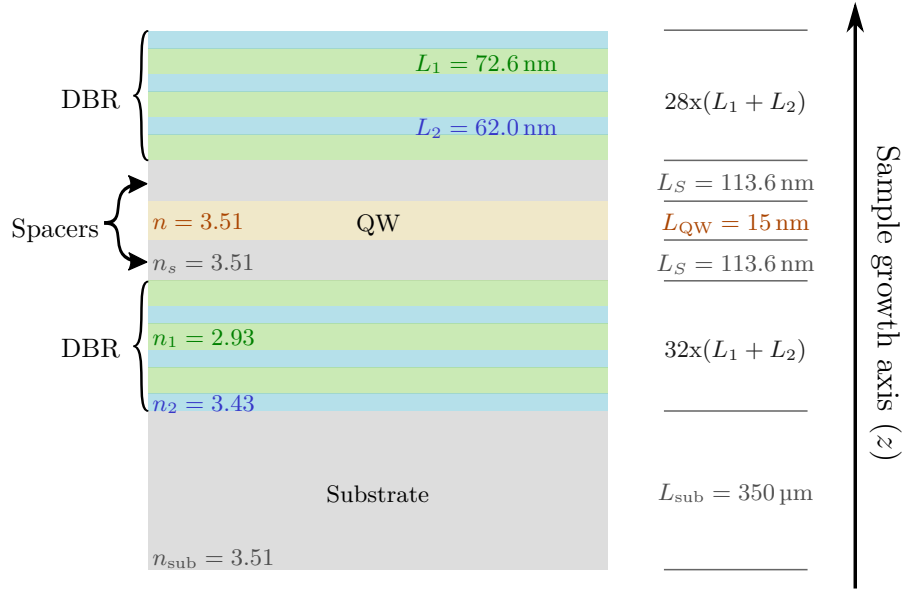


Figure 1.7: Schematic representation of the sample structure with nominal values considered for its growth.

on the Poincaré sphere and the measure of this pseudo-spin can be done by realizing the polarization tomography of photons escaping the cavity.

1.4 Experimental observation

This section is dedicated to the description of samples and experimental methods employed to study them. We first focus on the general description of the micro-cavity structure considered in experiments reported in this thesis and introduce the experimental setup used to characterize it.

1.4.1 Sample structure

In this manuscript we mostly focused on a single type of sample dedicated to study non-linear phenomena. As it will be detailed later in Sec. 1.5, these experiments are done considering a quasi-resonant excitation and it is therefore convenient to operate measurements in a transmission geometry. Indeed, by collecting the light propagating through the cavity, we avoid being blinded by the intense field that is reflected by the top of the first cavity mirror. To operate in transmission, the energy of the polaritons thus needs to be lower than the gap of the sample substrate which consist in 300 μm of GaAs. The quantum well is thus doped with indium (In)²

The samples considered in this thesis were grown by Aristide Lemaître and Martina Morassi in the clean-room facilities of C2N. It consists in a single 15 nm $\text{In}_{0.05}\text{Ga}_{0.95}\text{As}$ quantum well, corresponding to an exciton transition at $E_X = 1.455$ eV ($\lambda_X = 852$ nm) with a linewidth of typically 0.5 meV, embedded in a λ GaAs cavity. We use two DBRs with 28 (top mirror) and 32 (bottom mirror) pairs of

²This doping results in alloy fluctuations which induce an inhomogeneous broadening of the exciton. In practice a compromise as to be found between the residual absorption in the cavity mirrors and inhomogeneous broadening of the exciton.

$\text{Ga}_{0.9}\text{Al}_{0.1}\text{As}/\text{Ga}_{0.05}\text{Al}_{0.95}\text{As}$ yielding a nominal finesse of about $\mathcal{F} = 140000$ ³. By design, the quantum well position coincides with the maximum of the cavity mode electric field (itself in the center of the cavity for $L_{\text{cav}} = \lambda_0/n_{\text{GaAs}}$). A sketch of the structure is presented in Fig. 1.7.

To increase the range of parameters accessible on a single sample, a wedge in the spacer thickness is introduced during the growth procedure. It results in a spatial gradient of the cavity mode energy in the (Oxy) plane. Probing different regions of such 2D structure thus allows varying the cavity-exciton detuning $\delta(\mathbf{k}=\mathbf{0})$.

1.4.2 Experimental setup

The samples are cooled down to cryogenic temperatures using closed-cycle cryostations. Non-linear experiments and associated linear characterizations were realized with a sample cooled down and stabilized to 4 K.

Note that some spectroscopy measurements only involving the linear behavior of polaritons were done in a continuous-flow cryostation. In such equipment liquid helium is continuously injected and its flow is manually controlled to set the cold finger temperature to about 7-10 K.

All characterizations and experiments reported in this work were done optically, under a continuous wave excitation produced by a monomode Ti:Sapphire laser. Its wavelength can be tuned over a range covering the 750-880 nm spectrum and its linewidth is below 10 MHz (40 neV). To filter the spatial mode of the laser, its output beam is coupled into a polarization maintaining fiber. The fiber output produces a spatially gaussian beam with 2 mm waist.

The excitation path contains a power control stage followed by a polarization filtering stage. A coarse modification of the optical power is done using neutral density filters (ND) and a finer control is realized using a half-wave plate (HWP) followed by a polarizing beam-splitter (PBS). The latter allows to realize continuous scans of the power by rotating the HWP. Measurements of the optical power are realized using a beam-splitter placed just before the cryostation. The polarization state, which is already filtered by the PBS, can be tuned to any point of the Poincaré sphere using a quarter-wave plate (QWP) followed by a HWP. Depending on the accessibility to the sample, given by the considered cryostation, the light is focused on the cavity surface either using a microscope objective with magnification 50x and long working distance (\sim cm), mounted outside the cryostation, or using an aspherical lens with short focal length ($f' = 4.51$ mm) that is placed inside the cryostation and moved using nanopositioners. In both cases the numerical aperture is $NA = 0.55$.

Photons transmitted through the cavity are collected using a microscope objective or an aspherical lens, and focused on the entrance split of a spectrometer. The entrance plane of the spectrometer is imaged onto a CCD camera with a 1x magnification. Depending on the measurement, we either collect the zeroth or first

³Higher finesse could theoretically be reached by increasing the number of pairs ($\mathcal{F} \sim 2 \times 10^6$ for $\mathcal{L}_{\text{pairs}} \sim 40$). However experimental observations show that the residual absorption in the cavity is already limiting the linewidth to $\mathcal{F} \sim 65000$ for $\mathcal{L}_{\text{pairs}} \sim 30$ and a higher reflectivity of the mirrors would thus simply lead to a weaker output signal.

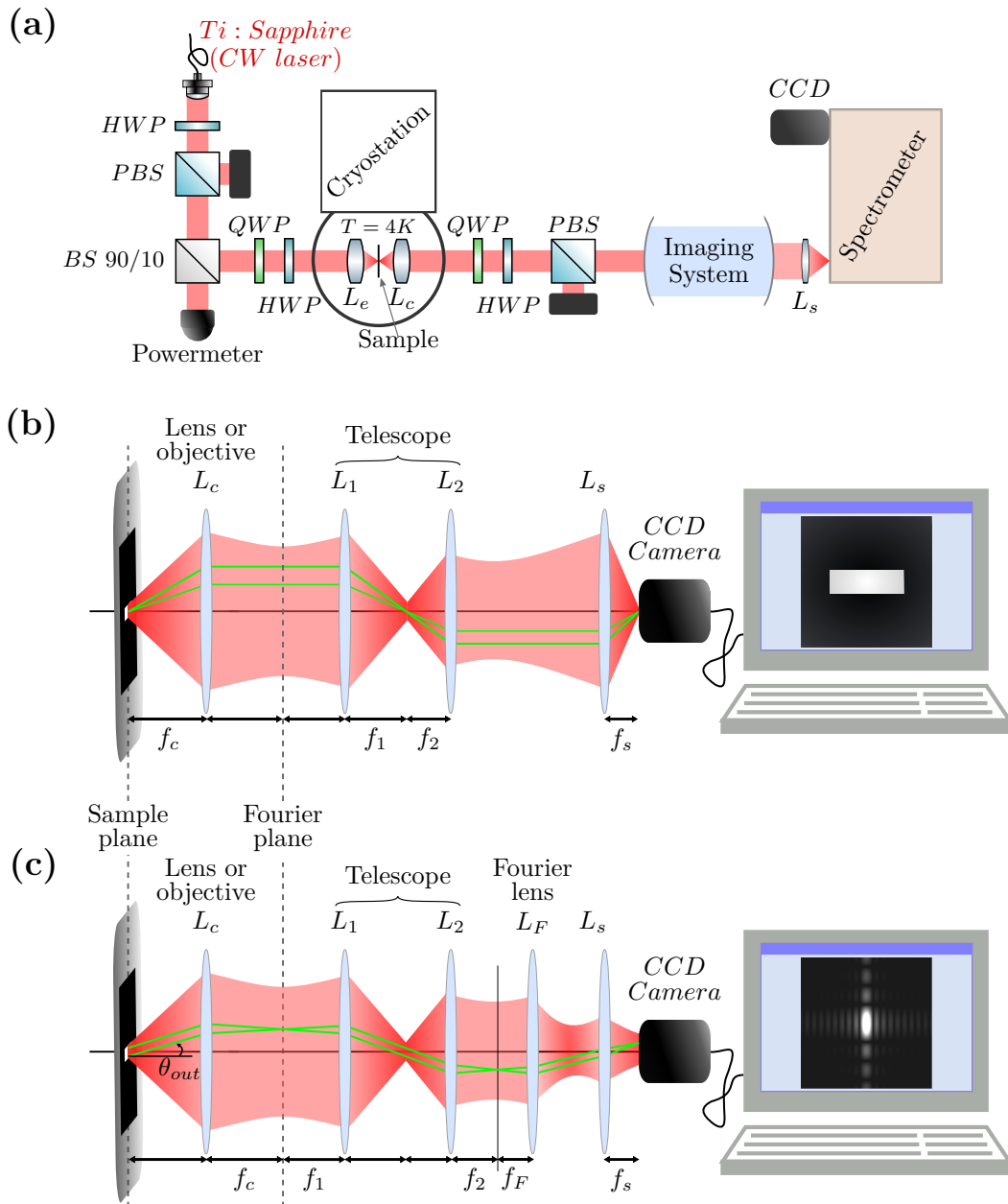


Figure 1.8: **a**, Schematic representation of the experimental setup. The two possible configurations for the imaging system are presented in the two bottom panels, green solid lines display the optical paths. **b**, Real-space imaging configuration: the front focal plane (sample plane) of the collection optic is imaged on the camera. **c**, Fourier-space imaging configuration: the back focal plane of the collection optic (Fourier plane) is imaged on the camera, the sample output angle θ_{out} is thus mapped to a position on the camera.

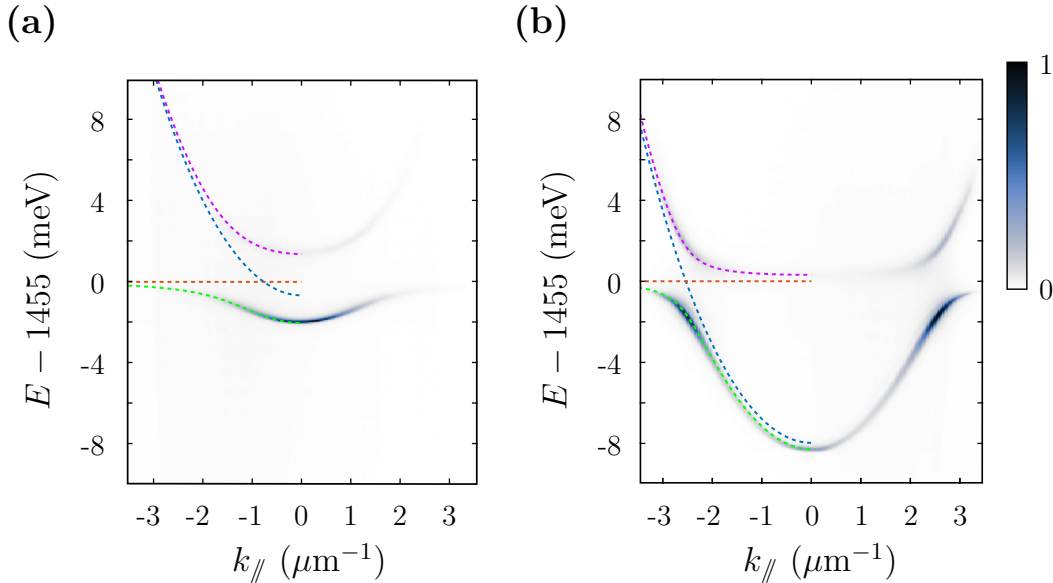


Figure 1.9: Spectrally resolved photoluminescence intensity as a function of the in-plane momentum $k_{//}$ measured under non-resonant excitation, on two different regions of the same planar cavity sample. Dashed lines plotted on the left of each panel correspond to fits of the different dispersions.

diffraction order of the spectrometer, removing the selection slit in the first case. We thus obtain an image which respectively corresponds to the 2D profile of the intensity distribution in the entrance plane of the spectrometer, or to the 1D spatial profile filtered by the entrance slit which is spectrally resolved along the orthogonal direction. We can realize various optical pre-processing of the light transmitted through the cavity including polarization selection using a QWP followed by a HWP and a PBS, but also spatial or angular filtering using slits or apertures in the focal plane of telescopes.

Moreover, as illustrated in Fig. 1.8, we can either chose to image the front focal plane of the collection lens, thus obtaining an intensity distribution in the entrance plane of the spectrometer corresponding to the spatial distribution of polariton in the structure, or the back focal plane (or Fourier plane) of the collection lens to get an intensity profile corresponding to the angular distribution of the cavity transmission. In the latter case, the momentum conservation gives a one to one mapping of the polariton momentum to the collection angle of the photon resulting from the polariton deexcitation. Imaging the Fourier plane of the collection lens allows directly accessing the momentum dispersion of polaritons inside the cavity (Fourier space or momentum-space imaging).

1.4.3 Characterization of a planar sample

To characterize a planar micro-cavity sample, we use probe the photo-luminescence (PL) of the cavity under non-resonant excitation. To do so, we tune the laser energy to one of the transmission dips above the cavity stop-band (typically $\lambda \approx 780$ nm). This non-resonant excitation generates electron-hole pairs that relax toward the $1s$ exciton energy and the polariton branches *via* emission of phonons. Note that only a fraction of the electron-hole pairs generated at high energy lead to the formation of a radiative state that enters the strong coupling. Most of these pairs lead to the

formation of a reservoir of long-lived excitons that can interact with polaritons (see Sec. 1.5). To avoid any excitation-induced modification of the polariton dynamics, measurements are realized considering a weak optical pump: $P \sim 0.5 \mu\text{W}$ are typically focused on a $S = 10 \mu\text{m}^2$ surface and the signal received on the camera is integrated over $T_{\text{int}} \sim 30 \text{ s}$.

The photons escaping the cavity are collected using the experimental setup introduced in the previous section. Due to the translation invariance of the cavity, the in-plane momentum of polaritons \mathbf{k}_{\parallel} is conserved and can be related to the angle with which photons are collected outside the cavity *via*: $|\mathbf{k}_{\parallel}| = E \sin(\theta_{\text{out}})/\hbar c$ where E is the energy of the photon. Using the spectrometer combined with the Fourier-space imaging scheme, we obtain images corresponding to the angularly and spectrally resolved emission of polaritons [21]. Examples of such images are presented in Fig. 1.9 where we observe the two polariton branches. For each vertical array of pixel, associated to an average value of $|\mathbf{k}_{\parallel}|$, one can observe two intensity peaks corresponding to the upper and lower polariton branches at energies corresponding to $E_{\text{UP}}(k)$ and $E_{\text{LP}}(k)$. Tracking the position of the two peaks as a function of k , one can extract the experimental values of the main parameters characterizing the dispersions: Ω_R , $\delta_0 = E_C(\mathbf{k}_{\parallel} = 0) - E_X$ and m_{ph}^* . From equations 1.3.2 and in presence of an anti-crossing, the minimum of $E_{\text{UP}}(k_0) - E_{\text{LP}}(k_0) = \sqrt{\delta(k_0)^2 + \Omega_R^2}$ is obtained for $k_0 = k_{\text{min}}$ such that $\delta(k_{\text{min}}) = 0$. We thus obtain $\Omega_R = E_{\text{UP}}(k_{\text{min}}) - E_{\text{LP}}(k_{\text{min}})$. Moreover, considering $\delta(k_{\text{min}}) = 0 \implies E_C(k_{\text{min}}) = E_X$ we deduce the value of the exciton energy $E_X = E_{\text{UP}}(k_{\text{min}}) + E_{\text{LP}}(k_{\text{min}})$. The two remaining parameters are obtained *via* a parabolic fit: $E_C(k_0) = E_{\text{UP}}(k_0) + E_{\text{LP}}(k_0) - E_X = E_C(0) + \hbar^2 k_0^2 / 2m_{\text{ph}}^*$. Dashed lines corresponding to fits of the cavity, exciton and polaritons dispersions in Fig. 1.9 where obtained using such a procedure, yielding $\Omega_R = 3.3 \text{ meV}$, $E_X = 1.455 \text{ eV}$, $m_{\text{ph}}^* = 3.5 \times 10^{-5} m_e$ and $\delta_0 = -0.6 \text{ meV}$ for panel (a) and $\delta_0 = -8.0 \text{ meV}$ for panel (b).

Both spectra of Fig. 1.9 where obtained on two regions of the same piece of sample: due to the cavity wedge we are able to access different values of the cavity-exciton detuning and thus measure polariton branches with different excitonic and photonic fraction for a given \mathbf{k}_{\parallel} . Note that a gradient of the exciton energy is also present but much smaller than the cavity mode gradient, which is typically on the order of $6.5 \text{ meV}/\mu\text{m}^4$.

1.5 Polariton fluids

Up to now we restricted ourselves to the description of micro-cavity polaritons linear physics. However, one of the key assets of the polariton platform resides in the strongly non-linear behavior observed in experiments and which justifies the terminology of polariton “fluids”. In this section, we address the different collective behaviors that polariton fluids can exhibit: polaritons being quasi-bosons, they can undergo bosonic condensation and additionally, two polaritons can interact *via* a

⁴Note that in this planar sample, no lift of the degeneracy between polarization state was realized: the measured dispersion do not depend on the filtered polarization. It is however possible to realize a TE-TM splitting of the cavity polarization modes [15] which considerably enriches the physics of polaritons: the couplings between pseudo-spin states, acting as an effective spin-orbit coupling, led to the emulation of an optical equivalent of the spin Hall effect [22–25].

contact interaction due to their matter component. The dynamics of dense polariton fluids is therefore not captured by the single particle Hamiltonian previously considered. We will first introduce the exciton many-body Hamiltonian and then discuss the consequences for polariton fluids. We will discuss two different approaches for polaritons injection: a non-resonant excitation scheme where the polariton states are populated *via* coupling to an exciton reservoir, and a quasi-resonant excitation approach where polaritons are coherently injected inside the cavity *via* direct coupling to the electromagnetic field. An exhaustive description of the polariton fluids physics can be found in [26].

1.5.1 The polariton-polariton interaction

One of the strong interest for the polaritonic platform is its capability to explore strongly non-linear dynamics in engineered potentials for relatively weak pumping powers with typical polariton densities as low as $n_P \sim 100 \mu\text{m}^{-2}$. The interaction originates from polaritons excitonic component and corresponds to a Kerr-like (χ^3) interaction. We will here detail the interaction mechanism and explain how the polariton fluid dynamics can be described by a non-linear Schrödinger equation with Kerr non-linearity, which is also called the Gross-Pitaevskii equation.

1.5.1.1 Exciton-exciton interaction

The model introduced to describe excitons in Sec. 1.1 only accounts for the linear regime where the dynamics can be described by the single exciton Hamiltonian. Excitons are quasi-particles composed of two fermions, they are thus quasi-bosons. This bosonic behavior is observable at low exciton density only, in the limit of negligible screening of the Coulomb interaction and low filling of the electron-hole fermionic states [27–29]. Above this limit, excitons are dissociated into a plasma of electron-hole pairs. The transition between these two regimes occurs for an exciton density $n_x \sim 1 \times 10^{11} \text{ cm}^{-2}$ [30], in this thesis all experimental results were obtained for excitonic densities bellow this limit. In this mesoscopic density range, the many-body dynamics can be described in the excitonic basis with bosonic operators [28, 31, 32]. The dominant term of the interaction comes from carriers exchange between excitons: two scattering excitons can simultaneously exchange electrons or holes of each bound pairs. Other smaller contributions come from the direct Coulomb interaction between two excitons as well as for the simultaneous exchange of both electrons and holes.

The Hamiltonian describing the interaction between two excitons reads:

$$\mathcal{H}_{XX} = \frac{1}{2} \int \frac{d^2\mathbf{k}}{(2\pi)^2} \int \frac{d^2\mathbf{k}'}{(2\pi)^2} \int \frac{d^2\mathbf{q}}{(2\pi)^2} \sum_{\sigma, \sigma'} V_{\sigma, \sigma'}(\mathbf{k}, \mathbf{k}', \mathbf{q}) b_{\mathbf{k}-\mathbf{q}, \sigma}^\dagger b_{\mathbf{k}'+\mathbf{q}, \sigma'}^\dagger b_{\mathbf{k}', \sigma'} b_{\mathbf{k}, \sigma} \quad (1.35)$$

where \mathbf{q} is the momentum exchange between exciton *via* the scattering process, σ and σ' represent the excitons spins and $V_{\sigma, \sigma'}$ is the interaction potential.

For the case of the polariton-polariton interaction, the effective mass of the exciton being much greater than the photon one, the momentum dependence of the exciton interaction can be neglected: $V_{\sigma, \sigma'}(\mathbf{k}, \mathbf{k}', \mathbf{q}) \approx V_{\sigma, \sigma'}(0, 0, 0)$. We thus

consider the following contact interaction:

$$\mathcal{H}_{XX} = \frac{1}{2} \int d^2\mathbf{r} \sum_{\sigma,\sigma'} V_{\sigma,\sigma'}^0 b_{\mathbf{r},\sigma}^\dagger b_{\mathbf{r},\sigma'}^\dagger b_{\mathbf{r},\sigma'} b_{\mathbf{r},\sigma} \quad (1.36)$$

where $b_{\mathbf{r}}$ is the Fourier conjugate of $b_{\mathbf{k}}$. Note that the rotational invariance of the contact interaction imposes the total conservation of the spin and the two equalities $V_{\sigma+,\sigma+}^0 = V_{\sigma-,\sigma-}^0$ and $V_{\sigma+,\sigma-}^0 = V_{\sigma-,\sigma+}^0$.

The exciton interaction Hamiltonian contains a second term, corresponding to a saturation of the exciton oscillator strength [28, 31–34]. This term accounts for the fermionic nature of the exciton leading to a phase-space filling: two excitons with the same spin cannot be generated at a distance less than their Bohr radius a_B . It yields:

$$\mathcal{H}_{\text{sat}} = \frac{1}{2} \int d^2\mathbf{r} \sum_{\sigma,\sigma'} V_{\sigma,\sigma'}^{\text{sat}} b_{\mathbf{r},\sigma}^\dagger b_{\mathbf{r},\sigma'}^\dagger b_{\mathbf{r},\sigma'} a_{\mathbf{r},\sigma} \quad (1.37)$$

where a is the annihilation operator associated to photons. This term becomes relevant for polariton density $n \propto 1/a_B^2$, which is at least one order of magnitude above the polariton densities we will consider in the experiments described in this thesis. This contribution will thus be neglected.

1.5.1.2 Estimation of the polariton interaction constant

As hybrid particles of photon and excitons, polaritons experience a polariton-polariton interaction mediated by their excitonic component. The interaction amplitude depends on the excitonic fraction of the considered polaritons. For the lower polariton branch, it yields:

$$\mathcal{H}_{\text{LP-LP}} = \frac{1}{2} \int d^2\mathbf{r} \sum_{\sigma,\sigma'} V_{\sigma,\sigma'}^{\text{LP}} p_{\sigma}^\dagger(\mathbf{r}) p_{\sigma'}^\dagger(\mathbf{r}) p_{\sigma'}(\mathbf{r}) p_{\sigma}(\mathbf{r}) \quad (1.38)$$

with p and p^\dagger the annihilation and creation operators associated to the lower polariton branch and

$$V_{\sigma,\sigma'}^{\text{LP}} = |X(\mathbf{k}_{\parallel})|^4 V_{\sigma,\sigma'}^0 + 2|X(\mathbf{k}_{\parallel})|^2 X(\mathbf{k}_{\parallel}) C(\mathbf{k}_{\parallel}) V_{\sigma,\sigma'}^{\text{sat}} \quad (1.39)$$

$X(\mathbf{k}_{\parallel})$ and $C(\mathbf{k}_{\parallel})$ being the Hopfield coefficients introduced in Sec. 1.3.2.

As previously stated the saturation of the exciton oscillator strength will be neglected in the rest of the manuscript and solely $V_{\sigma,\sigma'}^0$ terms are considered. The strongest contribution comes from the scattering of excitons possessing the same spins. The amplitude hierarchy between same spin and opposite spin interaction originates from the nature of the interaction: the interaction between polariton with the same spin involves a virtual state with $|J| = 1$ excitons, it is thus a resonant interaction, whereas the interaction between polaritons of opposite spin involves a virtual state with dark excitons ($|J| = 2$), it is thus non-resonant. The same spin interaction is repulsive while the interaction of excitons with opposite spins is found to be attractive [35]. An estimation of the repulsive interaction term was realized in [31, 32] yielding: $V_{\sigma=\sigma}^{\text{XX}} = 6e^2 a_B / \varepsilon_l$ where a_B is the 2D exciton Bohr radius and ε_l is the dielectric constant of the material. For the type of samples considered in this thesis, it yields a repulsive exciton-exciton interaction constant $V_{\sigma=\sigma}^{\text{XX}} \sim 5 - 10 \text{ peV} \cdot \mu\text{m}^2$.

The experimental measured values of the interaction are subject to discussion: the constant is often computed from dense polariton fluids and the precise determination of the polariton density being complex, it leads to a consequent uncertainty on the extracted value. Moreover the determination often relies on the measure of the blueshift induced by the interaction and one has to be very careful to the possible presence of an exciton reservoir which would also interact with the polariton fluid *via* exciton-polariton scattering. A first idea developed in Ref. [36] was to spatially separate the reservoir from the polariton fluids. A similar approach was implemented in Ref. [37] but a counter experiment done on the same sample showed that the interaction with the exciton reservoir could not be neglected [38]. The estimation often considered in the literature is $V_{\sigma=\sigma}^{XX} \sim 10 \mu\text{eV} \mu\text{m}^2$ [36, 39–42], which is in agreement with theoretical estimations.

In our case the precise determination of the interaction constant is not crucial as the relevant term will be the induced blueshift. A lower or higher value of the interaction constant simply leads to an higher or lower polariton density required to observe the effects we will discuss. In the following the exciton-exciton and polariton-polariton interaction constant will respectively be labeled g_X and g .

1.5.1.3 Mean-field description

The interaction energy between two polaritons depends on the area S on which they are confined $E_{\text{int}} = g/S$ and as we will explain in Chap. 2, the minimal area that we can experimentally consider is restricted due to the increase of the exciton linewidth by surface recombination events. The typical radius of a micro-pillar cannot go below $1 \mu\text{m}$ with an associated linewidth on the order of $25 \mu\text{eV}$. It means that in the samples that we consider, the typical interaction energy between two polaritons is at least one order of magnitude smaller than the linewidth which does not enable observing strong quantum effects as theoretically proposed [43].

In our samples, strong non-linear regimes can be reached for densities $n_{\text{LP}} \sim 10^2 \mu\text{m}^{-2}$. For such relatively high densities, the effects associated to quantum fluctuations can be neglected and we can consider a mean-field approach where the quantum field and associated operators are replaced by classical quantities corresponding to their mean expectation values [26]. The spatio-temporal evolution of the wavefunction $\Psi_{\text{LP}}(\mathbf{r}, t)$ is described by the following non-linear Schrödinger equation:

$$i\hbar \partial_t \Psi(\mathbf{r}, t) = \left(-\frac{\hbar^2}{2m^*} \nabla^2 + V(\mathbf{r}) + g|\Psi(\mathbf{r}, t)|^2 \right) \Psi(\mathbf{r}, t) \quad (1.40)$$

where $V(\mathbf{r})$ represents an external potential (cavity gradient, etc...). This equation also called the Gross-Pitaevskii equation [44, 45] was initially introduced to describe vortices in Bose gases and is used to study the dynamics of dilute gases of interacting bosons in conservative systems, notably in the case of χ^3 non-linearities in optical media. Polariton micro-cavities are intrinsically dissipative and consequently a non-Hermitian term, accounting for losses, has to be added to the equation to fully describe polariton fluids dynamics. The problem is treated considering a dissipative equivalent of the Gross-Pitaevskii equation [46, 47]. Additionally, as we previously explained, the dissipative nature of the system allows us to inject particles in the system *via* resonant or non-resonant optical excitation: these two excitation schemes

have to be treated differently as they rely on different mechanisms for the injection of polaritons.

1.5.2 Non-resonant excitation

In the non-resonant excitation scheme, the optical pumping consists in injecting particles at an energy above the stop-band. In our case the laser-cavity detuning is typically $\Delta_{L-C} \sim 100$ meV. Being well above the semiconductor band gap, the optical excitation leads to the formation of free electron-hole pairs that relax toward polariton branches *via* scattering and emission of phonons. The vast majority of electron-hole pairs give rise to the formation of a reservoir of excitons. Those excitons can also relax and populate the lower polariton branch. When photoluminescence measurements are realized at sufficiently low input power, polariton branches are unaffected by the presence of the exciton reservoir. In that case the polariton occupation in each state is much smaller than one polariton per lifetime. When considering a higher pumping amplitude, stimulated relaxation from the reservoir toward the lower polariton branch can occur: the QW acts as a gain medium for lower polariton states. In that case the description of the system can be done by considering two coupled non-linear equations, the Gross-Pitaevskii equation where the injection of polaritons is given by an homogeneous term assimilated to a gain (neglecting spontaneous relaxation), coupled to a rate equation governing the evolution of the reservoir density [48]:

$$i\hbar \partial_t \Psi(\mathbf{r}, t) = \left(-\frac{\hbar^2}{2m^*} \nabla^2 + V(\mathbf{r}) + g|\Psi(\mathbf{r}, t)|^2 + 2g_R n_R(\mathbf{r}, t) - i\frac{\hbar}{2} (\gamma - R n_R(\mathbf{r}, t)) \right) \Psi(\mathbf{r}, t) \quad (1.41)$$

$$\partial_t n_R(\mathbf{r}, t) = P(\mathbf{r}, t) - (\gamma_R + R|\Psi(\mathbf{r}, t)|^2) n_R(\mathbf{r}, t) \quad (1.42)$$

where $P(\mathbf{r}, t)$ is the pumping rate from the laser to the reservoir, n_R is the exciton density in the reservoir, R is the relaxation rate from the reservoir toward the lower polariton branch and γ_R accounts for losses in the exciton reservoir. As previously explained, the exciton reservoir interacts with the polariton fluid *via* polariton-exciton interactions. This interaction is described by the term $2g_R n_R(\mathbf{r}, t)$ with $g_R = |X|^2 g_X > g$. Note that the n_R is much larger than $|\Psi(\mathbf{r}, t)|^2$, as a consequence, the polariton-polariton interaction term is often negligible.

1.5.2.1 Polariton condensation

If the relaxation rate exceeds the decay rate, the polariton occupation for a given state can exceed one polariton per lifetime and we observe a macroscopic occupancy of a given state (see Fig. 1.10 (a-b)) which is referred to as polariton condensate or polariton laser [51]. Unlike Bose-Einstein condensates such as those observed in cold-atoms experiments, polariton condensates can be out of thermodynamic equilibrium [52, 53]. The first observation of polariton condensation was realized in the groups of B. Deveaud and D. Le Si Dang using cadmium telluride (CdTe) micro-cavities [49]. Polariton condensation has been reported by many groups ever since (see Ref. [26, 54, 55] for a review) and was also observed in lattices [56, 57]. The formation of vortices [58] and other density patterns has been reported by the

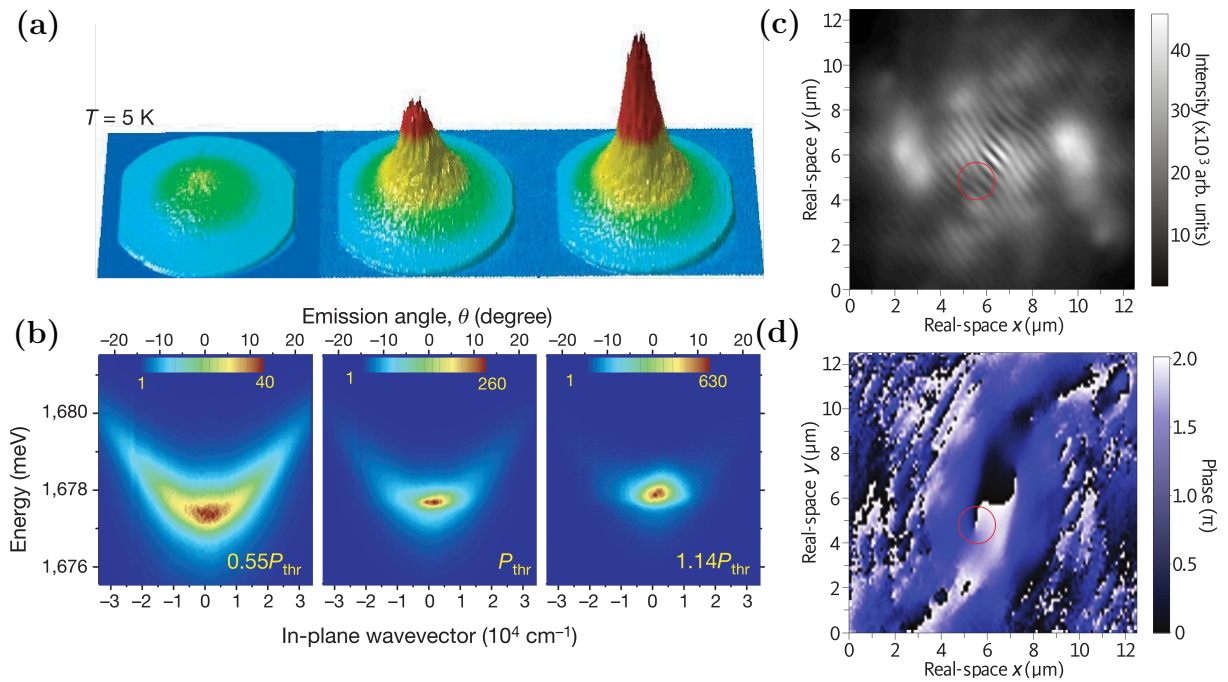


Figure 1.10: **a**, quasi-3D representation of the Fourier-space emission of the planar microcavity under non-resonant excitation resolved along k_x and k_y , the quasi-vertical axis represents the emission intensity. **b**, Energy resolved emission along k_y associated to **(a)**. One can observe that above P_{thr} , the cavity emission mostly comes from $k_{\parallel} = 0$, evidencing the macroscopic occupancy of the ground state. Images taken from Ref. [49]. **c**, Interferogram of a condensate, the pitch-fork bifurcation encircled in red evidences the presence of a vortex. **d**, Real-space phase profile calculated from **(c)**, the red circle encloses the vortex. Images taken from Ref. [50].

group of B.Deveaud [50,59,60] (see Fig. 1.10 (c-d)). This group also reported on the synchronization between condensates [61] which offers perspectives on the emulation of XY models [62]. The non-resonant injection of vortices has now been reported by other research groups [63–65] with realization of all optical spin switching of a vortex triggered by a probe pulse [66]. The formation of vortex lattices was reported by the group of J.Baumberg [67] by spatially shaping the off resonant drive and is still a very active research field [68].

The condensation of polaritons has been achieved up to room temperature using GaN [69,70] and ZnO [71,72] based microcavities, organic materials [73,74], transition metal dichalcogenides [75,76] or Perovskites [77–79] for example.

In the case of too large n_R and $|\Psi(\mathbf{r}, t)|^2$, the phase-space filling and Coulomb interaction screening induce a dissociation of the bound electron-hole pairs, which corresponds to a bleaching of the strong coupling. In such case a regime of lasing in weak-coupling is reached which is equivalent to a standard photon laser [80–82]. A difference between weak and strong coupling regimes can notably be observed through the response to a strong magnetic field: a reduction of the Zeeman splitting, originating from the exciton component, is observed at the transition from strong to weak coupling [83,84].

Note that experimental evidences show that the relaxation of the electron-hole pairs can transfer some information from the non-resonant input laser to the polariton fluid: the $\sigma+$ or $\sigma-$ polarization of the laser can be partially transferred to the reservoir and can be used to induce lasing in one polarization or the other [85].

1.5.3 Resonant excitation

Another possible excitation scheme is the coherent injection of particles inside the cavity *via* resonant excitation. This allows us probing polariton many-body physics where the polariton-polariton interaction plays a crucial role. This excitation scheme is the one which was considered for all experimental results described in this thesis.

1.5.3.1 Coherently-driven dissipative Gross-Pitaevskii equation

In the case of a resonant or quasi-resonant drive, the laser energy is directly tuned to be in resonance or in the vicinity of the polariton resonance. Consequently, a first approximation leads to neglecting the presence of an exciton reservoir as excitations are directly injected in the polariton modes without involving any relaxation processes. The polariton-polariton interaction can therefore play a predominant role as they are not screened by interaction with the exciton reservoir. To capture the polariton fluid dynamics under such excitation scheme, we consider a dissipative Gross-Pitaevskii equation with coherent drive [46]. It reads:

$$i\hbar \partial_t \Psi(\mathbf{r}, t) = \left(-\frac{\hbar^2}{2m^*} \nabla^2 + V(\mathbf{r}) + g|\Psi(\mathbf{r}, t)|^2 - i\frac{\hbar\gamma}{2} \right) \Psi(\mathbf{r}, t) + iF(\mathbf{r}, t)e^{-i(\omega_p t)} \quad (1.43)$$

where we include the source term as an inhomogeneous coherent term of amplitude $F(\mathbf{r}, t)$ oscillating at the laser pulsation ω_p .

As we already explained, the polariton-polariton interaction is equivalent to a Kerr (χ^3) non-linearity which allows us reaching strongly non-linear regime for reasonable densities ($n_{LP} \sim 100 \mu\text{m}^{-2}$). Such polariton populations can be injected

with relatively small pump power ($I \sim 0.1 \text{ mW } \mu\text{m}^{-2}$) and experiments can be run using continuous wave excitation. The energy conservation associated to this resonant excitation process fixes the energy of the polariton fluid to the one of the pump. In that case it is convenient to rewrite equation 1.43 in the rotating frame of the pump using the ansatz $\Psi(\mathbf{r}, t) = \Psi_0(\mathbf{r}, t)e^{-i(\hbar\omega_p t)}$. It yields:

$$i\hbar \partial_t \Psi_0(\mathbf{r}, t) = \left(-\frac{\hbar^2}{2m^*} \nabla^2 + V(\mathbf{r}) - \hbar\omega_p + g|\Psi_0(\mathbf{r}, t)|^2 - i\frac{\hbar\gamma}{2} \right) \Psi_0(\mathbf{r}, t) + iF(\mathbf{r}, t) \quad (1.44)$$

In addition to its energy, the phase and polarization of the polariton field are directly linked to those of the laser beam through this resonant excitation process. More constraints can thus be applied to the fluid by tuning the polarization, phase and amplitude spatial distributions of the pump laser. A considerable theoretical study of the relation between the pump polarization and the injected polariton fluids was developed by N.Gippius and the groups of G.Malpuech and A.Kavokin [86]: the spin anisotropy of the polariton-polariton interaction was predicted to induce polarization multi-stability of the fluid [87] and spin-polarized solitons (called half-solitons) where extensively studied [88–91].

Very rich phenomena were also theoretically studied in the scalar model including parametric scattering and bistability [92] or pioneering propositions for the observation of a polariton superfluid by I. Carusotto and C. Ciuti [47]. In a dense polariton fluid, interactions induce a renormalization of the excitation spectrum (also called Bogoliubov spectrum) and the dispersion becomes linear in the vicinity of the fluid energy. This allows for the definition of a speed of sound $c_s = \sqrt{\hbar gn/m^*}$. Moreover, tilting the excitation beam allows to inject polaritons with a well defined momentum which forms a fluid flowing at speed $\mathbf{v}_f = \hbar\mathbf{k}_p/2m^*$. If this flow speed is lower than the sound velocity in the fluid, a superfluid regime is reached in the sense of the Landau criterion [93]. It was proposed to observe the transition toward superfluidity *via* the suppression of Rayleigh scattering of the polariton fluid flowing across a defect: in the regime $c_s > |\mathbf{v}_f|$, the renormalization of the excitation spectrum induced by the interactions is such that no states are available for polaritons to scatter.

1.5.3.2 Non-linear fluids in planar cavities

The presence of polariton-polariton interactions widely enriches the range of observable phenomena in micro-cavities. Already in planar samples, a considerable variety of effects originating from inter-particle interactions has been reported. We here propose an overview of experimental results obtained in 2D polariton micro-cavities.

One of the most characteristic phenomenon, directly linked to the nature of the interaction (χ^3), is the parametric scattering of polaritons (OPO process). In this four wave mixing process, polaritons injected at the energy of the pump E_p with a momentum \mathbf{k}_p scatter to generate signal and idler polaritons. This process has to conserve energy and momentum, the signal and idler are thus generated with energies $E_s = E_p - \delta E$ and $E_i = E_p + \delta E$ associated to momenta $\mathbf{k}_s = \mathbf{k}_p - \delta\mathbf{k}$ and $\mathbf{k}_i = \mathbf{k}_p + \delta\mathbf{k}$. Early demonstrations by the group of J.J. Baumberg showed that pumping close to the inflection point of the lower polariton branch ensures conservation of both quantities through a resonant scattering process [94, 96, 97]. In

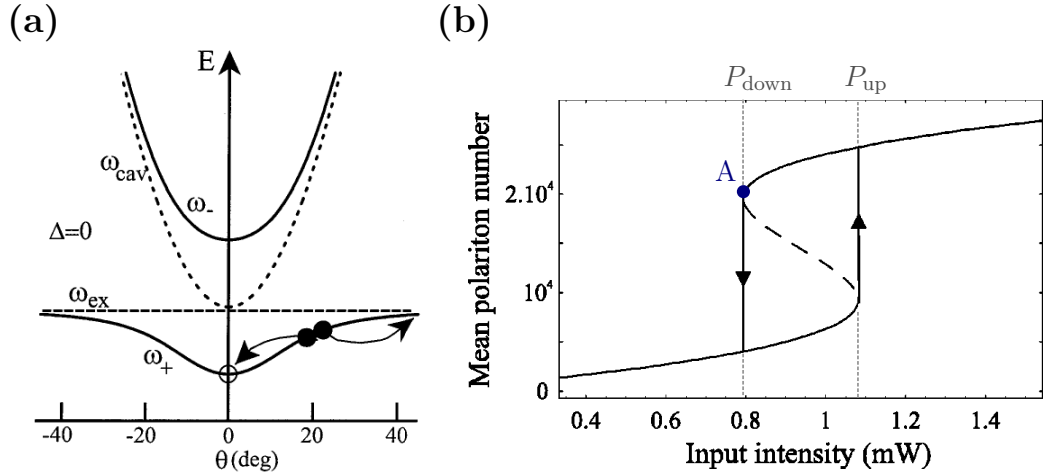


Figure 1.11: **a**, Scheme of the optical parametric amplification process where polaritons generated by the weak probe (empty circle) stimulate scattering from polaritons injected by the pump (filled circles) toward the bottom of the lower polariton branch. Image taken from Ref. [94]. **b**, Analytical calculation of the hysteresis cycle observe in the polariton population as a function of the input power. Point A corresponds to the unstable point where the laser is resonantly injecting the polariton mode. Image taken from Ref. [95].

addition, stimulated scattering of the signal toward the bottom of the dispersion was observed when increasing the pump power [96] or was triggered using a weak resonant probe [94] to realize parametric amplification (OPA, see Fig. 1.11 (a)). This parametric process was demonstrated to be efficient up to $T = 120$ K in GaAs micro-cavities [98] and a reduction of the linewidth of polariton states (associated to Goldstone modes) was measured in the vicinity of the signal energy [99]. Different scattering schemes have then been reported which do not need pumping at the inflection point of the lower polariton branch. A resonant scattering process where signal and idler polariton fields possess different energies but the same momentum ($\mathbf{k}_s = \mathbf{k}_i = \mathbf{k}_p = 0$) was realized in a structure containing three coupled cavities [100]. Complementarily, a scheme where the idler and the signal are generated at the energy of the pump was demonstrated through a non degenerate four wave mixing process where two pumps are injected with opposed wave vectors $\mathbf{k}_{p'} = -\mathbf{k}_p$ [101]. At low pumping powers, idler and signal are uniformly generated on the elastic circle such that $\mathbf{k}_s = -\mathbf{k}_i$ and $|\mathbf{k}_s| = |\mathbf{k}_p|$ whereas increasing the pumping power leads to stimulated scattering along a preferential crystalline axis. Note that, being resonant, this scattering processes are particularly efficient compared to what is commonly achieved with standard non-linear crystals: OPO and OPA processes can be obtained for low pump powers with possibilities to observe squeezing or quantum correlations [102, 103].

Another well know non-linear effect observable with polariton micro-cavities, originating from both the non-linear and driven-dissipative nature of the system, is the optical bistability. Considering a quasi-resonant excitation blue-detuned from the cavity resonance by δ_0 , polaritons can be injected in the system *via* the energy tail of the mode. The repulsive interaction results in a blueshift of the polariton resonance which reduces the effective detuning between the laser and this resonance.

The interaction thus favors the injection of polaritons in the system. When increasing the pumping power, this positive feedback leads to a sharp jump of the polariton density when the non-linear blueshift approaches the bare laser-cavity detuning δ_0 , the laser being brought to resonance with the cavity mode. Above this power threshold P_{up} , an optical saturation regime is observed as the laser is now red-detuned with respect to the cavity resonance. Interestingly, decreasing the pump power after the jump, the high polariton density is preserved as long as the injection is strong enough to compensate for the system losses: as long as $gn > \delta_0$, corresponding to a second power threshold P_{down} . The balance between drive, dissipation and non-linearities leads to the opening of a hysteresis cycle when ramping the power up and down, which is illustrated in Fig. 1.11 (b). An observation was reported in Ref. [95] using the cavity gradient to probe the detuning dependence of the effect. The vicinity of bistability thresholds were shown to allow for noise squeezing [104]. The spatial distribution of the high density fluid was later studied in Ref. [105] and it was shown that, depending on the detuning and incident power, the upper bistability branch can correspond to dark or bright solitonic solutions.

Beyond the scalar model, using the spin degree of freedom and the spin anisotropy of the interaction, it was possible to demonstrate spin multi-stability of polaritons with and without the action of a strong magnetic field [106, 107]: the Zeeman splitting allows to lift the degeneracy between the circularly polarized branches. In Ref. [108], the polarization of the pump was shown to strongly affect the transmission of the sample and the formation of polarized spatial patterns was reported. Spin switching of a large area triggered by a small circularly polarized probe was realized in Ref. [109]. Using a linearly polarized beam, a large area is pumped with $P_{\text{down}} < P < P_{\text{up}}$, such that the system initially remains in the lower stable branch of the hysteresis cycle and that none of the two circular polarizations is favored. A circularly polarized probe is then used to locally bring the injected power above P_{up} for one of the two circularly polarized states only. As a consequence, a high polariton population is injected which is co-polarized with the probe. The high spin-polarized polariton density was shown to not only covers the vicinity of the probe but the whole area pumped above P_{down} . This effect highlights the spin-anisotropy of the polariton-polariton interaction. Finally, the group of B.Deveaud demonstrated a competition between attractive and repulsive contributions of the spin dependent exciton-exciton interactions with the observation of a Feshbach resonance in presence of a biexciton [110, 111].

Among all effects originating from the renormalization of the polariton dispersions occurring through the hysteresis cycle, one of the most remarkable is superfluidity. This hydrodynamic effect is only observable thanks to the strong polariton-polariton interaction and highlight the “fluid” character of polaritons. The first experimental realization was done by the group of A. Bramati, demonstrating the suppression of resonant Rayleigh scattering of a polariton fluid on a defect [112]. The suppression of elastic scattering as well as a calculated excitation spectrum is presented in Fig. 1.12. Additionally, if the fluid flow speed exceeds the speed of sound, a Čerenkov radiation cone is instead observed in the wake of the defect encountered by the supersonic flow. The superfluid behavior of polaritons was further demonstrated by the group of D.Sanvitto which evidenced the stabilization of quantized vortices [113] theoretically predicted in a superfluid [114]. More recently, superflu-

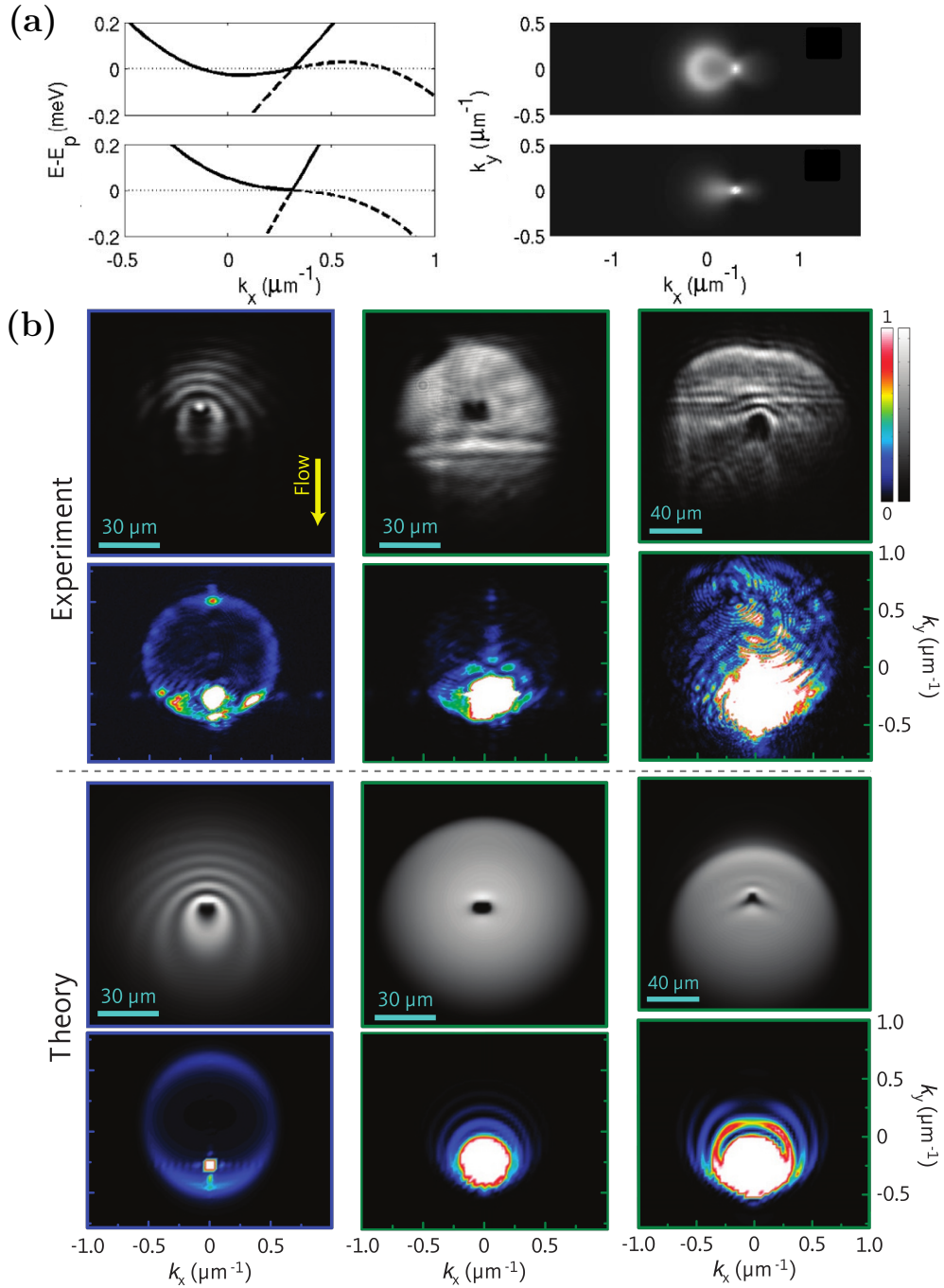


Figure 1.12: **a**, Simulated excitation spectrum (left panels) and reciprocal space distribution of the polariton resonant Rayleigh scattering (right) in cases where the speed of the polariton fluid exceeds the sound speed (top panels) and in the superfluid regime (bottom panels). On left panels, solid lines correspond to the normal branches of the Bogoliubov spectrum while dashed lines correspond to the so called “ghost branches”. Both cases correspond to the operating point A of the bistability cycle presented in Fig. 1.11 (b). **b**, Experimental images and theoretical calculations of the polariton fluid density (top sub-panels) and of the \mathbf{k} -space distribution of the fluid (bottom sub-panels) corresponding to a low density (left), superfluid (middle) and supersonic regimes (right). In the superfluid regime, density fluctuations due to polariton scattering are suppressed while a cone characteristic of Čerenkov radiation is observed in the supersonic regime. Images are respectively taken from Ref. [47] and Ref. [112]

idity was observed up to room temperature by the same group [115]. Vortices being non-trivial topological defects, a huge interest was devoted to their study in the groups of B.Deveaud [116, 117], D.Sanvitto [113, 118, 119] and A.Bramati [120, 121]. The resonant pump imposing the phase of the fluid, different solutions have been employed to form vortices with direct injection of angular momentum using a Laguerre-Gauss beam [113, 119, 120] or spatial arrangement of pump spots [121]. Interestingly the spontaneous nucleation of vortices was observed at the wake of a defect using a pulsed excitation [116]: the formation of vortices is observed when the polariton fluid is at the breakdown of superfluidity: $|\mathbf{v}_f| = c_s$. Techniques were developed to enhance their stability as vortices propagate away from the strongly pumped region: a low power pump is used to main the system above the lower bistability threshold P_{down} [122, 123].

Observations of the excitation spectrum on top of a non-linear fluid, also called Bogoliubov spectrum, have been reported in the case of polariton fluids at rest (pumped in $\mathbf{k} = 0 \rightarrow |\mathbf{v}_f| = 0$) [124–127]. The excitation spectrum and its renormalization induced by non-linearities have attracted a particular interest in the context of polariton analog gravity emulation where polariton fluids are used to study cosmological problems [128–132].

1.5.4 Solitons in polariton fluids

Solitons are among the fundamental non-linear stable solutions of the Gross-Pitaevskii equation which are observed in polariton fluids. Historically, the first report on the observation of a soliton is attributed to John Scott Russell [133] who followed for several kilometers a solitary wave propagating upstream in a canal. Using a water tank, he reproduced the phenomenon which he called “Wave of Translation” (see Fig. 1.13 (a)). The first modelization of the hydrodynamic effect was done in 1972 by Joseph Boussinesq [134] but the extensive exploration of non-linear waves followed the very first numerical experiment in 1955: the Fermi-Pasta-Ulam-Tsingou experiment [135]. This simulation demonstrated that a system of coupled harmonic oscillators can become non ergodic as soon as a small anharmonicity is introduced. At long times after an excitation, the system does not exhibit any sign of thermalization: no equipartition of the energy over the vibrational modes is observed and a quasi periodic behavior of the wave packet was observed. A plethora of theoretical and experimental developments followed this discovery in order to frame the physics of non-linear waves. Several paradigmatic non-linear equations are worth mentioning: The Korteweg-de Vries (KdV) equation (and its generalization, gKdV) is a continuum limit of the equations governing the dynamics of a string with a quadratic force term, shallow-water waves or collisionless plasma:

$$\begin{aligned} \text{KdV: } \partial_t \Psi + \partial_x (\partial_x^2 \Psi + \Psi^2) &= 0 \\ \text{gKdV: } \partial_t \Psi + \partial_x (\partial_x^2 \Psi + \Psi^p) &= 0 \end{aligned} \tag{1.45}$$

The sine-Gordon which is a continuum limit of the Frenkel-Kontorova model from crystalline materials:

$$\partial_t^2 \Psi - \partial_x^2 \Psi + \sin(\Psi) = 0 \tag{1.46}$$

and the non-linear Schrödinger equation with cubic non-linearity which we call Gross-Pitaevskii equation and is also referred to as Lugiato-Lefever equation.

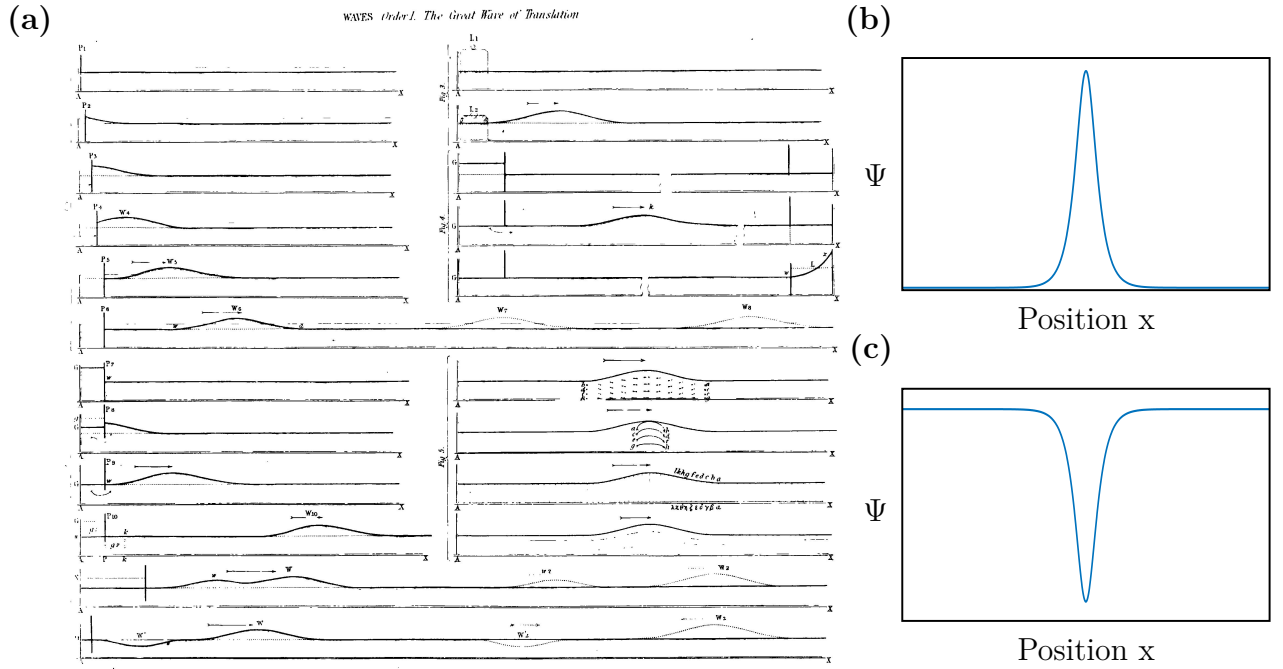


Figure 1.13: **a**, Schematic representation of the observation realized by J.S. Russell in a water tank. Image extracted from Ref. [133]. **b**, Calculated profile of a bright soliton. **c**, Calculated profile of a dark soliton.

Besides their relevance for many physical systems, these equations were extensively studied due to the existence of stable solutions in the form of solitary-waves or solitons which present a particle-like behavior [136]. The term soliton was introduced in 1965 by N.J. Zabusky and M.D. Kruskal in a computational study of the KdV equation [137]. In this pioneering paper, interactions between solitons were already discussed. Such solutions have now been observed in many systems and solitons have been considered for use in optical telecommunication as they allow reducing the number of required repeaters [138, 139]. The case of solitonic solutions on lattices has also broadly been studied. The reader can refer to [140] for an exhaustive introduction to the field.

Initially, solitons were defined as non-linear solutions which remain unperturbed through the interaction with other solitons, however the notion has now broadened to also include the so called *near*-solitons which are not preserved *via* soliton-soliton interactions. Solitons are localized wave-packets which are self-sustained and propagate without deformation. Their existence originates from a balance between non-linearities and the dispersion relation of the material. In the Gross-Pitaevskii equation, different types of solitons can be observed. Spatial solitons are wave-packets spatially confined by the competition between inter-particle interactions and spatial dispersion of the medium: for example, in the case of optics, this dispersion can correspond to a spatial variations of the refractive index $n(\mathbf{r})$. A spatial soliton can be composed of a monochromatic wave-packet and thus be delocalized in the time domain. Equivalently, temporal solitons are temporally localized wave-packets: in optics, the spatial confinement of the electromagnetic field in optical fibers allows the observation of solitons which originate from the competition between non-linearities and the energy dispersion of the refractive index $n(\lambda)$ (light pulses, poly-chromatic). Additionally, depending on the relative sign of the interaction and dispersion terms,

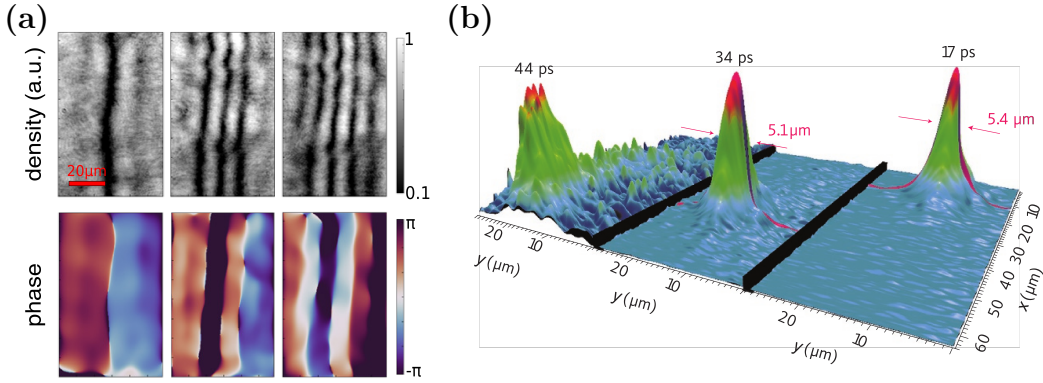


Figure 1.14: **a**, Density and phase of the polariton fluid presenting an odd number of dark solitons channels. Each density dip (top images) is associated to the presence of a π phase jump of the fluid (bottom images). Image extracted from Ref. [142]. **b**, Time resolved propagation of a bright soliton along the x axis. 2D profiles were measured with a streak camera. The vertical axis represents the measured intensity. Image taken from Ref. [143].

one can observe the formation of bright or dark solitons [141]. Let us consider the case of the conservative Gross-Pitaevskii equation describing the dynamics of massive particles with $m^* > 0$ in a 1D infinite channel:

$$i\hbar \partial_t \Psi = -\frac{\hbar^2}{2m^*} \partial_x^2 \Psi + g|\Psi|^2 \Psi \quad (1.47)$$

In the case of an attractive interaction ($g < 0$) particles tend to coalesce and form dense wave-packets which correspond to bright solitons. On the contrary, for repulsive interactions ($g > 0$), particles tend to separate as much as possible. In the presence of dense ensemble of particle, the strong repulsion between constituents can be accommodated *via* the formation of a local density dip which corresponds to a dark soliton. This dip is associated with a π jump of the field phase. In both cases the general solution takes the form of an hyperbolic secant $\Psi \propto 1/\cosh([x - x_0]/a)$ (see Fig. 1.13 (b-c)) where a represents the width of the soliton which depends on m^* and g .

The polariton platform is particularly suited for the observation of dark solitons as polaritons present a low effective mass and interact *via* strongly repulsive inter-particle interactions [144, 145]. Similarly to vortices, pairs of spatial dark solitons were observed in planar samples at the wake of a defect [117, 146–148] or *via* engineering of the drive [142, 149, 150]. Interestingly, this latter scheme allows for the generation of odd numbers of dark solitons (including single solitons, see Fig. 1.14 (a)). The formation of half-solitons with circular polarization was demonstrated in Ref. [147]. The resonant beam was linearly polarized along the flow direction of the polariton fluid, polarization resolved measurement revealed that the two solitons of the pair are orthogonally and circularly polarized [147]. The stabilization of dark solitons is an active topic [122, 142] and theoretical propositions have been made using the soliton pair instability to solve maze problems [151]. Additional propositions were made for the observation of temporal dark solitons *via* resonant [152] or non-resonant excitation [153].

The formation of bright solitons was also demonstrated using polaritons in pla-

nar microcavities, by pumping above the inflection point of the lower polariton branch [39, 143, 154]: in that particular region the lower polariton branch presents a negative mass dispersion which is required to form bright solitons of particles with repulsive interactions. These bright solitons were shown to be spatially and temporally localized (see Fig. 1.14 (b)) and the generation of a bright soliton train was triggered *via* pulsed excitation [155].

Another method to observe the formation of bright solitons in polariton micro-cavity samples relies on the confinement of polaritons in lattices: one can engineer bands with a negative mass. Interestingly, one can also observe the formation of bright gap solitons in the mini-gaps open by periodic modulation of the energy landscape. These solitons are stabilized by a self-trapping mechanism which originates from the balance between interactions and the presence of the energy gap: even though they strongly repel each other, particles forming the soliton cannot scatter to any other state and the wave-packet remains spatially localized. The confinement of polaritons in an engineered potential and the description of the associated non-linear equation is the subject of the next chapter.

1.6 Summary

In this chapter we introduced the basic concepts of micro-cavity exciton-polaritons physics. Polaritons are quasi-particles arising from the strong coupling between the electromagnetic field confined in a high quality cavity and excitons confined in a semiconductor quantum well. These hybrid light-matter quasi-particles inherit properties from both photonic and excitonic component which makes polaritons particularly suited for the exploration of non-linear physics. Their excitonic part is responsible for giant Kerr non-linearities. Particularly interesting characteristics of polaritons originate from their photonic component: it endows them with a low effective mass, allowing for their propagation on long distances and renders the system intrinsically dissipative which enables to monitor the state of the system by collecting photons escaping the micro-cavity.

A last important advantage brought up by the photonic component of polaritons lies in the possibility to confine polaritons at micron scale by tailoring the micro-cavity structure. At C2N, the employed technique consists in deep-etching the structure enabling us to engineer Hamiltonians with nearest neighbor coupling as will be presented in the next chapter.

Chapter 2

Polaritons in lattices

This chapter is dedicated to the confinement of polaritons in tailored structures. We describe the linear and non-linear behaviors of these quasi-particles in patterned micro-cavity samples. In addition, we present the numerical methods employed throughout the manuscript to describe and interpret our experimental findings.

Changing the polariton band structure requires to master the propagation of particles by tailoring the energy landscape of the micro-cavity. To do so, different approaches have been considered. These methods rely on the confinement of polaritons by acting either on their excitonic or photonic components. In Sec. 2.1, we start by describing the different approaches employed to confine polaritons and especially describe the deep-etching technique used at C2N. Section 2.2 is dedicated to the description of the two main approaches considered to design and to model polariton micro-structures. The nearly-free or continuous model provides an accurate description of polaritons dynamics in etched structures and is often considered for the case of modulated wires. The tight-binding approach simplifies the description of structures composed of coupled micro-pillars. In each case we present the numerical methods employed for the linear description of polariton states in engineered structures. Numerical simulations not only allows us to reproduce experimental results as well as to predict the distribution of polaritons states in a given structure in order to engineer our samples. Finally, in Sec. 2.3, we address the quasi-resonant excitation of polaritons in tailored structures and the numerical methods used to describe the non-linear dynamics of these confined quasi-particles.

2.1 Engineering an energy landscape for Polaritons

The confinement of polaritons can be done in two different manners, confining either the excitonic or photonic component of the quasi-particles. In both cases the confinement technique has to preserve, as much as possible, the quantum well and cavity qualities. A description of the various techniques employed in the literature can be found in [156], hereafter we briefly introduce some of these techniques and especially the deep-etching technique used at C2N.

2.1.1 Potential acting on the excitonic component

In order to preserve the sample quality, engineering of a potential for excitons cannot rely on a reduction of the quantum well dimension in the (x, y) plane *via* etching of the structure: increasing the surface to volume ratio would lead to an increased probability for surface recombination events and thus to a broader exciton linewidth. Consequently, the methods used to confine the exciton wavefunction rely on its sensitivity to strain, electric field control or on using the exciton-exciton interaction, for example.

The strain-induced confinement consists in a local modification of the semiconductor band-gap. Indeed, the band-gap strongly depends on the inter-atomic distance between lattice neighbors of the crystalline structure. Inducing a local deformation of the crystal leads to a local variation of the semiconductor band-gap that can play the role of a trap or a barrier. A first technique involving the use of strain consists in the application of mechanical pressure on the substrate surface with a pin tip, see Fig. 2.1 (a). This method developed by the group of D. Snoke creates a local decrease of the exciton energy at the pin position and can be used to trap polaritons. It was for example used to trigger polariton condensation away from the exciton reservoir by displacing the pump spot from the position of the tip [157]: polaritons injected at the laser location flow and relax toward the potential energy minimum induced by the strain. The main disadvantage of this technique is its lack of scalability as it hardly enables the engineering of more complex geometries. A second technique, which offers the possibility to engineer lattices, was developed by the group of P. Santos and relies on the use of surface acoustic waves (SAWs). A surface acoustic wave creates a periodic variation of the inter-atomic displacement with respect to the crystalline structure at rest. This resulting strain pattern propagates with the SAW and so do the associated effective traps for polaritons. By superimposing several SAW patterns, one can achieve the engineering of 1D or 2D potentials for the exciton and so the emulation of lattices (see Fig. 2.1 (b)). Using this technique, the condensation of polaritons has been reported in 1D and 2D lattices [158, 160, 161]. Note that, technically speaking, the strain also affects the photonic component *via* a modification of the refractive index and the thicknesses of cavity layers but the effect is weaker than the one observed on the excitonic component.

A second approach is to use polariton interactions with a locally injected exciton reservoir. As seen in Chap. 1.5.1, the exciton-exciton interaction is repulsive and the presence of an exciton reservoir thus induces a local blueshift of the exciton

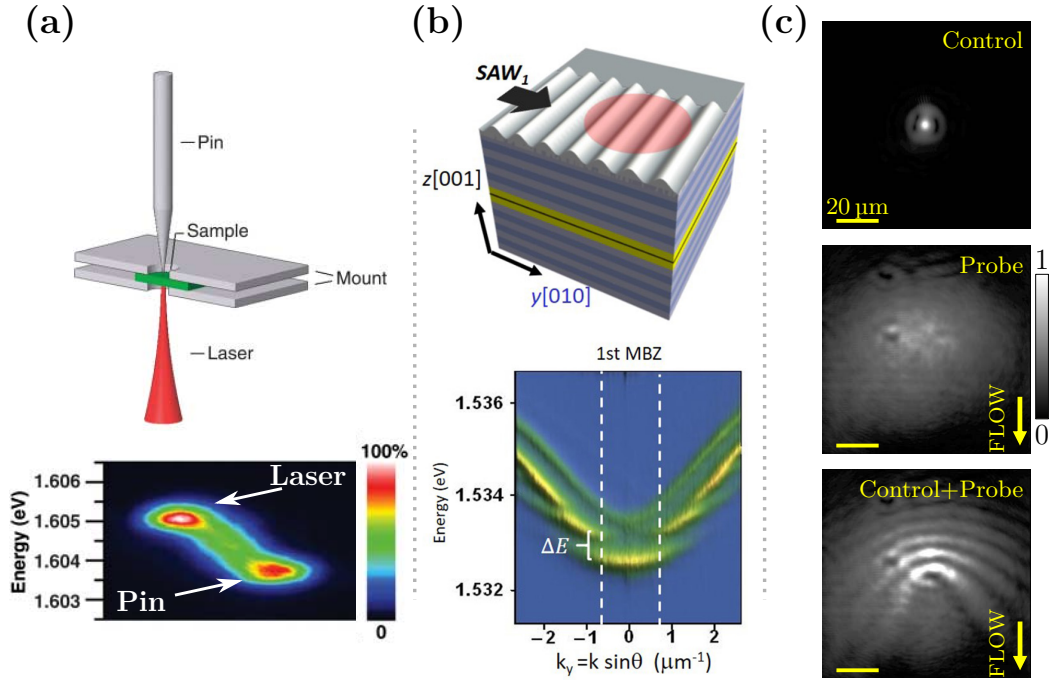


Figure 2.1: Illustration of the methods employed to create potentials confining the excitonic component of polaritons. **a**, Pressure induced traps with a scheme of the setup (top) and measured luminescence from the sample showing trapping of polaritons at the position of the pin (bottom). Image taken from Ref. [157]. **b**, Surface Acoustic Waves with a representation of the SAW (top) and a dispersion obtained *via* resolved PL measurements (bottom) showing the opening of energy gaps. Image taken from Ref. [158]. **c**, Optically pumped exciton reservoir. Top panel shows the luminescence generated by the trapping laser (control). Middle panel shows the luminescence pattern of a polariton fluid flowing in the direction of the yellow arrow (probe). Finally, bottom panel shows the scattering pattern obtained when the polariton fluid encounters the trap generated by the exciton reservoir. Image taken from Ref. [159].

energy, acting as a potential barrier for polaritons. Harnessing the possibility to use the optical beam to confine or control the flow of polariton being quite versatile, this technique has been employed in many groups [63, 67, 118, 162, 163]. One of the first realization was done by the group of A. Bramati, reporting the observation of a polariton fluid scattering on a defect constituted by an exciton reservoir [159] as illustrated in Fig. 2.1 (c). This all-optical technique also enables to imprint 2D lattices [62, 164] as the beam geometry can be tailored at will using spatial light modulators (SLM). There is however one inconvenience: the non-resonant excitation incoherently injects particles in all polariton states with a spatial profile correlated to the one of the pump beam. This puts some limitations on the effects that one could study.

2.1.2 Potential acting on the photonic component

The confinement of polariton modes *via* the photonic part of the polaritons is based on the 3D design of the dielectric constant $\epsilon_l(x, y, z)$. The methods employed in the literature are illustrated in Fig. 2.2.

The first technique, developed by the group of Y. Yamamoto, consists in the deposition of a patterned thin metallic layer (typically AuTi) on top of the cavity. If the number of Bragg layer pairs in the top mirror is small enough, the change between boundary conditions for the electromagnetic field at a metal/semiconductor versus a vacuum/semiconductor interface leads to a change of the cavity mode energy. As it is external to the cavity, this patterning of the dielectric constant only induces a shift of the optical resonance on the order of ~ 0.1 -1 meV. This is yet sufficient to induce an effective potential for polariton and engineer 1D or 2D lattices [56, 165–167].

A second technique, developed in the group of B. Deveaud, relies on a shift of the cavity mode energy induced by a modification of the cavity thickness. Such effect is obtained by an etch-and-overgrowth method: the cavity spacer is selectively etched before growing the top DBR ¹. This procedure leads to the formation of structures called mesas in which the polariton modes are confined, see illustration in Fig. 2.2 (b). Being a direct modification of the cavity structure, it allows applying a confinement with characteristic energies on the order of a few meV. The mesas were initially used to create 0D traps [168, 170, 171]. The group of S. Höfling recently demonstrated the possibility to hybridize polaritonic modes from different mesas and the realization of lattices [172–174].

The technique used at C2N, which was developed in parallel in the group of J. Bloch [175] and M. Bayer [176], consist in etching of the cavity sample from the top mirror down to the substrate after its growth. Due to the high refractive index contrast between the vacuum ($n = 1$) and the cavity ($n \sim 3.3$), the photonic mode is strongly confined in the resulting structures. This methods allows designing architectures with variable geometries, from 0D to 2D, with a precise tailoring of the polariton band structure. A large diversity of architectures have been realized in our group and in the groups of M.Bayer [169, 177] and S.Höfling [83, 178]. A limitation

¹Note that only the top part of the cavity spacer is partially etched to preserve the quantum well and avoid any degradation of the exciton optical properties.

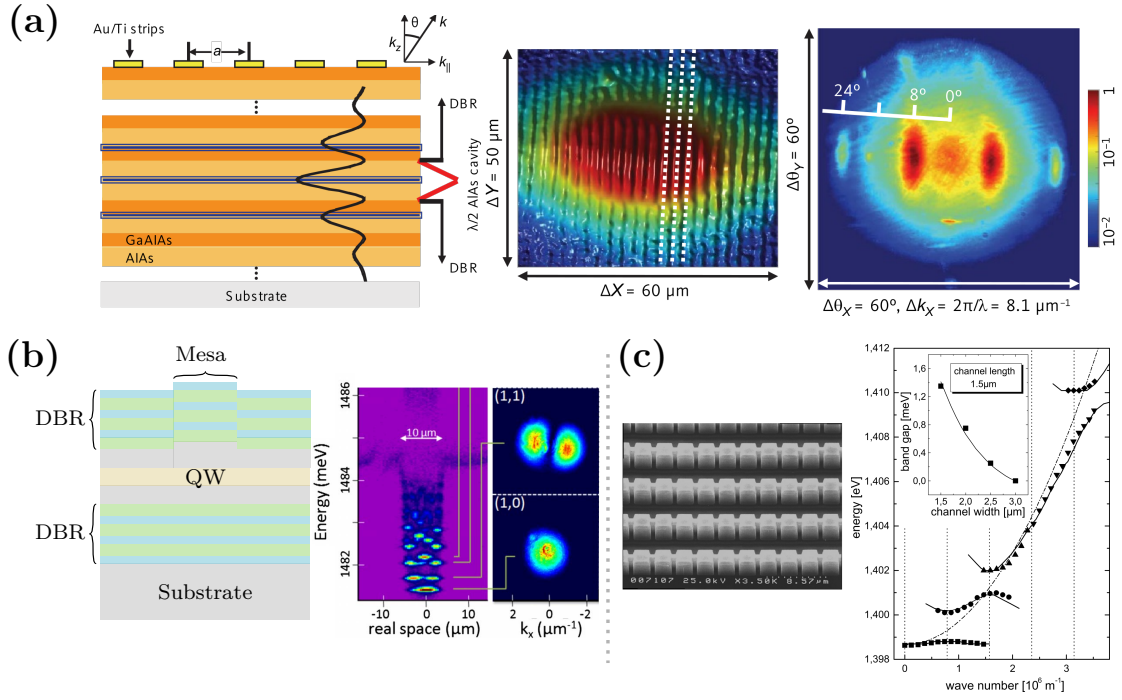


Figure 2.2: Illustration of the methods employed to create potentials confining the photonic component of polaritons. **a**, Patterned metal deposition with a scheme of the structure (left) and measured emission from a polariton condensate in the real space (middle) and the reciprocal space (right). Image taken from Ref. [165]. **b**, Growth of a mesa with scheme of its structure (left) and real space photoluminescence of a circular mesa ($10 \mu\text{m}$ diameter) along with a space tomography of the two lowest energy states (right). Image taken from Ref. [168]. **c**, Deep-etching: Scanning Electron Microscope image of periodic 1D structures (left) with the associated energy dispersion of one structure along the longitudinal direction (right). Image taken from Ref. [169].

of this technique resides in the minimal size of the structure one can etch without observing a degradation of the exciton linewidth due to surface recombinations. To circumvent this issue, some groups envisaged etching of the top mirror only, in order to preserve the quantum well [179–183].

All methods presented above involve cavities made of two distributed Bragg reflectors. An alternative approach is given by hybrid cavities where the top mirror is replaced by an alternative reflective item which can be a photonic crystal [184, 185] or the tip of an optical fiber where a DBR is deposited. In the latter case, the fiber tip can be preprocessed in order to realize a non-planar DBR which can be concave [186] or present a more elaborated structure to engineer coupled traps [187].

2.1.3 Etching the planar cavity

After the growth of the planar cavity and its characterization, we select a wafer portion of about $0.5 \text{ cm} \times 1.5 \text{ cm}$ with a cavity-exciton detuning accessible range which depends on the experimental problematic we want to tackle. The etching process start with the deposition of a layer ($2 \mu\text{m}$) of silicon nitride (Si_3N_4) by vapor deposition (PECVD), followed by a layer of polymethyl methacrylate (PMMA) *via* spin-coating. The micro-structure pattern is then imprinted on the polymer layer

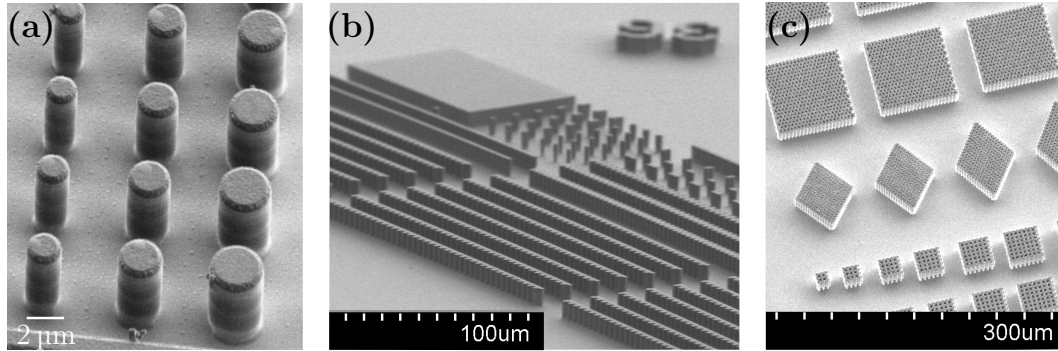


Figure 2.3: Scanning electron microscope images of different structures produced in the C2N clean-room facilities. **a**, Circular micro-pillars of various radii. **b**, Sample patch presenting a rectangular planar cavity, micro-pillars and 1D structures. **c**, Portion of a sample presenting 2D structures.

via electron-beam (e-beam) lithography. A selective chemical development allows removing the insulated regions of the PMMA. This step is followed by a deposition of 60 nm of nickel. Nickel is only left in the masked region of the e-beam mask after lift-off of the remaining PMMA. Finally, the etching is realized with inductively-coupled plasma (ICP), to etch out the regions that are not protected by the nickel layer.

Figure 2.3 presents examples of structures realized using this procedure in the C2N clean-room facilities. The images were obtained using a scanning electron microscope (SEM). The processing of the sample used in this thesis was realized by Luc le Gratiet, Abdelmounaim Harouri and Isabelle Sagnes.

2.2 Modeling polaritons in deeply etched lattices

This section is dedicated to the description of the different approaches used to model polariton modes and band structures. The strong confinement of the electric-field due to the DBRs allows us to separate the z dependence of the electromagnetic field and consider that polaritons are confined in 2D potential wells in the (Oxy) plane. Given the strong refractive index contrast between the cavity and vacuum, the associated potential barriers are considered to be infinite which is equivalent to imposing a zero of the polariton wavefunctions at the structure edges.

We first focus on a continuous description of the effective energy potential imposed by the structure to the polariton fluid: polaritons are treated as free particles propagating in the QW plane and edges of the structure are treated as boundaries of the box potential $V(\mathbf{r})$. This description allows fully reproducing the energy dispersion of polariton states observed experimentally. However the full treatment of the 2D structure can become numerically heavy, especially when it comes to the simulation of quasi-periodic structures. It is therefore convenient to reduce the dimensionality of the problem when possible: for structures with dimensions $L_x \times L_y$ such that $L_x \gg L_y$, we usually consider a transverse approximation of the confinement potential and treat the 1D effective problem.

The second approach that we use is dedicated to modeling arrays or lattices of coupled micro-pillars. Such structures can be particularly well described by a tight-

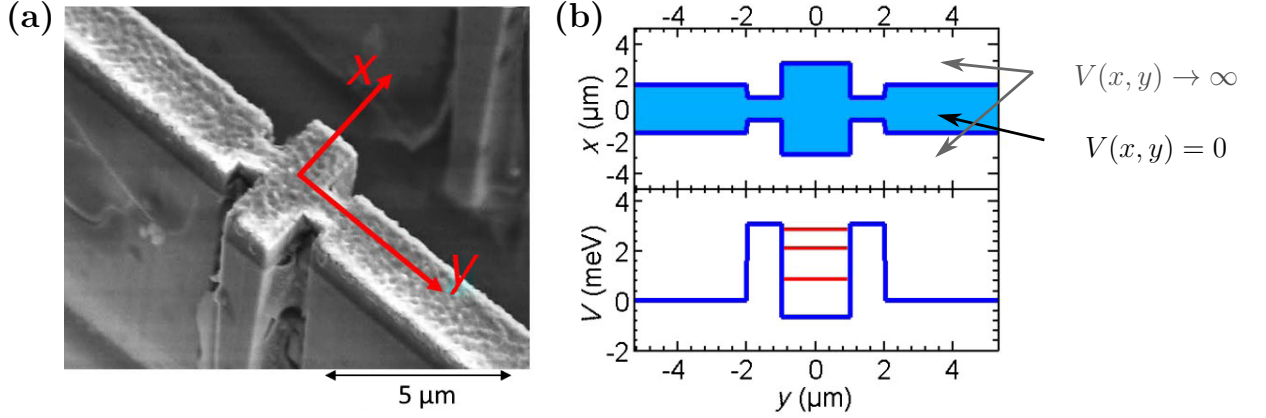


Figure 2.4: **a**, Scanning electron microscope image of a polariton trap created by modulating a wire. **b**, 2D description of the structure (top) and associated effective 1D potential (bottom).

binding approximation. In this approach, micro-pillars are assimilated to discrete sites of a tight-binding lattice and thus as photonic like atoms. This description is valid for the first lowest eigenstates of micro-pillars with radii on the order of the micron and allows the emulation of small structures like benzene molecules but also 1D or 2D models such as graphene.

2.2.1 The nearly-free model to describe 1D and 2D structures

Let us start with the continuous description of cavity structures. The linear eigenstates and associated eigenenergies of a given structure \mathcal{S} are solutions of the 2D Schrödinger equation:

$$E\Psi(x, y) = -\frac{\hbar^2}{2m^*}\nabla^2\Psi(x, y) + V(x, y)\Psi(x, y) \quad (2.1)$$

$$V = 0 \quad \forall (x, y) \in \mathcal{S} \quad \text{and} \quad V \rightarrow \infty \quad \forall (x, y) \notin \mathcal{S}$$

m^* is the polariton effective mass and $V(x, y)$ is a 2D box potential representing the polariton confinement due to the refractive index contrast between the structure and vacuum. In the case of 2D structures this equation can be numerically solved without further approximations².

For quasi-1D structures such as the one presented in Fig. 2.2 (c), it is often convenient to reduce the problem dimensionality by considering a transverse approximation of the potential. Let us consider the case of a simple wire: the structure has a finite width w along y and, for simplicity, the wire is considered infinite along the x direction ($x, y) \in \mathcal{S} \quad \forall |y| \leq w/2$). The wavefunction is thus separable $\Psi(x, y) = \psi(x)\varphi(y)$ and, as for the case of a planar cavity, the solutions along the

²Note that for periodic structures, according to Bloch theorem, the problem can be numerically simplified by considering the description of a single unit-cell. The associated 2D Schrödinger equation with periodic boundary conditions is then solved as a function of momentum \mathbf{k} which dictates the phase picked up at the boundaries.

x direction are plane waves. In the y direction, the problem is the one of a free particle in an infinite square potential well. The solutions of the problem thus read:

$$\varphi_n(y) = \cos(k_{y,n}y) \quad \text{with} \quad k_{y,n} = \frac{n\pi}{w} \quad (2.2)$$

with n the integer describing the quantization of the wave-vector along y . The associated eigenenergies correspond to a set of 1D parabolic dispersions:

$$E_n(k_x) = \frac{\hbar^2\pi^2}{2m^*w^2}n^2 + \frac{\hbar^2}{2m^*}k_x^2 \quad (2.3)$$

where n is playing the role of subband index.

The approach introduced here consists in considering the different sub-bands independently and treating the 1D Schrödinger problem associated to the effective potential V_n :

$$E\Psi(x) = -\frac{\hbar^2}{2m^*} \partial_x^2\Psi(x) + V_n\Psi(x) \quad (2.4)$$

$$V_n = \frac{\hbar^2\pi^2}{2m^*w^2}n^2$$

This treatment becomes particularly interesting when considering wires with a modulated width $w(x)$: the solutions which are no longer separable in x and y are approximated to $\Psi(x, y) = \psi(x) \cos(k_{y,n}(x)y)$ with $k_{y,n}(x) = n\pi/w(x)$. Plugging this ansatz in the 2D Schrödinger equation, it yields:

$$E\Psi(x, y) = -\frac{\hbar^2}{2m^*} \left[\cos\left(\frac{n\pi}{w(x)}y\right) \partial_x^2\psi(x) + \psi(x) \partial_x^2 \cos\left(\frac{n\pi}{w(x)}y\right) + \psi(x) \partial_y^2 \cos\left(\frac{n\pi}{w(x)}y\right) \right] \quad (2.5)$$

Neglecting the spatial derivative of $w(x)$ we obtain the effective 1D potential:

$$V_n(x) = \frac{\hbar^2\pi^2}{2m^*w(x)}n^2 \quad (2.6)$$

An experimental illustration of this method, extracted from Ref. [188], is presented in Fig. 2.4. The authors consider the case of a localized rectangular modulation of a wire to engineer a diode. Using an exciton reservoir to tune the energy of the eigenstates localized in the island structure, it is possible to control the transmission of the total structure. Treating the effective 1D problem was here sufficient to capture the behavior of the system. Several works have been realized in the group considering quasi-1D structures [162, 189–191]. Treating the effective 1D model appeared to be a powerful tool, especially when considering quasi-periodic structures which requires simulating a significant length of the structure to capture the physics.

Note that, when necessary, more complicated ansatz functions can be considered for the effective 1D potential: for example, the spatial derivative of $w(x)$ can be treated by a Taylor expansion. This treatment was done for example in Ref. [192] (see supplementary materials for demonstration), where neglecting the spatial variations of $w(x)$ did not allow to capture all minimal ingredients necessary to describe the physics of polaritons in Fibonacci quasi-periodic structures.

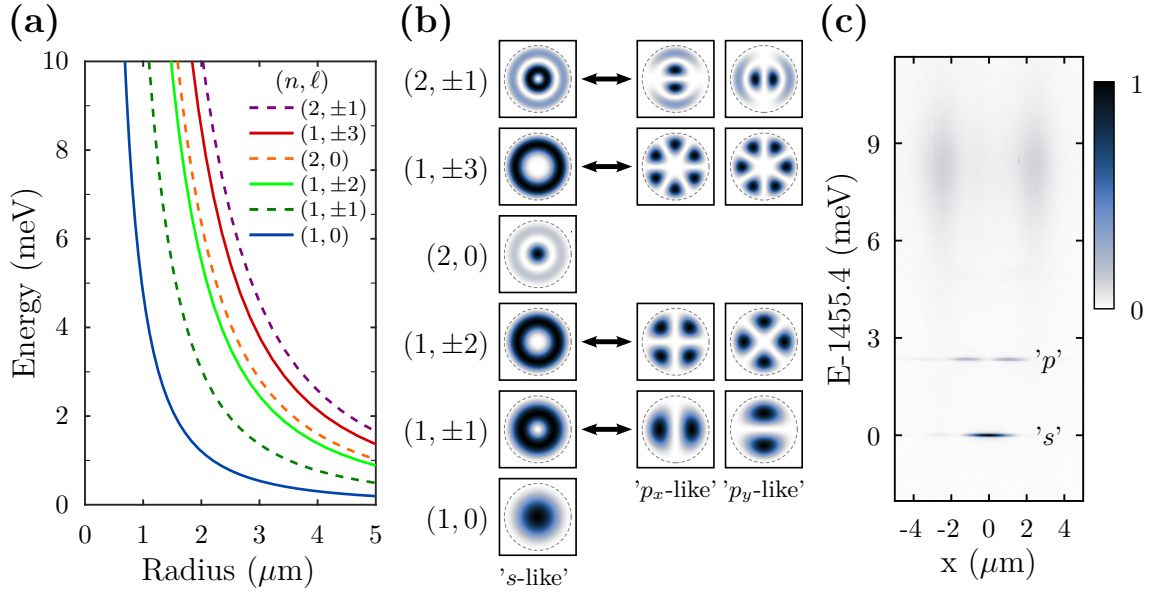


Figure 2.5: **a**, Evolution of the energy of a circular well lowest eigenstates as a function of the well radius. **b**, Squared moduli of the wavefunctions for the circular well lowest eigenstates. For $\ell \neq 0$ modes a representation in the Cartesian basis is also provided, evidencing the p_x and p_y character of the $(n = 1, \ell = \pm 1)$ states. **c**, Real space photoluminescence of a $4 \mu\text{m}$ diameter micro-pillar.

2.2.2 Micropillars as artificial atoms

In the view of emulating Hamiltonians described by a tight-binding formalism, the simplest way to engineer the equivalent of a tight-binding site (atom) with polaritons is to consider a circular micro-pillar. The photonic modes associated to a circular pillar with radius R are given by the solution of 2D Maxwell equations describing a free particle trapped in an infinite circular potential well. Note that, as the structure preserves the cylindrical symmetry, there is no lift of the degeneracy between polarization states. As a result, we can simply solve the scalar problem considering that the real eigenstates consist in a degenerate doublet, with orthogonal polarizations, of the obtained solutions. The spatial profiles of the circular potential well eigenstates are given by Bessel functions of the first kind denoted $\mathcal{J}_\ell(r)$, where ℓ is the order of the Bessel functions. The associated eigenenergies read:

$$E_{n,\ell} = \frac{\hbar^2}{2m^*R^2} j_{n,\ell}^2 \quad (2.7)$$

where $j_{n,\ell}$ is the n -th zero of the Bessel \mathcal{J} function of order ℓ . Note that for $|\ell| \neq 0$ two degenerate solutions are obtained, corresponding to $\ell = \pm|\ell|$ and representing the two possible circulations for the phase gradient of the wavefunction (clockwise or counter-clockwise). Figure 2.5 shows the simulated profiles of the first eigenstates of a circular well and the evolution of the associated eigenenergies as a function of the well radius. These results were obtained *via* numerical resolution of the 2D Schrödinger equation, as described in the previous section. The first eigenstate $\{n = 1, \ell = 0\}$ can be assimilated to the ' s ' orbital of an artificial atom while we can select the description basis of the two degenerated eigenstates $\{n = 1, \ell = 1\}$ and $\{n = 1, \ell = -1\}$ so that they correspond to p_x and p_y atomic orbitals ($\{n = 1, \ell = \pm 1\} = p_x \pm ip_y$). The measured photoluminescence of a $R = 2 \mu\text{m}$ pillar

showing these first eigenstates is presented in Fig. 2.5 (c). Since the spectrometer slit is centered on the pillar, a zero of amplitude is observed in the middle of the ($n = 0, l = \pm 1$) state: the intensity distribution is equivalent to the p_x orbital longitudinal profile.

Restricting ourselves to the lowest eigenstates of the structure, we can therefore assimilate circular micro-pillars to artificial atoms whose eigenenergies can be varied by choosing the pillar radius. Similarly to molecular bonding, coupling micro-pillars leads to the formation of artificial molecules whose eigenstates result from hybridization of micro-pillars ones. In first approximation, this hybridization is described as a linear combination.

2.2.3 Coupling micropillars to build photonic molecules

Let us consider two pillars, labeled A and B , with radii R separated by a distance d . In the case $d < 2R$ the two pillars overlap and the solution of the associated 2D Schrödinger problem is not analytical. Yet the solution can be numerically computed or it can be approximated by linear combinations of the two pillar individual eigenstates: $|\Psi'_j\rangle = \sum_{n,\ell} \alpha_{j,n,\ell} |\Psi_{n,\ell,A}\rangle + \beta_{j,n,\ell} |\Psi_{n,\ell,B}\rangle$. To restrict ourselves to the simple hybridization of ‘ s ’ orbitals, we consider the case where the energy splitting between ‘ s ’ and ‘ p ’ states is infinite. The two ‘ s ’ states described by $|\Psi_{s,A}\rangle$ and $|\Psi_{s,B}\rangle$ hybridize to form two new eigenstates given by the symmetric (bonding) and anti-symmetric (anti-bonding) combination of the bare pillar states:

$$\Psi_{\pm} = \frac{|\Psi_{s,A}\rangle \pm |\Psi_{s,B}\rangle}{\sqrt{2}} \quad (2.8)$$

The associated eigenenergies are given by $E_{\pm} = E_0 \mp J$ where J represents the coupling (hopping) strength between the two bare eigenstates. J can be related to the overlap integral $S = \int \langle \Psi_{s,B} | \Psi_{s,A} \rangle$. The coupling strength can thus be tuned by varying the distance between pillars.

Simply put, this coupled system is described by the tight-binding Hamiltonian:

$$\mathcal{H}_0 = \begin{bmatrix} E_0 & -J \\ -J & E_0 \end{bmatrix} \quad (2.9)$$

The 2D Schrödinger problem, restricted to the two lowest eigenstates, is mapped to the 0D Schrödinger equation $\mathcal{H}_0|\Psi\rangle = E|\Psi\rangle$ in the basis of ‘ s ’ modes $\{|\Psi_{s,A}\rangle, |\Psi_{s,B}\rangle\}$ abbreviated $\{|A\rangle, |B\rangle\}$. This mapping can also be separately applied to p_x and p_y states. Indeed, the overlap between p_x and p_y modes of two different micro-pillars is equal to zero. A 2D simulation of the energy diagram along with mode profiles of two coupled pillars is presented in Fig. 2.6. Due to the stronger overlap of the wavefunctions, the energy splitting between p_x bonding and anti-bonding states is higher than the one observed between hybridized p_y states [193].

One can notice that the two states resulting from the hybridization of s modes are not symmetrically split in energy with respect to the bare s mode of a single micro-pillar contrary to what is expected from the tight-binding mapping. It originates from the non-orthogonality of the description basis which was analyzed in Ref. [194]. As we consider a spatial overlap between single pillar states $|m, n, \ell\rangle$, these states do not constitute an orthogonal basis contrarily to what is assumed in the tight-binding description. The small spatial overlap of the s mode of a micropillar with

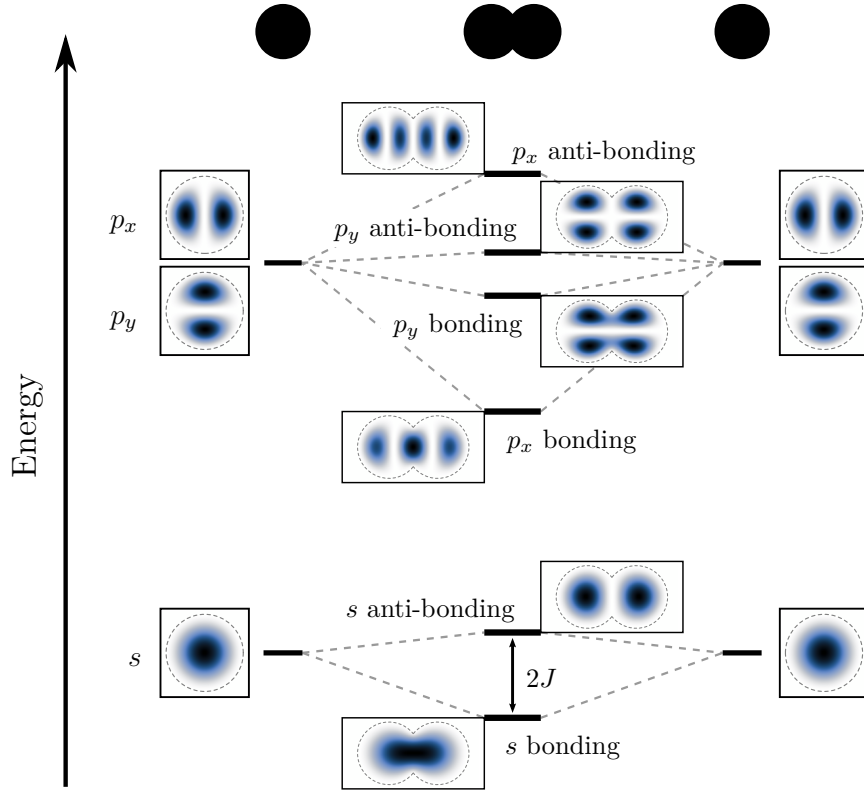


Figure 2.6: Calculated energy diagram of the hybridization between eigenstates of two micro-pillars. Energy diagrams associated to the two bare micro-pillars are represented on the left and right of the one of the hybridized structure. We here restricted our description to the three lowest energy-states of the single micro-pillar (s and p modes). Under each structure, presented on top, black solid lines mark the calculated energy position of the associated eigen-modes. 2D density probability profiles associated to each mode are plotted as insets. Simulations were realized for $R = 2\ \mu\text{m}$ and $d = 2.85\ \mu\text{m}$.

the p_x mode of its first neighbors results in a small deviation from the tight-binding calculation.

The tight binding description remains valid as long as we can consider that the contribution of each pillar comes from a single energy state which is equivalent to saying that the coupling is treated as a perturbation to the onsite energies. Otherwise, deviations due the non-orthogonal nature of the basis complicates the use of a tight-binding description: more parameters have to be included and adjusted.

Note concerning the sign of J : The notation considered in this manuscript is such that a coupling strength is positive when the symmetric coupled state is stabilized: the bonding mode is the lowest energy one.

Coupling more pillars, the lowest eigenstates of the resulting micro-pillar array can be approximated as the hybridization of the ‘ s ’ orbitals of all the individual pillars. Under this approximation, eigenstates are approximated by solutions of a

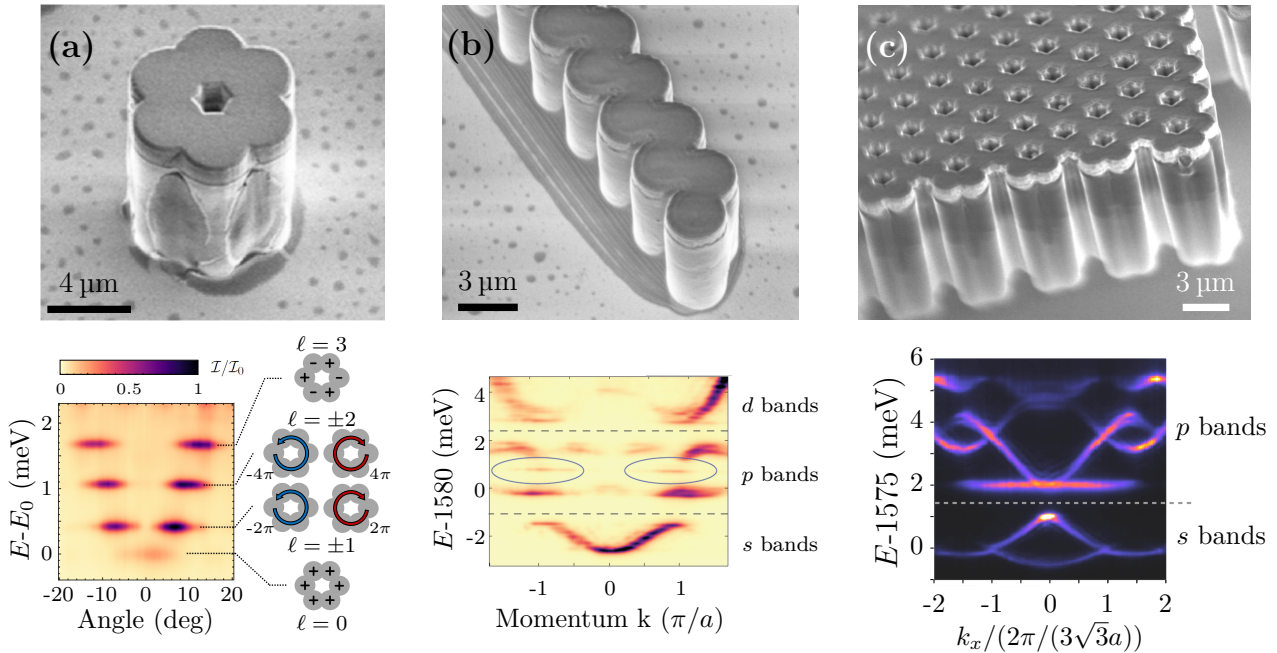


Figure 2.7: Scanning electron microscope images and Fourier-space spectra of coupled micro-pillar structures described by a tight-binding Hamiltonian: **a**, benzene molecule **b**, 1D SSH lattice for p orbitals (“zigzag”) and **c**, 2D honeycomb lattice (graphene).

tight-binding Hamiltonian:

$$\mathcal{H} = \sum_m E_m |\Psi_m\rangle \langle \Psi_m| - \sum_{m,m'} (J_{m,m'} |\Psi_{m'}\rangle \langle \Psi_m| + h.c.) \quad (2.10)$$

where $|\Psi_m\rangle$ is the wavefunction of the m^{th} pillar s state, E_m is the onsite energy of the m^{th} pillar and $J_{m,m'}$ represents the hopping strength from the m^{th} pillar to the m' -th one. The eigenstates of \mathcal{H} and their associated eigenenergies are obtained by diagonalization of the matrix associated to \mathcal{H} . When it is meaningful, the Fourier transform of eigenstates can be computed to access the band dispersion³.

Multiple realizations of tight-binding polariton lattices have been realized in our group⁴ such as the emulation of the 1D Su-Schrieffer-Heeger (SSH) model for p orbitals with the first demonstration of a topological laser [197] or 2D lattices such as analog graphene [198]. In this latter case the polariton platform enables the observation of p -bands of the model or to emulate strained sheets of graphene. Interestingly, one can emulate strain amplitudes beyond what would be physically realizable with real graphene, which enabled the observation of merging and tilting

³Note that the model can also be slightly complexified by considering the two possible polarization states of each micro-pillars. Applying this procedure to a ring of six coupled micro-pillars allowed capturing the polarization fine-structure of this analog benzene molecule [195]. It can be viewed as resulting from an effective spin-orbit coupling. Selective lasing on one of these fine-structure eigenstates was demonstrated and lead to the generation of a micro-laser emitting photons carrying an orbital angular momentum [85, 196].

⁴Note that tight-binding Hamiltonians can be mapped to a lattice of coupled micro-pillars as long as it is allowed by the geometrical limitation linked to the etching and the sample structure. For example, the coupling being given by pillar overlap, only short range hoppings can be considered.

of Dirac cones [199]. SEM images of the corresponding structures as well as their measured band structures are presented in Fig. 2.7.

Note that the engineered coupling are *a priori* restricted to be positive. Yet, considering hybridization of orbitals with different symmetries, it could be possible to increase the versatility of hopping engineering [200, 201].

The structures studied during this thesis are formed by coupled micro-pillars. The tight-binding description will thus be considered most of the time. A nearly-free description of polaritons will only be considered when necessary to reproduce the experimental findings.

2.3 Interacting non-linear polariton fluids in lattices

We now turn to the description of non-linear behaviors of polaritons fluids under quasi-resonant excitation of tailored structures. In this thesis we only consider the case of non-linear behaviors originating from the polariton-polariton interaction and effects such as lasing will not be discussed. Confining polaritons, and thus decreasing their mode volume, eases the observation of non-linear effects. Additionally, the interplay between non-linearities and the energy distribution of polariton states is responsible for an enriched diversity of observable effects. Here, we start with a short presentation of the various phenomena observed with fluids of light in tailored structures, from micro-pillars to 2D lattices. We then introduce the numerical methods used during this thesis to reproduce experimental results and gain insight into the physics of non-linear polariton fluids.

2.3.1 Experimental realizations

We have seen that confining polaritons inside tailored structures allows emulating complex Hamiltonians. So far most studies of polariton fluids in extended (1D, 2D) polariton lattices have focused on linear physics. To date, experimental explorations of polariton lattices in the nonlinear regime remain relatively marginal: most realizations in engineered structures were done in single or couples of micro-pillars despite the existence of theoretical proposals dealing with non-linear fluids in 1D [202, 203] or 2D lattices [8, 204–207].

2.3.1.1 Single pillar:

Contrary to the planar case, where quasi-resonant excitation and non-linearity lead to a bistable behavior (see Chap. 1.5), a single polariton micropillar already offer many extra degrees of freedom that enrich to physics. Indeed, each of the spatial modes described in Fig. 2.5 that are below the pump energy can experience a blueshift due to the interaction, and are thus susceptible to cross the pump energy, leading to a non-linear jump. Such observation was first realized in a mesa by the group of B. Deveaud [208]. The authors showed that each stable branch of the multi-stability diagram is associated to a polariton spatial distribution that resembles the linear eigenstates ones. An illustration is presented in Fig. 2.8 (a).

Harnessing the polariton spin degree of freedom, this group also demonstrated a multi-stability diagram involving several branches corresponding to different polarization states [209]. The exploration of the stability diagram was realized by ramping up and down the pump power but also tuning the excitation beam polarization. More recently the anisotropy of the interaction was used to demonstrate an effective Zeeman splitting [210]: a lift of the degeneracy between circular polarization was realized without the application of a magnetic field.

A resonant scattering process mediated by two different modes of a micro-pillar was demonstrated [211]. Considering solely the s state of a single pillar, the noise squeezing of the reflected light was demonstrated by the group of A. Bramati [212] and a dynamical study of the bistability was realized in our group [213]. Ramping the pump power up and down across the hysteresis region over a time τ_0 , the evolution of the hysteresis area was monitored. This experiment unveiled a dissipative phase transition evidenced by two different power scaling laws at large and short τ_0 .

2.3.1.2 Two coupled micro-pillars:

A system of two coupled micro-pillars already represents a complex non-linear problem as, restricting ourselves to the description of the hybridized s orbitals only, up to nine stable branches can be obtained for a given operating point. Several realizations in such structures were done by our group considering pulsed and continuous wave excitation. Under pulsed excitation, a transition between Josephson oscillations and interaction induced self-trapping was observed when increasing the number of injected polaritons [216]. The exploration of the multi-stability diagram revealed that pumping only one of the two pillars leads to the appearance of a stable branch where the polariton population is mostly localized in the undriven cavity [217]. This phenomenon is due to a destructive interference between polaritons directly injected by the pump and those hopping back from the undriven cavity to the driven one. A parametric oscillation process was also demonstrated between the s bonding and anti-bonding states [214]. Driving the system at the energy of the anti-bonding state and increasing the pump power, interactions induce a blueshift of both states. When the polariton density is such that the blueshift is equal to the coupling strength between the two pillars, the laser energy is exactly at the center between the two resonances and a scattering process can occur (see Fig. 2.8 (b)). Imaging the transmitted light from the cavity using a spectrometer, the obtained spectra revealed the presence of side pics spectrally equally spaced with respect to the laser energy.

2.3.1.3 1D lattices:

In quasi one dimensional structures two realizations were done by our group in wires, the first one considering the hydrodynamics of a polariton superfluid encountering a defect resulting in the formation of an analog black-hole horizon for acoustic waves [130] as predicted in Ref. [128, 129]. The second realization demonstrated the control of a dark soliton train *via* modulation of the pump phase [215], as was originally proposed by M. Petrov et al. in Ref. [218]. Two laser beams are used to inject contra-propagating non-linear fluids. In the nonlinear regime, intensity dips can be observed at the interface between the two fluids (see Fig. 2.8 (c)) each

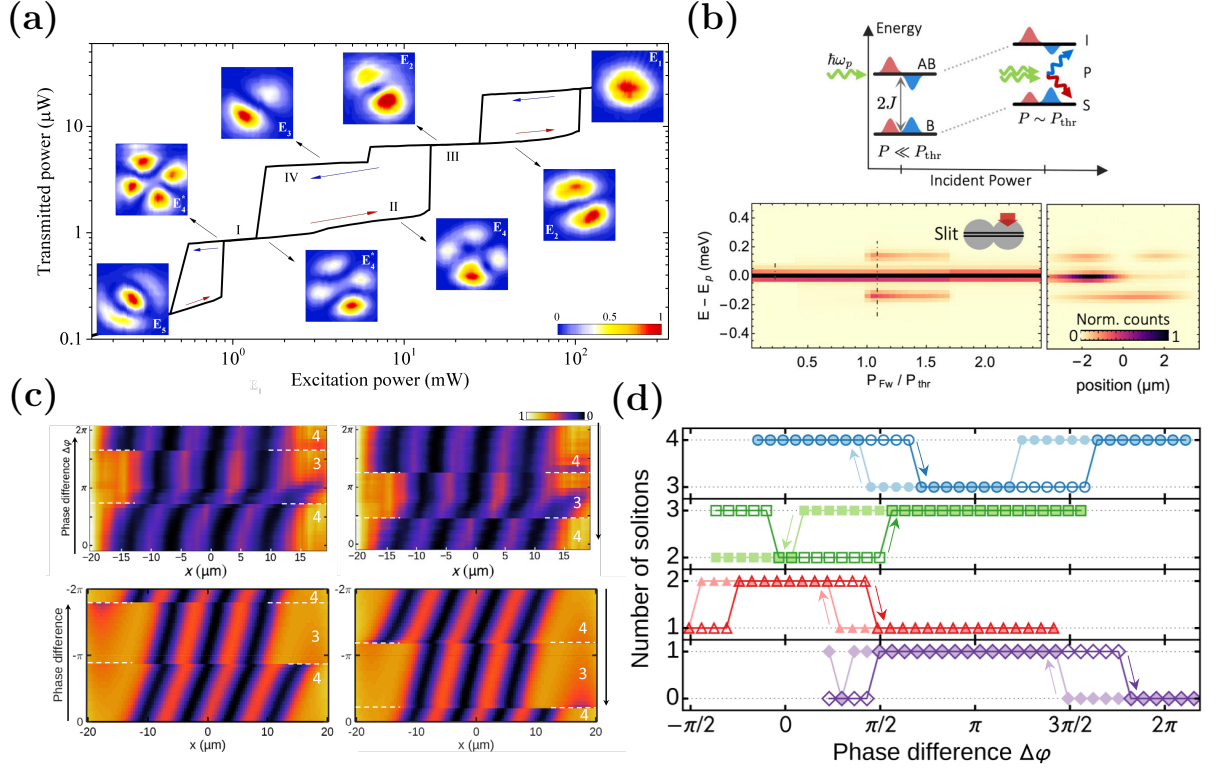


Figure 2.8: **a**, Multi-stability diagram of a circular mesa. Each stable branch presents a profile given by a Bessel J function, inherited from one of the eigenstates. Image taken from Ref. [208]. **b**, Resonant polariton parametric scattering between hybridized s states of two coupled micro-pillars. A scheme of the process is presented on top and the evolution of the emission spectrum as a function of the incident power is presented in the bottom left panel. Bottom right panel corresponds to the emission resolved in energy and position at the input power indicated by a dashed line. The emission profile confirms the bonding and anti-bonding nature of signal and idler. Images adapted from Ref. [214] **c**, Measured (top) and calculated (bottom) intensity profiles of the merging of two contra-propagating non-linear fluids: a dark soliton train is observed. Scanning the phase difference between pump spots up (left) and down (right), phase hysteresis is observed between two branches presenting a different number of dark solitons. **d**, Power dependence of the dark soliton train bistability. More dark solitons are observed when the power is increased and, for a given input power, tuning the phase allows switching a dark soliton on and off. Images taken from Ref. [215].

of them corresponding to a dark soliton. Tuning the pump power and the relative phase difference between the two beams was shown to enable controlling the number of dark solitons in the train (see Fig. 2.8 (c-d)). Finally, a third realization was made in a periodic structure of coupled micro-pillars emulating a 1D Lieb lattice [219]. The unit cell of this lattice is composed of three sites and the lattice spectrum is therefore composed of three bands. The particularity of the Lieb lattice is that, due to a phase frustration, the middle sub-band of the model is flat. In this band, particles can be described as having an infinite effective mass. Injecting a non-linear polariton fluid in this frustrated band resulted in the formation of bright gap solitons presenting abrupt edges, that can be assimilated to compactons [220]. The exploration of the multi-stability diagram *via* scans of the pump power revealed a complex structure where each non-linear jump is associated to lighting or extinction of a discrete number of unit cells as predicted in Ref. [221]. The large non-linear structures observed in this work, which are formed of contiguous ensembles of gap solitons and present abrupt edges have also been named Truncated Bloch Waves (TBW).

The term of Truncated Bloch Wave was introduced by the group of Y. S. Kivshar to describe the formation of gap solitons clusters which take the form non-linear Bloch waves truncated to a discrete number of unit cells [222, 224, 225]. In a band, particles at the edge of the soliton can propagate outside of the dense region with a velocity given by the local band curvature and the soliton profile thus exhibits a smoothed decay into the surrounding material. In a gap, on the contrary, no states are available for particles to propagate outside of the dense region. This lack of spatial decay channels leads to the formation of a self-trapped wave-packet presenting abrupt edges. Particles are trapped in between these edges and the fluid profile in the dense region is the one of a non-linear Bloch wave as illustrated in Fig. 2.9. These TBWs have been experimentally observed in cold atoms experiments [226], coupled waveguides [227] or also fiber loops [223]. An illustration of the latter is presented in Fig. 2.9 (b).

2.3.1.4 2D lattices:

In the case of 2D lattices, a single realization was made using surface acoustic wave confinement of polaritons where a parametric injection lead to the formation of bright gap solitons [161].

During this thesis, we pursued the exploration of polariton fluids confined in lattices and especially studied the non-linear behavior of polariton fluids injected in a 1D topological lattice. In parallel of our experimental realizations, we performed numerical calculations which reproduced and sometimes predicted the behavior of polaritons in our samples. The next section introduces the employed methods.

2.3.2 The discrete Gross-Pitaevskii equation

In Chap. 1.5.3 we introduced the quasi-resonant excitation of polaritons in planar cavities and the driven-dissipative Gross-Pitaevskii equation governing the evolution

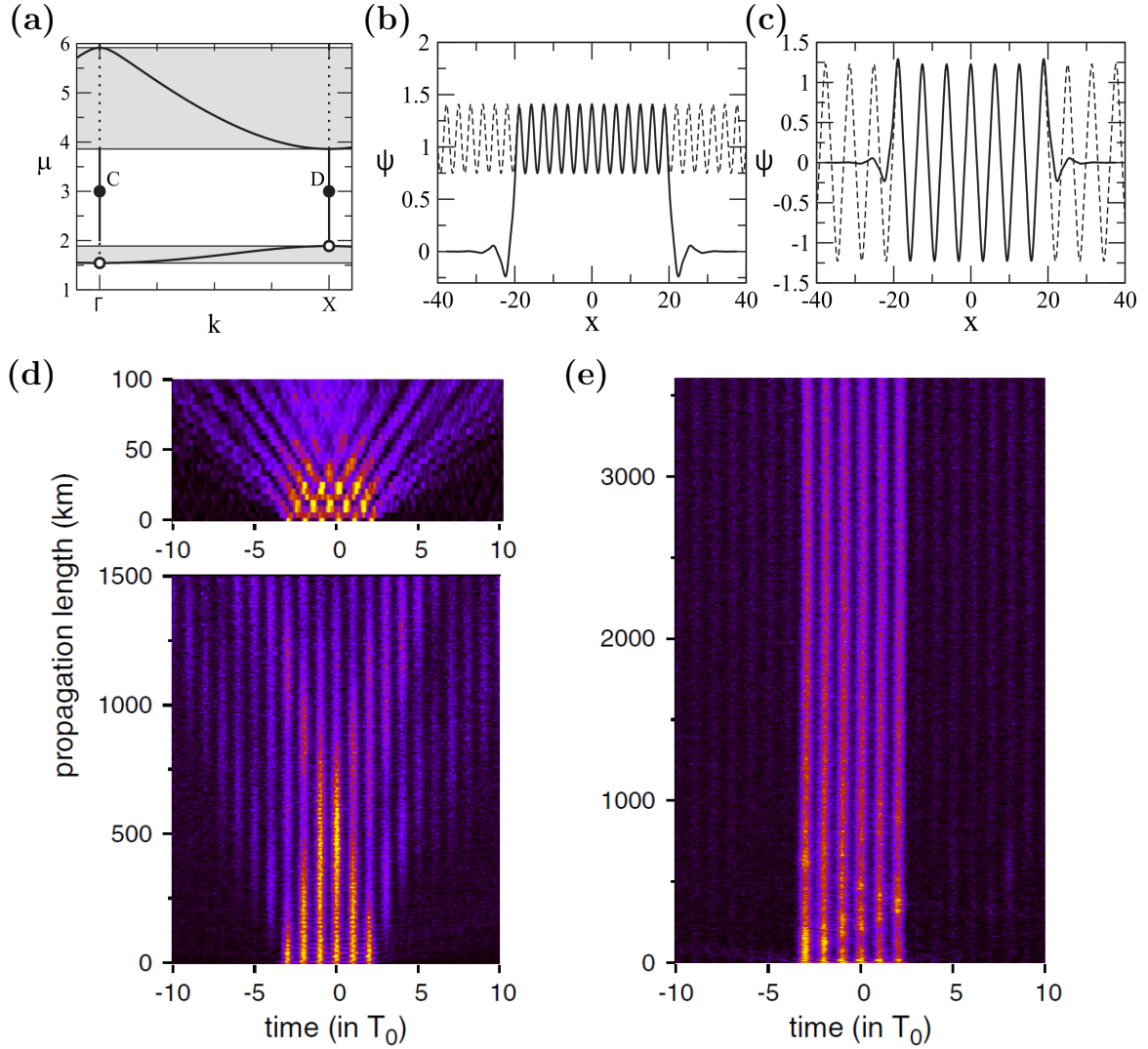


Figure 2.9: **a**, Band diagram of a 1D periodic lattice. C and D black dots mark the operating points considered for the injection of Truncated Bloch Wave presented in panels **(b)** and **(c)**. **b-c**, Simulated profiles of TBW respectively generated at the center and edge of the Brillouin zone. **d-e**, Experimental observation of a TBW in fiber loops. In the linear regime **(d)**, the wave-packet is shown to diffract while propagating whereas the stable propagation of a TBW is observed in the non-linear regime **(e)**. Images taken from [222] and [223].

of the system. We recall that in the rotating frame of the pump this equation reads:

$$i\hbar \partial_t \Psi_0(\mathbf{r}, t) = \left(-\frac{\hbar^2}{2m^*} \nabla^2 + V(\mathbf{r}) - \hbar\omega_p + g|\Psi_0(\mathbf{r}, t)|^2 - i\frac{\hbar\gamma}{2} \right) \Psi_0(\mathbf{r}, t) + iF(\mathbf{r}, t) \quad (2.11)$$

The dynamics of polariton fluids confined in deep-etched structures can be captured by the very same equation once the sample structure is included in the potential $V(\mathbf{r})$. Most generally, numerical simulations of the 2D Gross-Pitaevskii equation can be considered. However they are very heavy so that whenever possible, we will resort to a description in lower dimensions using a transverse approximation of $V(\mathbf{r})$ for quasi-1D structures or a tight-binding approximation. In the latter case, we consider the discrete driven-dissipative Gross-Pitaevskii equation:

$$i\hbar \partial_t \Psi = \left(\mathcal{H} - (\hbar\omega_p + i\frac{\hbar\gamma}{2})\mathbb{1} \right) \Psi + g[|\Psi_m|^2 \Psi_m]_M + i\mathbf{F} \quad (2.12)$$

where Ψ and \mathbf{F} are column vectors respectively representing the amplitude of the polariton fluid and of the driving field in each pillar of the lattice. The amplitude of the polariton fluid and of the driving field in the m^{th} pillar of the lattice will respectively be written Ψ_m and F_m . \mathcal{H} is a tight-binding Hamiltonian which general form was introduced in equation 2.10 and $\mathbb{1}$ is the identity. We use the notation $[|\Psi_m|^2 \Psi_m]_M$ to represent the vector column with M elements where $|\Psi_m|^2 \Psi_m$ is the m^{th} element.

For a lattice of M coupled pillars this vector equation can be rewritten as a set of coupled equations:

$\forall m$ such that $1 \leq m \leq M$:

$$i\hbar \partial_t \Psi_m = \left(E_m - \hbar\omega_p - i\frac{\hbar\gamma}{2} + g|\Psi_m|^2 \right) \Psi_m - \sum_{m'=1}^M J_{m,m'} \Psi_{m'} + iF_m \quad (2.13)$$

All measurements performed during this thesis were realized under slow variations of the drive parameters and using a CCD camera with an integration time ($\sim 0.1 - 1$ s) much longer than the polariton lifetime ($\sim 10 - 100$ ps). Here, we only focus on the steady-state of the set of equations 2.13 which already represents a challenge: for a set of M coupled equations, the number of steady-state solutions is up to M^3 . For small systems (single pillars or two coupled pillars), we can perform the direct calculation of all possible steady-state solutions. For larger lattices, we resort to a time evolution of the set of equations 2.13, starting from $\Psi = 0$ and $\mathbf{F} = 0$. \mathbf{F} is then adiabatically ramped following the protocol considered in the experiment.

We consider a split-operator method where interactions and drive are treated in perturbation ⁵ (assuming Ψ to be constant over a time step dt). The steps of the iteration loop are presented below, where we define $\tilde{\mathcal{H}} = \mathcal{H} - (\hbar\omega_p + i\frac{\hbar\gamma}{2})\mathbb{1}$ and $d\mathbf{F}$ corresponds to the variation of the drive amplitude during the time step:

⁵In the case of the continuous model we apply the equivalent Fourier method: ∇^2 is applied after Fourier transform of $\Psi(\mathbf{r})$ as applying the Laplacian is a linear operation in the reciprocal space.

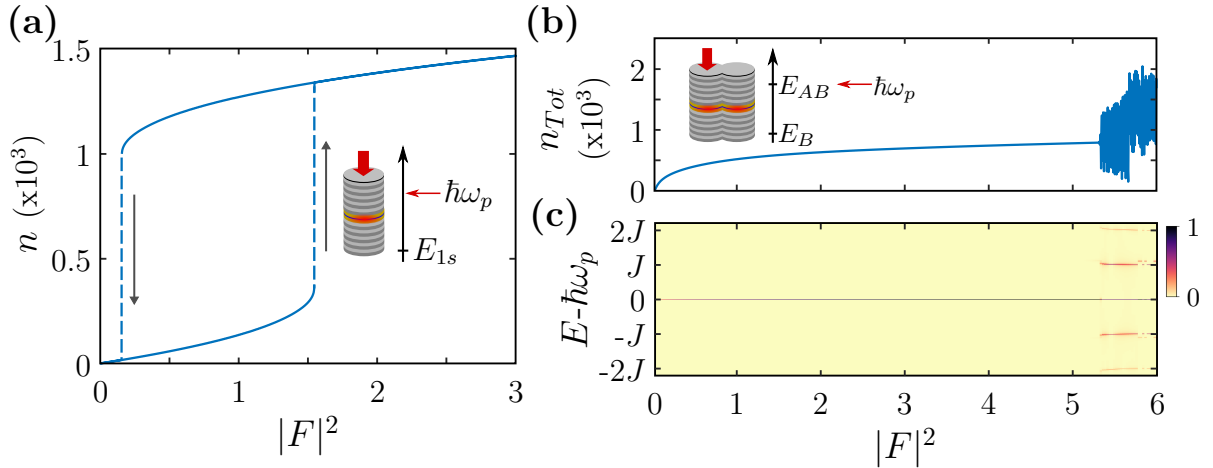


Figure 2.10: **a**, Numerical bistability experiment: we considered a single site with $g = 0.1 \mu\text{eV}$, $\gamma = 25 \mu\text{eV}$ and we simulated a ramp up and down of the input power $|F|^2$ while monitoring the field in the system. The pump energy was set to $\hbar\omega_p = E_{1s} + 100 \mu\text{eV}$. Plotting the particle density n as a function of the input power $|F|^2$, we observe the existence of an hysteresis cycle. Gray arrows indicate the direction of the density jumps. A sketch of the system is displayed in inset. **b**, Reproduction of the OPO process presented in Fig. 2.8. We considered two sites, with same parameters as in **(a)**, coupled with a hopping strength $J = 100 \mu\text{eV}$. Top: evolution of the total particle density in the system. A sketch of the system is displayed in inset. Bottom: spectrum of the fluid obtain by Fourier transform of the temporal evolution of the system.

- 1st step, we apply the temporal propagator for half a time step:

$$\Psi = \exp\left(-i\frac{\hat{\mathcal{H}}}{\hbar}\frac{dt}{2}\right)\Psi$$

- 2nd step, the interaction term is treated in perturbation:

$$\Psi = \left[\exp\left(-i\frac{g|\Psi_m|^2}{\hbar}dt\right)\Psi_m\right]_M$$

- 3rd step, we treat the drive term:

$$\Psi = \Psi + (\mathbf{F} + \mathbf{dF})dt/\hbar$$

- 4th step, we apply the temporal propagator for half a time step:

$$\Psi = \exp\left(-i\frac{\hat{\mathcal{H}}}{\hbar}\frac{dt}{2}\right)\Psi$$

To ensure adiabaticity of the simulation and avoid calculation errors, the parameters have to fulfill several criterion. The time step dt has to be smaller than any other characteristic time scale of the simulation such as the polariton lifetime $dt \ll 1/\gamma$. Also, one has to be careful with the time scale associated to the interaction term, which can play a predominant role at density jumps for example. Additionally, the particle injection rate must not exceed the losses: $\forall m, |dF_m|/dt < \gamma$ ⁶.

To illustrate the method, we first simulated the hysteresis cycle obtained when driving a single pillar at an energy slightly blue-detuned with respect to the micropillar s mode (Fig. 2.10 (a)). As a second illustration, we reproduced the OPO

⁶The employed numerical methods do not represent a state of the art procedure. More involved numerical methods could be used to efficiently compute the temporal evolution of the system: adaptative methods such as Runge-Kutta-Fehlberg (RK45) or multi-step ones such as Adams-Bashforth.

process illustrated in Fig. 2.8 (b) which was observed in Ref. [214] with two coupled resonators (Fig. 2.10 (b-c)).

- In Fig. 2.10 (a) we considered a pillar with $g = 0.1 \mu\text{eV}$, $\gamma = 25 \mu\text{eV}$ and drove the system $100 \mu\text{eV}$ above the pillar onsite energy. We then ramped F up and down while monitoring the polariton density n . The evolution of n as a function of the input power $|F|^2$ is presented in Fig. 2.10 (a), which exhibit a clear hysteresis cycle.
- In Fig. 2.10 (b) we considered two of these pillars coupled with a hopping strength $J = 100 \mu\text{eV}$ and reproduced the driving protocol considered in Ref. [214]: only one of the two resonators is driven at the energy of the anti-bonding s state $\hbar\omega_p = E_{AB} = E_{1s} + J$. The evolution of the total density $n_{\text{Tot}} = |\Psi_1|^2 + |\Psi_2|^2$ is presented in Fig. 2.10 (b). No density jump is observed when ramping F as the pump is resonant with the anti-bonding mode: at low power ($|F|^2 < 1$) we observe a rapid increase of n which then saturates and corresponds to an optical limiter regime. Interestingly, we observe strong fluctuations of n_{Tot} above $|F|^2 = 5.3$. For each value of $|F|^2$, we computed the temporal evolution of the system and observed periodic fluctuations of n_{Tot} above $|F|^2 = 5.3$. Calculating the Fourier transform of the temporal evolution of the field, we obtained the energy spectrum which is presented in Fig. 2.10 (c). Above $|F|^2 = 5.3$ we observe the appearance of equally spaced side peaks close to $\hbar\omega_p \pm J$ and $\hbar\omega_p \pm 2J$. In Ref. [214] this phenomenon was attributed to a scattering process onto the blueshifted bonding and anti-bonding states of the system, as illustrated in the bottom right panel of Fig. 2.8 (b). The OPO process is enabled when the blueshift is such that the two resonances are equally spaced with respect to the laser energy. To determine the energy position of the blueshifted bonding and anti-bonding states, we have to compute the excitation spectrum of the system.

2.3.3 Bogoliubov theory

The excitation spectrum is a particularly useful tool to characterize the state of the system in presence of a non-linear fluid. For example, the superfluidity of polariton fluids was explained as a result of the renormalization of the excitation spectrum induced by inter-particle interactions [47] (see Chap. 1.5.3). To compute this spectrum, we use the Bogoliubov method [228, 229] which consists in a linearization of the Gross-Pitaevskii equation around the steady-state. Assuming the system to have reached its steady-state Ψ^S , the set of equations 2.13 reads:

$$\forall m \text{ such that } 1 \leq m \leq M : \quad \left(E_m - \hbar\omega_p - i\frac{\hbar\gamma}{2} + g|\Psi_m^S|^2 \right) \Psi_m^S - \sum_{m'=1}^M J_{m,m'} \Psi_{m'}^S + iF_m = 0 \quad (2.14)$$

We now consider a small perturbation around the steady-state using the ansatz $\Psi(t) = \Psi^S + \delta\Psi(t)$ and inject it in equations 2.13. After linearization of the equations (we discard terms of second and third order in $\delta\Psi$), it yields:

$\forall m$ such that $1 \leq m \leq M$:

$$i\hbar\partial_t\delta\Psi_m = \left(E_m - \hbar\omega_p - i\frac{\hbar\gamma}{2}\right)\delta\Psi_m + 2g|\Psi_m^S|^2\delta\Psi_m + g(\Psi_m^S)^2\delta\Psi_m^* - \sum_{m'=1}^M J_{m,m'}\delta\Psi_{m'} \quad (2.15)$$

where $\delta\Psi_m^*$ is the complex conjugate of $\delta\Psi_m$. This set of equations governs the dynamics of small density and phase fluctuations on top of the non-linear fluid described by Ψ^S . To solve this problem which couples the field $\delta\Psi$ to its complex conjugate, we look for solutions in the form of plane waves: $\delta\Psi = \mathbf{U} \exp(-i\mathcal{E}t/\hbar) + \mathbf{V}^* \exp(i\mathcal{E}^*t/\hbar)$. \mathbf{U} and \mathbf{V} are the amplitudes which only depend on position and \mathcal{E} is their associated energy which is *a priori* complex due to the dissipative nature of the system. Replacing this ansatz in equations 2.15 and identifying terms with the same temporal evolution, it yields two sets of equations on \mathbf{U} and \mathbf{V} ⁷:

$\forall m$ such that $1 \leq m \leq M$:

$$\begin{aligned} \mathcal{E}U_m &= \left(E_m - \hbar\omega_p - i\frac{\hbar\gamma}{2}\right)U_m + 2g|\Psi_m^S|^2U_m + g(\Psi_m^S)^2V_m - \sum_{m'=1}^M J_{m,m'}U_{m'} \\ \mathcal{E}V_m &= \left(-E_m + \hbar\omega_p - i\frac{\hbar\gamma}{2}\right)V_m - 2g^*|\Psi_m^S|^2V_m - g^*(\Psi_m^{S*})^2U_m + \sum_{m'=1}^M J_{m,m'}^*V_{m'} \end{aligned} \quad (2.16)$$

These two sets of equations can be written in the form $M_B\Psi = \mathcal{E}\Psi$ where $\Psi = \begin{bmatrix} \mathbf{U} \\ \mathbf{V} \end{bmatrix}$ and M_B is the Bogoliubov matrix which reads:

$$M_B = \begin{bmatrix} A & B \\ -B^* & -A^* \end{bmatrix} \quad \text{with} \quad \begin{cases} A = \tilde{\mathcal{H}} + \text{diag}\left(2g\left[|\Psi_m^S|^2\right]_M\right) \\ B = \text{diag}\left(g\left[(\Psi_m^S)^2\right]_M\right) \end{cases} \quad (2.17)$$

where $\text{diag}(\Psi)$ is a diagonal matrix whose m^{th} diagonal element corresponds to the m^{th} element of the vector Ψ .

The diagonalization yields eigenstates and eigenenergies which corresponds to the excitation spectrum of the system in presence of the non-linear fluid described by Ψ^S . These excitations, which are often called Bogolons, present energies which are defined with respect to those of the driving field (rotating frame). Note that for a lattice with M sites, the associated Bogoliubov matrix is $2M \times 2M$. We obtain $2M$ eigenstates which present the particle-hole symmetry: if $\Psi_0 = \begin{bmatrix} \mathbf{u} \\ \mathbf{v} \end{bmatrix}$ is eigenstate

of M_B for the energy \mathcal{E}_0 , then $\Psi'_0 = \begin{bmatrix} \mathbf{v}^* \\ \mathbf{u}^* \end{bmatrix}$ is eigenstate for the energy $-\mathcal{E}_0^*$:

$$\begin{aligned} M_B\Psi_0 = \mathcal{E}_0\Psi_0 &\rightarrow \begin{cases} A\mathbf{u} + B\mathbf{v} = \mathcal{E}_0\mathbf{u} \\ -B^*\mathbf{u} - A^*\mathbf{v} = \mathcal{E}_0\mathbf{v} \end{cases} \\ M_B\Psi'_0 = \begin{bmatrix} A\mathbf{v}^* + B\mathbf{u}^* \\ -B^*\mathbf{v}^* - A^*\mathbf{u}^* \end{bmatrix} &= \begin{bmatrix} -(-A^*\mathbf{v} - B^*\mathbf{u})^* \\ -(B\mathbf{v} + A\mathbf{u})^* \end{bmatrix} = \begin{bmatrix} -\mathcal{E}_0^*\mathbf{v}^* \\ -\mathcal{E}_0^*\mathbf{u}^* \end{bmatrix} = -\mathcal{E}_0^*\Psi'_0 \end{aligned} \quad (2.18)$$

⁷Note that we consider the possibility for the interaction to be complex: as we will see later in Chap. 3 it is sometimes necessary to consider non-linear losses which are introduced as a complex term in g .

In the linear regime we can consider $|\Psi^S|^2 \approx 0$ which yields B to be the Zero matrix of size M by M ($0_{M,M}$). As a result, the eigenstates of M_B with a non-zero \mathbf{U} correspond to the eigenstates of $\hat{\mathcal{H}}$ and M_B eigenstates with zero \mathbf{U} and non-zero \mathbf{V} components represent their particle-hole symmetric. Consequently, we refer to \mathbf{U} (\mathbf{V}) as the particle (hole) component of M_B eigenstates.

In the non-linear regime, $B \neq 0_{M,M}$ and eigenstates of M_B are thus mixed states of particles and holes. Among them, those originating from the linear particle states are often called “normal” or “+” modes while their particle-hole symmetric are referred to as “ghost” or “-” modes. Dispersion of the excitation spectrum displayed in the following will always correspond to the \mathbf{U} component of the $2M$ Bogolons states. The spectrum associated to \mathbf{V} is obtained by a mirror symmetry in energy and momentum with respect to those of the pump.

Writing the Bogoliubov method in a quantized formalism consists in looking for excitations described by creation and annihilation operators β and β^\dagger . These operators are linear combinations of p and p^\dagger , the creation and annihilation operators of the lower polariton. It reads: $\beta^\dagger = u_k p_k^\dagger + v_k p_{-k}$.

The particle and hole nature of \mathbf{U} and \mathbf{V} is much clearer in this case as they appear as eigenstates of the creation and annihilation operators. Note that in our case Bogolons are bosons which implies $[p_k, p_{k'}^\dagger] = \delta_{k,k'}$ and yields the normalization $|u_k|^2 - |v_k|^2 = 1$.

As a simple illustration, we computed the Bogoliubov spectrum associated to the numerical experiment presented in Fig. 2.10 (b-c) and which aimed at reproducing the OPO process reported in Ref. [214], see Fig. 2.8 (b). For each value of F , we diagonalized the Bogoliubov matrix associated to the steady-state $\Psi^S(F)$. The evolution of the real part of the four eigenenergies as a function of $|F|^2$ is presented in the bottom panel of Fig. 2.11 (a). At low power, the pump is resonant with the anti-bonding state (and its “ghost” mode) while the bonding state lies at $\mathcal{E} = -2J$. When $|F|^2$ is increased between $|F|^2 = 0$ and $|F|^2 = 5.3$, the two “normal” modes (in solid lines) blueshift while the associated “ghost” modes redshift. As expected, parametric instabilities develop when the two blueshifted states reach the vicinity of $\mathcal{E} = \pm J$. The steady-state Ψ^S is not defined in presence of density fluctuations and consequently, the calculation of the excitation spectrum *via* the presented method is not possible above $|F|^2 = 5.3$.

As a second illustration, we reproduced the energy spectrum associated to superfluidity presented in Fig. 1.12 (a). To do so we considered a linear chain of $M = 400$ coupled sites with a constant hopping $J = 100 \mu\text{eV}$ and periodic boundary conditions, the resulting band structure is presented in Fig. 2.11 (b). We drove the system at $\hbar\omega_p = -J/2$ and using an homogeneous pump ($\forall m, |F_m| = F_0$) with a momentum $k_p \approx \pi/7$ (see Fig. 2.11 (b)). Ramping the power up and down, we observe the opening of a hysteresis cycle in the total density $n_{\text{Tot}} = |\Psi|^2 = \sum_{m=1}^{400} |\Psi_m|^2$, see Fig. 2.11 (c). Computing the energy spectrum for the working point A , just before the lower bistability threshold, we obtained the dispersion presented in Fig. 2.11 (d). Above $\text{Re}(\mathcal{E} = 0)$ we observe the renormalized “normal branch” of the spectrum. The “ghost branch”, which appears below $\text{Re}(\mathcal{E} = 0)$, presents a much weaker intensity. No other state is available with $\text{Re}(\mathcal{E} = 0)$ for polaritons to elastically scatter, which is characteristic from the superfluid regime. Additionally, we recover the linear dispersion expected in the vicinity of $\text{Re}(\mathcal{E} = 0)$ where Bogolons thus behave as

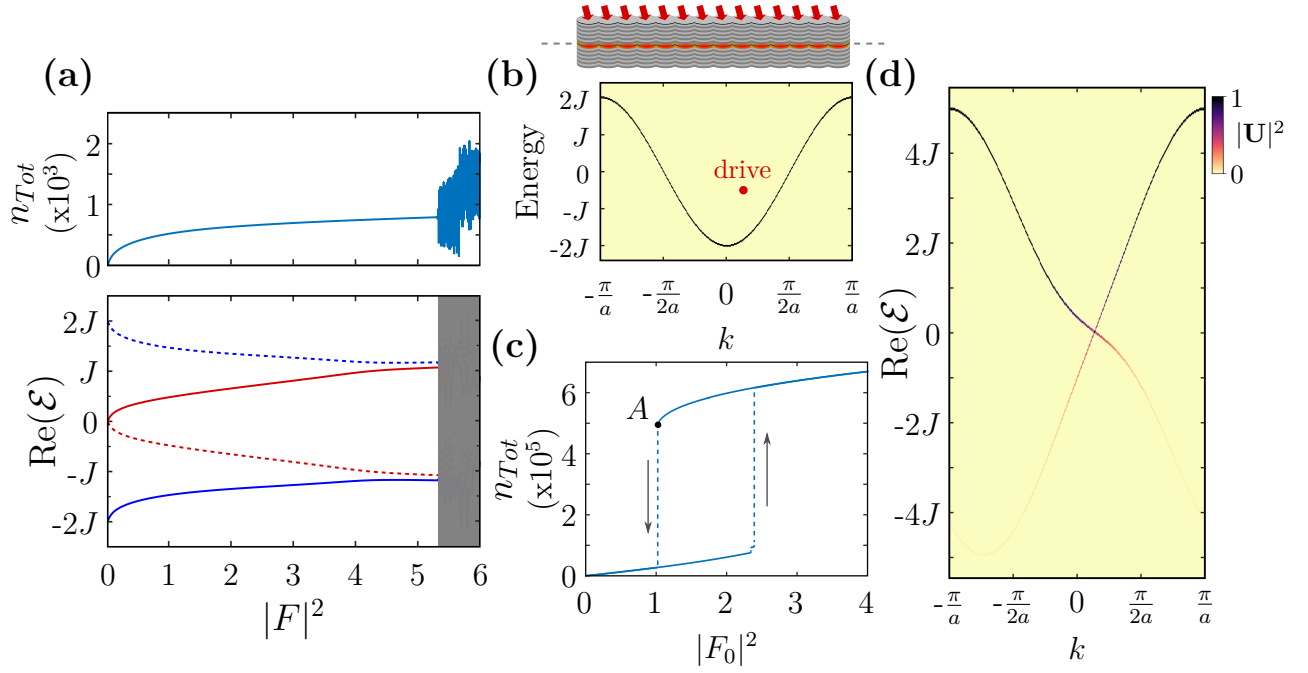


Figure 2.11: **a**, Top: Fig. 2.10 (b) is reproduced for comparison. Bottom: spectrum of excitations as a function of the input power $|F|^2$ corresponding to the simulation presented in Fig. 2.10 (b-c), we only plot the real part of the four eigenenergies. Blue (red) curves correspond to eigenstates with bonding (anti-bonding) symmetry. Solid and dashed lines respectively represent "normal" and "ghost" modes. Gray region signals the presence of parametric instabilities. In this region the steady-state Ψ^S is not defined and the calculation is thus meaningless. **b**, Calculated dispersion of a chain of 400 coupled pillars. **c**, Bistability diagram obtained ramping the power using a pump with energy and momentum indicated by the red dot in (b). A sketch of the system is displayed on top of panel (b). Gray arrows indicate the direction of the jumps. **d**, \mathbf{U} component of the Bogoliubov spectrum computed for the working point A marked with a black dot in (c).

phonons, with a well-defined speed of sound.

2.4 Summary

In this chapter we presented the various methods employed to confine polaritons, which can be done *via* the photonic or the excitonic components of the quasi-particles. We introduced the deep-etching technique used at C2N which results in a confinement due to the strong variation of the refractive index in the (Oxy) plane. Two different approaches can be considered to tailor the polariton band structure: we either design the lateral profile of a quasi-1D wire or consider a mapping to a tight-binding model using coupled micro-pillars. We then presented the different experimental realizations studying interacting fluids of polaritons in lattices and introduced the numerical methods that we use to model and reproduce experimental data.

In the next chapters, we pursue the exploration of non-linear polariton fluids in lattices and we especially focus on the formation and control of gap solitons in the topological gap of a Su-Schrieffer-Heeger (SSH) lattice.

Chapter 3

Gap solitons in a 1D topological lattice

The discovery of topological insulators [230, 231] demonstrated the pertinence and importance of the mathematical field of topology to describe the physical properties of matter. Topological insulators are a class of materials that possess a bulk band gap, as regular insulators, but yet exhibit a non-zero conductance due to the presence of conducting edge states at their surface [2]. The existence of these states is imposed by the non-trivial topological nature of the bulk material [232] and, as a consequence, no deformation of the surface can alter the conduction properties of the object (see Sec. 3.1). Moreover, inter-particle interactions appeared to further enrich the phenomenology of topological insulators as quasi-particle with fractional elementary charge were unveiled [233, 234]. The development of such materials is thus extremely appealing and, as it has often been done, transferring these ideas to photonic platforms promised considerably important applications such as the development of integrated non-reciprocal devices, conduction lines for photons or the generation of robust correlated photon states. Beyond the development of applications, the high versatility of photonic platforms allowed pushing the fundamental exploration of topological matter with the development of Floquet physics [235] or high-dimension insulators using synthetic dimensions [236]. The field of non-linear topological photonics aims at unraveling the consequences of inter-particle interactions on topological properties: for example, topological phase transitions can be induced and novel non-linear structures are expected to benefit from symmetry protection (see Sec. 3.2).

The polariton platform belongs to a particular class of non-Hermitian system as drive and dissipation play a crucial role in the dynamics of the quasi-particles. To explore the interplay between inter-particle interaction and topology in presence of drive and dissipation we will focus on one of the simplest model exhibiting edge states possessing a topological origin, the Su-Schrieffer-Heeger (SSH) model. In this chapter we describe the specificity of bright gap solitons generated in the topological gap of the SSH lattice. In Sec. 3.3 we show that the solitons generated in the topological gap of an SSH lattice present a profile specific from the topological gap and which is dictated by the symmetry of the Hamiltonian. In Sec. 3.4 we probe the robustness of these solitons and show that the profile symmetry is responsible for the protection of gap solitons against certain types of defects. Finally, in Sec. 3.5, we demonstrate the importance of coherent driving in the case of open systems: engineering of the

driving field allows stabilizing novel solutions, akin to a topological edge state and that solely exist due to the driven-dissipative nature of the system. Interestingly, the density profile of the such driven-dissipative soliton is responsible for the emergence of a localized state in the topological gap of the excitation spectrum. The analysis of the calculated Bogoliubov spectra shows that harnessing the driven-dissipative nature of the polariton platform enables to realize a topological phase transition.

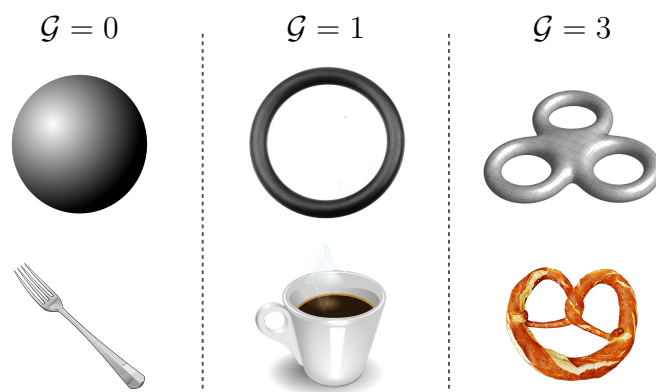


Figure 3.1: Six different objects that can be grouped into three couples as they present identical genus numbers \mathcal{G} and are thus equivalent in the sense of topology.

3.1 Introduction to topology

3.1.1 The mathematical field of topology

Topology is a field of mathematics aiming at classifying geometrical objects based on global properties that are preserved under continuous deformations as twisting or stretching. Contrary to geometrical considerations where one would care about the metric and local organization of the object, thus making a distinction between spheres and cubes for example, a topological description will address more fundamental properties of the object and, extending the example, treat spheres and cubes as identical entities as they can be transformed into one another by smooth deformations: without cutting or pasting parts of the object. The field of topology emerged in the middle of the 16th century with L. Euler's answer to the Königsberg bridge problem, which is considered as the beginning of graph theory. This was followed by his discovery of the polyhedron formula, which states that for regular polyhedra: $V - E + F = 2$ with V the number of vertices (corners), E the number of edges and F the number of faces of the polyhedron. This formula exhibits a crucial concept in topology, the notion of topological invariant: a global property that is conserved under continuous deformations. The most common example of topological invariant given as an introduction to topology is a generalization of this formula for orientable surfaces: the genus number \mathcal{G} which counts the number of holes in the surface. Creating or removing a hole in a structure is not allowed since it would require to cut or paste part of the object. As a consequence, spheres are topologically distinct from tori as their genus numbers differ by 1 (see Fig. 3.1). Holes can be displaced across the structure but as long as one only considers continuous deformations, the genus number of the object will be conserved. Note that \mathcal{G} is a global property of the object which can be computed *via* integration of a local quantity, the curvature K : $1 - \mathcal{G} = 1/4\pi \int_S K dA$. To better understand the interest of an approach considering only global properties of objects, the reader can for example refer to the elegant answer to the "Inscribed Rectangle Problem" brought by topology [237, 238].

Topological considerations have important consequences in various scientific domains, not only in mathematics but also, for example, in biology [239] to understand the structural stability of living beings through morphogenesis [240] or to describe proteins folding [241–243]. In this introduction we will focus on the importance of

topology in the case of condensed matter physics where topological invariants can be used to distinguish phases of matter described by band theory.

3.1.2 A new phase of matter: topological insulators

In the 1920s, the development of band theory of solids allowed explaining the insulator or conductor nature of crystalline materials. In a crystal, electrons occupy eigenstates corresponding to the hybridization of the different atomic orbitals which form bands separated by energy gaps. The conductive nature of a crystal can be inferred by the electronic filling of its energy bands: an insulator exhibits only completely filled bands and the energy gap between the highest fully occupied band and the lowest fully unoccupied band represents the energetic cost required to set an electron into motion.

The discovery of the Quantum Hall Effect (QHE) in 1980 by K. von Klitzing [1] demonstrated that a separation between metals and insulators solely based on bulk band fillings is not sufficient to completely describe electronic motion. The first demonstration of the QHE was realized using a 2D electron gas in a MOSFET (metal-oxide-semiconductor field-effect transistor) at cryogenic temperature. Despite electrons being confined in the bulk of the material, a finite number of unidirectionally propagating states emerged at the surface of the sample under a strong magnetic field (15 T). The sample was thus strikingly shown to be an insulator in the bulk with a quantized surface conductance with direct consequence for metrological applications. The effect of the magnetic field was analyzed in terms of Landau levels and the number of chiral conductive edge states was shown to be related to a topological invariant of energy bands, the Chern number [2] which is also referred to as the TKNN invariant in reference to the authors of the demonstration: D. J. Thouless, M. Kohmoto, M. P. Nightingale and M. den Nijs. Soon after, the experimental evidence of fractional quantized conductance [233] demonstrated the importance of many-body interactions [234], unveiling the quantized transport of quasi-particles carrying a fractional elementary charge. This effect is called the Fractional Quantum Hall Effect (FQHE). A blossoming theoretical and experimental development followed the discovery of QHE, especially with F. D. M. Haldane demonstrating that a global magnetic field breaking the time reversal symmetry is not necessary to induce the formation of unidirectional conducting edge states and that the crucial ingredient is the non-trivial topology of energy bands [244]. An extension of this model preserving the time reversal symmetry was then proposed by C. L. Kane and E. J. Mele [245, 246] demonstrating the Quantum Spin Hall Effect (QSHE) associated to a \mathbb{Z}_2 topological invariant. In this case both spin components realize a Chern insulator with opposed invariants, edge states appear as contra-propagating spin-polarized pairs resulting in a spin current without charge current, an effect which was experimentally observed two years later [247].

Classification of topological insulators were realized [248–250], characterizing observable effects in a given material based on symmetry classes. The considerable enthusiasm caused by the discovery of edges states at the surface of topological insulators comes from the fact that their existence is directly linked to the topology of the bulk material. Consequently, any local modification of the interface or of the bulk induced by disorder does not invalidate the existence of the edge state. Removing

a topological edge state requires a strong restructuring of the bulk material: the energy gap has to be closed.

The origin of a band topology can be understood as the presence of a non-vanishing geometric phase integrated over the Brillouin zone. Introduced in 1984 by M. V. Berry [251] the geometric phase or Berry phase, analogous to the Pancharatnam phase introduced in the case of optics [252], represents the non-dynamical phase acquired by a state $|\Psi_\lambda\rangle$ under adiabatic evolution of a parameter λ of the system's Hamiltonian $\mathcal{H}_{\lambda(t)}$. At each point of time, the system is supposed to verify the Schrödinger equation:

$$\mathcal{H}_{\lambda(t)}|\Psi_{\lambda(t)}\rangle = E_{\lambda(t)}|\Psi_{\lambda(t)}\rangle \quad (3.1)$$

Under adiabatic evolution the system is expected to remain in the initial state and at a time t' , the state of the system can be approximated as:

$$|\Psi_\lambda(t')\rangle \approx e^{i\phi_{\text{Tot}}(t')}|\Psi_\lambda(0)\rangle \quad (3.2)$$

where the acquired phase $\phi_{\text{Tot}}(t')$ is the sum of two contribution:

$$\begin{aligned} \text{the dynamical phase } \phi_d(t') &= -\frac{1}{\hbar} \int_0^{t'} E_{\lambda(\tau)} d\tau \\ \text{the geometric phase } \phi_{\text{geo}}(t') &= i \int_0^{t'} \langle \psi_{\lambda(\tau)} | \partial_\tau \psi_{\lambda(\tau)} \rangle d\tau \end{aligned} \quad (3.3)$$

Introducing the Berry connection $A_\lambda = i\langle \psi_\lambda | \partial_\lambda \psi_\lambda \rangle$, the geometric phase acquired on a closed loop can be written as an integral of the Berry flux $\Omega_\lambda = \vec{r} \dot{t} (A_\lambda)$ through the enclosed surface.

According to Bloch theorem, eigen-states of a system composed of a particle of mass m in a periodic potential $V(x)$ can be decomposed in plane waves multiplied by a periodic envelope function u_k . u_k is eigen-state of the periodic Hamiltonian $\mathcal{H}_k = (\hat{p} + \hbar k)^2 / 2m + V(x)$ with \hat{p} the momentum operator. On a band, the geometric phase acquired on an adiabatic close loop of k across the first Brillouin zone reads $\phi_{\text{geo}} = i \int_0^{2\pi} \langle u_k | \partial_k u_k \rangle dk$. The periodicity of u_k imposes the geometric phase to be $\phi_{\text{geo,BZ}} = 2\pi C$ with C an integer: the Chern number. Changing the Chern number of a band can only be done by a non-continuous deformation of this band, breaking the adiabatic approximation: it requires to close and reopen an energy gap. Note that in analogy between the Chern number and the genus number, the Berry flux is also called Berry curvature.

The presence of topological edge states at the interface between two materials is explained by the bulk-edge correspondence argument [253–255] which states that the number of topological edge states existing at an interface between two materials is equal to the variation of topological invariants across this interface. If the topological invariant changes through the interface, it can only happen by a closing an reopening of the energy gap, the interface therefore host states crossing the gap whose existence is imposed by the bulk topology of the surrounding materials. *Note that vacuum is trivial. The number of topological edge states observed at the interface between a material and vacuum is thus equal to the topological invariant of this material bands.*

3.1.3 Experimental realizations of topological phases with photonic platforms

Considerable efforts have been put in the experimental realization of 2D and 3D electronic topological insulators, the integer QHE was notably observed up to room temperature in graphene [256]. An exhaustive overview of these works is presented in Ref. [230,231,257,258]. More recently, the realization of topological insulators based on transition metal dichalcogenides attracted interest as these materials exhibit a strong spin-orbit interaction allowing to open a topological energy gap on the order of a few tens of milli-electronvolts and thus to observe the QSHE at relatively high temperatures $T \sim 100$ K [259]. The emulation of the QHE and QSHE with photons represents quite a challenge as, contrarily to electrons, photons are neutral particles. Synthetic materials have thus been developed to mimic the physics of electrons in topological insulator. Various systems were shown to reproduce not only the QHE and QSHE physics but also other topological effects such as topological pumping. An exhaustive description of these results can be found in Ref. [3,4].

A first emulation of the analog Quantum Hall Effect for photons was done with microwaves using gyromagnetic photonic crystals [260]. Unidirectional transport was observed on the edge of the material while its bulk was shown to be insulating. To probe the robustness of the chiral edge state, a metal slab was placed between the two antennas used to inject and probe microwaves. No back-scattering was observed while the forward transmission showed no significant perturbation, highlighting the topological robustness of the edge state: its existence is preserved under local perturbation and it follows the surface of the material edge no matter its shape as illustrated in Fig. 3.2 (a). A demonstration of the 2D analog QHE was also demonstrated using coupled waveguides [235], circuit-QED [201] or exciton-polaritons [182] for example. In each case, careful engineering of the bands and breaking of the time-reversal symmetry led to the observation of unidirectional transport along the edge. The case of coupled waveguides is particular as the 2D insulator is a mapping of a 3D structure: the wave propagation direction is considered as an effective time dimension and the system is described as a 2D Floquet Hamiltonian, this particular class of insulators are thus referred to as Floquet topological insulators. In Ref. [235], the authors engineered a honeycomb lattice of coupled waveguides where the time reversal symmetry breaking required to observe chiral edge modes was obtained by carving helical waveguides (see Fig. 3.2 (b)).

The observation of the analog QSHE for photons was done in coupled ring resonators [261], followed by implementations with meta-crystals [262], RF-circuits [263] or also twisted cavities [264]. In those experiments the time reversal symmetry is preserved while an effective magnetic field is induced: the two spin states experience an effective magnetic field with opposite sign. Consequently, each of the two associated spin components present topological bands emulating the QHE with opposed Chern numbers and thus opposed chirality. These states are referred to as helical edge states which benefit from a weaker protection against perturbations as a spin flipping interaction with a defect would induce back scattering. In Ref. [261], an asymmetry is introduced in the ring resonators which induces a different path length for clockwise and counterclockwise propagating modes (see Fig. 3.2 (c)) which thus pick an opposite effective phase when hopping from a lattice site to another one.

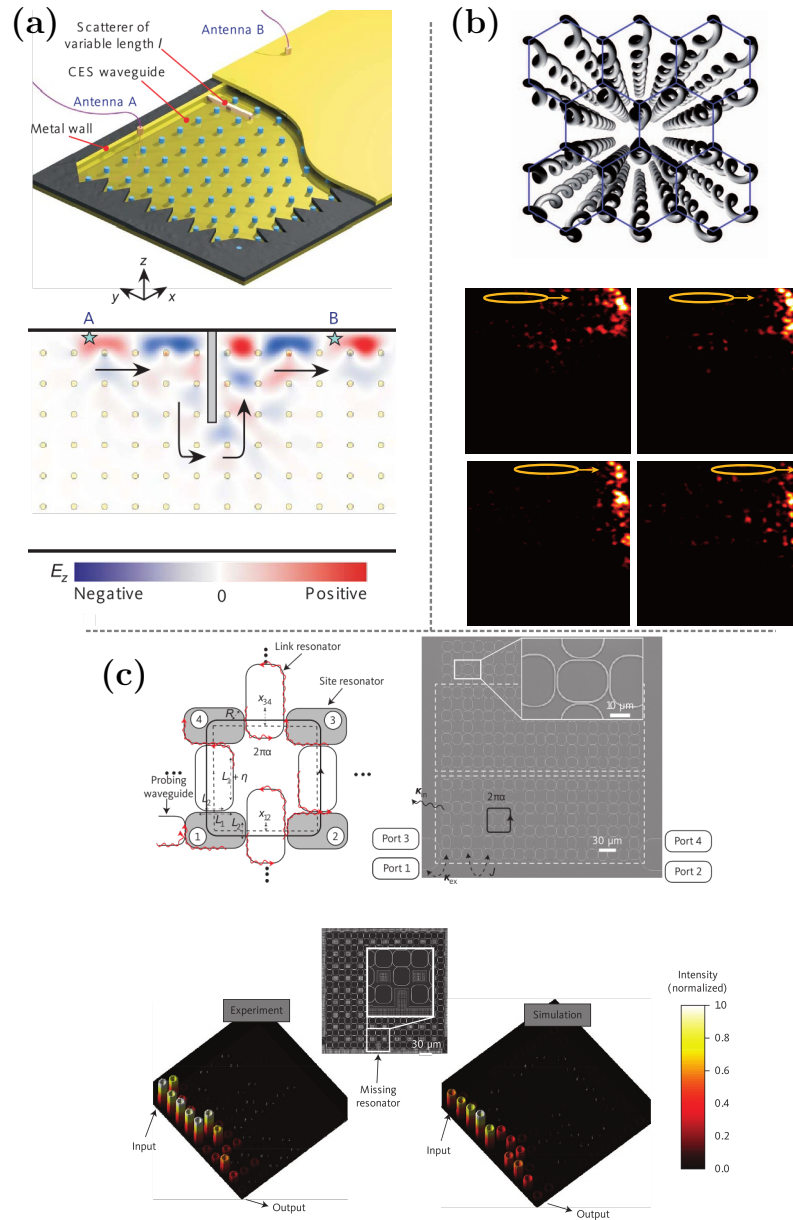


Figure 3.2: **a**, Scheme of the gyromagnetic photonic crystal (top) and simulation of the propagation of electromagnetic waves injected in the chiral edge mode *via* antenna *A* (bottom). Light propagates around the defect represented by the grey rectangle and no back-scattering or scattering in the bulk is observed. Images taken from Ref. [260]. **b**, Schematic representation of the helical coupled waveguide array (top) and experimental measurement of the output field as a function of the injection spot position represented by a yellow ellipse (bottom). Images taken from Ref. [235]. **c**, Representation of the coupled ring resonator unit cell (top left) and of the resulting array (top right). Red arrows highlight the path followed by light cycling clockwise in the lattice sites. The length asymmetry introduced in link resonator between sites 1-2 and 3-4 results in an phase picked up over a unit cell round trip. The bottom panel shows the experimental and numerical results obtained when injecting light in the resulting helical edge mode: propagation around a defect without scattering is observed. Images taken from Ref. [261]

As a result this structure corresponds to two realizations of the Harper-Hofstadter model. The Harper-Hofstadter model [265] is a tight-binding equivalent of the Landau levels problem, the well-known Harper-Hofstadter butterfly describing the energy spectrum of a periodic lattice as a function the applied magnetic field.

Interestingly, the versatility of photonic platforms allowed pushing the exploration of topological phases beyond the two 2D paradigmatic effects (QHE and QSHE) and observing various topologically induced phenomena. Coupled waveguides demonstrated anomalous Floquet topological insulators where the non-trivial topology originates from a periodic modulation of the Hamiltonian in time [266,267] and is associated to the existence of non-trivial winding numbers. Measurement of the Berry curvature was done using a fiber loop architecture [268] and direct measurement of a topological invariant was done with micro-waves [269]. Photonic artificial graphene enabled observing the zero-energy edge modes of the gapless model [270–272] which originate from the winding of the Berry Phase around Dirac cones. A mapping with the 1D Su-Schrieffer-Heeger (SSH) model allowed to directly measure the topological invariant associated to this winding [273]. Higher order topological insulator (HOTI) states were observed in a Kagome lattice [274], demonstrating topological states with a dimension differing from the bulk one by more than 1: here the authors report on the existence of 0D states localized in the corners of the 2D structure. 3D topological structures were also demonstrated with for example the engineering of Weyl points [275] which are the 3D equivalent of Dirac cones, or also the realization of 3D topological insulators [276,277]. Topological structures of even higher dimensions were also probed using synthetic dimensions with the observation of the edge states of the 4D Quantum Hall Effect *via* topological pumping [236].

In this chapter we address the non-linear behavior of the paradigmatic model for topology in 1D, which is the Su-Schrieffer-Heeger model. Note that other 1D models exist, most of them consisting in the implementation of quasi-crystalline lattices. Their implementation allowed the observation and study of the topological edge states of these exotic structures [278,279] and to realize topological pumping [278,280].

3.1.4 The SSH model: notion of chiral symmetry

The Su-Schrieffer-Heeger (SSH) model is one of the simplest models to highlight the importance of the geometric phase. It is a one dimensional lattice that was first introduced by W. P. Su, J. R. Schrieffer and A. J. Heeger to describe the electronic properties of the poly-acetylene [281]. The topological properties of the SSH model originate from the chiral symmetry which leads to the appearance of edge states at the center of an energy gap [282]. The SSH model is a paradigmatic example of the formation of topological edge states and is useful to explain the physics of several higher dimensional lattices [273,274]. Studying the non-linear response of the SSH model therefore appears as a first important step for the exploration of many-body topological physics.

3.1.4.1 Chiral symmetry of the SSH Hamiltonian

The SSH model describes particles on a one-dimensional bipartite lattice with staggered hopping amplitudes and constant on-site energies. Each unit cell of the lattice is therefore composed of two sites that we label A and B . The single particle Hamiltonian describing a chain of M unit cells reads:

$$\hat{\mathcal{H}}_{\text{SSH}} = -J \sum_{m=1}^M (|m, B\rangle\langle m, A| + h.c.) - J' \sum_{m=-\infty}^{+\infty} (|m+1, A\rangle\langle m, B| + h.c.) \quad (3.4)$$

where $|m, A\rangle$ ($|m, B\rangle$) describes the amplitude of the particle wavefunction on site A (B) of the m^{th} unit cell, J is the intra-cell hopping constant, it couples elements of the m^{th} unit cell only and J' is the inter-cell hopping constant. The onsite energy was here arbitrarily chosen to be equal to zero. Note that J and J' can be assumed to be real and positive as any phase could be gauged away by redefining the state basis. A sketch illustrating the architecture of the SSH lattice for $M = 5$ is presented in Fig. 3.3 (a).

The chiral symmetry of the model can be highlighted by emphasizing the spinor nature of the internal degree of freedom (sub-lattice index) of the Hamiltonian. Using the Pauli matrices:

$$\hat{\sigma}_0 = \hat{\mathbb{1}}_2, \quad \hat{\sigma}_x = \begin{bmatrix} 0 & 1 \\ 1 & 0 \end{bmatrix}, \quad \hat{\sigma}_y = \begin{bmatrix} 0 & -i \\ i & 0 \end{bmatrix} \quad \text{and} \quad \hat{\sigma}_z = \begin{bmatrix} 1 & 0 \\ 0 & -1 \end{bmatrix} \quad (3.5)$$

Rewriting $|m, A\rangle = |m\rangle \otimes \begin{bmatrix} 1 \\ 0 \end{bmatrix}$ and $|m, B\rangle = |m\rangle \otimes \begin{bmatrix} 0 \\ 1 \end{bmatrix}$, we can write the Hamiltonian in a form where internal and external degrees of freedom are clearly decoupled:

$$\hat{\mathcal{H}}_{\text{SSH}} = -J \sum_{m=1}^M |m\rangle\langle m| \otimes \hat{\sigma}_x - J' \sum_{m=-\infty}^{+\infty} \left(|m+1\rangle\langle m| \otimes \frac{\hat{\sigma}_x + i\hat{\sigma}_y}{2} + h.c. \right) \quad (3.6)$$

An Hamiltonian $\hat{\mathcal{H}}$ is said to possess the chiral symmetry if there exists an operator $\hat{\Gamma}$ that is unitary, Hermitian, local (does not couple a unit cell to another one) and that anti-commutes with $\hat{\mathcal{H}}$ ($\hat{\Gamma}\hat{\mathcal{H}} = -\hat{\mathcal{H}}\hat{\Gamma}$). In the case of the SSH Hamiltonian it is straightforward to verify that the operator $\hat{\Gamma} = \mathbb{1} \otimes \hat{\sigma}_z$ satisfies all of these conditions¹.

The chiral symmetry has direct consequences not only on the spectrum but also on the wavefunction of the eigenstates. The chiral operator $\hat{\Gamma}$ highlights the existence of two independent sub-lattices defined by the projectors $\hat{P}_{\pm} = \frac{1}{2}(\mathbb{1} \pm \hat{\Gamma})$. In the case of the SSH model, it corresponds to projectors on A and B sites of each unit cell. The chiral symmetry also imposes the spectrum to be symmetric with respect to the zero energy, if $|\Psi_l\rangle$ is an eigenstate for the energy E_l then $\hat{\Gamma}|\Psi_l\rangle = |\Psi_{-l}\rangle$ is an eigenstate for $-E_l$:

$$\hat{\Gamma}\hat{\mathcal{H}}|\Psi_l\rangle = \hat{\Gamma}E_l|\Psi_l\rangle \implies -\hat{\mathcal{H}}\hat{\Gamma}|\Psi_l\rangle = E_l\hat{\Gamma}|\Psi_l\rangle \quad (3.7)$$

¹Note that, as it is usually the case (especially in chemistry), the chiral symmetry defined here is as a mirror symmetry. In the present case it operates on the B sublattice of the model.

This imposes the wavefunction of non-zero energy state to present an equally distributed intensity on both sub-lattices:

$$\langle \Psi_l | \Psi_{-l} \rangle = 0 = \langle \Psi_l | \hat{I} | \Psi_l \rangle \implies \langle \Psi_l | \hat{P}_+ | \Psi_l \rangle - \langle \Psi_l | \hat{P}_- | \Psi_l \rangle = 0 \quad (3.8)$$

Conversely the chiral symmetry imposes zero energy states to be localized on a single sub-lattice:

$$\hat{H} \hat{I} | \Psi_l \rangle = 0 = \hat{H} | \Psi_l \rangle \implies \hat{I} | \Psi_l \rangle = \pm | \Psi_l \rangle \implies \hat{P}_+ | \Psi_l \rangle = 0 \text{ or } \hat{P}_- | \Psi_l \rangle = 0 \quad (3.9)$$

The chiral operator actually allows the definition of a pseudo-spin associated to projectors. In the case of SSH, it is the sub-lattice pseudo-spin \tilde{S} :

$$\tilde{S} = \frac{\langle \Psi | \hat{P}_+ | \Psi \rangle - \langle \Psi | \hat{P}_- | \Psi \rangle}{\langle \Psi | \hat{P}_+ | \Psi \rangle + \langle \Psi | \hat{P}_- | \Psi \rangle} = \frac{\langle \Psi | \hat{I} | \Psi \rangle}{\langle \Psi | \Psi \rangle} = \frac{\sum_m |\Psi_{m,A}|^2 - |\Psi_{m,B}|^2}{\sum_m |\Psi_{m,A}|^2 + |\Psi_{m,B}|^2} \quad (3.10)$$

where $|\Psi_{m,A}|^2$ ($|\Psi_{m,B}|^2$) represents the probability density of $|\Psi\rangle$ on the A (B) sub-lattice on the m^{th} unit cell. \tilde{S} measures the intensity imbalance of the wavefunction $|\Psi\rangle$ with respect to the A/B sub-lattices and takes values between 1 and -1 . $\tilde{S} = 0$ for non-zero energy eigenstates and $\tilde{S} = \pm 1$ for zero energy eigenstates which are localized on a single sub-lattice.

Note that the chiral formalism is a very powerful tool to engineer flat bands as the energy symmetry imposes their existence at zero energy for any chiral system with an odd number of sites per unit cell [283], common examples being the 1D and 2D Lieb lattices or the 2D Kagome lattice.

3.1.4.2 Topology of the SSH gap

To describe in more detail the bulk properties of the SSH model and to show how its chiral symmetry leads to topological properties, we consider an infinite chain ($M \rightarrow \infty$) and use the reciprocal space (or momentum space) description of the Hamiltonian. The translation invariance of the bulk allows applying Bloch Theorem and writing the bulk reciprocal space Hamiltonian and its decomposition on Pauli matrices:

$$\tilde{\mathcal{H}}_{\text{SSH}}(k) = - \begin{bmatrix} 0 & J + J' e^{-ika} \\ J + J' e^{ika} & 0 \end{bmatrix} = - \sum_{j=0,x,y,z} d_j(k) \hat{\sigma}_j \quad (3.11)$$

$$d_0(k) = 0, \quad d_x(k) = J + J' \cos(ka), \quad d_y(k) = J' \sin(ka) \quad \text{and} \quad d_z(k) = 0$$

where a is the length of the unit cell and the momentum k is scalar and takes values in the first Brillouin zone ($|k| \leq \frac{\pi}{a}$).

Solving the Schrödinger equation we find the dispersion relation $\mathcal{E}_{\pm}(k)$ and the corresponding eigenstates $|\Psi_{\pm}(k)\rangle$ of the system:

$$\mathcal{E}_{\pm}(k) = \pm \sqrt{J^2 + J'^2 + 2JJ' \cos(ka)} \quad \text{and} \quad |\Psi_{\pm}(k)\rangle = \frac{1}{\sqrt{2}} \begin{bmatrix} 1 \\ \pm e^{i\phi(k)} \end{bmatrix} \quad (3.12)$$

with $\phi(k) = \tan^{-1} \left(\frac{J' \sin(ka)}{J + J' \cos(ka)} \right)$

Figure 3.3 (b) shows the energy dispersion for different values of the couple $\{J, J'\}$ along with, Fig. 3.3 (c), the close path described by $\mathbf{d}(k)$ in the (d_x, d_y)

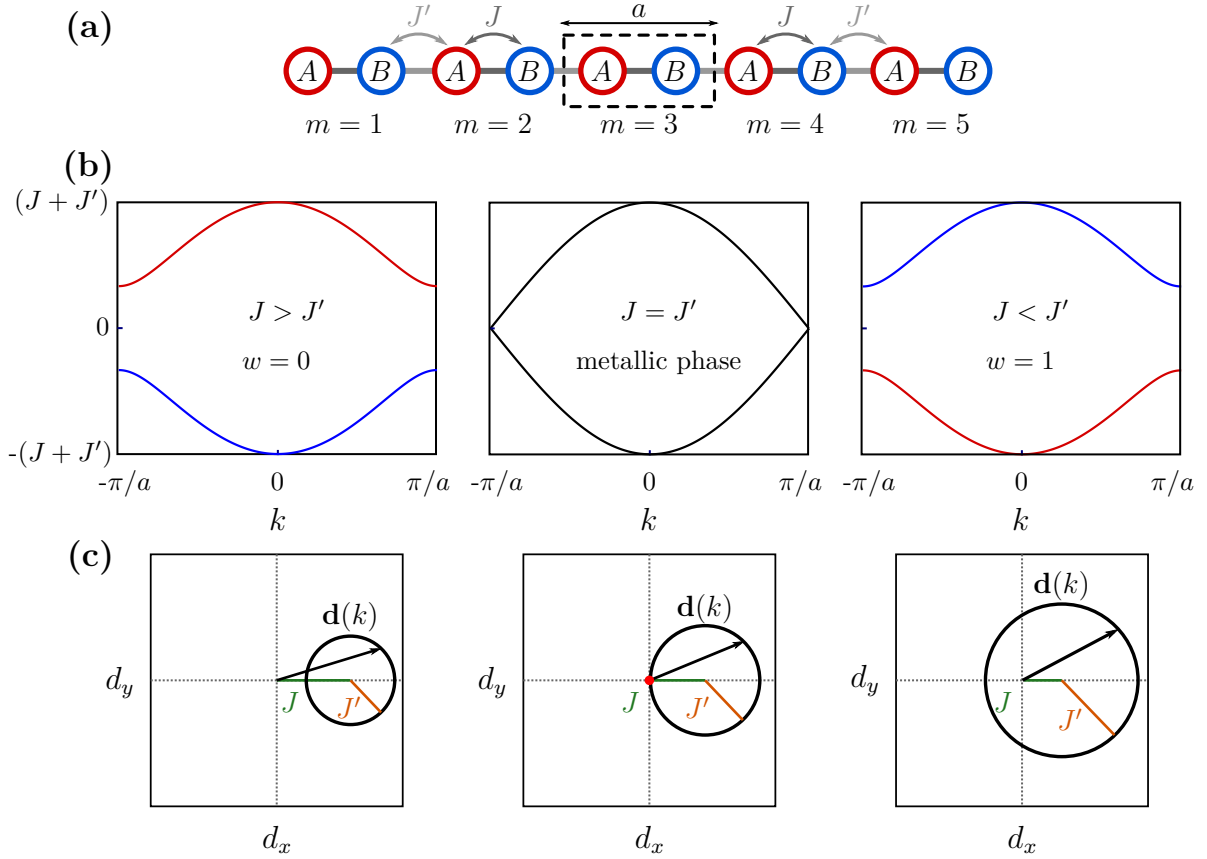


Figure 3.3: **a**, Schematic representation of the finite SSH chain for $M = 5$, the unit cell is highlighted using a black dashed box. **b**, Band structure of the SSH model for three sets of $\{J, J'\}$, characteristic of the different phases of the model. **c**, Corresponding closed trajectory of $\mathbf{d}(k)$ when k is scanned across the Brillouin zone. When $J < J'$ this trajectory circles around the origin, evidencing the non-trivial phase of the model with a winding number $w = 1$.

plane when the momentum k is scanned across the first Brillouin ($k : -\frac{\pi}{a} \rightarrow \frac{\pi}{a}$). Note that the trajectory of the vector $\mathbf{d}(k)$ is confined to this plane as long as the chiral symmetry holds ($d_z = 0$).

The energy spectrum of the system is gaped as long as $J \neq J'$ which is equivalent to a trajectory of $\mathbf{d}(k)$ avoiding the origin of the (d_x, d_y) plane. This gap of amplitude $\Delta_{\text{gap}} = 2(|J - J'|)$ is the topological gap of the SSH model, it is characterized by an invariant called the winding number w . A visual representation of the winding number is given by the trajectory of $\mathbf{d}(k)$ as w is the number of times that the vector $\mathbf{d}(k)$ circles (winds around) the origin when k is scanned across the first Brillouin zone. The winding number can also be obtained by computing the geometric phase (in this case called the Zak phase [284]) acquired across the Brillouin zone:

$$w = \frac{i}{\pi} \oint_{BZ} \langle \Psi_{\pm} | \nabla_k | \Psi_{\pm} \rangle dk = \frac{1}{2\pi} \int_{-\pi/a}^{\pi/a} \partial_k \phi(k) dk \quad (3.13)$$

A non-zero value is obtained for $J' > J$ due to the presence of a pole in the expression of $\tan(\phi(k))$. Note that this pole coincides with the trajectory of $\mathbf{d}(k)$ crossing the d_y axis of the plane.

As long as the chiral symmetry is preserved, a change of w can only occur by closing the topological gap: the number of times that the trajectory of $\mathbf{d}(k)$ circles the origin can only be increased or decreased by having this trajectory to cross the origin. In the canonical form of the SSH model, this invariant can take only two different values: $w = 0$ when $J > J'$ and $w = 1$ when $J < J'$. It is yet possible to access other values by introducing long range hopping terms that couple sites of different sub-lattice ($d_z \neq 0$) [285–287].

The description of the bulk SSH topological phases is ambiguous since it relies on the definition of the unit cell: swapping A and B labels leads to exchanging the role of J and J' and thus to attributing winding numbers $w = 0$ and $w = 1$ to the same lattice. This description makes sense when considering semi-infinite lattices as the edge unequivocally defines the unit cell and thus the associated winding. In that case, one can refer to the bulk-edge correspondence [288] to explain the existence of an edge state at the end of lattice presenting a winding number of $w = 1$. Due to chiral symmetry, this edge state is localized at the center of the gap and presents a sub-lattice pseudo-spin $S = \pm 1$ (see Fig. 3.4 (a)). The wavefunction of the state presented in Fig. 3.4 (a) is given by $|m, A\rangle = -(J'/J)^m |0, A\rangle$ and $|m, B\rangle = 0 \forall m$. Mid-gap states originating from the lattice topology can also be observed at the interface between the non-trivial lattice and any material presenting a different winding of the Zak phase. The simplest way to engineer such states is to couple a SSH chain of winding $w = 1$ to a chain of winding $w = 0$ through a bound J_{link} . In this case the structure of the interface states depends on the amplitude of the coupling between lattices but the symmetry protection of the lattice imposes the resulting state to be localized at the center of the gap and to present a sub-lattice pseudo spin as illustrated in Fig. 3.4 (b). The interface state presents spin-polarized exponentially decaying tails on each side of the interface with $|m, A\rangle = -(J'/J)^m |0, A\rangle \forall m > 0$, $|m, A\rangle = -(J'/J)^{|m|} |-1, A\rangle \forall m < -1$ and $|m, B\rangle = 0 \forall m$. The evolution of the modulus amplitude of $|0, A\rangle$ and $|-1, A\rangle$ as a function of the amplitude of the link coupling the two semi-infinite lattices is presented in Fig. 3.4 (c).

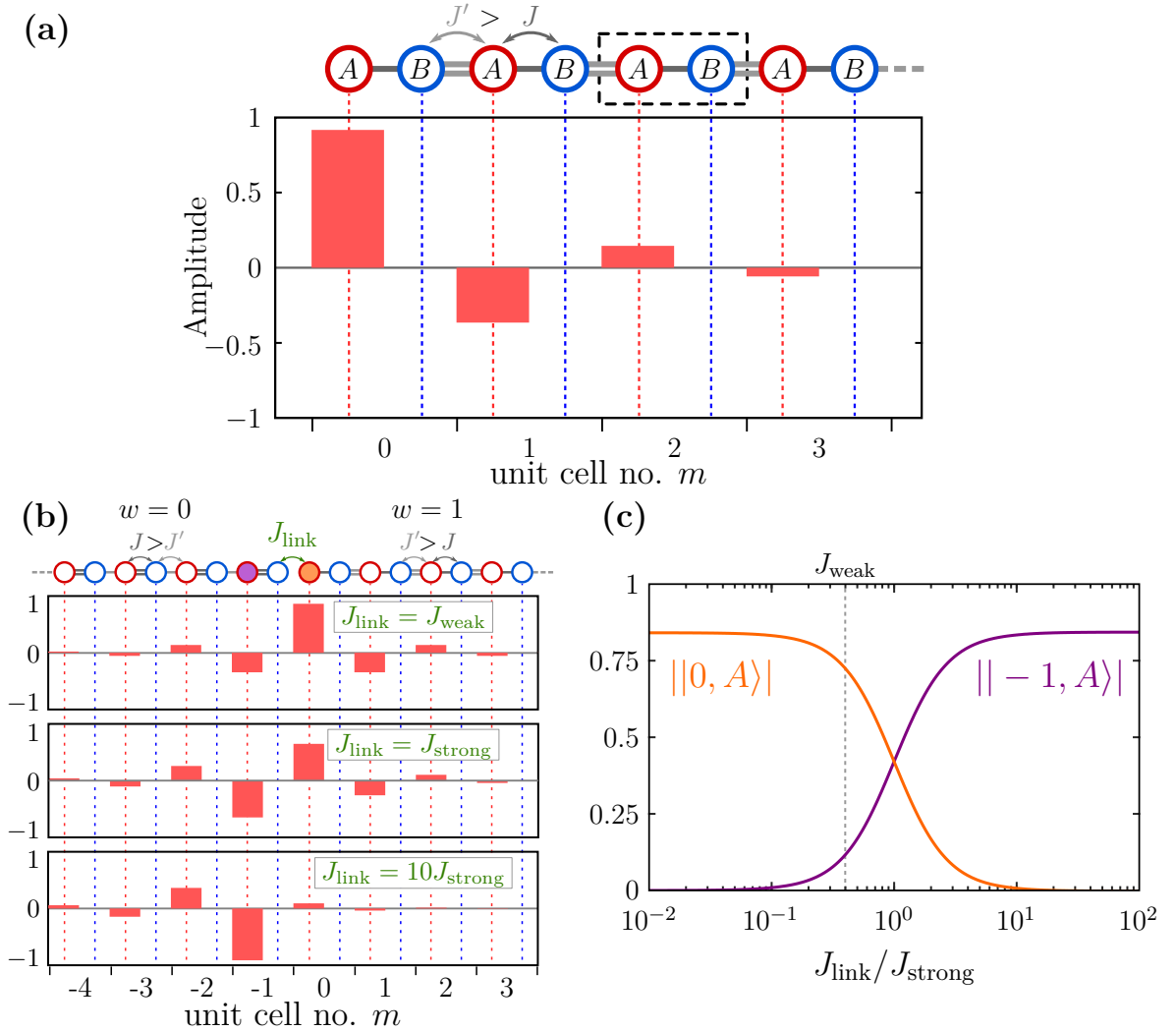


Figure 3.4: **a**, Spatial distribution of the topological edge state wavefunction. A schematic representation of the topologically non-trivial semi-infinite SSH chain is presented on top and dashed vertical lines indicate the sites positions. Two coupling constant are considered: the strong (weak) coupling J_{strong} (J_{weak}) is represented by a double (simple) bond. **b**, Spatial distribution of the topological interface state wavefunction for three different values of the coupling link J_{link} between trivial (left) and non-trivial SSH lattices (right). A sketch of the lattices is depicted on top. In all cases, the wavefunction is fully localized on the A sub-lattice, corresponding to a pseudo-spin $\tilde{S} = +1$. **c**, Evolution of the wavefunction absolute value on first A pillar of each lattice as a function of the link amplitude J_{link} . Purple and orange curves respectively correspond to trivial and topological emulations of the chain, associated pillars are filled with corresponding color on schematic representation of panel (b). Depending of the link coupling amplitude, the state can be localized on either one or both lattices.

A plethora of photonic realizations of the SSH lattice have been reported, evidencing the topological mid-gap states characteristic of the model. The first photonic emulation of the lattice was realized with photonic superlattices [289] without establishing the link with the topological model. A stack of waveguides was produced, pairs of waveguides being alternatively separated by high and low refractive index layers. Depending on the superlattice termination, the authors demonstrated that light injected in the last waveguide could be trapped at the surface of the sample, evidencing the presence of the localized topological edge state of the SSH model. Due to its relative simplicity this model has now extensively been implemented on various platforms and a polariton emulation of the SSH model was notably used to demonstrate the first topological laser [197]. Another important aspect of photonic platforms is the ease with which engineering of losses and gain can be done in most of systems. Photonics platforms are thus extremely pertinent for the exploration of the interplay between non-Hermiticity and topology [290]. Tailoring gain and losses in photonic systems, it was possible to engineer topological phases [5, 291, 292] in $\mathcal{P}\mathcal{T}$ symmetric emulation of the SSH model.

In this chapter we aim at exploring the properties of the SSH model in the presence of non-negligible inter-particle interactions. The exploration of the interplay between non-linearities and topology is an emerging field which promises the realization of robust active devices. In this regard, photonic platforms are particularly appealing due to their high versatility in the implementation of topological structures but also to the ease to observe significant non-linearities by injecting extremely dense wave-packets thanks to pulsed lasers. The polariton platform can play a particular role in the exploration of non-linear photonics as the strong Kerr non-linearity allows the generation of strongly non-linear fluids of light using a relatively lower pump power. Additionally, the driven-dissipative character of the system is a strong asset of polariton lattices since it gives us the ability to coherently and continuously drive the system with on demand engineering of the excitation field. These are the tools we will use to generate gap solitons in a SSH polariton lattice.

3.2 An emerging field: non-linear topological photonics

The discovery of the Fractional Quantum Hall Effect [233, 234] demonstrated that topological phases of matter become even richer when inter-particle interactions are considered. non-linear topological photonics is an emerging field aiming at extending the fascinating properties of topological states and phases of matter to the realm where interactions between the system constituents cannot be neglected. The modifications induced by interactions especially raises the question of the need for an expression of the Berry phase taking non-linear effect into account [293, 294]. Here we will describe some of the important research axes opened by the interplay between topology and non-linearities. An overview of the recent developments regarding this field can be found in Ref. [295].

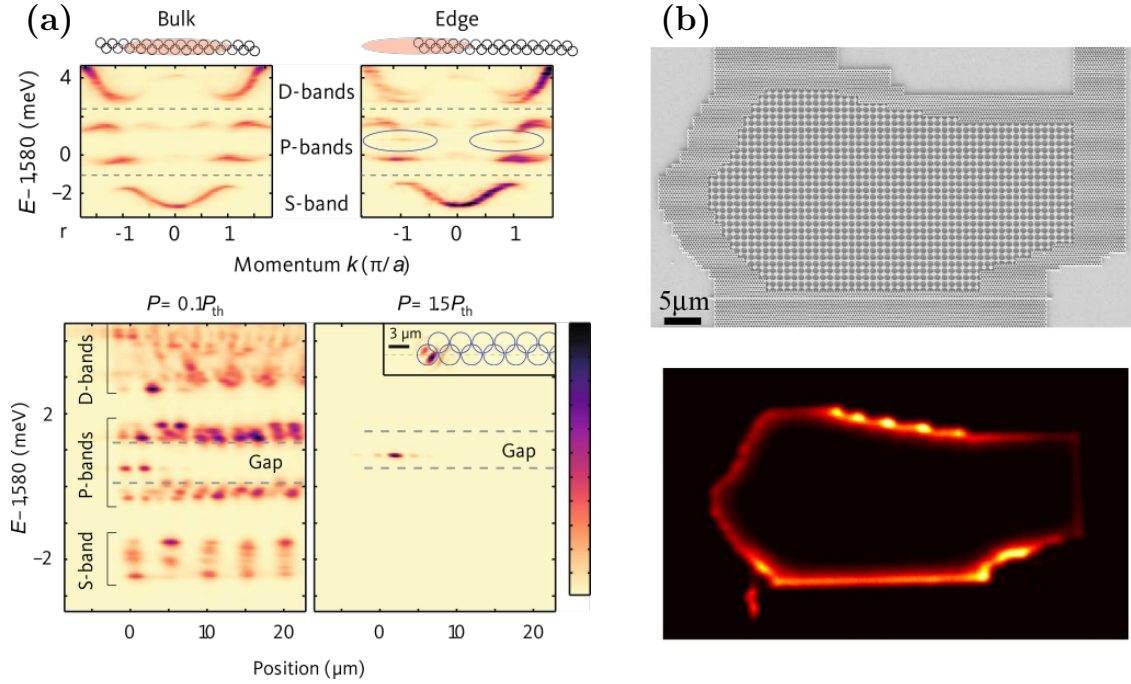


Figure 3.5: **a**, Energy dispersions of polariton modes in the bulk and at the edge of the structure, measured by non-resonant spectroscopy (top): the edge state localized in the middle on the “ p ” bands gap is highlighted by ellipses. Real space energy distribution of polaritons at the edge of the structure below (bottom left) and above lasing threshold (bottom right). Above the lasing threshold the light is emitted from the gap state, which is shown to be localized on the edge pillar (inset). Image taken from [197]. **b**, Top view SEM image of the sample (top), one can see an interface between two photonic crystals presenting different geometries. In the lasing regime, the light is shown to be confined at the interface between the two materials (bottom). Image taken from [298].

3.2.1 Topological lasers

One of the most striking phenomenon originating from the non-Hermitian nature of photonic platform is the possibility to realize topological lasers. The topological origin of edge states endows them with a robustness against local disorder which is inherent to fabrication processes, aging of the materials or simply due to ambient fluctuations. Consequently, the generation of topological edge state lasers is very promising as the resulting laser would benefit from these robustness properties. Despite not being at the origin of the lasing effect, the influence of inter-particle interactions can be predominant: in standard lasers, the high intra-cavity particle density above the lasing threshold is known to induce a rich diversity of phenomena such as instabilities, chaotic behavior [296], or also self focusing which is used for mode-locking [297]. One can thus wonder whether topological lasers would be subjected to the same phenomena or if new dynamics could be observed in such structures.

The first realization of a topological laser was realized by our group in a polariton 1D lattice emulating the SSH model [197]. Lasing on the edge states engineered with “ p ” orbitals was reported as illustrated in Fig. 3.5 (a) and the robustness of such laser was discussed. The system was shown to spontaneously lase on the topological edge

state, which is significantly advantaged in the mode competition for lasing due to its spatial localization. In addition, this topological edge state was shown to remain strongly localized at the edge as long as perturbations do not exceed the amplitude of the gap. Further exploration of the SSH topological polariton laser was done by the group of S. Höfling [299]. Other implementations of lasing on a topological edge state of the SSH model were reported in coupled-ring resonators [300,301], in photonic crystals [302], vertical-cavity surface-emitting laser (VCSEL) array [303] and recently up to room temperature using organic materials [304].

The first lasing effect in a 1D edge state of a 2D topological lattice was reported using photonic crystals [298] on a yttrium iron garnet substrate (see Fig. 3.5 (b)) implementing a Chern insulator, the time reversal symmetry being broken *via* the magneto-optic effect. A relatively small topological gap was opened (42 pm) but it was yet sufficient to observe unidirectional lasing on the chiral edge state localized at the surface of the sample when pumping the whole sample. This unexpected behavior is still under study as a uniform pumping should have led to multi-mode lasing of bulk modes [305]. 1D topological lasers have also been implemented using ring resonators [306] and polariton lattices [182] while more recently, lasing in corner states of a 2D photonic crystal lattice was reported at room temperature [307]. Note that the polariton platform appears to be very appealing for the generation of topological lasers which could be realized *via* electric injection [308].

In addition to their robustness to disorder in terms of energy and spatial localization, a recent theoretical development demonstrated the advantage of topological lasers in terms of temporal and spatial coherence [309]. These results comfort the importance of topologically protected states in the view of developing robust active devices.

3.2.2 Non-linear phase transitions and wave-mixing

Considering the richness of non-linear phenomena in trivial materials, the exploration of the interplay between non-linearity and topology promises the discovery of exotic behaviors in addition to the stabilization and protection of already known effects.

In the case of wave-mixing, the generation of correlated photon pairs mediated by topologically protected states have been reported in a 2D ring resonator lattice [310]. The authors demonstrated the robustness of the signal energy by probing seven different realizations of the topological insulator and comparing it to a third harmonic generation process in a trivial 1D channel. Triggering a third harmonic generation (THG) process on the edge state of a 2D topological insulator was shown to enable realizing correlated photon pairs with a well defined energy, whereas disorder induced fluctuations are detrimental in absence of topological protection (see Fig. 3.6 (a)). A similar result was obtained by the group of Y. S. Kivshar [311] where the THG process was mediated by the edge state of a 1D SSH lattice made of dielectric nano-particles. The author observed that, under small perturbations of the lattice, the THG process remains significantly localized on the edge of the lattice.

Topological phase transitions are expected to appear when the energy associated to the non-linear interaction becomes comparable to other characteristic energy

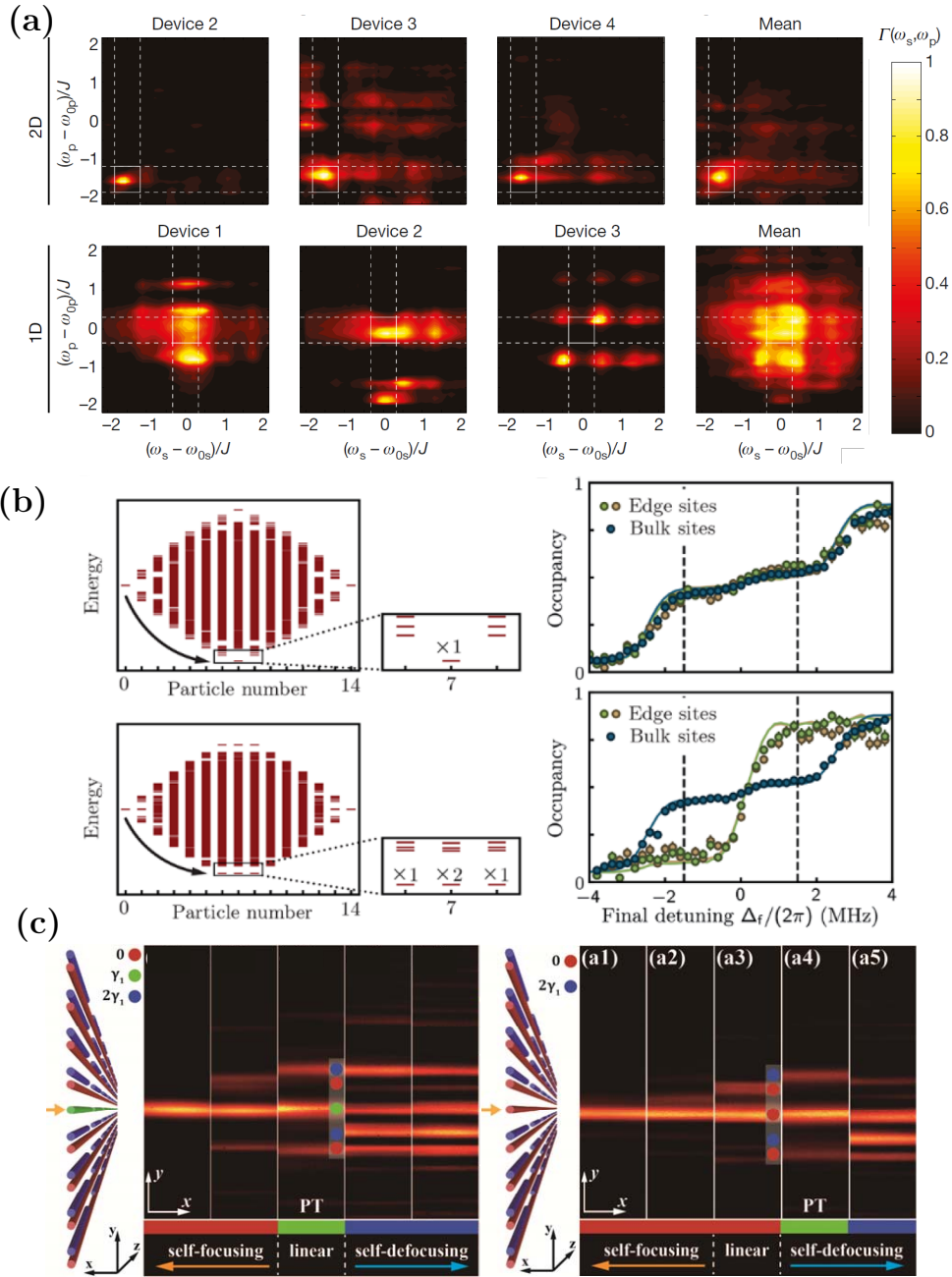


Figure 3.6: **a**, Spectral correlation maps between signal and pump photons in a 1D topologically protected (top) and trivial channel (bottom). In each row, the last image represents the mean value computed over seven realizations. Images taken from Ref. [310]. **b**, Calculated energy spectra of the many body system (left) and measured occupancy of the bulk and edge sites (right) in the case of a trivial (top) and a topological lattice (bottom). Image taken from Ref. [312]. **c**, Output intensity distribution as a function of the non-linearity amplitude for a SSH waveguide array pumped at the defect position (yellow arrow). Two cases are here illustrated with: a linear $\mathcal{P}-\mathcal{T}$ symmetric device (left) and a non- $\mathcal{P}-\mathcal{T}$ symmetric array (right) presenting a central waveguide with a gain excess. Images taken from Ref. [6].

scales of the system. In the strongly interacting case of hard-core bosons, a new topological symmetry-protected phase of the SSH model has been reported using Rydberg atoms [312]. In case of a non-trivial termination of the SSH chain the ground state is four time degenerate, whereas in the case of the trivial lattice, a unique ground state corresponding to a half-filling of the lattice sites is observed. In the non-trivial case, a sharp transition between zero and full occupancy of the edge sites was observed as a function of the number of particles stored in the lattice (see Fig. 3.6 (b)).

A photonic implementation of the FQHE physics as been realized in the group of J. Simon [313] using Rydberg polaritons formed by the strong coupling between Rydberg atoms and photons confined in a twisted cavity. The twisted cavity supports photonic modes carrying angular momentum which are analogous to the lowest Landau levels of electron under a strong magnetic field. Additionally the strong interaction between Rydberg atoms, enabling to observe a polariton blockade, is equivalent to the repulsive Coulomb interaction between electrons. When the $|l = 3\rangle$, $|l = 6\rangle$ and $|l = 9\rangle$ cavity modes are brought to resonance, the polariton blockade is frustrated as a photonic equivalent of a Laughlin state is formed in resonance with the laser energy.

In the case of weakly interacting particles, interaction induced energy-shift of the topological edge state of an SSH lattice has been reported [314], demonstrating the interactions as a potential knob to tune the properties of topologically protected states. Experimental evidence of topological phase transitions of the SSH model have been reported in coupled LC resonators [315] and waveguides [316] where a renormalization of the hopping constants is induced by interactions. In Ref. [315] the non-linearity induced modification of coupling strengths led to a global phase transition from the trivial to the topological phase of the SSH model while in Ref. [316] a local injection at the edge of a trivial SSH chain is demonstrated to become self-trapped in the edge waveguide when the input power is increased. Several mechanisms for topological phase transitions in a $\mathcal{P}\text{-}\mathcal{T}$ symmetric configuration have been reported in Ref. [6]. In this work, the self-focusing and self-defocusing non-linearity is used as a mean to control the losses of the waveguides: in the case of self-focusing the reduction of diffraction and leakage provides an effective gain in the material while on the contrary, the self-defocusing interaction enhances the losses experienced by photonic modes. Probing the existence of an edge state, the authors demonstrated the destruction of a preexisting $\mathcal{P}\text{-}\mathcal{T}$ symmetric topological phase *via* either self-focusing or self-defocusing non-linearity (see Fig. 3.6 (c)) and the transition of a lossy (gainy) non- $\mathcal{P}\text{-}\mathcal{T}$ symmetric chain to a $\mathcal{P}\text{-}\mathcal{T}$ symmetric topological phase *via* self-focusing (self-defocusing) interaction.

In the case of 2D lattices, the group of A. Szameit recently realized a trivial lattice supporting topologically protected non-linear edge states [317]. The authors engineered a trivial band-gap supporting no single particle edge state but yet present a many-body chiral edge state. In presence of a strong photon density, the Kerr non-linearity induces a renormalization of the couplings between waveguides which leads to the presence of a non zero winding of the phase. non-linear injection of light on the edge of the lattice was shown to generate a wave-packet unidirectionally propagating along the edge of the structure.

A theoretical proposal for an all-optical (no external magnetic field) polariton

non-linear 2D insulator was proposed by the group of G. Malpuech [318] where the spin-anisotropy of the interaction is used to induce an effective magnetic field breaking the time reversal symmetry. As a consequence, the bands associated to Bogolons present a non zero Chern number similarly to the one induced for linear eigenstates in Ref. [182,319] under the action of a true magnetic field.

3.2.3 Topological solitons

Localized non-linear defects such as solitons constitute a strong perturbation to the energy landscape of a lattice. The generation of such non-linear defects, breaking the translation invariance, may for example offer the possibility to induce domain walls in topological lattices or to form solitons or vortices with a non-trivial structure which could be protected by symmetries of the underlying model. Reference [317] is a good example showing that localized dense wave-packets can be subjected to a non-trivial many-body dynamics. The formation of solitons in a photonic topological bandgap has recently been reported by the group of M.Rechtsman using a Floquet topological insulator [320]. Exciting the bulk of a topological square lattice with a light pulse, the formation of a localized wave-packet was measured by scanning the input power injected in one of the waveguides and a cyclotron-like motion of the corresponding soliton was observed. The same group very recently reported on the observation of Floquet solitons with edge-state like propagation [321] and on the Thouless pumping of a soliton [322].

Numerous theoretical works explored solitonic solutions emerging in topological bandgaps [202, 205, 323, 324] or bands [325] and in Floquet systems [326, 327]. The interaction between gap solitons and topological edge states was studied in Refs. [203,328]. Interestingly, novel solitonic solutions with a ring shape are expected to emerge in hexagonal boron nitride (hBN), a gaped analogue of graphene where the two unit cell sites present different onsite energies [206]. The Chern number of bands was recently discussed as strongly affecting the dynamics of solitons [329,330].

In the following, we will investigate the driven-dissipative counterpart of the physics discussed in Refs. [202,203]: i.e driven-dissipative gap solitons generated in the topological of the SSH model. The theoretical study of gap solitons in the SSH model has been reported in Refs. [202,203] for conservative systems. These works unveiled the existence of topological gap solitons presenting an intensity distribution reflecting the symmetry of the underlying Hamiltonian: they possess chiral exponentially decaying tails. This particular distribution of the soliton wavefunction strongly affects their interaction with defects: depending on the defect localization, the topological gap soliton dynamics was shown to evidence an interaction that can be either attractive or repulsive. In the next section we explore the dissipative counterpart of these solitons in the gap of a polariton SSH lattice.

3.3 Non-linearities in the topological gap of SSH: formation of topological gap solitons

The exciton-polariton platform appears to be extremely suited for the exploration of non-linear topological photonics: not only the high versatility of the confinement engineering enables implementing almost arbitrary geometries and thus topological

phases of matter [182, 197, 319] but the strong polariton-polariton interactions are responsible for the observation of non-linear behavior of the system even under continuous excitation [217, 219].

Taking advantage of the strong inter-particle interaction, we will discuss the continuous injection of solitons in topological band-gaps in the bulk and at a topological interface of the SSH model. A robustness of solitons due to their chiral symmetry will be demonstrated against defect localized on one sub-lattice.

Interestingly, we will show that the manipulations of the non-linear fluid enabled by the driven-dissipative nature of the system allows reaching and stabilizing steady-state solutions with a profile strongly reminiscent of the one of a topological edge state. To the best of our knowledge, these solutions have never been experimentally observed nor discussed theoretically. These new solitons will be shown to be inaccessible to conservative systems as they require to maintain a phase frustration which is made possible by the inhomogeneous nature of the driving field. Reaching non-linear steady states is predicted, under careful engineering of the drive, to lead to the appearance of topologically non-trivial excitation spectra [8, 318, 331]. Numerically reproducing the obtained experimental results, we will calculate the excitation spectrum on top of bulk gap solitons and show that the onset of the phase frustration leads to the appearance of a localized state in the topological band-gap which is akin to an non-trivial edge state.

3.3.1 Emulating the SSH model with “s” modes

Previous implementations of the Su-Schrieffer-Heeger model with polaritons relied on the hybridization of “p” orbitals of coupled micro-pillars in a “zigzag” chain [197]. The advantage of this initial implementation is that p_x and p_y orbitals are orthogonal and separately emulate the two different phases of the model: if the p_x orbital chain ends with a strong coupling, thus emulating the trivial phase, the coupling between associated p_y orbitals is weak and it corresponds to a non-trivial end of the lattice hosting an edge state. The band structure thus consists in a set of degenerate bands associated to each possible winding number of the canonical SSH Hamiltonian.

In the present work we engineered a chain of coupled micro-pillars where the emulation of the SSH model relies on the hybridization of the lowest eigenstates (s-states) of each micro-pillar. The etched structure consists in a periodic chain of micro-pillars with a diameter of $D = 3\ \mu\text{m}$ with alternated short ($d_s = 2.2\ \mu\text{m}$) and long ($d_l = 2.75\ \mu\text{m}$) center to center distances, which results in a respectively strong and weak coupling between the pillars “s” modes. An SEM image of a lattice portion is presented in Fig. 3.7 (a) along with the measured energy distribution of the polariton eigenstates resolved in momentum (Fig. 3.7 (b)) obtained by spectroscopy under non-resonant excitation at 4K. A fit obtained by solving the 2D Schrödinger equation for this structure is superimposed to the Fourier space dispersion. Fig. 3.7 (c) corresponds to a zoom on the lowest energy bands of the spectrum, which are the ones of interest in this chapter, and Fig. 3.7 (d) corresponds to the spectral density of polariton modes resolved in position. A polarization filtering was applied to only collect the component aligned with the transverse direction of the lattice. The strong spatial asymmetry due to the quasi-1D nature of the lattice leads to a lift of the degeneracy between polarization components and the horizontal and vertical directions of the linear basis aligned with the lattice axes are a good

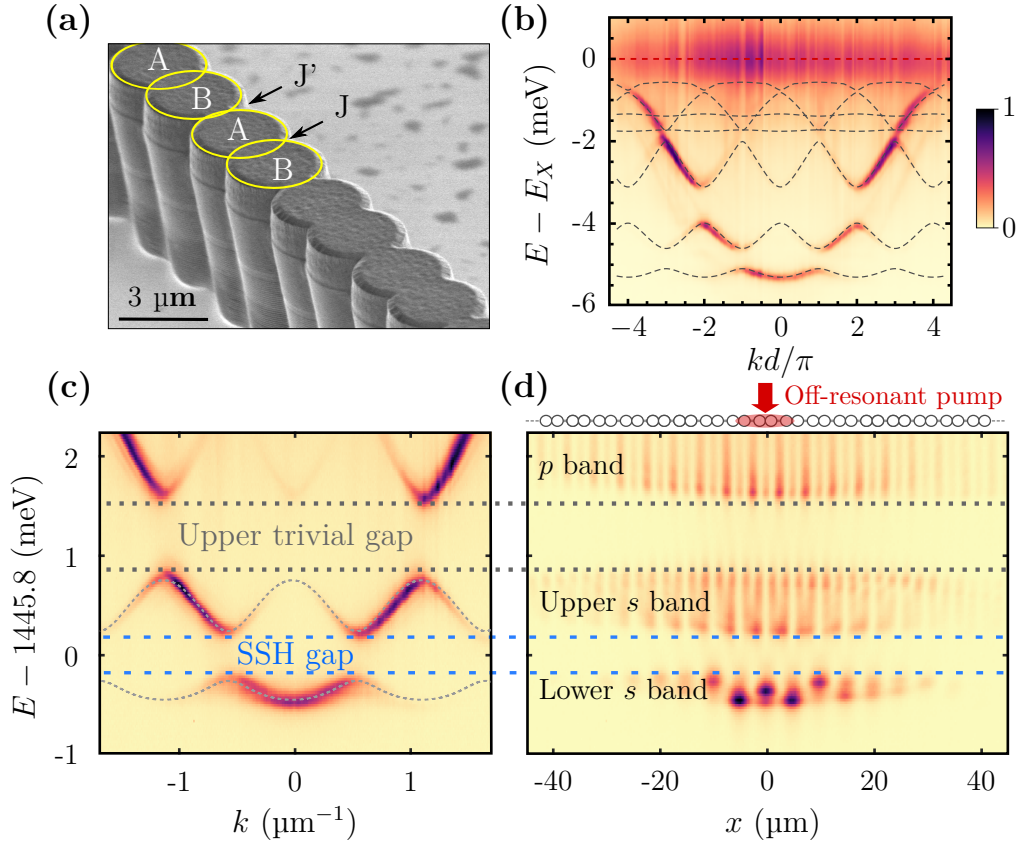


Figure 3.7: **a**, Scanning electron microscope image of the SSH polariton lattice. Some of the micro-pillars are highlighted with yellow circles. **b**, Spectrally resolved photoluminescence intensity measured as a function of momentum k . Superimposed dashed lines correspond to a fit realized by solving the 2D Schrödinger equation governing the structure. **c**, Zoom of (b) around the lowest bands emulating the SSH model. Superimposed grey dashed lines correspond to a fit of the “s” band by a tight binding approximation. **d**, Spectrally resolved photoluminescence intensity measured as a function of position x along the lattice and corresponding to the energy range of (c). The red circles in the sketch on top of (d) represent the non-resonantly pumped sites.

3.3. Non-linearities in the topological gap of SSH: formation of topological gap solitons

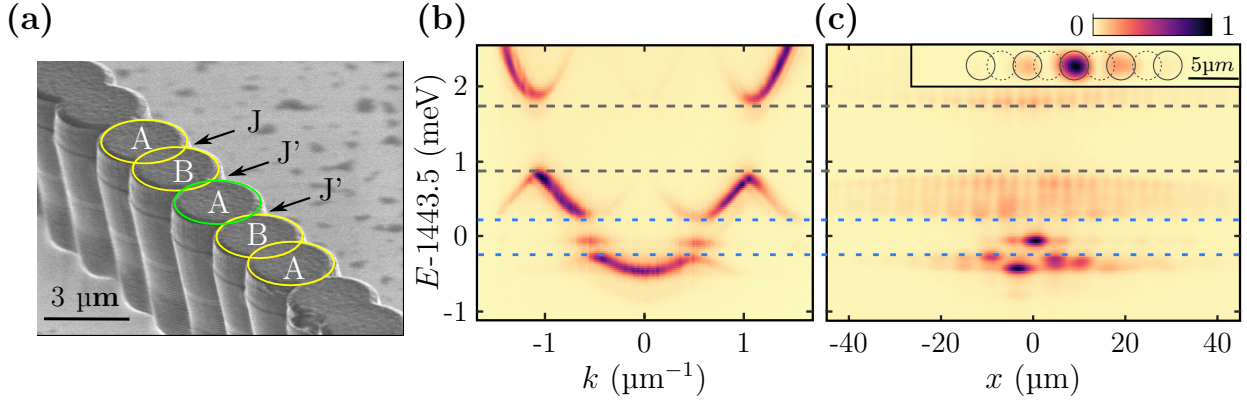


Figure 3.8: **a**, Scanning electron microscope image of the interface between SSH polariton lattice, the weakly coupled pillar is highlighted by a green circle. **b**, Spectrally resolved photoluminescence intensity measured as a function of momentum k . **c**, Spectrally resolved photoluminescence intensity measured as a function of position x . The inset presents the 2D spatial distribution of the state localized in the gap. Dark solid (dashed) circles delimit the A (B) pillars.

description basis: both components can be considered independently in the linear regime.

The two lowest energy bands observed on Fig. 3.7 (b-c) correspond to the gaped energy bands of the SSH model formed by the hybridization of the “ s ” modes while higher energy bands originate from the hybridization of “ p ” orbitals. Looking at the eigenstate distribution in real space (Fig. 3.7 (d)), the bonding and anti-bonding character of, respectively, the lower and upper “ s ” bands can be identified: the lower band wavefunctions present a maximum in between strongly bound pillars while the intensity distribution exhibits a clear zero in the case of the upper band. Each sub-band can be interpreted as resulting from the hybridization of dimerized orbitals and this feature is clearly observable in the real space intensity distribution of the upper band. The lowest energy part of the sub-band exhibits a non-vanishing intensity between coupled dimers which gradually becomes a clear zero as the energy increases and reaches the top of the band: the bottom (top) of the band correspond to a bonding (anti-bonding) hybridization of anti-symmetric dimer states. We measure a width $E_{\text{gap}} = 450 \mu\text{eV}$ of the topological gap between these “ s ”-bands.

A small asymmetry between the two bands is observed. This deviation originates from a residual coupling between the “ s ” and “ p ” orbitals of neighboring pillars. In a tight-binding description of these bands, this phenomenon can be produced by phenomenologically including a next nearest neighbor coupling. This adds a coupling between pillars belonging to the same sub-lattice and constitutes a perturbation to the chiral symmetry giving rise to an asymmetry between the upper and lower “ s ” bands. A numerical fit of the energy bands (superimposed on Fig. 3.7 (c)) allowed estimating the different hopping energies involved in the structure. We obtain a strong coupling $J = 0.49 \text{ meV}$ and a weak coupling $J' = 0.20 \text{ meV}$ which are one order of magnitude higher than the sub-lattice effective coupling $J_s = -0.04 \text{ meV}$. In the following we neglect this perturbation.

To illustrate the topological nature of the engineered lattice, we design a defect in the lattice periodicity: the alternation between strong and weak couplings is locally broken by introducing a pillar weakly coupled to both its neighbors (see

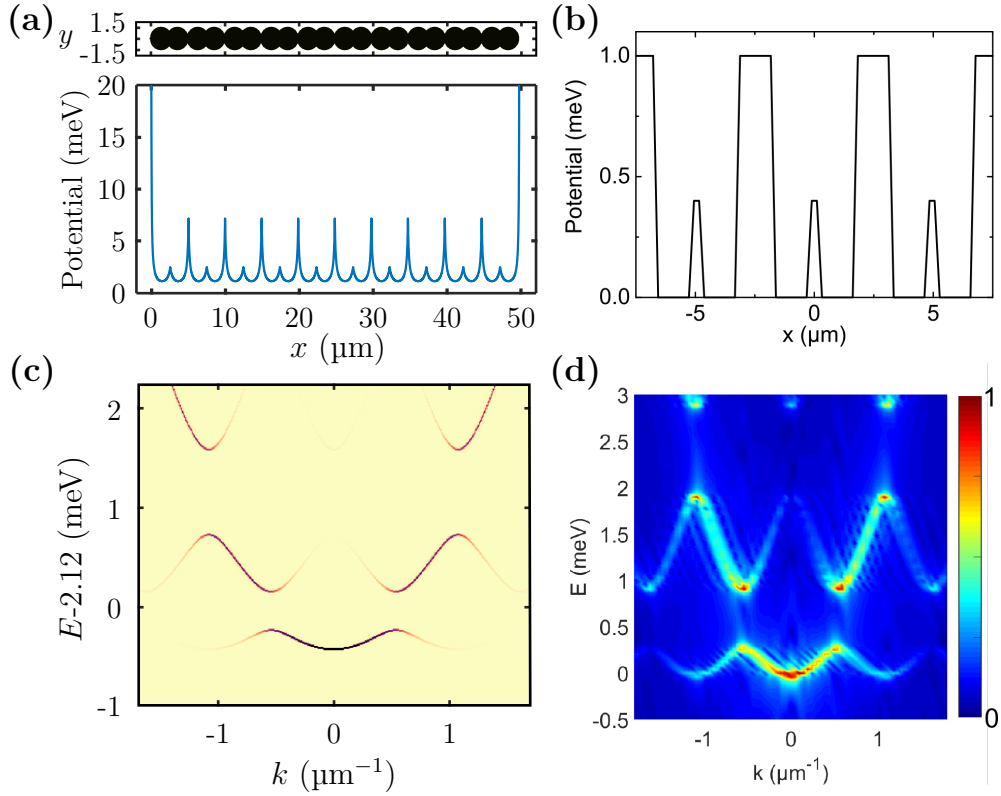


Figure 3.9: Numerical simulations: **a**, 2D description of a SSH lattice with 10 unit cells (top) and associated 1D potential calculated by transverse approximation (bottom). **b**, Square potential model developed by D. Solnyshkov. The height and width of the barriers were optimized to reproduce experimental results. **c**, Calculated band structure of the 1D continuous SSH model described by the potential of panel (a). **d**, Calculated band structure of the 1D continuous SSH model described by the potential of panel (b). Panels (b) and (d) were taken from the supplementary materials from Ref. [332].

SEM image in Fig. 3.8 (a)). This defect is equivalent to an interface between the two different phases of the SSH model (as described in Fig. 3.4 (b) top sub-panel) and one thus expects the formation of a topologically protected localized state inside the topological gap. By performing the same non-resonant spectroscopy measurement on the chain of pillars presenting an interface defect, we obtain the momentum and position resolved energy distributions of polariton modes presented in Fig. 3.8 (b-c). A localized mode is clearly observed inside of the gap at the interface, which presents the spatial intensity distribution of a topological state: its wavefunction is only localized on the A sub-lattice corresponding to a positive total sub-lattice pseudo spin $\tilde{S} = 1$ (see inset of Fig. 3.8).

All experimental results are reproduced by numerical simulations. For the sake of simplicity, a tight-binding approach, restricting ourselves to “ s ” bands only, will be considered to focus on the essential physics of the SSH model. When discrepancies between the tight-binding mapping and experimental results cannot be solved by simple means, 1D continuous simulations of the lattice can be realized. These simulations can either be ran considering a transverse approximation of the confinement potential for polariton, leading to the energy potential presented in Fig. 3.9 (a) which is directly obtained from the 2D structure of the micro-pillar lattice (see top

panel of Fig. 3.9 (a)), or using a square potential model (see Fig. 3.9 (b)) developed by Dmitry Solnyshkov and Guillaume Malpuech, the two theoreticians who contributed to the development and analysis of these results. This latter model is very close to the tight-binding approach: each site is represented by a square potential well and the coupling strength from site to site can be chosen by tuning the high and width of the energy barriers. In Fig. 3.9 (c-d) we display the calculated band structure obtained *via* both methods: in both case, careful tuning of the 1D potential parameters enables reproducing the energy dispersion measured experimentally. Note that the asymmetry between the two “*s*” bands, which originate from a coupling between “*s*” and “*p*” modes of neighboring sites, is well captured by these two models.

3.3.2 Bistability of a topological interface state: a topological soliton

To start our exploration of the interplay between topology and non-linearities in driven-dissipative systems, we begin by probing the non-linear response of the topological interface state *via* the optical bistability. The discrete Gross-Pitaevskii equation governing the system can be written as a set of coupled non-linear equations which yields:

$\forall m < 0 :$

$$\begin{aligned} i\hbar\partial_t\Psi_{A,m} &= -J\Psi_{B,m} - J'\Psi_{B,m-1} - (\Delta E + i\frac{\gamma_0}{2})\Psi_{A,m} + g|\Psi_{A,m}|^2\Psi_{A,m} + iF_{A,m} \\ i\hbar\partial_t\Psi_{B,m} &= -J\Psi_{A,m} - J'\Psi_{A,m+1} - (\Delta E + i\frac{\gamma_0}{2})\Psi_{B,m} + g|\Psi_{B,m}|^2\Psi_{B,m} + iF_{B,m} \end{aligned}$$

$\forall m > 0 :$

$$\begin{aligned} i\hbar\partial_t\Psi_{A,m} &= -J\Psi_{B,m-1} - J'\Psi_{B,m} - (\Delta E + i\frac{\gamma_0}{2})\Psi_{A,m} + g|\Psi_{A,m}|^2\Psi_{A,m} + iF_{A,m} \\ i\hbar\partial_t\Psi_{B,m} &= -J\Psi_{A,m+1} - J'\Psi_{A,m} - (\Delta E + i\frac{\gamma_0}{2})\Psi_{B,m} + g|\Psi_{B,m}|^2\Psi_{B,m} + iF_{B,m} \end{aligned}$$

for $m = 0 :$

$$\begin{aligned} i\hbar\partial_t\Psi_{A,0} &= -J'\Psi_{B,-1} - J'\Psi_{B,0} - (\Delta E + i\frac{\gamma_0}{2})\Psi_{A,0} + g|\Psi_{A,0}|^2\Psi_{A,0} + iF_{A,0} \\ i\hbar\partial_t\Psi_{B,0} &= -J'\Psi_{A,1} - J'\Psi_{A,0} - (\Delta E + i\frac{\gamma_0}{2})\Psi_{B,0} + g|\Psi_{B,0}|^2\Psi_{B,0} + iF_{B,0} \end{aligned} \tag{3.14}$$

where $\Psi_{A,m}$ ($\Psi_{B,m}$) and $F_{A,m}$ ($F_{B,m}$) respectively represent the amplitude of the polariton and pump field on the *A* (*B*) pillar of the m^{th} unit cell. In the present case only $F_{A,0}$ is non-zero as we focus the laser on the interface pillar. ΔE represents the detuning between the drive energy and the center of the topological gap. We here consider a SSH lattice with a -7.0 meV detuning between the topological state and the exciton, thus corresponding to an excitonic fraction $|X|^2 \approx 4.7\%$ and to an effective non-linearity per site $g \sim 0.01$ μeV .

We optimize the injection efficiency by resonantly exciting the topological edge state: we focus a linearly polarized cw laser on the interface pillar and tune its energy to be resonant with the topological state. Photons escaping the lattice are

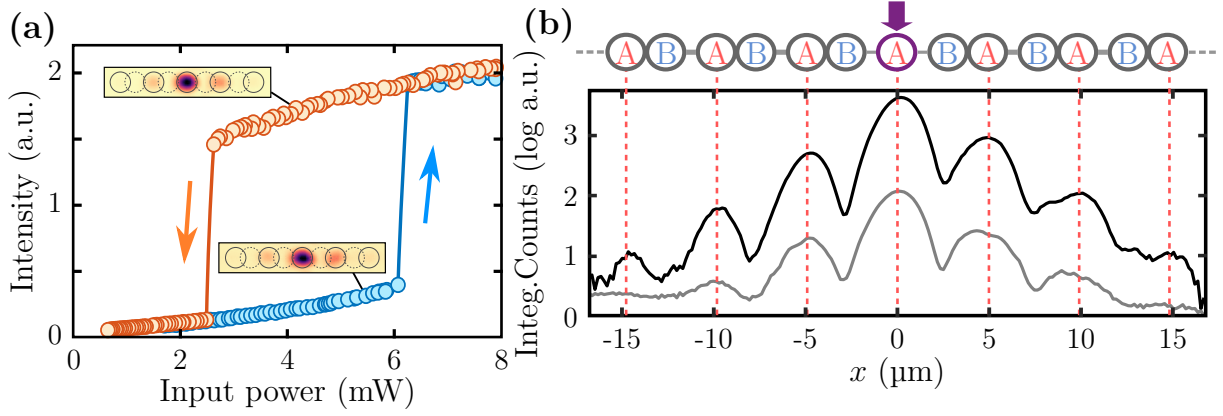


Figure 3.10: **a**, Transmitted intensity as a function of the input power. Blue and orange points respectively correspond to the upward and downward scans. A hysteresis cycle is observed and blue and orange arrows indicate the direction of the non-linear jumps. Typical 2D profiles of the intensity pattern on each stable branch are plotted as insets. **b**, Integrated intensity profile of the non-linear fluid on the upper branch (black solid line) and of the edge state (grey solid line). A sketch of the lattice is displayed on top with a purple arrow indicating the position of the pump. For each unit cell, a vertical dashed line indicates pillars presenting a high polariton density, which here correspond to the A sub-lattice.

collected in transmission and the obtained real space image is monitored while we tuned the excitation beam parameters. Maximizing the injection efficiency relies on two knobs: on the one hand we optimize the spatial overlap with the topological edge state wavefunction by moving the laser spot towards the center of the weakly bound pillar. On the other hand we rotate the incident beam polarization direction to match the edge state one: in the linear regime a post selection of the polarization is sufficient to monitor the dynamics of one set of modes independently from the other, whereas when inter-particle interaction starts to play a predominant role, the particles density in one of the linearly polarized modes directly influences the dynamics of polaritons with an orthogonal polarization *via* polariton-polariton cross interaction. To minimize the injection of polaritons in cross-polarized states and thus be able to consider the scalar model described by the set of equations 3.14, a particular care has to be given to the polarization purity of the excitation beam: an additional thin film polarizer is thus placed just before the cryostation.

Since polariton-polariton interactions are repulsive, the laser energy has to be blue detuned with respect to the polariton state to observe the opening of an hysteresis cycle when the injection power is ramped up and down. Observing an optical bistability phenomenon with an isolated pillar requires a minimal laser detuning of $\delta_{LM} = \sqrt{3}\gamma_0$, with γ_0 the polariton mode linewidth (a demonstration can be found in Ref. [95]). A Lorentzian fit of a spectrum obtained by resonant spectroscopy of the topological state yields a linewidth of $75 \mu\text{eV}$. The laser energy is tuned such that the detuning with the mode is $\delta = 206 \mu\text{eV} \approx 2.7\gamma_0$ and the input power is then slowly ramped up and down. The measured evolution of the total transmitted intensity as a function of the input power is presented in Fig. 3.10 (a): a hysteresis cycle is clearly observed with two distinct power thresholds $P_{\text{up}} = 6.1 \text{ mW}$ and $P_{\text{down}} = 2.5 \text{ mW}$.

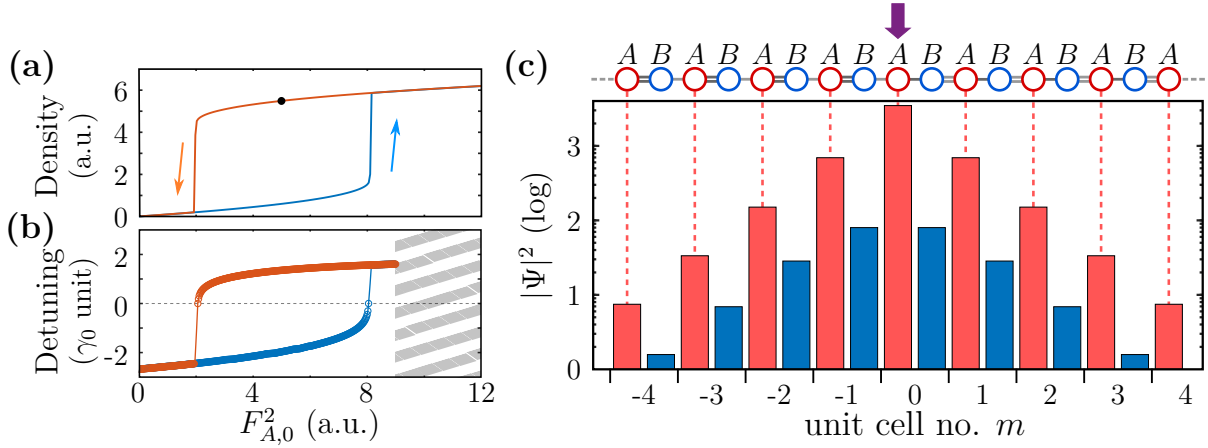


Figure 3.11: **a**, Simulated evolution of the total polariton density in the lattice as a function of the driving power. Blue and red curve respectively correspond to upward and downward power scans. **b**, Calculated effective detuning between the interface state resonance and the pump. **c**, Calculated density profile of the non-linear fluid on the upper bistability branch. The corresponding operating point is marked by a black dot in panel (a). *A* and *B* sub-lattices are respectively colored in red and blue. Purple arrow indicates the pump position.

Typical 2D intensity emission patterns associated to each stable bistability branch is plotted in inset of the diagram. The intensity distribution on the upper bistability branch is found to be very similar to the profile of the topological interface state with a clear localization on the *A* sub-lattice and a maximum on the weakly coupled pillar. To compare the non-linear fluid distribution with the one of the interface state, we integrate the intensity along the transverse direction of the lattice and obtain the 1D profiles presented in Fig. 3.10 (b). The profile of the non-linear fluid on the upper bistability branch presents the same 1D profile as the topological interface state with intensity maxima localized on *A* pillars and minima on *B* pillars. The sub-lattice pseudo spin of the non-linear fluid can be measured by separately integrating the number of counts on the *A* and *B* sub-lattice and computing the mean field equivalent of the pseudo spin defined in equation 3.1.4.1. Restricting ourselves to the 5 central unit cells where the signal is significantly larger than the noise, we integrate the intensity in regions of interest (ROIs) centered on each pillar and compute the resulting pseudo-spin. It yields $\tilde{S} = 0.88 \pm 0.09$. The uncertainty level is given by the precision of pillars positions and corresponds to three standard deviations calculated over values of \tilde{S} computed by tuning the size and position of the ROIs.

To numerically reproduce these results, we can solve the set of equations 3.14. Computing the steady state at each point of a power ramp allows reproducing the opening of a hysteresis cycle which is presented in Fig. 3.11 (a). A calculation of the excitation spectrum allows tracking the effective detuning between the blueshifted resonance and the pump: as expected, power thresholds coincide with resonances between the pump and the blueshifted state. Above $F_{A,0}^2 \approx 9$, the localized state mixes with the upper band of the model and the definition of the detuning becomes irrelevant, the corresponding area has thus been hatched. The profile of the non-linear fluid on the upper stability branch is presented in Fig. 3.11 (b) and corroborates the

localization of polaritons on the A sub-lattice: the computed sub-lattice pseudo-spin yields $\tilde{S} = 0.92$.

The gap soliton discussed in this section is the driven-dissipative counterpart of the topological edge soliton described in conservative systems. Since it bifurcates from the topological interface state, this non-linear steady state is called a dissipative topological gap soliton.

3.3.3 Generation of gap solitons in the bulk

We now turn to the exploration of the non-linear response of the bulk of the lattice, in which D. Solnyshkov et al. predicted, in Ref. [202], the formation of bright gap solitons in the case of conservative systems. These gap solitons have a particular spatial profile: they exhibit exponentially decaying tails with a sub-lattice localization, similarly to a topological edge state. To observe the driven-dissipative counterpart of these solitons, we consider a structure where polariton interactions are sufficient to induce a significant blueshift ($g|\psi|^2 \sim E_{\text{gap}}/2$) of the lower band eigen-states. We select a SSH lattice with a $\delta = -4.9$ meV detuning between the bottom of the lower “ s ” band and the exciton, corresponding to an excitonic fraction of $|X|^2 \approx 8\%$. The associated dispersions were presented in Fig. 3.7.

The localized laser spot is now focused in the center of a strongly coupled dimer in order to maximize the overlap of the driving field with states of the lower band (bonding symmetry). The laser energy is tuned to be in the center of the topological gap ($\Delta E = 0$) and we monitor the transmission of the structure as we perform a power ramp. In this case the set of discrete Gross-Pitaevskii equations governing the system can be written:

$\forall m :$

$$\begin{aligned} i\hbar\partial_t\Psi_{A,m} &= -J\Psi_{B,m} - J'\Psi_{B,m-1} - (\Delta E + i\frac{\gamma_0}{2})\Psi_{A,m} + g|\Psi_{A,m}|^2\Psi_{A,m} + iF_{A,m} \\ i\hbar\partial_t\Psi_{B,m} &= -J\Psi_{A,m} - J'\Psi_{A,m+1} - (\Delta E + i\frac{\gamma_0}{2})\Psi_{B,m} + g|\Psi_{B,m}|^2\Psi_{B,m} + iF_{B,m} \end{aligned} \quad (3.15)$$

where $F_{X,m}$ is here a Gaussian distribution centered on the unit cell $m = 0$. One can also simply set $\forall m \neq 0, F_{A,m} = F_{B,m} = 0$ and $F_{A,0} = F_{B,0} = F_0$. A better agreement is obtained between experimental and numerical results by considering the true Gaussian nature of the pump spot.

The evolution of the measured transmitted intensity as a function of the input power is presented in Fig. 3.12 (a). The opening of two consecutive hysteresis cycles is evidenced with four distinct power thresholds, two for the upward scan labeled $P_{1,u} \approx 9.3$ mW and $P_{2,u} \approx 62$ mW and two for the downward scan $P_{1,d} \approx 4.0$ mW and $P_{2,d} \approx 54$ mW. For each upper stable branch, a typical 2D intensity profile is presented in inset. In both cases we observe the formation of bright domains showing a strong polariton density: after the first non-linear threshold the polariton fluid is localized on both pillars of the pump dimer and symmetrically expands to the two neighboring dimers above $P_{2,u}$. This localized structure is typical from

discrete bright gap solitons [333,334]. In the present case, the dissipative nature of the system and driving conditions imposes the solitons to be pinned to the vicinity of the pump which breaks the lattice translation invariance.

By integration of the intensity in the direction transverse to the SSH chain, we obtain 1D profiles which are presented in Fig. 3.12 (b-c) and respectively correspond to operating points just above $P_{2,u}$ and $P_{1,u}$. The evolution of the profile of the non-linear fluid as a function of the input power is presented in panel (d) and (e) for the upward and downward scans. A correspondence between power thresholds and expansion or reduction of the high density domain is clearly evidenced: each upward (downward) non-linear jump is accompanied by the growth (contraction) of the bright domain by a discrete number of unit cells, similarly to what has been reported in the case of the 1D Lieb lattice in Ref. [219]. Each non-linear jump occurs when the local polariton density is such that the resulting interaction energy is equal to the spectral detuning between the top of the lower “s” band and the pump ($gn \sim (J - J')$).

Analyzing in more detail the profiles presented in panels (c-d), three different regions can be delimited corresponding to the central high density region and the two exponentially decaying tails on each side of the soliton core. The influence of the underlying chiral symmetry is evidenced: in the dense region, polaritons are evenly spread on both sub-lattices whereas the fluid shows a net sub-lattice polarization in the exponentially decaying tails. On the left of the bright domain, polaritons are mostly localized on A pillars while they are localized on the B sub-lattice on the right. This sub-lattice polarization of the soliton tails is a direct consequence of the chiral symmetry of the SSH model which imposes zero-energy states to be localized on a single sub-lattice: due to the low polariton density in the exponential tails, the associated interaction energy is locally negligible compared to other energy scale of the system and the dynamics of polariton is thus governed by the underlying linear model. Each side of the bright domain can be viewed as setting the boundary condition for the decaying field: on the left (right), the last intense pillar is a A (B) pillar, which corresponds to the sub-lattice localization of the associated exponential tail. Again restricting ourselves to the unit cells where the signal is significantly larger than the noise, we can independently compute the pseudo-spin of each tail. The measured pseudo-spins are presented on corresponding profiles in Fig. 3.12: \tilde{S}_L and \tilde{S}_R respectively correspond to the pseudo-spin restricted to the left and right exponential tails. Due to the inversion symmetry of the lattice, left and right tails present pseudo-spin of opposite sign and roughly equal absolute amplitudes. Consequently, the pseudo-spin computed over the entire profile of solitons is almost vanishing with $\tilde{S}_{\text{Tot}} = -0.10 \pm 0.06$ after $P_{1,u}$ and $\tilde{S}_{\text{Tot}} = 0.09 \pm 0.04$ after $P_{2,u}$.

As described in conservative systems, the gap solitons generated in the bulk of the SSH lattice present a peculiar spatial profile. Due to the chiral symmetry of the SSH Hamiltonian, the exponentially decaying tails of the solitons are localized on a single sub-lattice: one sub-lattice on the left and the other on the right. As the quasi-resonant excitation power is scanned up and down, the soliton can laterally grow by a discrete number of unit cells.

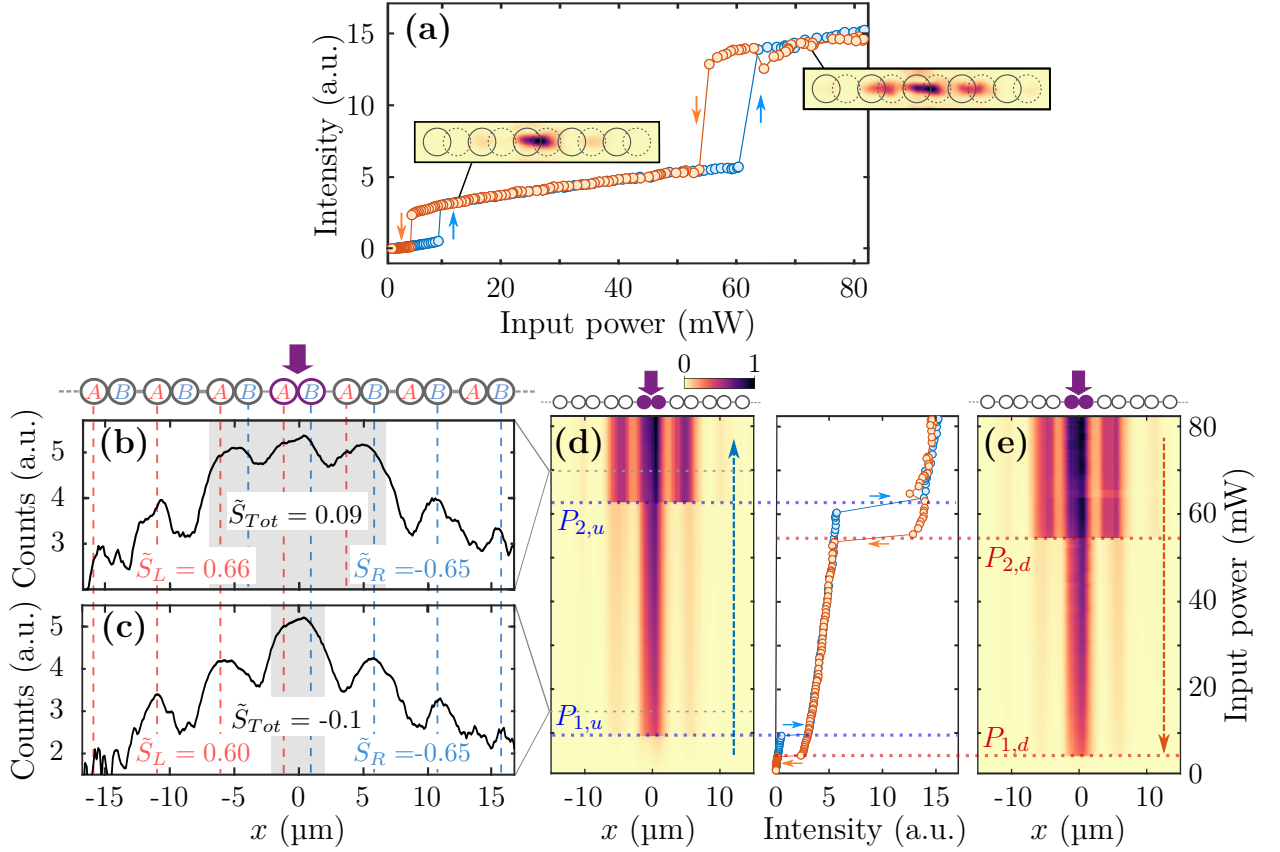


Figure 3.12: **a**, Transmitted intensity as a function of the input power. Blue and orange points respectively correspond to the upward and downward scans. Blue and orange arrows indicate the scan direction at the non-linear jumps. Typical 2D profiles of the intensity pattern are plotted as insets for each upper stable branch. **b-c**, Integrated intensity profiles of the non-linear fluid on, respectively, the second and first upper branches (corresponding to $P_b = 70$ mW and $P_c = 15$ mW). A sketch of the lattice is displayed on top with a purple arrow indicating the position of the pump. For each unit cell, a vertical dashed line indicates pillars presenting a high polariton density and a gray area highlight the soliton core. **d-e**, Evolution of the 1D intensity profile as a function of the input power respectively for the upward and downward scans. A copy of the hysteresis diagram is presented to highlight the correspondence between power thresholds and the expansion or contraction of the non-linear domain.

3.3.4 Numerical simulations: Gap solitons as Truncated Bloch Waves

Our results can numerically be reproduced by simulating the temporal evolution of the set of tight-binding equations 3.15. The resulting hysteresis diagram and associated profiles of the solitons obtained for $\Delta E = 0$ are presented in Fig. 3.13. Note that to reproduce the system of disjoint hysteresis cycles it is numerically necessary to introduce a term of non-linear losses, otherwise a different multi-stability diagram is observed (see inset in Fig. 3.13 (a)). This additional loss term was introduced in the form of an imaginary part of g ($g = g_0 + i\gamma'$ with $\gamma' \sim 10^{-4}\gamma_0$). The necessity to add non-linear losses has already been discussed by Paraïso et al., in Ref. [209], where the authors observed a multi-stability diagram involving the different polarization modes of a circular mesa. The non-linear loss term was introduced as a cross polarization term: the density of σ_+ polaritons is increasing the losses experienced by cross-polarized polaritons. The presence of this non-linear loss term was attributed to the existence of a bi-exciton line and spin-flip scattering with dark excitons. In the present case the driving field only couples to a single linear polarization mode, which decomposes as a superposition of σ_+ and σ_- states. We measured the amplitude of the fluid injected in the cross polarized direction which showed that polaritons were purely injected in the desired state and no rotation of the fluid polarization could be measured. This tends to invalidate this mechanism as in case of a circular polarization mode experiencing additional losses, our polariton fluid would become elliptically polarized. Another plausible explanation which does not rely on polariton scattering towards other excitonic states is a local increase of the lattice temperature: the laser intensity focused on the structure and the higher polariton density in the presence of a three dimer soliton are such that the material could locally be heating. As a result, the GaAs semiconductor gap would decrease, red-shifting and broadening the exciton line and thus the polariton one. Answering this question would require to perform a polarization resolved pump-probe spectroscopy of the polariton modes to observe the possible broadening as the pump power is scanned up and down.

Note that a wide hysteresis cycle, equivalent to the one in inset of Fig. 3.13 (a), is obtained considering simulations of the nearly-free model. The issue does not originate from the simplification of our model.

Calculated density profiles of the solitons corresponding to the first and second upper bistability branches are presented in Fig. 3.13 (b-c). The square amplitude on A and B sub-lattices are respectively represented by red and blue bars. Complementarily, the associated evolution of the unit cell pseudo-spin as a function of the position is displayed in Fig. 3.13 (e-f). To understand these spatial profiles, let us step back and start by considering the case of a continuous system. As discussed in Chap. 1.5.4, the solitonic solutions of an homogeneous potential are known to take the form of an inverse hyperbolic cosine (hyperbolic secant): $\Psi(x) \propto 1/\cosh(x/a_0)$ with a_0 the width of the soliton. In order to described topological gap solitons of the continuous SSH model, D. Solnyshkov et al. proposed an ansatz in Ref. [202], which consists in considering two hyperbolic secant functions, each of them being associated to a different sub-lattice:

$$\Psi(m) = \begin{bmatrix} \Psi_{A,x_m} \propto 1/\cosh([x_m - x_0]/a_0) \\ \Psi_{B,x_m} \propto 1/\cosh([x_m + x_0]/a_0) \end{bmatrix} \quad (3.16)$$

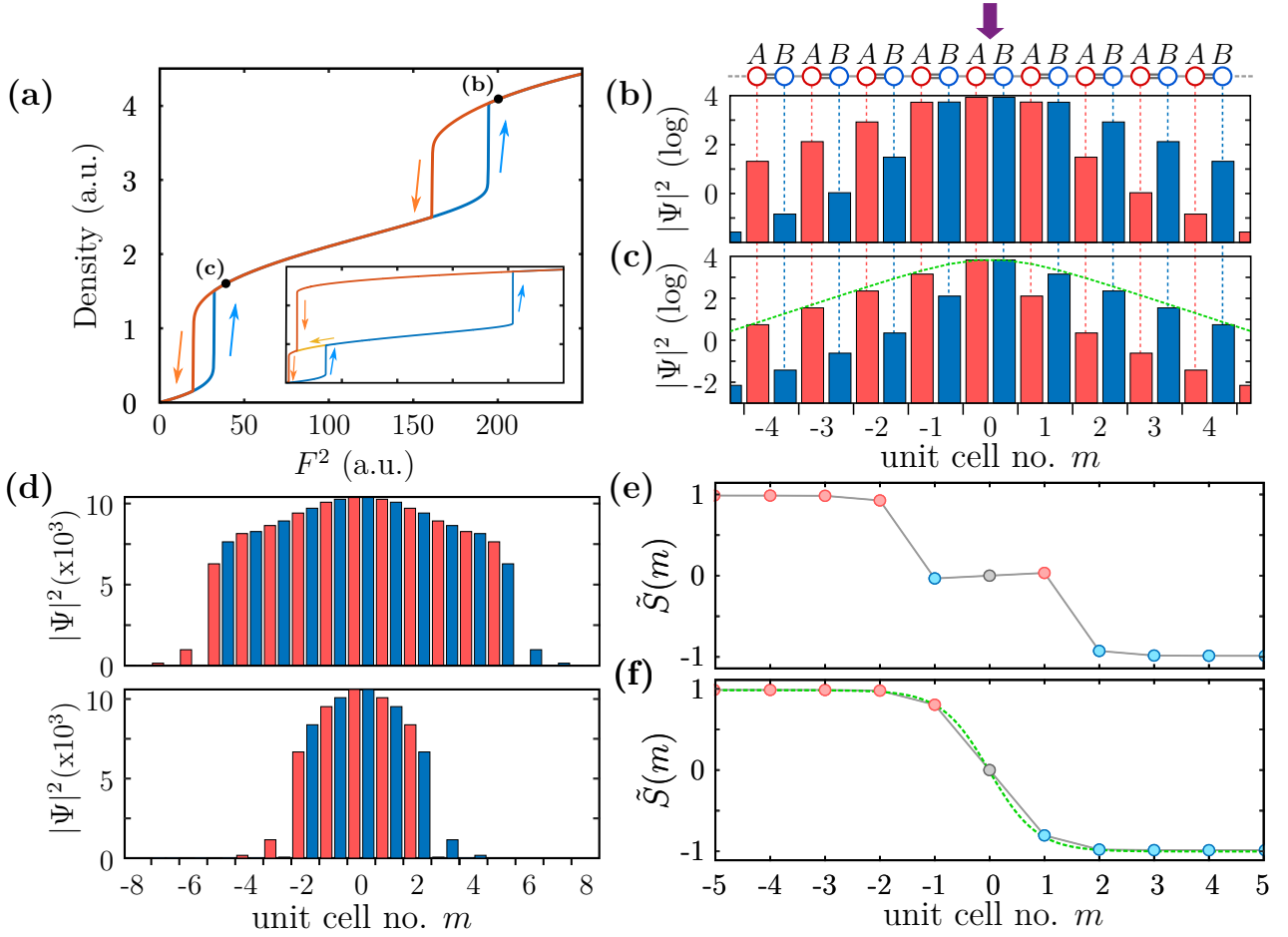


Figure 3.13: **a**, Simulated evolution of the total polariton density in the lattice as a function of the driving power when including non-linear losses. Blue and red curve respectively correspond to upward and downward power scans and colored arrows indicate the direction of the non-linear jumps. Black dots mark the operating points corresponding to panels **(b)** and **(c)**. Inset in the bottom corresponds to the multi-stability diagram obtained without additional loss term. **b-c**, Calculated density profile of the non-linear fluid respectively on the upper and middle bistability branches. A and B sub-lattices are respectively colored in red and blue. Purple arrow indicate the center of the pump. Green dashed line is a fit by a sum of two hyperbolic secant. **d**, Calculated density profiles of solitons presenting a wider non-linear domain with respectively 11 and 5 bright uni-cells for top and bottom. **e-f**, Evolution of the sub-lattice pseudo-spin as a function of the position, respectively corresponding to profiles in **(b)** and **(c)**. In the latter, the green dashed line correspond to a fit by a hyperbolic tangent. Color of the bullet points indicate the sign of $\tilde{S}(m)$.

where x_0 is a parameter quantifying the displacement of each sub-lattice component with respect to the center of mass. The use of such ansatz allows to reproduce the envelope of the tight-binding driven-dissipative soliton profile (green dashed curve in Fig. 3.13 (b)). The main interest of this ansatz resides in the prediction of the spatial evolution of the pseudo spin. It yields an hyperbolic tangent behavior with a sign transition inside the soliton core (see Fig. 3.13 (f)). The soliton is thus analogous to a wall between two opposite spin polarized domains. The analytical derivation of the pseudo-spin texture yields $\tilde{S}(m) = \tanh(b/a_0) \tanh(m/a_0)$ with b a fixed parameter conditioning the amplitude of the pseudo-spin for $m \rightarrow \infty$, this parameter will later be shown to depend on the laser detuning. In Fig. 3.13 (f), the green dashed line corresponds to a fit of the soliton pseudo-spin texture by the hyperbolic tangent ansatz which yields $a_0 = 0.87$. Consequently, the pseudo-spin polarization of the soliton tails reaches $\tilde{S} = \pm 0.99$ at the unit cell $m = \pm 2$ (calculated from Taylor expansion). It means that in these tight-binding simulations, the core of the soliton spreads on unit cells $m = \pm 1$. The results that we will present in the next section show that it does not seem to be the case in the experiments.

Beyond the first non-linear stable branch, the pseudo-spin texture deviates from a hyperbolic tangent: the whole non-linear domain shows an almost vanishing spin, which is imposed by the lower band symmetry. However the local pseudo-spin exhibit a small dependence on position: it is negative in unit cell $m = -1$ and positive in unit cell $m = +1$ which is opposite to the spin of the associated tails. This phenomenon originate from the competition between bonding symmetry of the non-linear domain, decay and spatial profile of the pump. To evidence it, larger non-linear domains can be formed by pushing further the increase of the input power or by increasing the size of the pump spot (see Fig. 3.13 (d)). The soliton growth occurs *via* consecutive displacement of the non-linear domain wall, associated to sudden jumps of the total particle density. The displacement of the domain walls is always given by an integer of unit cells. Similarly to the gap solitons observed in Ref. [219], these large non-linear structures which are formed of contiguous ensembles of gap solitons and present abrupt edges can be interpreted as Truncated Bloch Waves (TBW).

In the present case and as in Ref. [219], we are investigating the driven-dissipative counterpart of this family of non-linear solutions. One can notice a consequence of the open nature of the system on the fluid amplitude in the dense region: we do not observe a flat top profile characteristic from conservative systems, but a seemingly Gaussian profile since it results from the interplay between a spatially Gaussian drive and homogeneous loss. The specificity of the case of gap solitons in the topological gap of the SSH model is the inherited chiral symmetry properties of the wavefunction which is reflected in the sub-lattice polarization of the exponential tails of the TBW.

3.3.5 Spin polarized tails, a specificity of the topological gap

Let us now discuss the pseudo-spin properties of the soliton tails. We studied dependence of the tails pseudo-spin as a function of the energy detuning between the laser energy and the center of the “s” band gap ΔE (see Fig. 3.14 (a)). Generating gap solitons by tuning the energy of the laser in the energy gap, we can probe the evolution of the tails sub-lattice polarization as a function of the soliton position

in the gap. A set of measured intensity profiles is presented in Fig. 3.14 (b). To obtain the value of the spin, we integrated the intensity profiles in regions of interest centered on each pillar, the resulting graphs associated to Fig. 3.14 (b) are presented in Fig. 3.14 (c). Finally, the evolution of the spin as a function of ΔE is presented in Fig. 3.14 (d). One observes that the pseudo-spin amplitude is maximum at the center of the gap and eventually vanishes when the laser energy enters the lower band. As the soliton becomes closer to the band, the spectral overlap of the soliton tails and the lower “s” bands becomes stronger. As a result, the slope of the tails becomes shallower and their intensity distribution tend to inherit the bonding symmetry of the lower “s” band (see profiles in Fig. 3.14 (b)). In a nearly-free description of the structure, it is equivalent to say that the kinetic energy term associated to the amplitude of the band becomes more and more relevant compared to the detuning between the soliton energy and the band.

To demonstrate that this sub-lattice polarization is specific to the topological gap, we injected gap solitons in the trivial gap above the upper “s” band ($\Delta E = 1.0$ meV). To efficiently inject polaritons, it is necessary to focus the laser spot on a single pillar to maximize the spatial overlap with the upper “s” band modes which present an anti-bonding profile. The intensity profile of the resulting soliton is presented in Fig. 3.15 (a). The soliton profile presents a vanishing amplitude at the center of the central unit cell thus witnessing the anti-symmetric nature of the mode from which it bifurcates. The same anti-bonding profile is observed in the soliton tails, with both sub-lattice showing a non-negligible polariton density. Yet a sub-lattice polarization can be measured which corresponds to the exponential decay of the tails. Subtracting this exponential decay for this profile and the one presented in Fig. 3.12 (c), we obtained the corrected profiles presented in Fig. 3.15 (b). A clear sub-lattice polarization is only observed for the soliton generated in the center of the topological gap. The measurement of corrected pseudo-spins yields $\tilde{S}_L = 0.75$ and $\tilde{S}_R = -0.77$ for the soliton generated in the topological gap and $\tilde{S}_L = 0.09$ and $\tilde{S}_R = -0.06$ for the soliton in the upper gap between “s” and “p” bands.

The upper part of the topological gap could not experimentally be probed due to the too high pump power required to reach the non-linear regime. However we realized numerical simulations to extend the analysis to the upper part of the gap which shows the same behavior: the pseudo-spin of the tails vanishes as the laser energy enters the upper band (solid line in Fig. 3.14 (d)).

The calculated spatial evolution of the spin is presented in panel Fig. 3.15 (c-d) for, respectively, $\Delta E \leq 0$ and $\Delta E > 0$. One observes that the hyperbolic tangent behavior is only valid for $\Delta E < 0$: a peaked non-vanishing value of the spin, highlighted by green arrows, is observed in the vicinity of the soliton when the pump energy approaches and enters the upper “s” band. The symmetric phase profile of the fluid imposed by the drive is in phase opposition with the anti-symmetric phase profile of the underlying band. The field picks up a sub-lattice polarization to accommodate the phase twist between the linear domain far from the pump and the non-linear domain which here is restricted to the pumped unit cell.

Note that the tight-binding calculation yields a sub-lattice pseudo-spin reaching $\tilde{S}_{\text{Tail}} \approx \pm 0.9$ in the center of the gap while the measured value does not exceed $\tilde{S} = 0.7$. This discrepancy is partially due to stray light polluting the profile and to a limitation of the tight-binding approximation of the experimental lattice: the

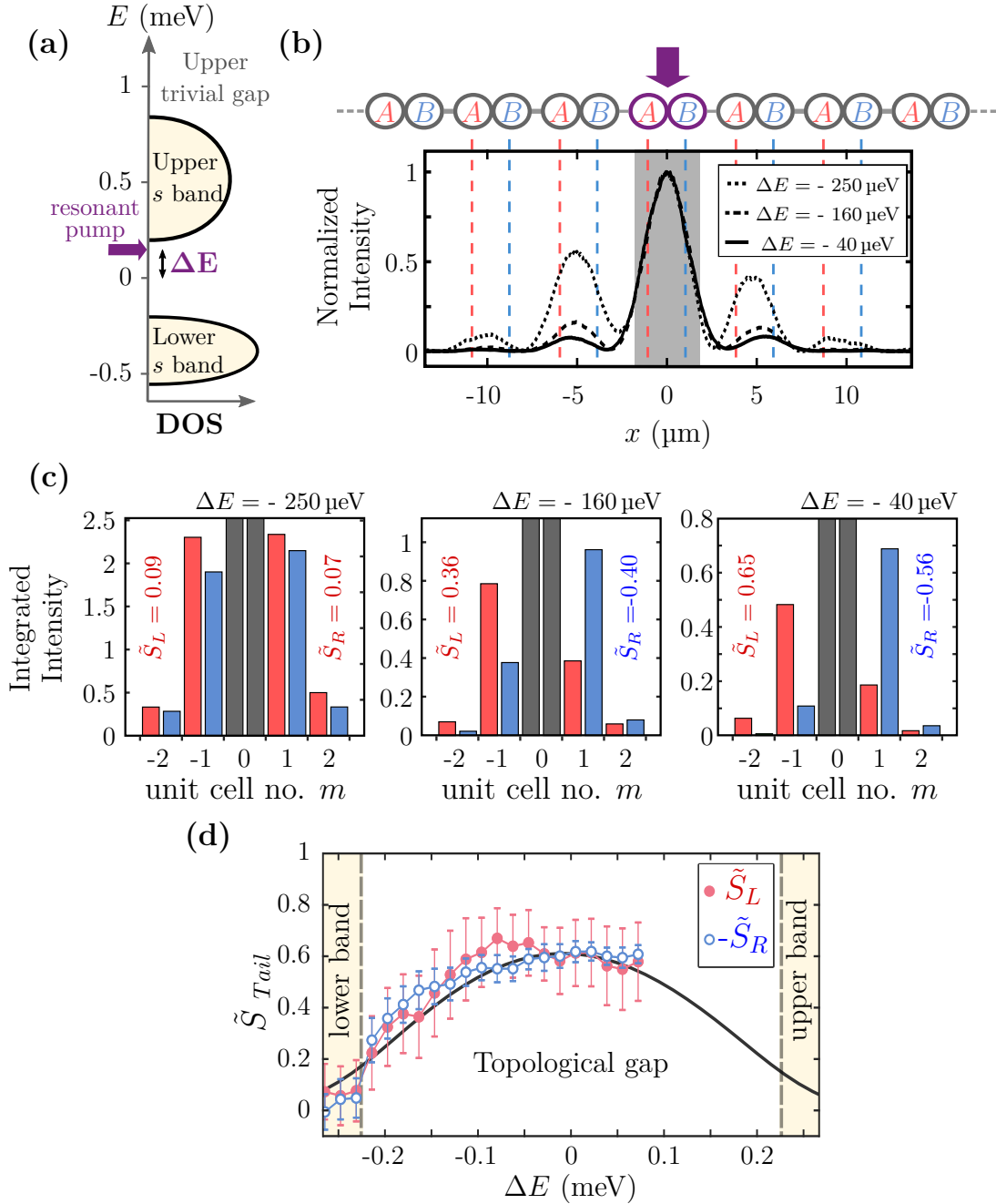


Figure 3.14: **a**, Schematic representation of the structure density of state as a function of the energy. **b**, Set of solitons profiles measured for different energy positions of the laser in the topological gap. **c**, Discretized intensity profiles associated to **(b)**. **d**, Evolution of the tails pseudo-spin as a function of the laser energy detuning with respect to the center of the topological gap. Black solid line corresponds to a numerical calculation.

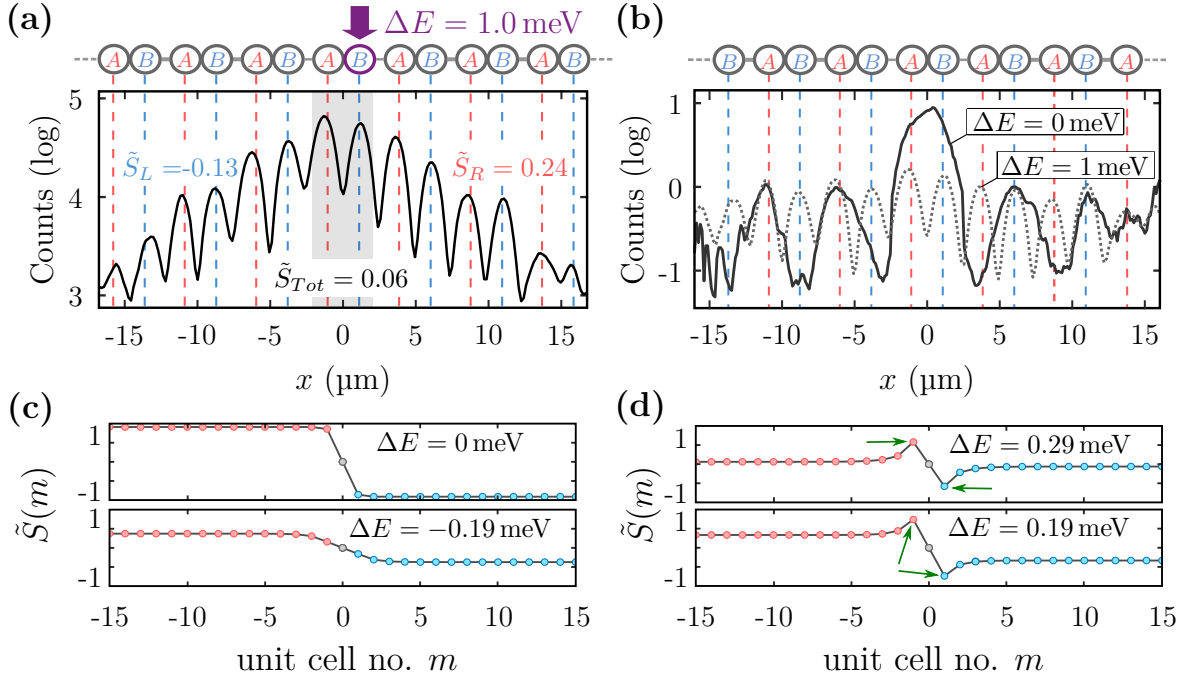


Figure 3.15: **a**, Profile of a gap solitons generated in the upper gap, between “*s*” and “*p*” bands. **b**, Soliton profiles corrected from the exponential decay due to dissipation for solitons generated in the topological gap (black solid line) and in the upper trivial gap (gray dotted line). **c-d**, Numerical calculation of the spatial evolution of the soliton pseudo-spin for (c): $\Delta E \leq 0$ and (d): $\Delta E > 0$.

intensity experimentally measured on the sub-lattice presenting a vanishing amplitude mostly comes from leakage of neighboring bright pillars. To reproduce this phenomenon and plot the solid curve presented in Fig. 3.14 (d), a smoothing was applied to the tight-binding soliton distribution using a Gaussian profile whose FWHM is adjusted to fit the experimental curve. The optimal FWHM is found to be slightly smaller than the one of a $D = 3 \mu\text{m}$ micro-pillar “*s*” orbital.

We observed the discrete formation of gap solitons in a driven-dissipative emulation of the SSH model. As predicted for conservative systems, solitons generated in the topological gap of the lattice present sub-lattice spin-polarized exponentially decaying tails. The driven-dissipative solitons are found to be very similar to conservative ones except for their bistability and small details of the TBW profiles. Tuning the energy of the pump laser, we evidenced the spin-polarized tails to be specific to solitons generated in the topological gap. More specifically, the pseudo-spin is found to be maximum in the center of the topological which correspond to the chiral symmetry axis of the SSH spectrum.

3.4 Robustness of a topological gap solitons

3.4.1 The case of conservative systems

Due to the localization properties of the field in the tails of the topological gap solitons, one can expect them to exhibit particular interactions with their environment. A first theoretical exploration of the interaction between these gap solitons

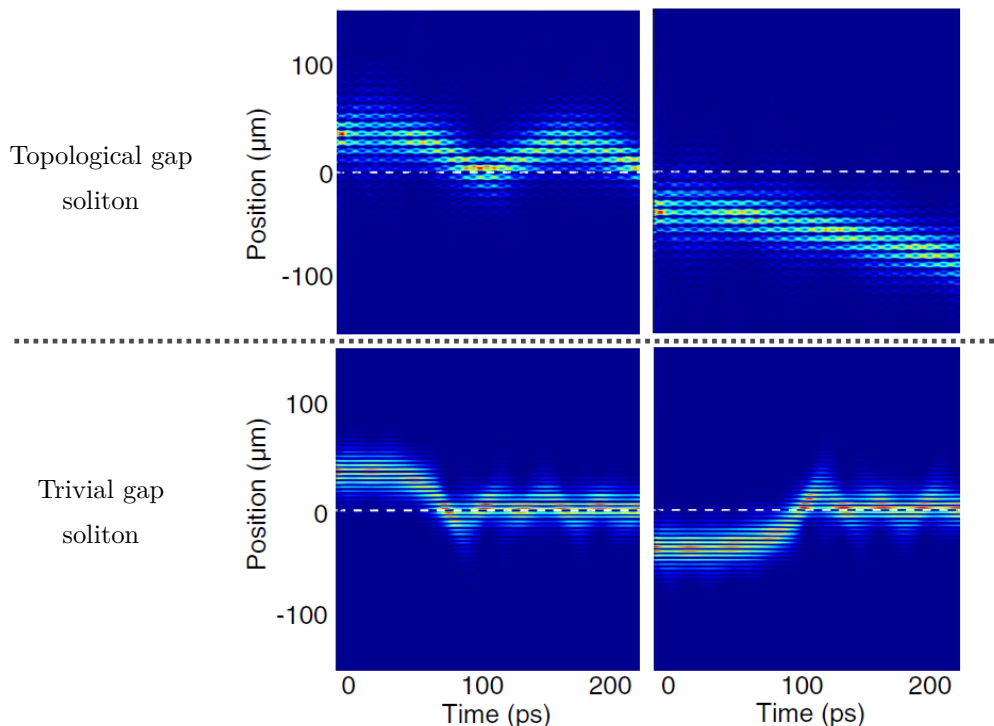


Figure 3.16: Simulated trajectories for topological (top) and trivial (bottom) gap solitons in the conservative case. In both cases two different initial positions are considered with respect to the defect, which is highlighted by an horizontal white line. Images taken from Ref. [202].

and localized defects was realized in conservative systems by Solnyshkov et al. in Ref. [202]. The authors probed the interaction of solitons generated in the topological and trivial gaps of the SSH model with a defect localized on a single sub-lattice.

The energy of both types of solutions was analytically derived as a function of the initial distance to the defect by a perturbative approach: the soliton energy is thus proportional to the overlap of the soliton distribution with the defect one. In this work the authors restricted their demonstration to a defect acting as a local blueshift of the energy landscape. This defect should behave as an attractor for gap solitons originating from a repulsive interaction ($g > 0$) since it allows minimizing their interaction energy.

Due to its pseudo-spin texture, the soliton generated in the topological gap presents an asymmetric response to the attractive defect: its energy depends on the initial *relative* position of the soliton. On the contrary, a soliton generated in the upper trivial gap is shown to present a symmetric response to the defect: the trivial gap soliton does not present any sub-lattice pseudo-spin and, as a consequence, no matter its relative position or the defect sub-lattice localization, the overlap of the soliton wavefunction with the defect only depends on the *absolute* value of the distance between the two objects.

Figure 3.16 presents numerical simulations of the soliton trajectories. The topological gap soliton is either attracted towards the defect, and presents an oscillatory trajectory or propagate away from it, whereas the trivial gap soliton is shown to be always attracted towards the defect.

A second important theoretical contribution to the description of topological gap

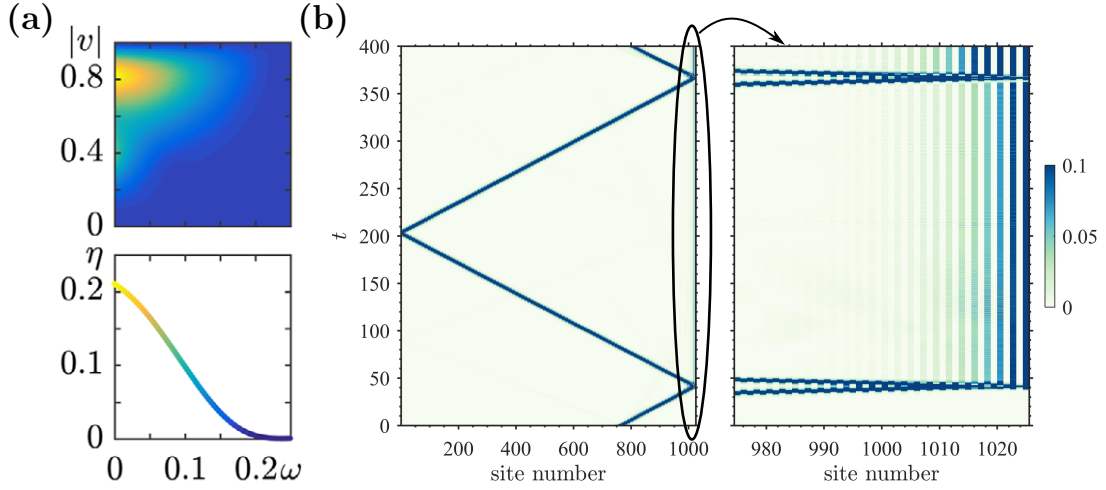


Figure 3.17: **a**, Top: numerical calculation of the scattering efficiency η as a function of the soliton velocity v and frequency difference ω , which is defined with respect to the topological edge state energy. Bottom: horizontal cut of top panel for $v = 0.75$. **b**, Left: tight-binding simulation of the propagation of a topological gap soliton on a SSH lattice with a trivial edge on the left and a non-trivial edge on the right. Right: zoom on the topological edge of the lattice, encircled portion of left panel. Images taken from Ref. [203].

solitons was done by Smirnova et al. in Ref. [203] who realized the analytical description of moving gap solitons. Importantly the authors studied the interaction of a topological gap soliton with a topological edge state and showed that a population transfer was possible between the soliton and the protected edge state. Using numerical simulations, the authors established that the conversion efficiency was optimal for a given velocity of the soliton. Additionally, the energy dependence of the conversion efficiency, they showed that the population transfer was maximized when the soliton frequency is resonant with the edge state. These results are summarized in Fig. 3.17 (a) which presents the evolution of the conversion efficiency as a function of the soliton velocity and frequency. A horizontal cut of top panel is presented in the bottom one for $v = 0.75$. The optimum of population transfer is observed for $\omega = 0$ which corresponds to the resonance between the soliton and edge state frequency. Finally, Fig. 3.17 (b) presents a tight-binding simulation of the scattering of a topological gap soliton on a non trivial edge of the lattice. A zoom on the edge is displayed on the right sub-panel where the sub-lattice localization of the intensity clearly evidences a population transfer occurring from the soliton towards the topological edge state. The authors extended their study to the case of a 2D lattice of hBN: bulk solitons could be used to excite 1D edge states at the interface between two hBN lattices with opposite onsite energies.

In the following, based on the theoretical proposal of D.Solnyshkov et al., we report on the interaction between driven-dissipative solitons and a defect localized on a single sub-lattice.

3.4.2 All optical engineering of a non-Hermitian defect

In the driven-dissipative case, a dynamical study of the interaction between a soliton and a localized defect is relatively complicated since the soliton is pinned to the

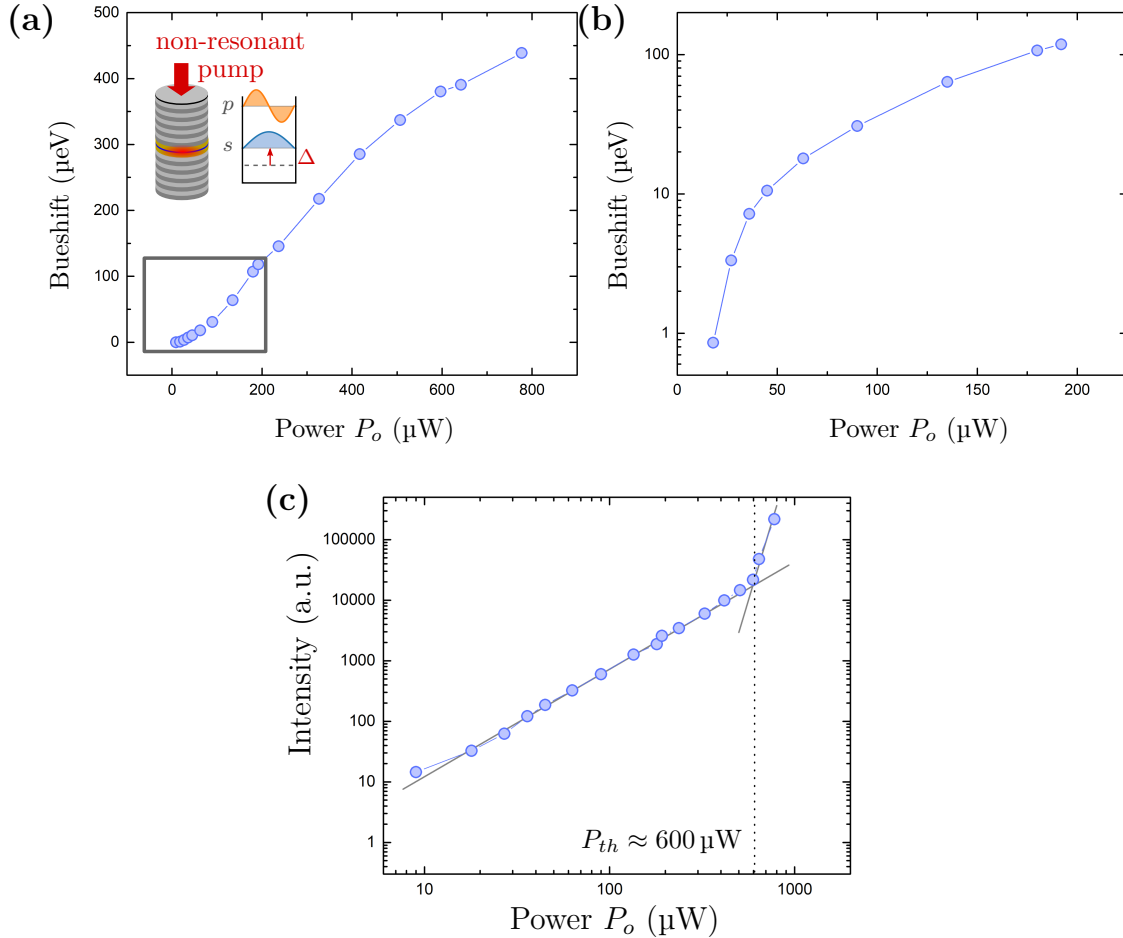


Figure 3.18: **a**, Evolution of the interaction induced blueshift as a function of the incident non-resonant power P_o . The black box delimits the zoom presented in panel **(b)**. Sketch of the experiment is displayed in inset. **b**, Evolution of the blueshift in the range relevant for the experimental results presented in Sec. 3.4.3. **(c)** Evolution of the emitted intensity collected in transmission as a function of the incident non-resonant power. A vertical dotted line mark the position of the lasing threshold.

vicinity of the pump: it results from the competition between a localized drive and dissipation. Stabilizing the soliton on the whole lattice would require to consider a pump and support scheme such as the one developed by the group of A. Bramati to stabilize dark solitons in 2D planar samples [122, 123]. However, it is possible to study the interaction of a static soliton with a localized defect as the amplitude of the interaction can be probed by monitoring the non-linear threshold value as a function of the defect amplitude. This defect will be induced optically.

To experimentally realize a localized defect, we used a second non-resonant cw laser and injected a reservoir of excitons. As stated in Chap. 2.1.1, a reservoir of excitons can be used to tailor the confinement potential for polaritons. Due to the repulsive exciton-polariton interaction, the presence of an exciton density induces a blueshift of the polariton resonances. Moreover, as it has been discussed in Chap. 1.5.2, the excitonic reservoir is known to provide gain for polaritons *via* stimulated relaxation which is the mechanism responsible for polariton lasing and condensation. The optical defect can thus be included in the model as a com-

plex term which locally modifies the pillar onsite energy (real part) and polariton linewidth (imaginary part).

To quantify both contributions, we first created this defect on a single pillar with the same diameter as those forming the SSH lattice ($D = 3\ \mu\text{m}$). The calibration of the blueshift is obtained by monitoring the energy of the micro-pillar “s” mode as a function of the non-resonant incident power, while the imaginary part is obtained by measuring the micro-pillar lasing threshold. The resulting calibration curves are presented in Fig. 3.18. Figure 3.18 (a) presents the evolution of the blueshift as a function of the non-resonant input power. A zoom on the blueshift range which is relevant for the experiments we will consider in Sec. 3.4.3 is presented in Fig. 3.18 (b). It corresponds to induced blueshifts smaller than half the energy gap amplitude. The evolution of the emitted intensity as a function of the incident non-resonant power is presented in Fig. 3.18 (c), a rupture of slope characteristic from the lasing threshold is observed for $P_{\text{th}} \approx 600\ \mu\text{W}$.

It is common to consider a system of two coupled equations to describe polaritons dynamics in presence of an excitonic reservoir. In the present case we assume the non depletion of the excitonic reservoir even in presence of a high polariton density and treat the equation governing the fluid density only. The gain is included as a local perturbation of the polariton linewidth $\gamma(P_o) = \gamma_0 + \gamma'(P_o)$ with $\gamma'(P_o)$ given by the ratio between the non-resonant power P_o and the lasing threshold P_{th} : at the lasing threshold the gain provided by the reservoir compensates the losses and we thus use the ansatz $\gamma'(P_o) \sim \gamma_0 P_o / P_{\text{th}}$.

The injection of an excitonic reservoir in the polariton platforms thus enables the engineering of non-Hermitian defects in the sense that this reservoir not only impacts the real part of the confinement potential but also its imaginary part. In the next section we will show that taking this imaginary term into account is crucial to fully reproduce experimental observations.

3.4.3 Sub-lattice robustness of a driven-dissipative soliton

We now turn to the study of the interaction between the topological gap soliton and a spatially localized defect. The non-Hermitian defect is created on the $m = 1$ unit cell which is the first unit cell on the right of the pumped one (see sketch on Fig. 3.19 (a)). We perform power ramps of the quasi-resonant pump controlling the injection of the soliton for various amplitudes of the non-resonant power. The defect was either injected on the A or B pillar of the considered unit cell. For each power scan, we integrate the collected intensity in the direction transverse to the chain. Figure 3.19 (b) presents the evolution of solitons intensity profiles as a function of the incident power for various power amplitude of the non-resonant laser beam. The first image (b1) is a reference scan without any defect ($P_{o,1} = 0$). The next three scans (b2-b4) correspond to a defect positioned on the B pillar and the last image (b5) was obtained for a defect positioned on the A pillar with a pump power equivalent to the one used for image (b4).

For a defect localized on the B pillar, the expansion of the soliton domain walls is dissymmetrized as we measure a clear reduction of the threshold for the expansion towards the right, where the defect is located. We label P_2^* the modified value of the power threshold in presence of a defect, the reference value obtained in absence of

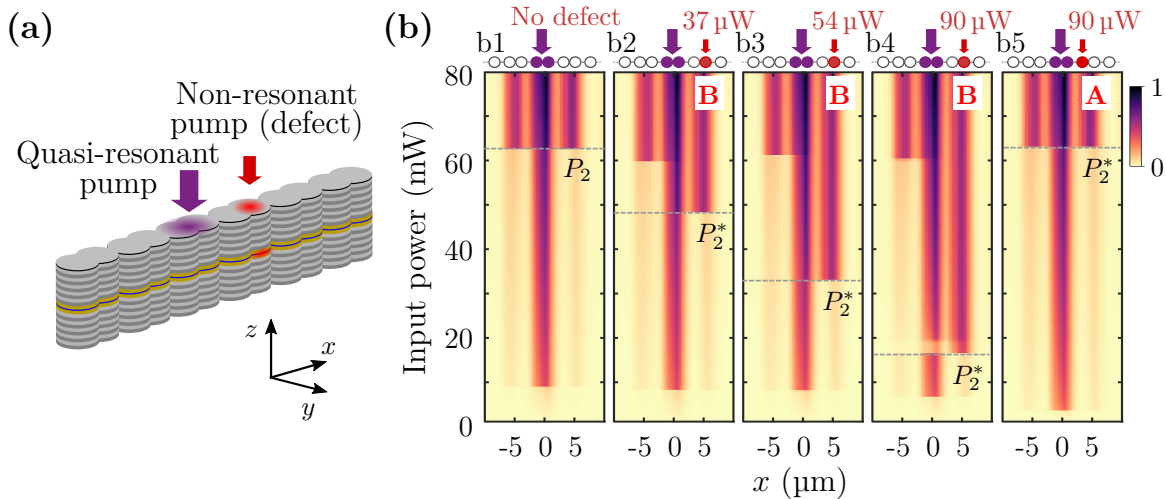


Figure 3.19: **a**, Schematic representation of the lattice with the quasi-resonant (purple) and non-resonant (red) pumps. **b**, Evolution of the soliton spatial profile as a function of the quasi-resonant pump power for various amplitudes of the localized defect. The power amplitude and position of the non-resonant beam is displayed in a sketch on top of each image. Horizontal dashed lines mark the position of the power threshold for the expansion of the soliton domain wall towards the right.

the defect is labeled P_2 . As expected, the soliton is attracted toward the blueshifted region and the stronger the pump amplitude the lower is P_2^* . The soliton exhibits a striking sensitivity to the presence of the exciton reservoir localized on the B pillar: for $P_o = 90 \mu\text{W}$ which corresponds to a blueshift on the order of half the mode linewidth ($\delta E \approx 30 \mu\text{eV} \sim \gamma_0/2$), the power threshold P_2^* is reduced by a factor of 4 with respect to P_2 . On the contrary when a defect of the same strength is created on the A pillar, where the amplitude of the soliton vanishes, the power threshold P_2^* remains unaffected and the growth of the soliton occurs simultaneously towards the left and the right.

Note that in the case of Fig. 3.19 (b4-b5), a decrease of the first power threshold is observed with a stronger effect in the case of panel b5. This reduction indicates that the defect is not purely localized on the non-resonantly pumped pillar but that the exciton reservoir also spreads under the resonant pump, the effect on the first threshold becoming non negligible as P_o is increased. The profiles obtained when further increasing the defect amplitude are presented in Fig. 3.20. In the case of a defect localized on B the power threshold saturates around $P_2^* \approx 11 \text{ mW}$ while the first threshold reduces with the increase of P_o . Note that in this case P_2^* corresponds to a threshold for which the soliton hops towards the right instead of growing to a two dimer width and, despite tremendous efforts to enrich the model, this feature was never captured by numerical calculations up to now. We have no explanation for this phenomenon. In the case of a defect localized on A for $P_o = 135 \mu\text{W}$ (see image 6), the growth of the soliton starts to present a small dissymmetry which is yet much smaller than the one observed in the case of a $P_o = 37 \mu\text{W}$ defect localized on the B pillar. This dissymmetry could be attributed to the spreading of the exciton reservoir onto the B pillar.

The experimental measurement of the evolution of P_2^* as a function of the defect amplitude and location is summarized in Fig. 3.21 as well as 1D numerical simula-

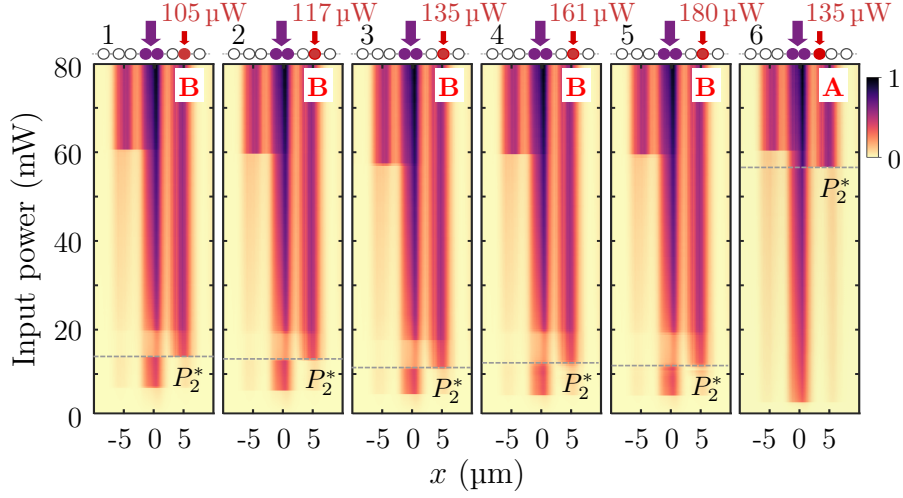


Figure 3.20: Evolution of the soliton spatial profile as a function of the quasi-resonant pump power for various off resonant pump power above $P_o = 90 \mu\text{W}$. The power amplitude and position of the non-resonant beam is displayed in a sketch on top of each image. Horizontal dashed lines mark the position of the power threshold for the expansion of the soliton domain wall towards the right.

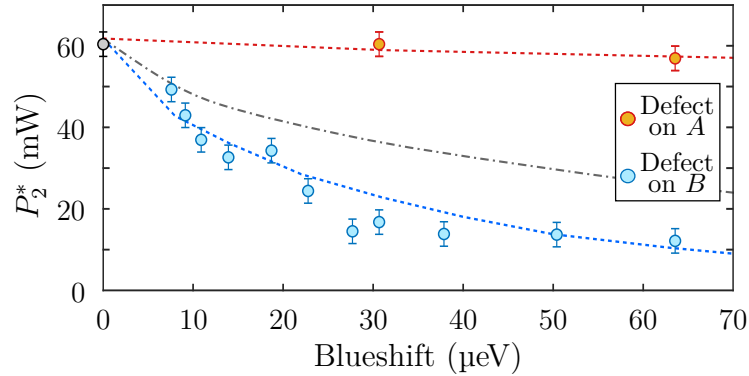


Figure 3.21: Evolution of the power threshold P_2^* as a function of the blueshift induced by the non-resonant pump. Red and blue dashed curves corresponds to numerical simulations for non-Hermitian defects respectively localized on the A and B pillar of the unit cell $m = 1$. Dashed gray line is a numerical simulation obtained for a Hermitian defect localized on the B sub-lattice: only the blueshift contribution of the defect is taken into accounts.

tions realized by D. Solnyshkov which allow demonstrating the importance of the non-Hermitian nature of the engineered defect. Numerical simulations based on the experimental calibrations of the defect reproduced experimental results (see blue and red dashed lines in Fig. 3.21). The soliton is insensitive to the presence of a defect localized on the sub-lattice where it shows a vanishing amplitude (here the A sub-lattice). To reproduce the threshold reduction observed in the case of a defect whose distribution is strongly overlapping with the soliton tails, it was necessary to take the non-Hermitian nature of the defect into account (blue curve). The gray dotted curve corresponds to the case of defect in the form of a pure blueshift: only a perturbation of the real part of the potential is taken into account. We observe a reduction of P_2^* which is yet not sufficient to reproduce experimental observation. Its it thus crucial to include an imaginary contribution of the defect in the form of gain.

We explored the interaction of a driven-dissipative gap soliton with defects localized on a single sub-lattice. The pseudo-spin polarization of the soliton tails are responsible for an asymmetric response to the defect: the gap soliton is robust against defects localized on the sub-lattice where its wavefunction vanishes. This is the first demonstration of the robustness of solitons in a topological gap.

Interestingly, experimental results could only be reproduced by taking the non-Hermitian nature of the optical defect into account. The defect not only induces a blueshift but also strongly affects the local effective lifetime of polaritons by providing a gain up to a third of the nominal mode linewidth. It constitutes a powerful resource of the polariton platform for the exploration of non-Hermitian physics.

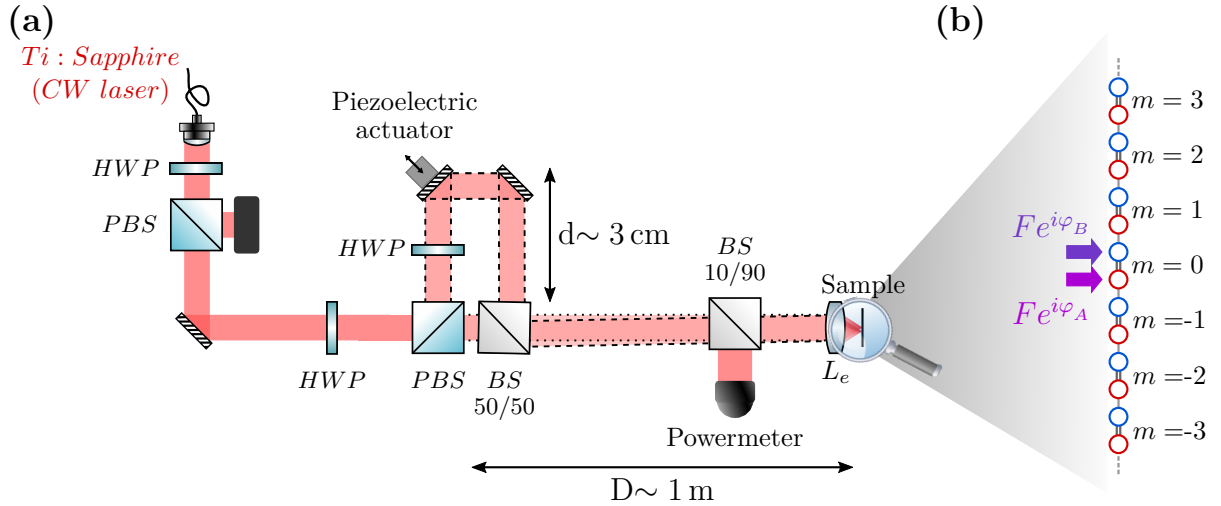


Figure 3.22: **a**, Schematic representation of the excitation path with a delay line allowing to control the phase difference $\Delta\varphi = \varphi_A - \varphi_B$, imposed between the two pump spots as illustrated in **(b)**. **b**, Schematic representation of the lattice with the two quasi-resonant pumps.

3.5 Novel solutions: spin-polarized topological gap solitons

Up to this point, driven-dissipative gap solitons only departed from their conservative counterpart by the presence of bistability. In this section we demonstrate that engineering of the phase of the drive allows to depart from this family of symmetric solutions. We unveil spin-polarized solitons in the bulk of the lattice which are inaccessible in the bulk of conservative systems as these new solutions require to be stabilized by the drive.

3.5.1 Experimental setup

The set of non-linear equations governing the system (3.15) is unchanged but the drive distribution is now written $F_{A,0} = F_0$, $F_{B,0} = F_0 e^{-i\Delta\varphi}$ and $F_{A/B,m} = 0 \forall m \neq 0$. We experimentally consider a two pump excitation scheme where the quasi-resonant beam path is split into two and each of the resulting beams are focused on a different pillar of the same unit cell. The two pumps are thus at the same energy which is tuned to the center of the topological gap ($\Delta E = 0$). The relative phase difference between the two pumps $\Delta\varphi$ is tuned by changing the relative path length between the two optical paths by shifting a mirror mounted on a piezoelectric actuator. The employed delay line scheme is presented in Fig. 3.22: a HWP followed by a polarization beam splitter are used to ensure the amplitude balance between the two beams and a second HWP is used to correct the polarization direction of the delayed beam ².

²In the experimental setup with a delay line, the displacement of the mirror by the piezoelectric actuator lengthens the optical path followed by the reflected beam but also induces a shift of the associated optical axis. However the beams are recombined such that both cross at the center of the entrance pupil of the excitation lens and thus, no displacement of the resulting spot is observed on the sample. The optical axis displacement could at most induce a variation of the transmitted intensity and coupling into the structure but due to the small amplitude of the axis shift ($\sim \mu\text{m}$)

3.5.2 A soliton with spin-polarized core

The cumulative incident power of reference and modulated beams is set to be higher than the second power threshold ($P_{\text{Tot}} \sim 80 \text{ mW} > P_2$), the profile observed for $\Delta\varphi = 0$ thus corresponds to a non-linear domain spreading on three unit cells. We then perform relative phase scan for this fixed input power.

We start from a configuration where the two beams are incident with the same phase on the sample, which is evidenced in reflection by the presence of a bright fringe in between the two pump spots. We then proceed by scanning the phase over a full period. The resulting evolution of the intensity distribution along the lattice is presented in Fig. 3.23 (a). As the phase is scanned towards $\Delta\varphi = 2\pi$, a cascade of abrupt intensity jumps is observed, which is associated to the formation of non-linear domains spreading on a varying number of pillars. Starting from $\Delta\varphi = 0$, we observe successive transitions from three bright dimers all the way to the linear regime as we approach $\Delta\varphi = \pi$. As the phase difference approaches π , the driving field becomes orthogonal to the Bloch modes in the lowest band thus strongly reducing light injection in the lattice. As a result, the total polariton density in the lattice decays from a non-linear regime, with a soliton core spreading on three unit cells $\Delta\varphi = 0$, all the way down to the linear regime for $\Delta\varphi = \pi$.

The phase twist imposed by the two pumps does not only decouple the driving field from the lattice, it is also responsible for a controlled localization of the fluid profile. Remarkably, as the phase difference departs from 0 up to a complete extinction of the soliton, the high-intensity part of the profile tends to localize towards one side of the pumped unit cell: the polariton fluid tends to localize towards the left of the pumped unit cell for $\Delta\varphi < \pi$ and towards its right for $\Delta\varphi > \pi$ and different phase thresholds are observed for the extinction/formation of the bright domains on unit cells $m = 1$ and $m = -1$.

Interestingly, before the reaching the linear regime, the soliton is strikingly found to be localized on a single pillar of the central unit cell: the other pumped pillar experiences destructive interference. This localization of the polariton fluid results in a total non-zero sub-lattice pseudo-spin measured over the intensity pattern. The evolution of the measured total pseudo-spin as well as the result of numerical simulations realized by D. Solnyshkov are shown in Fig. 3.23 (b). The total pseudo-spin clearly departs from $\tilde{S}_{\text{Tot}} = 0$ as the phase difference approaches $\Delta\varphi = \pi$ with a maximum value close to $|\tilde{S}_{\text{Tot}}| = 0.7$. Figure 3.23 (c) presents the intensity profile of the soliton measured for $\Delta\varphi = 1.13\pi$. Interestingly, the fluid distribution is akin to the one of a topological edge state: polaritons are mostly localized on the right single pillar of the pumped unit cell with an exponentially decaying tail on unit cells with $m > 0$, whereas the left pillar of the pumped unit cell undergoes a destructive interference and no signal is observed for unit cells with $m < 0$. As illustrated by the profile in gray, 1D numerical simulations confirm the suppression of intensity on one of the two pillars and the associated exponential tail. Profiles obtained in tight-binding simulations present a spin up to $|\tilde{S}_{\text{Tot}}| \sim 99.9\%$ which is improved when decreasing polariton linewidth.

This localization phenomenon is induced by the phase gradient imposed by the pump: the driving field does not only break the translation invariance of the lattice

these effects are negligible.

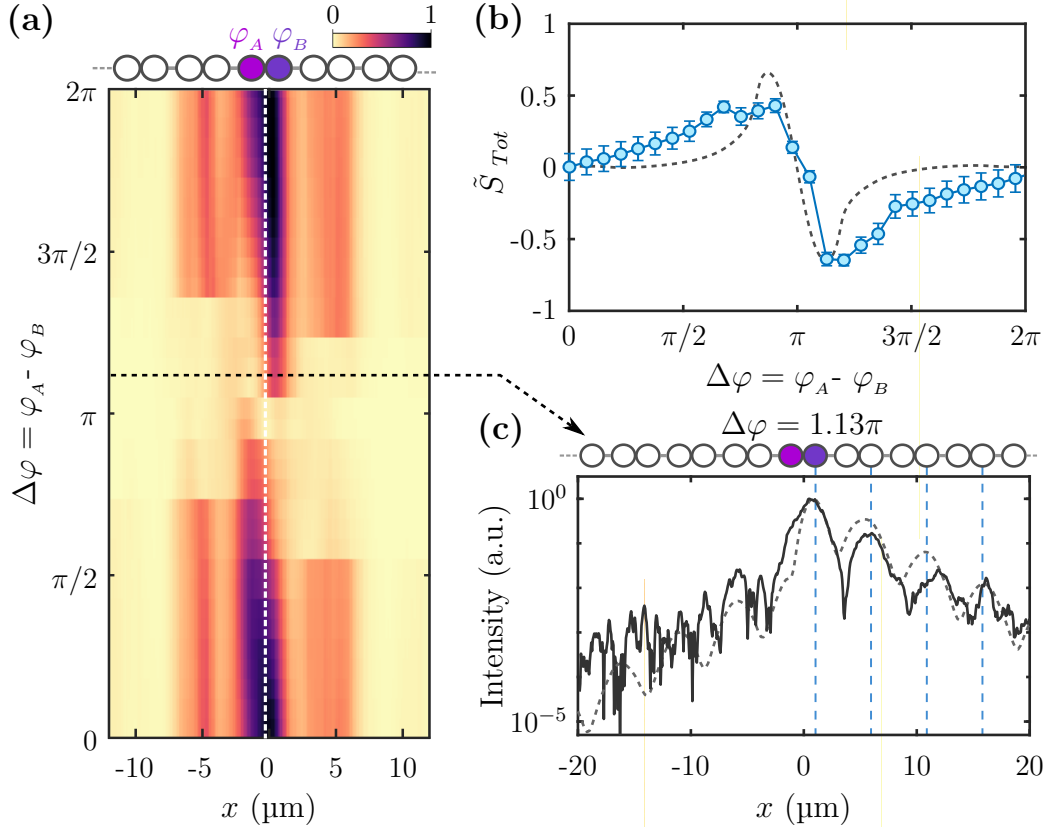


Figure 3.23: **a**, Evolution of the transmitted intensity profile as a function of the phase difference $\Delta\varphi$ imposed between the two pumps. Vertical black line marks the center of the pumped unit cell. Horizontal dashed line presents the position of the profile presented in **(c)**. **b**, Evolution of the sub-lattice pseudo-spin of the polariton fluid as a function of the phase difference. **c**, Intensity profile of the polariton fluid for $\Delta\varphi = 1.13\pi$ (black solid line) as well as the equivalent profile obtained *via* 1D numerical calculations (gray dashed line).

but also induces a flux of polaritons and breaks the inversion symmetry of the system. As a result we observe the formation of solutions which present a given chirality, which is evidenced by the sub-lattice total pseudo-spin of the soliton.

3.5.3 The spin-polarized bulk soliton, a solution stabilized by the drive

Spin-polarized solitons can be observed in conservative systems but their existence is pinned to non-trivial edges of the SSH lattice: they rely on the preexistence of a pseudo-spin polarized edge state. In the present case, we can trigger the formation of a spin-polarized soliton anywhere in the bulk of the lattice as its location is defined by the pump position. Actually, we can show that the possibility to observe spin-polarized solitons in the bulk of the SSH lattice is exclusive to driven-dissipative systems: spin-polarized solitons are not stable in the topological gap of a bulk conservative SSH lattice. We consider the set of equations given by 3.15 in absence of drive and losses ($F = 0$ and $\gamma_0 = 0$):

$\forall m :$

$$i\hbar\partial_t\Psi_{A,m} = -J\Psi_{B,m} - J'\Psi_{B,m-1} + g|\Psi_{A,m}|^2\Psi_{A,m} \quad (3.17)$$

$$i\hbar\partial_t\Psi_{B,m} = -J\Psi_{A,m} - J'\Psi_{A,m+1} + g|\Psi_{B,m}|^2\Psi_{B,m} \quad (3.18)$$

We look for a steady state solution with a maximum localized on the $m = 0$ unit cell, presenting a strong sub-lattice imbalance such that $|\Psi_{B,0}| \gg |\Psi_{A,0}|$ and exhibiting chiral exponentially decaying tails: $\Psi_{A,m} \sim -(J'/J)^m\Psi_{A,0}$, $|\Psi_{B,m}| \approx 0 \forall m < 0$ and $\Psi_{B,m} \sim -(J'/J)^m\Psi_{B,0}$, $|\Psi_{A,m}| \approx 0 \forall m > 0$. Injecting this ansatz in Eq. 3.18 for $m = 0$ directly leads to an inconsistency since it yields $|\Psi_{B,0}| \sim 0$. In absence of an additional ingredient breaking the inversion symmetry, a spin polarized gap soliton with chiral tails cannot exist in the bulk of a conservative SSH lattice.

To evidence this difference, D. Solnyshkov realized time dependent simulations evidencing that such a spin-polarized solution is not stable in the bulk of conservative lattices. The spin-polarized soliton was injected in the presence of drive and dissipation, the drive and losses were then suddenly turned off at a time called $t = 0$. A reference numerical experiment was conducted by applying the same process to a gap soliton with vanishing total spin which is known to be a stable solution in conservative systems. The result of these simulations is presented in Fig. 3.24. Before $t = 0$ the steady state solution is reached for both cases. For $t > 0$, the sudden change of parameters induces a strong perturbation of the system. The symmetric soliton is observed to conserve its localization (see Fig. 3.24 (b)), with a slow oscillation due to the relaxation from the driven-dissipative solution to the conservative one. In the case of the spin-polarized soliton (see Fig. 3.24 (a)), the fluid pattern is shown to rapidly delocalize: the evolution of the intensity profile evidences a diffractive propagation of the polariton fluid.

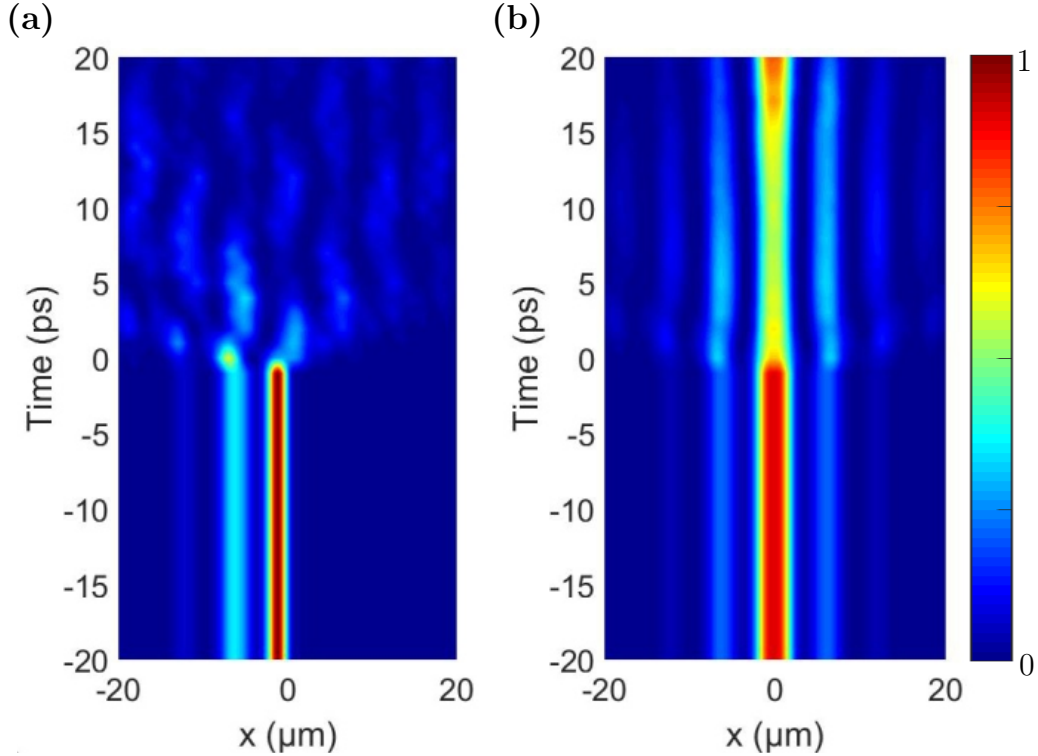


Figure 3.24: **a**, Simulated temporal evolution of a sub-lattice spin polarized soliton as the losses and drive are quenched at $t = 0$. **b**, Simulation equivalent to **(a)** in the case of symmetric soliton.

3.5.4 Bogoliubov spectrum in presence of a spin-polarized soliton

Here we discuss the spin-polarized gap solitons in terms of a non-trivial interface for excitations on top of the non-linear fluid (Bogolons). We propose to consider the renormalization of the potential induced by the presence of the different solitons considered in this work. To first approximation the interaction term can simply be interpreted as a local blueshift affecting pillars where the soliton is located. In this regard, all solutions observed previously locally create potential barriers localized on pillars presenting a high polariton density. An intuitive picture consists in considering that blueshifted pillars are decoupled from the lattice and do not participate to the band structure for the Bogolons: the soliton thus effectively breaks the lattice and creates an interface whose nature is dictated by the wavefunction of the non-linear steady state. Schematic representations of the different situations discussed in this chapter are presented in Fig. 3.25 (a), in each case we display the effective winding number of the resulting lattices based on the termination of the considered lattice. Interestingly, in the case of a spin-polarized soliton generated in the bulk of the lattice, the chain connected to the pumped pillar experiencing destructive interferences is terminated by a weak link and thus presents a winding of $w = 1$. The spin-polarized soliton creates a non-trivial interface which should host an edge state localized in the energy gap.

In our driven-dissipative platform, bringing a localized state at the center of the energy gap simply requires to drive the system with $\Delta E > 0$ and to increase the local polariton density *via* the input power. As illustrated in Sec. 3.3.2, a jump towards

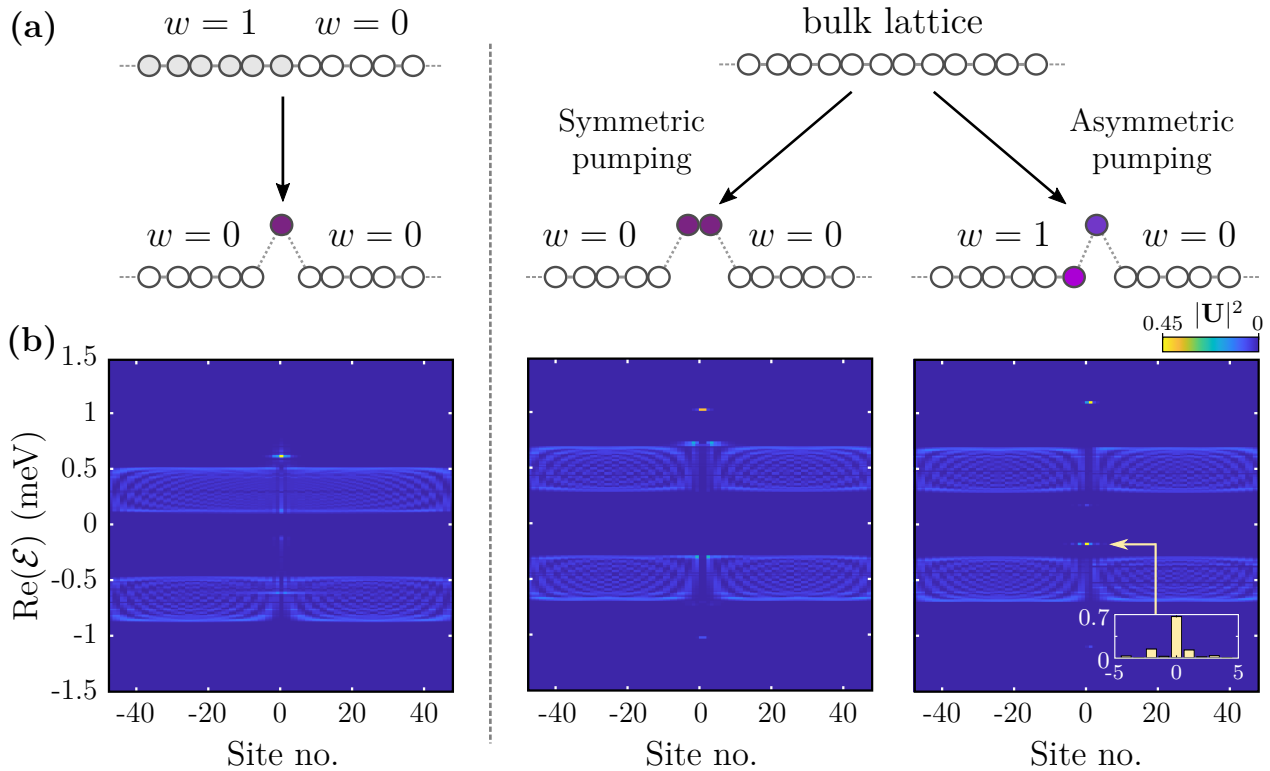


Figure 3.25: **a**, Top: Schematic description of the considered SSH lattice in the linear regime with a topological interface (left) and the bulk of the chain (right). Bottom: Schematic representation of the same lattices in presence of a non-linear fluid of polariton taking the form of a spin polarized soliton at an interface (left), a symmetric soliton in the bulk (middle) and a spin-polarized soliton in the bulk (right). **b**, Bogoliubov spectra resolved in position associated to the different situations described in **(a)**. In each case the energy zero corresponds to the energy of the pump E_p . The bulk spin-polarized soliton (right panel) corresponds to $\Delta\varphi = 1.13\pi$. A zoom of the localized state observed in the gap is presented in inset.

an upper bistability branch occurs when a blueshifted state comes to resonance with the pump energy. Pumping the system at $\Delta E > 0$, the blueshifted state will cross the $E = 0$ line. At this point the corresponding Bogoliubov state would present exponentially decaying tails with a clear sub-lattice polarization. However, one has to be careful when classifying states localized in the SSH topological gap in presence of a dense polariton fluid. Indeed, the definition of the winding number, and thus the topological nature of a localized gap state, requires the lattice sites to present no onsite energy (see Sec. 3.1.4). Consequently, one has to check, *a posteriori*, that the mid-gap state is localized on a pillar showing vanishing polariton density.

To confirm the model discussed above, we computed the spectrum of excitations on top of each type of solitons using the Bogoliubov method in a tight-binding context, as introduced in Chap. 2.3.3. The calculated spectra are presented in Fig. 3.25 (b). Away from the pumped region, solitons present a negligible amplitude and the excitation spectra correspond to the linear bands of the SSH model. Remarkably, in the case of the bulk spin-polarized soliton, a localized state is observed in the gap of the excitation spectrum. This state is mostly localized on the pumped pillar presenting a vanishing amplitude (labeled as pillar 0), the local polariton den-

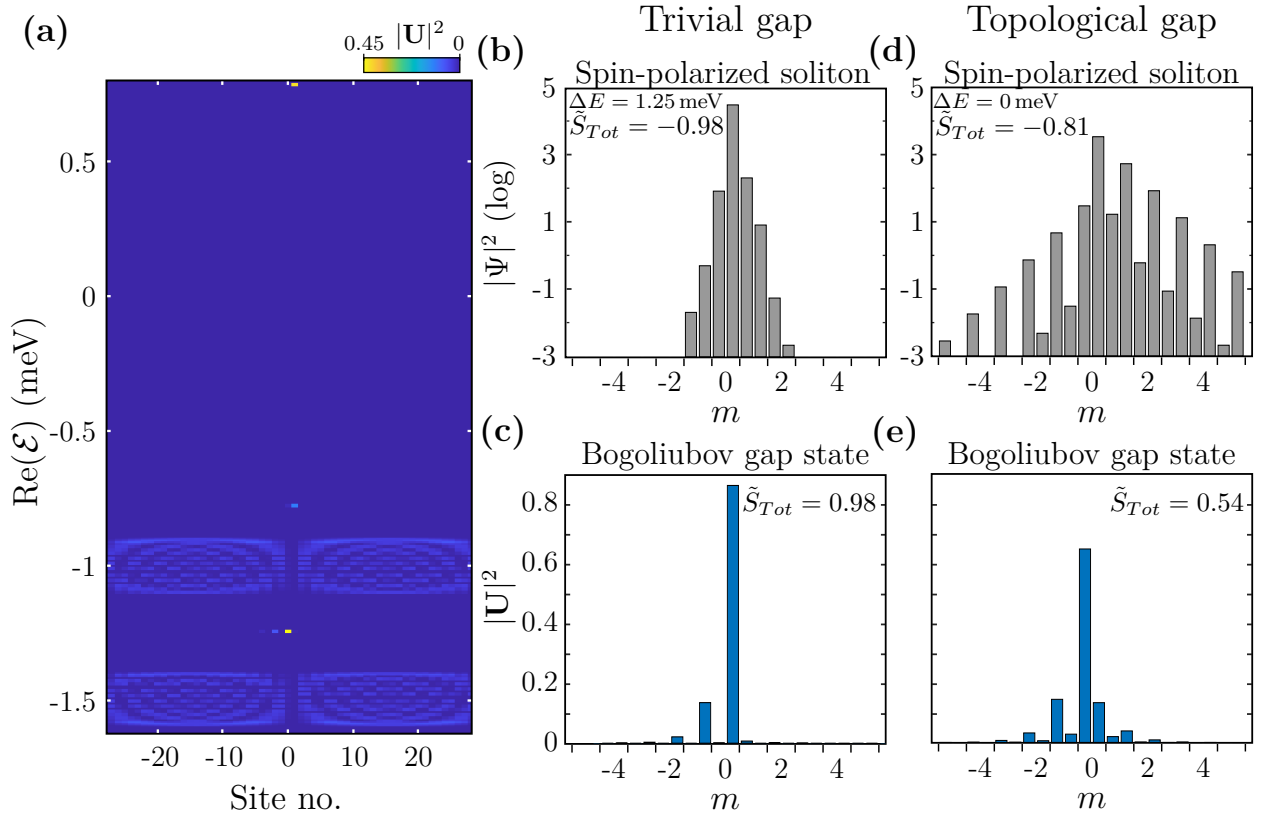


Figure 3.26: **a**, Bogoliubov spectrum calculated in presence of a spin-polarized gap soliton injected in the upper gap of the SSH model for $\Delta E = 1.25$ meV and $\Delta\varphi \approx 1.45\pi$. **b**, Profile of the gap soliton considered for the calculation of the spectrum presented in **(a)**. **c**, Profile of the localized state appearing in the topological gap of the excitation presented in **(a)**. **d-e**, Corresponding profiles of the spin-polarized soliton and localized state considered in the calculation of the Bogoliubov spectrum presented in Fig. 3.25 (b) for $\Delta E = 0$ meV and $\Delta\varphi = 1.13\pi$

sity induces a blueshift $g|\Psi_{A,0}|^2 = 4.2 \mu\text{eV}$ which is negligible compared to all energy scales of the system. Moreover, since it is localized inside the topological energy gap, it presents exponential tails with a sub-lattice localization. In the two other cases presented here, no states are observed in the energy gap of the excitation spectrum, which is in agreement with the previous analysis yielding winding numbers $w = 0$ for all effective lattices. In all cases, a significant decrease of the wavefunctions of blueshifted pillars is observed at the energy of the lower band, confirming that the presence of a dense polariton fluid tends to decouple these pillars from the rest of the lattice.

The generation of a bulk spin-polarized soliton presenting a wavefunction akin to the one of a topological edge state is accompanied with the appearance of a localized state in the gap of the excitation spectrum which also exhibit features reminiscent of a topological edge state. However, one has to note some discrepancies with respect to the case of a linear SSH edge state at an interface with vacuum. The localized state, appearing *via* the generation of a spin polarized soliton, presents a non negligible amplitude on the other side of the interface and does not lie at the center of the energy gap. These differences originate from the finite amplitude of the polariton density on the bright pillar. In the present case the pillar 1 is brought to an energy which presents a detuning comparable to the bands amplitude. The

associated localized state can be seen around $E \approx 1.1$ meV on the spectrum presented in the rightmost panel of Fig. 3.25 (b). As the blueshifted state possesses an energy detuning which is not significantly greater than the band amplitude (given by the coupling strength J'), the pillar 1 remains slightly coupled to the bands. This phenomenon is similar to the decrease of the spin-polarization and slope of the soliton tails observed in Sec. 3.3.5 when the drive energy was brought to resonance with "s" bands. As a consequence, the wavefunction of the mode localized on pillar 1 spreads over several pillars on both sides of the interface. Conversely, this means that other eigenstates of the spectrum present a non vanishing amplitude on this pillar: the pillar is still hybridized to the rest of the lattice and especially to the pillar 0. A perfect correspondence between the state localized on pillar 0 and a topological edge state could be obtained in case of sufficient number of polaritons localized on pillar 1, the pillar 1 would in this case be completely decoupled from the rest of the lattice.

A quick analysis of the set of equations 3.15 leads to conclude that reaching a steady state with $g|\Psi_{B,0}|^2 \gg \{J, J'\}$ and $|\Psi_{A,0}| \sim 0$ requires to consider a energy detuning $\Delta E \gg \{J, J'\}$. One simple way to obtain a dense spin-polarized soliton thus consists in increasing the energy at which this soliton is injected: the polariton density required to generate the soliton will increase accordingly. This imposes to inject polariton in the upper trivial gap of the model. To confirm these quick calculations, we realized tight-binding simulations aiming at generating a spin-polarized soliton in the upper gap of the SSH model: we performed power ramps for various energy detuning of the pump and relative phase difference $\Delta\varphi$. This procedure allowed us to observe spin-polarized solitons in the upper gap of the model and to optimize the extinction of one pumped pillar while increasing the polariton density on the second one. The most promising results are summarized in Fig. 3.26.

Injecting polaritons at an energy $\Delta E = 1.25$ meV and for $\Delta\varphi \approx -\pi/2$, we observed the formation of a spin polarized soliton whose profile is presented in Fig. 3.26 (b) and yields a total pseudo-spin $\tilde{S} = -0.98$. Computing the excitation spectrum on top of this non-linear steady state, we obtained the image displayed in Fig. 3.26 (a). In these driving conditions, the blueshifted pillar is brought to an energy $E - E_p = 0.78$ meV, which corresponds to a detuning $\Delta E = 2.03$ meV $\sim 10J$ with respect to the center of the gap. The blueshifted pillar can here be considered as decoupled from the lattice. As a result, a localized state presenting the distribution of a topological edge state is observed at the exact center of the topological gap ($g|\Psi_{A,0}|^2 = 3.7$ μ eV ≈ 0). The profile of this state is shown in Fig. 3.26 (c). The computation of the total pseudo-spin yields $\tilde{S}_{\text{Tot}} = 0.98$, which is very close to the value obtained for a topological edge state ($\tilde{S}_{\text{Tot}} = 1$). The profiles of the soliton and gap state obtained in the case considered in Fig. 3.25 are provided for comparison (see Fig. 3.26 (d-e)). In this case, the computation of the pseudo-spin of the state localized in the topological gap yields $\tilde{S}_{\text{Tot}} = 0.54$. Compared to the soliton with chiral tails, the soliton generated in the trivial gap presents a much higher density on pillar 1 and steeper exponential tails. As predicted, it results in a significant increase of the pseudo-spin of the Bogoliubov mid-gap state.

These results allow us to draw a clear distinction between the different characteristics considered here for solitons. The tail pseudo-spin, which endows solitons and topological edge-states with robustness properties against defects, originates from







the chiral symmetry and is a feature specific to the topological gap. On the contrary, the spin polarization of the soliton core originates from a destructive interference mechanism within the pumped sites. This driven-dissipative phenomenon can even be triggered in the upper trivial gap of the model and leads to the generation of a non-trivial interface for Bogolons.

Due to the driven-dissipative character of the polariton platform, the engineering of the driving field allows to impose frustration to the non-linear fluid. We here demonstrated the generation of a soliton with spin-polarized core in the bulk of the SSH lattice, which is unstable in conservative systems.

Interestingly, we showed that the presence of such soliton induces a non-trivial interface which hosts a spin-polarized localized state inside the topological gap of the excitation spectrum. We showed that to observe an interface state localized at the center of the gap, the blueshift induced by the soliton has to be significantly greater than the coupling strength J . A better agreement between the Bogoliubov state and a topological edge state is obtained by injecting a spin-polarized soliton in the upper trivial gap of the lattice.

A summary of the results presented in this chapter can be found in the chart below:

Gap solitons in a driven-dissipative SSH lattice

	Topological gap	Trivial gap
Spin-polarized tails		
Spin-polarized core	 Possible Max for $\Delta\varphi \approx \pi$	 Possible Max for $\Delta\varphi \approx \pm\pi/2$
Topological state in the Bogoliubov spectrum	 Possible not centered	

3.6 Perspectives

3.6.0.1 Summary

In this chapter we explored the solitonic solutions in the topological gap of the SSH model. We observed the formation of solitons presenting particular sub-lattice spin textures located at a topological interface of the model but also in the bulk of the lattice. Leveraging on the versatility of polariton micro-cavities, we showed that this sub-lattice localization of the soliton tails leads to robustness properties against non-Hermitian defects localized on a given sub-lattice. Finally we demonstrated that, by engineering the external driving field, it is possible to trigger the formation of new solutions presenting a non-zero sub-lattice pseudo-spin in the bulk of the lattice. These solutions were shown to be exclusive of open system as they required to be stabilized by an external drive. Interestingly, the novel solitonic solutions we discovered act as nontrivial interfaces for the Bogolons. We demonstrate that the engineering of the driving field can be used to modify the topology of the Bogoliubov spectrum.

3.6.0.2 Non-linear interfaces and the excitation spectrum

These latter results are an ongoing work and we plan to realize pump-probe experiments aiming at measuring the Bogoliubov spectrum in a polariton SSH lattice to directly evidence the appearance of spin-polarized states localized at interfaces induced by the formation of gap soliton.

This work opens the door to the exploration of the driven-dissipative topology in more complex geometries. The case of the SSH model is not a general example as a complete restructuring of the bulk of the lattice is not necessary to induce a phase transition: simply removing an edge pillar allows transitioning between the two possible phase of the model. As proposed by Bardyn et al. in Ref. [8], the next step could consist in the observation of a topological phase transition with a 2D lattice.

3.6.0.3 Probing interactions between topological solitons

Another thread to pull is the exploration of the interaction between solitons presenting sub-lattice spin polarized tails. As we showed in this chapter, those solitons are not affected by defects localized on the sub-lattice where they show a vanishing amplitude. Interestingly, one can remark that two spin-polarized solitons approaching each other would present opposed sub-lattice localization as the left soliton would be localized on the B sub-lattice while the right soliton would present a significant density on the A sub-lattice only. One can thus expect those solitons to behave differently than solitons exhibiting unpolarized exponential tails. The exploration of the consequences of the chiral symmetry on the interaction between gap solitons is the subject of the next chapter.

Chapter 4

Interaction between gap solitons on a driven-dissipative SSH lattice

In this fourth chapter we address the importance of the chiral symmetry to understand the interaction between two driven-dissipative solitons generated in the topological gap of the SSH model. As evidenced in the previous chapter, the chiral symmetry of the SSH model endows the solitons generated in the topological gap of the lattice with a chiral profile. Both exponential tails of those non-linear stable solutions indeed present sub-lattice localization with opposite chirality. Two distinct solitons would therefore necessarily approach each other by overlapping exponential tails with an opposed chirality. The tails chirality was shown to be of crucial importance for the description of the interaction between a soliton and a defect and one can thus expect it to affect the interaction between two solitons. We will start by a general description of the interaction between solitons and especially study the case of Kerr solitons on a conservative lattice. In this situation the phase profile of the soliton, which is related to the underlying band structure, will be shown to have strong consequences on the behavior of two interacting solitons. We will then study this problem in the context of a driven-dissipative SSH lattice. We first show a parallel between the case of open and closed systems where no clear impact of the chiral symmetry is observed. Interestingly, we unveil the existence of a symmetry breaking in the power dependent formation of solitons. Taking advantage of the dissipative nature of the system and of our ability to engineer the drive, we demonstrate a novel counter-intuitive effect of phase multi-stability in the vicinity of this broken symmetry phase. The chirality of the system response will be shown to depend on the helicity of the drive protocol (clockwise or counterclockwise phase scan): we thus call it “Helical bistability”.

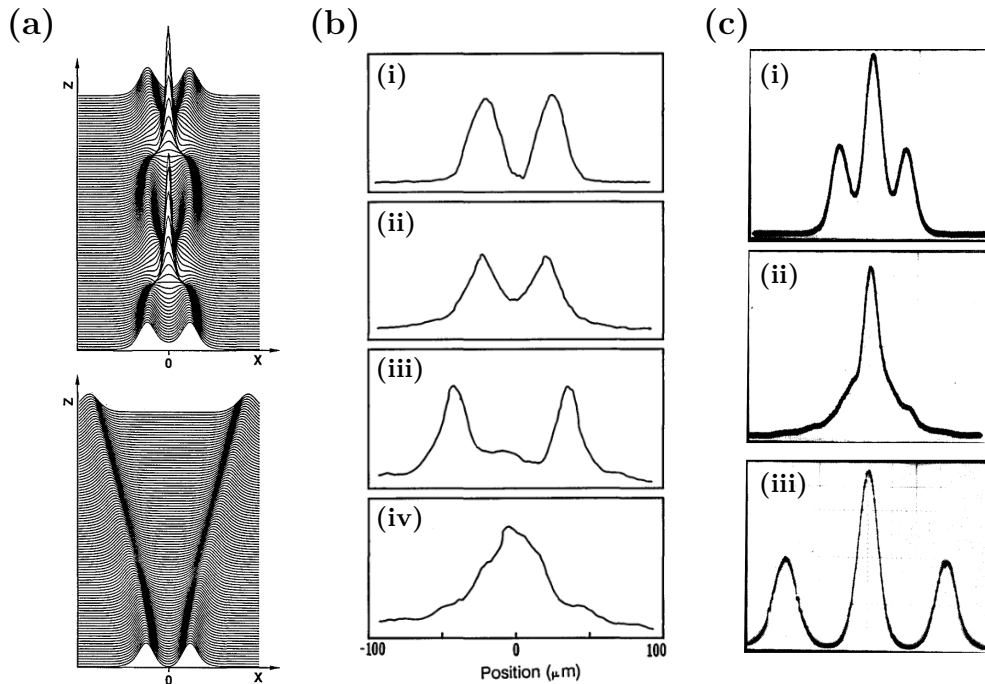


Figure 4.1: **a**, Numerical simulations showing the intensity profiles resulting from the interaction between two spatial solitons as they propagate along the z direction of a waveguide. Top and bottom panels respectively correspond to an in-phase and anti-phase relation between solitons. **b**, Experimental measurement of the interaction between two spatial solitons in a waveguide given by the spatial distribution of light at (i) the waveguide input, (ii) the output of the waveguide in the case where no temporal overlap is realized between the soliton and (iii-iv) the waveguide output in case of, respectively, an anti-phase and in-phase relation between solitons. **c**, Auto-correlation traces of temporal solitons injected in an optical fiber with the auto-correlation of: (i) the input signal constituted of two light pulses and (ii-iii) the output signal in the case of, respectively, in-phase and anti-phase light pulses. Images adapted from [339] and [340].

4.1 Introduction

4.1.1 General overview

The question of the interaction between solitons is a vast research field that has widely and actively been explored for more than three decades. Restricting ourselves to optics, the exploration of the interaction between solitons unveiled an incredible diversity of phenomena such as energy transfer between collisional partners, fusion, splitting and annihilation of solitons [335, 336], or soliton explosions [337, 338].

A generality of the phase dependence of the interaction between two solitons has been evidenced, which had early been predicted for solitons of the sine-Gordon and cubic non-linear Schrödinger equations [341–343]: the relative phase between solitons controls the sign of the short range force applied by a soliton on another one. Experimental demonstrations of the control of soliton-soliton interactions were realized for temporal [340] and spatial [339, 344] solitons respectively using optical fibers, cells containing carbon disulfide and planar waveguides. All these realizations confirmed the theoretically predicted behavior: two in-phase neighboring solitons

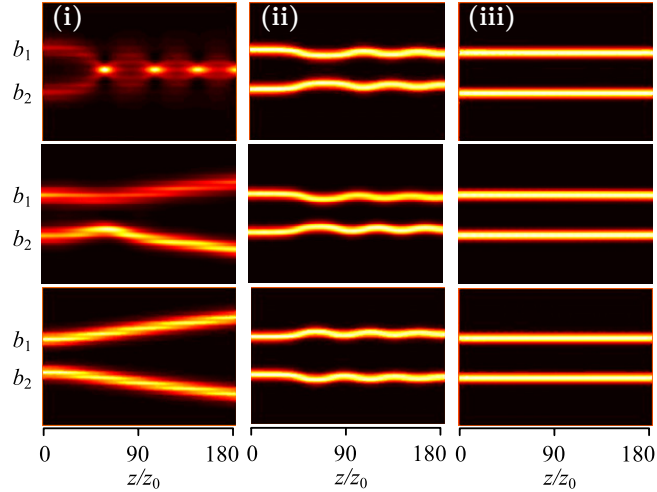


Figure 4.2: Numerical simulations of interaction between two spatial solitons on a photonic lattice. Top, middle and bottom panels respectively correspond to a phase difference of 0 , $\pi/4$ and π between the solitons. The different columns present the evolution observed for a growing optical power of the pump beam b_1 and b_2 .

attract each other while a repulsive interaction is observed between solitons in phase opposition. Additionally, the strength of the interaction decreases with the distance between the two objects. These results are illustrated in Fig. 4.1. This interaction of two solitons can be guessed from the overlap between tails of the two objects: two solitons in phase opposition exhibit destructive interference between their decaying tails which disfavors a merging of the two objects while the opposite effect occurs for in-phase solitons.

This description is yet only valid for solitons in an homogeneous landscape and the presence of an additional potential changes the soliton profile and may results in a modification of the interaction between two solitons.

4.1.2 Interaction between gap solitons on a lattice: role of the band symmetry

The question of the interaction between solitons on lattices has stimulated a lot of interest for the last two decades with, for example, the stabilization and interaction of soliton trains [345–347]. A plethora of works report on the study of the interaction between two elementary solitons either on lattices of homogeneously coupled waveguides [348–350] and optically induced sinusoidal potentials [351–354] or in modulated lattices [355]. These realizations confirmed the phase dependence of the interaction between solitons and some of them demonstrated a self-localization mechanism for high optical powers with an oscillatory behavior in the intermediate power range (an example of such behavior is illustrated in Fig. 4.2).

Interestingly, a deviation from this paradigmatic behavior was observed by Liu et al. in Ref. [352]: two solitons were shown to attract each other when generated in phase opposition. In this work, the authors realized an optically induced sinusoidal lattice using a photo-refractive crystal. In this configuration the light experiences an alternatively low and high refractive index as it propagates along the lattice, represented by light and dark regions on Fig. 4.3 (a). A band gap is observed in

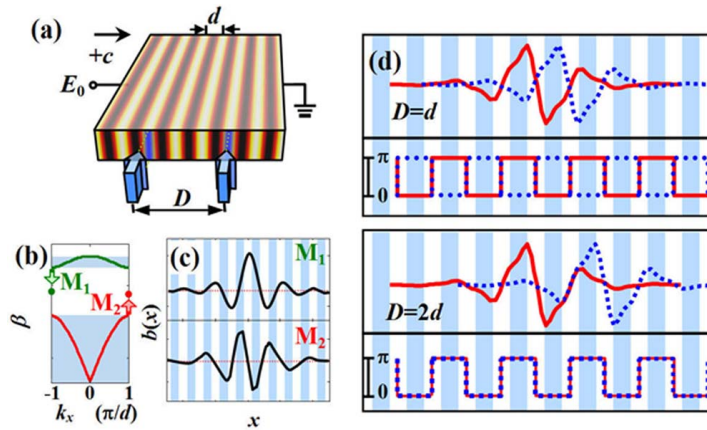


Figure 4.3: **a**, Schematic representation of the photonic lattice. **b**, Calculated band structure of the lattice. **c**, Calculated profile of symmetric and anti-symmetric solitons respectively bifurcating from the upper and lower band of panel (a). Dark arrows were added to highlight the interfaces where the soliton tails amplitude vanishes. **d**, Superimposed amplitude and phase profiles of two in-phase anti-symmetric solitons with a center to center distance of, respectively, one and two unit cells length d for top and bottom panels. Images taken from [352].

the energy spectrum of the structure (Fig. 4.3 (b)) and the authors studied the interaction between two solitons generated in its center. Note that in the present case the authors can play with the sign of the interaction term, light experiencing either a self-focusing or self-defocusing non-linearity. Consequently, they can trigger the formation of two types of solitons with either a symmetric or anti-symmetric profile as illustrated in Fig. 4.3 (c).

In this work the crucial ingredient resides in the staggered phase profile of the soliton: as it bifurcates from states formed at the edge of the Brillouin zone (see Fig. 4.3 (b)), the amplitude of the soliton wavefunction switches sign from one unit cell to the next one. Two solitons injected by in-phase pulses can thus effectively be in-phase or in anti-phase depending on the relative distance between their centers, this dependence is illustrated in Fig. 4.3 (d). The top panel of Fig. 4.3 (d) illustrates two solitons injected in phase on two neighboring unit cells ($D = d$): in each unit cell of the lattice, their wavefunctions are found to be in phase opposition. On the contrary, the soliton wavefunctions are found to be in phase if these two solitons are injected on disjoint unit cells separated by one unit cell ($D = 2d$), which is shown in the bottom panel of Fig. 4.3 (d). As a result, one can expect the interaction between solitons to depend on the phase difference $\Delta\varphi$ and distance D between the two injected beams. Numerical simulations carried by Liu et al., in Ref. [352], confirmed this analysis showing that, for a given phase difference, the attractive and repulsive nature of the interaction depends on the parity of the number of unit cells separating the two beams. These numerical results are summarized in Fig. 4.4. The authors experimentally confirmed these numerical results by observing the trajectories of two in-phase solitons for distance $D = d, 2d, 3d$ and $4d$ which revealed an alternatively repulsive or attractive nature of the interaction between the non-linear objects.

This work demonstrates the crucial importance of the soliton phase profile on the way two of those non-linear objects will interact. The profile of the soliton being

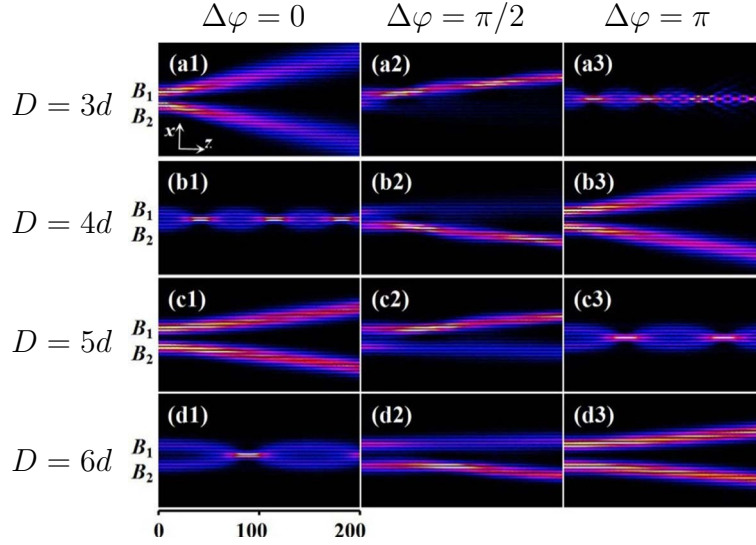


Figure 4.4: Simulated trajectories of two interacting solitons initially separated by $D = 3d$, $4d$, $5d$ and $6d$ for, respectively, (a-d). Each column corresponds to a given value of the input phase difference with $\Delta\varphi = 0$, $\pi/2$ and π for the first, second and third columns. Images taken from [352].

strongly correlated to the one of the state from which it bifurcates, it clearly appears that engineering of the lattice band structure provides one with the ability to tailor the effective interaction between solitons.

In the present chapter we will show how the Chiral symmetry of the SSH model strongly influences the interaction between two gap solitons.

4.2 A symmetry breaking revealed in the interaction phase diagram

In the driven-dissipative framework of our study, gap solitons cannot freely propagate on the lattice: they are pinned to the vicinity of the pump and, consequently, the study of the interaction between solitons cannot be done by looking at their propagation versus time. However, as demonstrated in the previous chapter, the nature of the interaction of a soliton with another object can be inferred from the spatial growth of the soliton as the pump power is ramped up. A first approach we employed here thus consist in probing the formation of non-linear domains as a function of the driving field distribution: we used two pump spots and varied their relative distance. Doing so we unveiled the existence of a symmetry breaking occurring for a phase difference of $\Delta\varphi = 0$ or $\Delta\varphi = \pi$ depending on the distance between pump spots.

4.2.1 Phase frustration in the solitons tails

To start our study of the interaction between gap solitons *via* chiral tails, we used the same experimental setup as described in Chap. 3.5 and performed power ramps for the two paradigmatic values of the phase difference ($\Delta\varphi = 0$ and $\Delta\varphi = \pi$) and various distances between pump beams: the pump spots were focused at the center

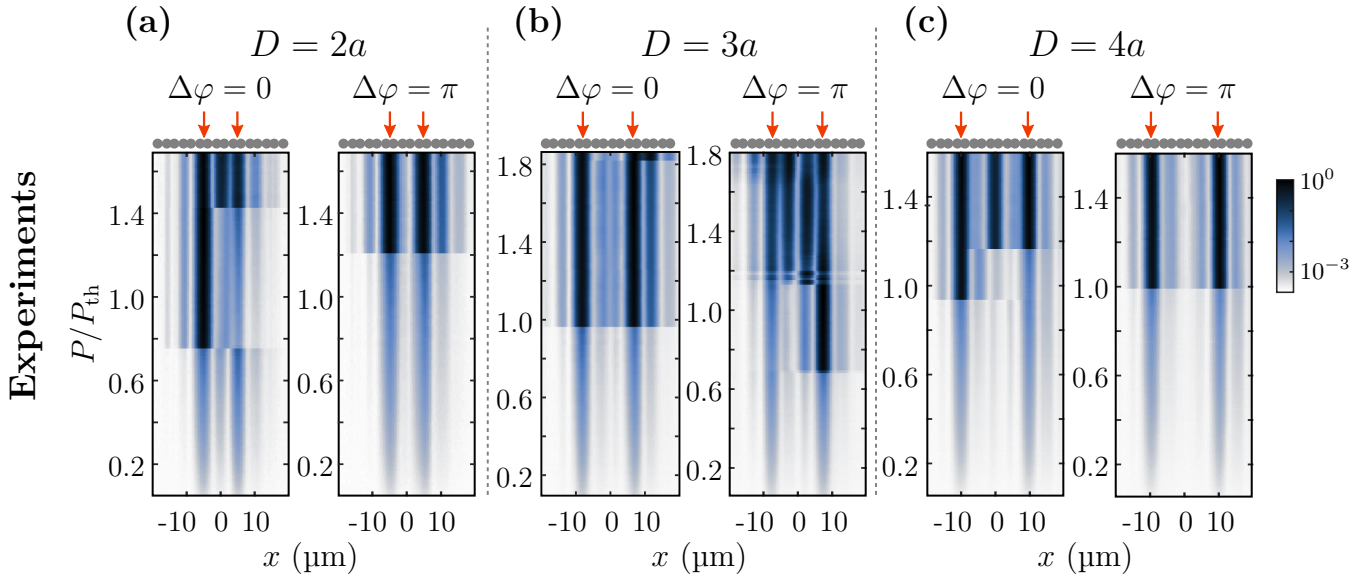


Figure 4.5: Evolution of the intensity profile in two pumps experiments as a function of the total pump power. We here displayed the intensity normalized to its maximum in logarithmic scale. Vertical axes are normalized to the power threshold for the formation of independent solitons. **(a-c)** respectively correspond to $D = 2a$, $3a$ and $4a$. In each case the left sub-panel corresponds to a phase difference of $\Delta\varphi = 0$, whereas the right one corresponds to $\Delta\varphi = \pi$. A scheme of the lattice and excitation setup is depicted on top of each image.

of two distinct dimers ($D = 2a, 3a, 4a$). Note that when exciting a single dimer, the threshold P_1 is found to be subject to fluctuations on the order of $\Delta P_1 \sim 1$ mW. This phenomenon is due to a local disorder of the onsite energy on the order of a fraction of the polariton linewidth ($\Delta E_0 \sim 10$ μ eV). To compensate for these fluctuations, a slight power imbalance is introduced between the two arms of the excitation setup such that the incident power is normalized to the non-linear threshold of each dimer. In the two pump experiments, P/P_{th} is the same for both pumped dimers. In the following, the two arms of the excitation setup will be called “arm-L” and “arm-R” for the reference and delayed path respectively. In all representations, the pumped dimer displayed on the left (right) will always correspond to the one pumped by the beam passing through arm-L (arm-R).

The results of the two pumps experiments are summarized in Fig. 4.5. In these images, the solitons appear as dark blue regions and their spin-polarized tails can be observed on the left and right of each panel. One can observe that the system response strongly depends on the relative distance D and relative phase $\Delta\varphi$ between the two pumps. Especially, one can notice that the formation of solitons occurs either simultaneously at both pumps positions (see Fig. 4.5 (a) for $\Delta\varphi = \pi$) or in only one of the two pumped dimers for $P < P_{\text{th}}$, a second soliton being formed at the other pump position for $P > P_{\text{th}}$ (see Fig. 4.5 (a) for $\Delta\varphi = 0$). This phenomenon will be discussed in the next section.

Let us first focus on the intensity distributions obtained for high pump power. In all cases, a bright soliton is observed under each of the pump spots and, for each value of the distance D , two different configurations are noticeable: the region in between the two pumps either presents a weak intensity or contains one or more

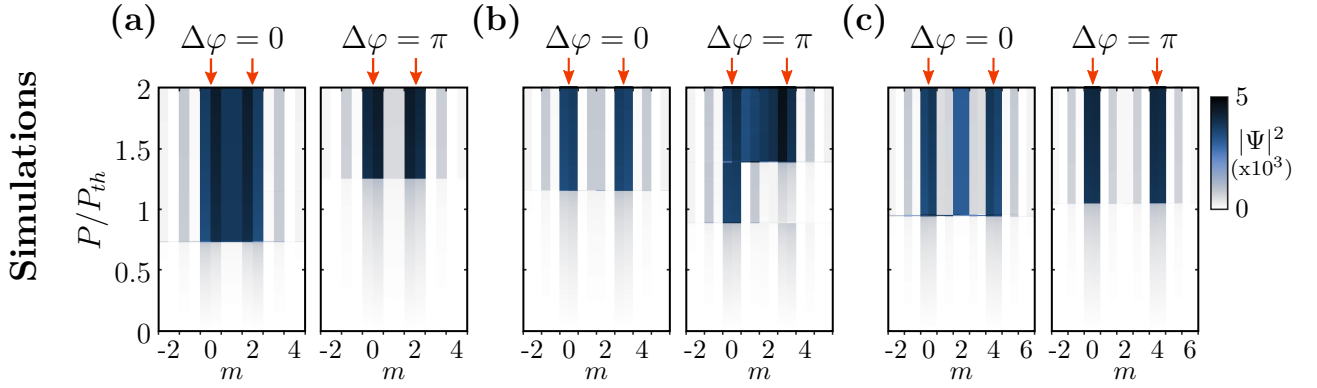


Figure 4.6: **a-c**, Simulated evolution of the intensity profile in two pumps experiments as a function of the total pump power. Vertical axis are normalized to the power threshold for the formation of independent solitons. **(a-c)** respectively correspond to $D = 2a$, $3a$ and $4a$. In each case the left sub-panel corresponds to a phase difference of $\Delta\varphi = 0$, whereas the right one corresponds to $\Delta\varphi = \pi$.

solitons. Solitons are observed in the central region for $\Delta\varphi = 0$ in the cases $D = 2a$ and $D = 4a$, and for $\Delta\varphi = \pi$ in the case $D = 3a$. A weak intensity is measured in the complementary cases. The interaction between two solitons seems to depend on the phase difference between the two injection pumps and on the parity of D/a . These trends are well reproduced by numerical simulations in a tight-binding framework¹, as shown in Fig. 4.6 (a-c).

A parallel can be drawn with the results obtained for conservative systems: distributions presenting additional solitons in between the two pumps are a driven-dissipative counterpart of attractive trajectories observed in absence of dissipation (fig. 4.4), whereas repulsive trajectories are replaced by distribution showing a weak central intensity originating from a phase frustration between solitons. However, this parallel works only in a certain limit: the two solitons considered in our experiments do not strictly interfere as it was the case in Ref. [352]. Indeed, the solitons considered here present opposite sub-lattice spin-polarization and thus almost no spatial overlap. To understand this merging or frustration between the two solitons, one needs to pay attention to the phase profile of a soliton and the resulting overlap with eigenstates of the lower s band. As described in the previous chapter, the exponential tails of a state localized in the center of the topological gap are localized on one sub-lattice s with the recurrence relation $\Psi_{s,m} = (-J'/J)^m \Psi_{s,0}$. The same equation applies to the solitons tails as the polariton density is weak enough to consider $g|\Psi_{A/B,m}|^2 \sim 0, \forall m \neq 0$. In the context of our polaritonic emulation of the SSH lattice, the two coupling constants J and J' are real positive quantities and the phase of the soliton tails (ϕ) thus alternates from a unit cell to the next one (see schematic representation in Fig. 4.7 (a)). As a consequence, two solitons injected with a phase difference $\Delta\varphi = 0$ can locally (inside a unit cell) be in-phase or in anti-phase depending on the relative distance between the two pump spots, as pictured in Fig. 4.7 (b-c). When the two pumps present the same phase on a given unit cell, the resulting field spectrally couples to the lower s band with a bonding profile. As

¹Note that we here simply aimed at confirming the distance and phase relation to the field profile at high power. Exactly reproducing the evolution of the profiles measured experimentally would require a fine tuning of the simulation parameters which is beyond what we intend to discuss here.

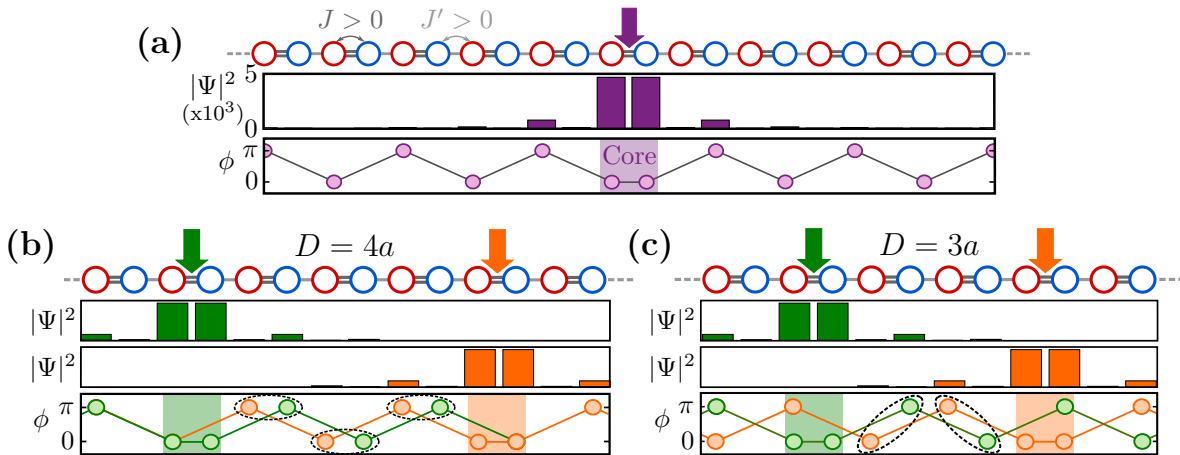


Figure 4.7: **a**, Density (top) and phase (bottom) profiles of a gap soliton in the SSH model with $J > 0$ and $J' > 0$. Data points of the phase profile are displayed only where the soliton presents a significant density. **b-c**, Schematic representation of the overlap between two solitons for $\Delta\varphi = 0$. Bottom panels show the superposition of solitons phase profiles for **(b)**: $D = 4a$ and **(c)**: $D = 3a$. Black dotted ellipses evidence each unit cell of the central region. Density profiles of each soliton are presented on top in green and orange bar histograms.

the power is ramped up, the non-linear term induces a blueshift of the bands which favors the injection of particles in the system as the lower band gets closer to the drive energy. On the contrary, two solitons presenting an opposed phase profile on each unit cell couples to the upper s band which has an anti-bonding profile. As the power is ramped up, the blueshift of the bands tends to decouple the driving field from the band as upper-band modes are pushed away from the pump energy.

To confirm the importance of the lower band symmetry in the interaction between solitons, we performed numerical simulations considering negative hopping constants which enable us to tune the phase profile of the lower band mode and thus the one of the soliton. The results of these calculations are presented in Fig. 4.8 (a-e) for $J > 0$ and $J' < 0$ and in Fig. 4.8 (f-j) for $J < 0$ and $J' > 0$. In each case, we display the calculated band structure with the real space profile of eigenstates at the top and bottom of each sub-band. We present the profile of the soliton obtained in the corresponding topological gap as well as evolution of the density profile of two of these solitons as a function of the power for different relative phases and distances between pumps ($D = 2a, 3a$ and $4a$ from left to right panels).

Firstly, let us consider the case $J > 0$ and $J' < 0$: the obtained lower band results from the hybridization of bonding dimer states as $J > 0$ but due to the negative amplitude of J' , the energy distribution of hybridized modes is reversed. The lowest and highest energy state of the band respectively results from the anti-symmetric and symmetric hybridization of dimerized states, these two characteristic eigenstates are depicted in Fig. 4.8 (a). The soliton bifurcating from the top of the band, it presents a density profile equivalent to the one previously studied and the soliton wavefunction thus only differs in its phase profile. The phase of the soliton tails does not flip from one unit cell to the next one (see Fig. 4.8 (b)). Consequently, two solitons injected with $\Delta\varphi = 0$ remain in-phase no matter their relative distance: their interaction thus does not depends on D/a as observed in Fig. 4.8 (c-e): the

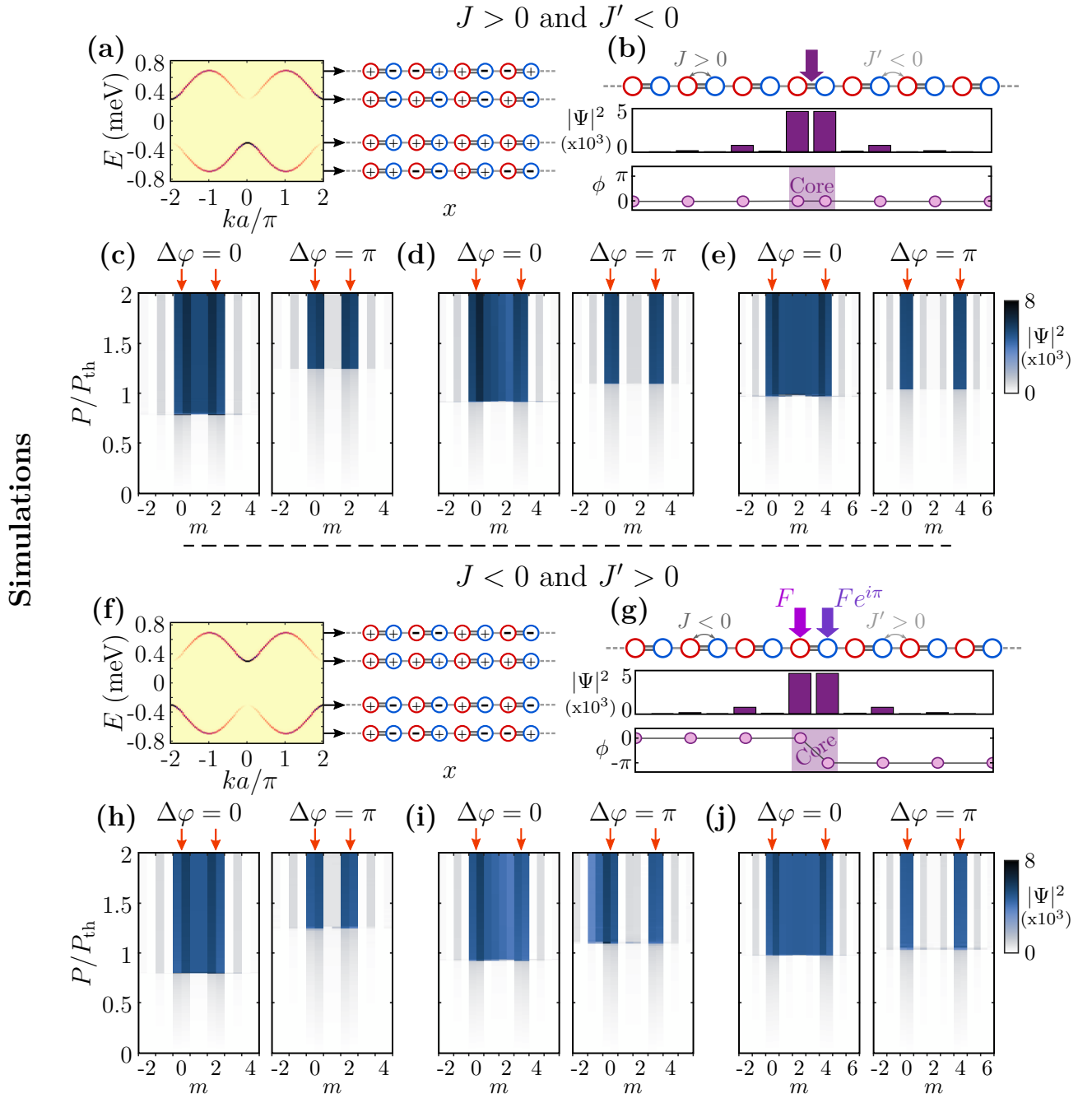


Figure 4.8: **a**, Calculated dispersion of the SSH lattice for $J > 0$ and $J' < 0$. Phase profiles of the characteristic eigenstates at the top and bottom of each energy sub-bands are presented on the right. **b**, Density (top) and phase (bottom) profiles of a gap soliton in the SSH model with $J > 0$ and $J' < 0$. Data points of the phase profile are displayed only where the soliton presents a significant density. **c-e**, Simulated evolution of the intensity profile in two pumps experiments as a function of the total pump power. Vertical axis are normalized to the power threshold for the formation of independent solitons. (**c-e**) respectively correspond to $D = 2a$, $3a$ and $4a$. In each case the left sub-panel corresponds to a phase difference of $\Delta\varphi = 0$, whereas the right one corresponds to $\Delta\varphi = \pi$. **f-j**, present data equivalent to (**a-e**) in the case $J < 0$ and $J' > 0$.

two solitons always merge when they are in phase ($\Delta\varphi = 0$).

Secondly, to show that this interaction is mediated by the bands and not by the in-phase relation between soliton tails we then considered the case $J < 0$ and $J' > 0$. In this configuration the lower band presents an anti-bonding profile and the upper band a bonding one as $J < 0$. Lowest and highest energy states of the lower band are depicted in Fig. 4.8 (f). The density and phase profiles of the soliton are presented in Fig. 4.8 (g): the soliton core presents a strong intensity on both sub-lattices with an anti-phase relation between the two pillars, signature of the anti-bonding nature of the lower band. As in the previous case, the phase of the tails does not alternate from one unit cell to the next one, however, due to the phase twist inside of the soliton core the two tails are in phase opposition. Once again the nature of the interaction does not depend on the relative distance between soliton cores but this time the frustration is observed when soliton tails are in-phase (see Fig. 4.8 (h-j)). The injection of particles and thus the formation of additional solitons in between the two source terms is favored when the field profile efficiently couples to the lower energy modes which have an anti-bonding symmetry.

The importance of the lower band structure is twofold: 1- the soliton profile is dictated by the eigenstate from which it bifurcates which is the top of the lower band in our case as the interaction is repulsive; 2- the lower band symmetry dictates whether the solitons growth is favored when the two solitons are locally in-phase or in anti-phase.

Those results highlight the importance of the lower band structure to understand the interaction between two solitons. We especially demonstrated that a particular attention has to be given to the mode from which the soliton bifurcate (the top of the lower band in this case) as it strongly affects the soliton wavefunction. These first results are very similar from those obtained in conservative systems for solitons without sub-lattice localization and the notion of Chiral symmetry thus does not seem to play an important role in the description of the interaction between gap solitons with chiral tails. We will now turn to a more detailed description of the formation of coupled solitons, to explain the transition from the linear to the highly non-linear regime and try to observe whether the underlying Chiral symmetry has any influence on the system.

4.2.2 A symmetry breaking induced by a phase frustration between the driving field and renormalized states

A noticeable feature we can observe on the experimental data presented in Fig. 4.5 is that under certain conditions (for instance in Fig. 4.5 (a) for $\Delta\varphi = 0$), only one soliton is injected in the system and is located under one of the two pumps. This phenomenon is quite counter intuitive as one would expect the system response to preserve the symmetries of the lattice and of the excitation field: we would thus expect to observe the simultaneous formation of a soliton under each pump spot. This asymmetric feature which signals the presence of a symmetry breaking is also observed in simulations as it is shown in Fig. 4.6 (b) for $\Delta\varphi = \pi$. A question that arises is how does the system chooses where to form the first soliton, is it stochastic?

We performed repeatability experiments for $D = 2a$ and $\Delta\varphi = 0$ to verify whether the first non-linear jump always corresponds to the formation of a single

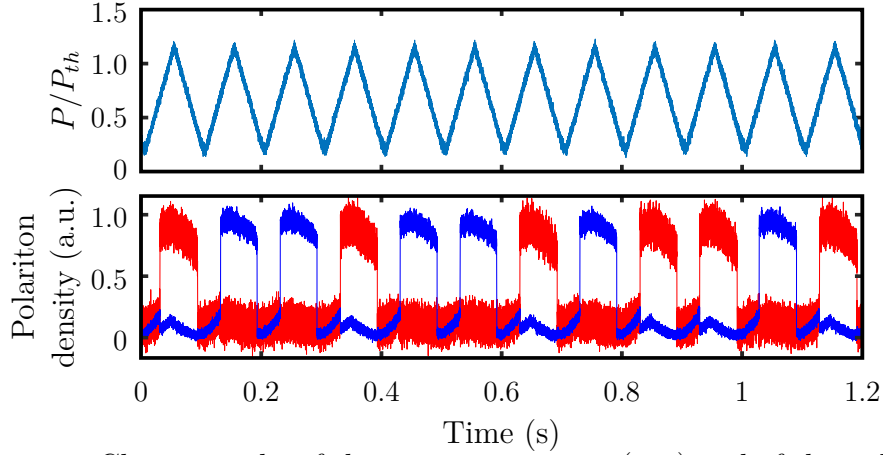


Figure 4.9: Chronographs of the excitation power (top) and of the polariton density in the two pumped unit cells (bottom) with the red and blue lines respectively corresponding to the left and right dimers (respectively associated to arm-L and arm-R) for $\Delta\varphi = 0$ and $D = 2a$.

soliton and if this soliton can be formed under each of the pump spots in a non-deterministic fashion. We thus performed experiments in which the input power was continuously ramped up and down between $P = 0$ and $P > P_{\text{th}}$ while we continuously monitored the emission from the two pumped unit cells and the central one. To avoid any perturbation due to long time drifts of the setup alignment and to ease the collection of data we slightly modified the experimental setup: each of the considered unit cells was imaged on a different photodiode and the HWP controlling the excitation power was mounted on a homemade fast rotating motor. These modifications accelerate the collection of data by a factor of one thousand (at the cost of some loss of spatial resolution in the distribution of polaritons). A portion of the measured signals is presented in Fig. 4.9 where the blue (red) curve correspond to the polariton density measured in the dimer pumped by the beam passing through arm-L (arm-R). One clearly observe the signatures of a symmetry breaking: only one soliton is formed during each power ramp and the non-linear jump of the polariton density can occur under each of the pump spots. Note that this latter result is extremely sensitive to the value of the phase difference imposed between the two pump beams: introducing a small phase difference leads to significantly favoring the formation of the soliton on one dimer or the other depending on the sign of $\Delta\varphi$.

Fortunately, due to the improvement on the speed with which we collect data and the stability of the setup, we were able to observe a consequent number of events before a significant drift of the alignment which occurs on a timescale $\tau_{\text{drift}} \sim 3$ min. As a result, we can perform some statistics on this symmetry breaking process and check its stochasticity. To do so we used a shutter to rapidly switch the laser on and off at $P = 1.2 P_{\text{th}}$. We then treated each time interval where the laser was on as a distinct event and extracted two binarized signals D_1 and D_2 associated to each pumped dimer: if a soliton was formed on a dimer $i = 1$ or 2 during the n^{th} interval, then $D_i(n) = 1$ and $D_i(n) = 0$ otherwise. In case of a spontaneous symmetry breaking one expects no correlation between $D_1(n)$ and $D_2(n)$ and between $D_i(n)$ and $D_i(n')$. The correlation product of two signals $S_1(n)$ and $S_2(n)$ is noted $S_1(n) \otimes S_2(-n)$.

The obtained results are summarized in Fig. 4.10. The auto-correlations of D_1

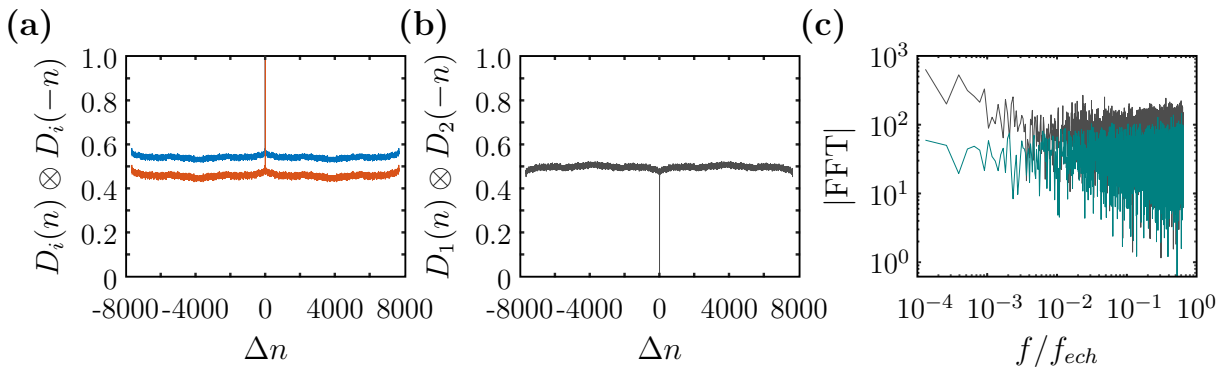


Figure 4.10: **a**, Auto-correlation functions respectively associated to D_1 and D_2 for red and blue curves. **b**, Cross-correlation of D_1 and D_2 . **c**, Absolute value of the Fast Fourier Transform of D_1 (gray) and of a random sequence of zeros and ones (green).

and D_2 presented in panel (a) are clearly peaked around 0 and show plateaus at values close to 0.5². The amplitude difference between the two plateaus is due to the too small number of acquired events and highlights their non-equipartition: 46% of the non-linear jumps occurred under the reference spot for a total of 7675 events. The cross-correlation of D_1 and D_2 presents the same characteristics with a peaked feature around 0 attesting that the formation of solitons always occurred under a single of the two pump spots at each event (see panel (b)). Finally Fig. 4.10 (c) presents the absolute value of the Fourier transform of D_1 , which is equal to the one of D_2 (one gets $D_2(n) = 1 - D_1(n)$ from the value of the cross correlation for $\Delta n = 0$). We observe no clear evidence of a periodicity in the signals and the Fourier transform of a random sequence of 0 and 1 is provided for comparison. Proving this symmetry breaking process to be spontaneous would require measuring all possible sources of noise in the setup, which is beyond the scope of this study. We can at least say that the mechanism triggering the asymmetric formation of the soliton appears to be stochastic.

A spontaneous symmetry breaking between two negatively coupled cavities as already been reported by the group of A.Giacomotti using a non-resonant [356] or resonant excitation of the system [357]. This spatial symmetry breaking between two coupled Kerr resonators can be observed regardless of the hopping sign, by adjusting the relative phase imposed by the driving field. As described in Ref [358], observing the symmetry breaking requires to pump both pillars of a positively (negatively) coupled dimer in anti-phase (phase) and at an energy lower than the anti-bonding (bonding) mode. The symmetry breaking occurs when the effective blueshift is such that the lower eigen-state is brought to resonance using a strong driving field presenting the opposite symmetry. Note that, in this sense, the asymmetric solitons presented in Chap. 3.5 of this manuscript could be obtained by power ramps for a given phase difference instead of a phase scan at a given power.

We now need to verify whether our experiments can be interpreted in terms of anti-symmetrically pumped resonance. To do so it is insightful to consider that the injection of polaritons under each pump induces a local blueshift β of the bonding

²The correlation function defined in MATLAB is not normalized and decays due to the finite size of data. In the present case, the signals were periodized to compute correlations. This explains why we observe plateaus and not a linear decay of the results.

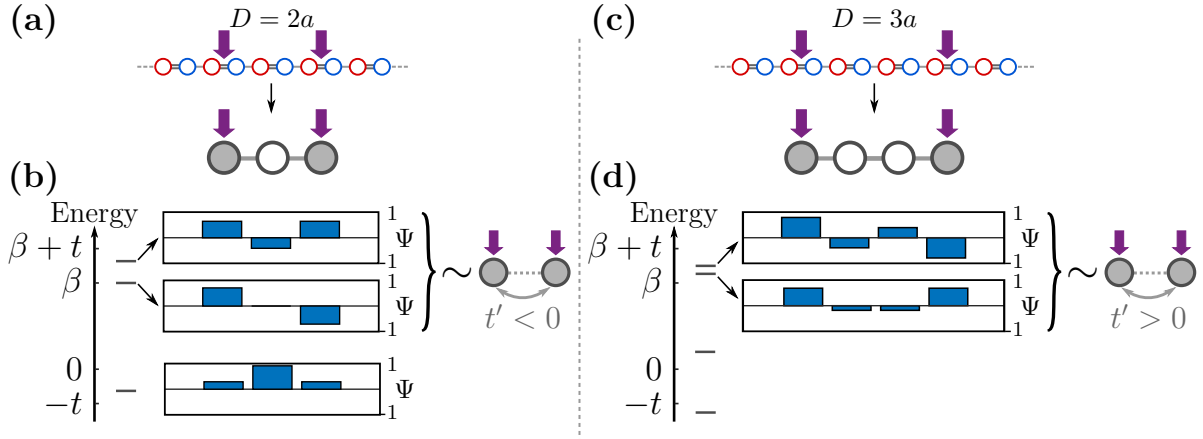


Figure 4.11: **a**, Mapping between the chain of coupled pillars to the reduced system described by $M(D = 2a)$ **b**, Energy and real space distribution of the eigenstates of the reduced system for $D = 2a$. **c-d**, same as **(a-b)** for $D = 3a$. In **(d)**, spatial distributions are represented for the two highest eigenstates only.

resonances and to analyze the eigenstates of the reduced system composed of the two pumped unit cells and the central undriven ones. To be more specific, we approximate each unit cell to a single resonator and diagonalize the matrix $M(D)$ associated to the reduced system which in the case of $D = 2a$ yields:

$$M(D = 2a) = \begin{pmatrix} \beta & -t & 0 \\ -t & 0 & -t \\ 0 & -t & \beta \end{pmatrix} \quad (4.1)$$

where t is the effective hopping from one unit cell to the next one which can be approximated by $t \approx J'$ and just before the non-linear jump the effective onsite energy of the driven dimers can be approximated by $\beta \approx J$. The diagonalization of the resulting matrix yields three eigenstates presented in Fig. 4.11. The two highest energy ones present a strong amplitude on the blueshifted sites while the lowest energy one is mostly located on the central site: as long as $\beta \gg t$ we can forget about the central dimer to describe the physics of the pumped dimers. We hereby assimilate our system to two coupled Kerr resonators.

The sign of the effective hopping is given by the hierarchy between the two highest eigenstates of the system: in the case $D = 2a$ the highest energy state corresponds to the bonding hybridization of the two blueshifted sites while the central mode presents the anti-bonding symmetry. In the limit where the energy difference between the lowest eigenstate and the two higher ones is significantly greater than the linewidth, the system can be approximated by two coupled resonators with an effective negative hopping constant. In this framework, when the blueshift brings the first eigenstate in resonance with the pump, the efficient injection of polaritons rapidly brings the second one to resonance which presents a symmetry opposed to the driving field and thus leads to a symmetry breaking. Calculating the eigenstates of M for $D = 3a$ and $D = 4a$, we find that the sign of the effective hopping between pumped unit cells is given by the parity of D/a : it is positive for $D/a = 3$ and negative for $D/a = 4$. This simple analysis is corroborated by our experimental results as we observed a symmetry breaking for $\Delta\varphi = \pi$ with $D = 3a$ and $\Delta\varphi = 0$ with $D = 4a$. In the next chapter we will address the symmetry breaking observed between two neighboring

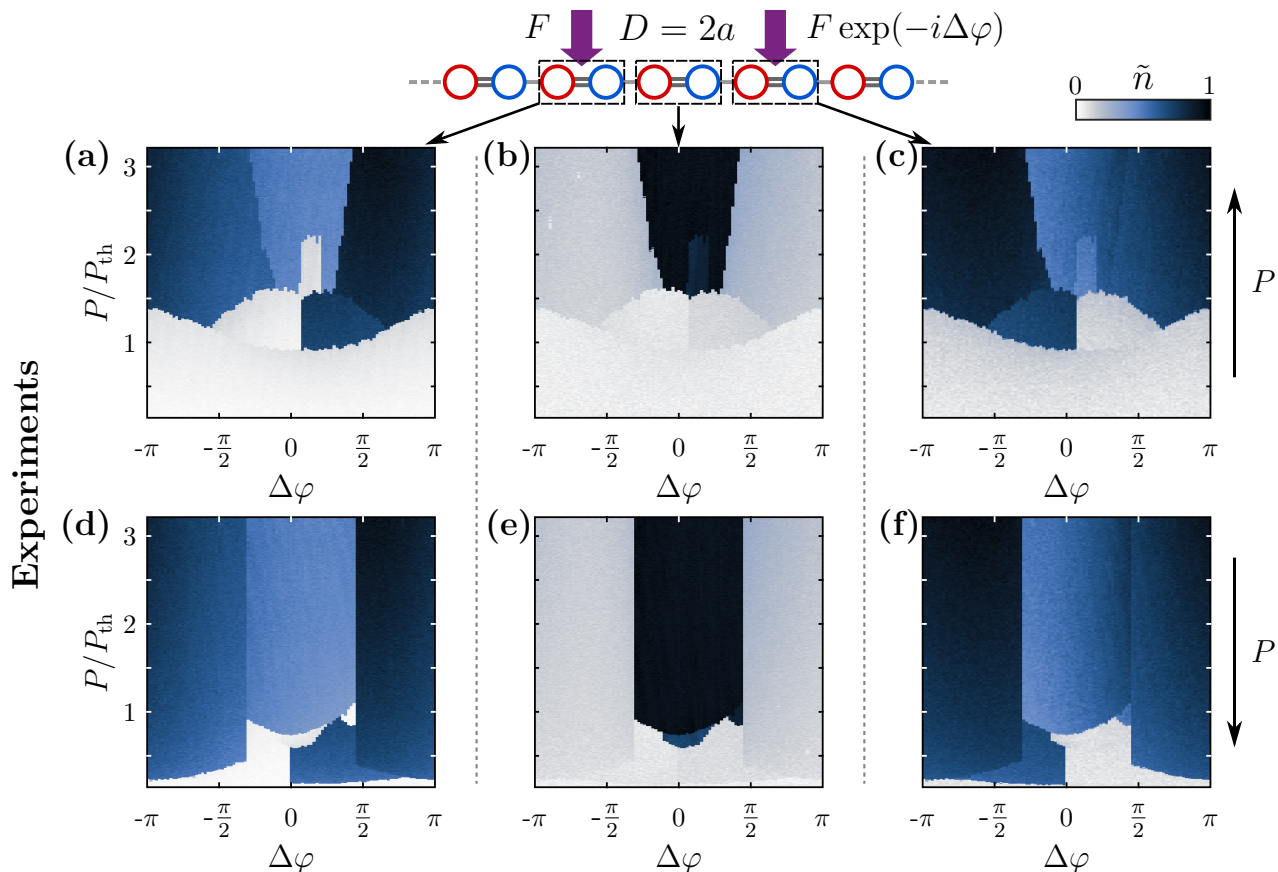


Figure 4.12: Phase-Power diagrams of the normalized polariton density \tilde{n} on the three central unit cells for $D = 2a$. **(a-c)** were obtained for upward scans of the input power starting from the linear regime and respectively correspond to the evolution of the polariton density on the left, undriven and right unit cells. **(d-f)** are equivalent to **(a-c)** for downward scans of the input power starting from the highest power presented in **(a-c)**.

dimers ($D = a$) for $\Delta\varphi = \pi$.

4.2.3 Phase diagram of coupled solitons formation for $D = 2a$

Up to now we restricted our discussion to the two cases $\Delta\varphi = 0$ and $\Delta\varphi = \pi$. To extend our study, we performed power ramp experiments for many different values of $\Delta\varphi$ within the range $[-\pi, \pi]$ and for pump spots separated by $D = 2a$. We used a frequency generator to synchronously control the excitation power and the relative phase by externally driving the power control device and the piezoelectric actuator. We slowly scan the phase difference $\Delta\varphi$ introduced between the two pumping beams ($f_0 = 10$ mHz) while the input power P is rapidly modulated ($f_0 = 10$ Hz). By collecting the signal emitted by each considered unit cell with photodiodes, we can reconstruct the emission pattern as a function of power and phase. Figure 4.12 presents the diagrams obtained by performing up and down power ramps as a function of a fixed phase difference $\Delta\varphi = \varphi_L - \varphi_R$ imposed between the two pumps.

Let us first focus at panels (a-c) of Fig. 4.12 which corresponds to upward scans of the excitation power. We clearly observe the signature of the spatial symmetry

breaking around $\Delta\varphi = 0$ with a single soliton forming on the left dimer for $\Delta\varphi \sim [0, \frac{\pi}{2}]$ and on the right one for $\Delta\varphi \sim [-\frac{\pi}{2}, 0]$. At higher powers ($P/P_{\text{th}} > 2.5$) the non-linear domains spreads on three unit cells. In the vicinity of $\Delta\varphi = \pm\pi$, two solitons are simultaneously formed under each of the pump spots and the central unit cell remains dark up to the maximum accessible input power. Note that a general residual asymmetry is observed in the diagram: the symmetry breaking here occurs slightly above $\Delta\varphi = 0$ and we clearly do not observe a mirror symmetry between Fig. 4.12 (a) and (c), respectively associated to the unit cells pumped by beams passing through arm-L and arm-R. This asymmetry can be attributed to a residual misalignment in the setup or to a weak local disorder on the onsite energies or couplings whose effect is exacerbated by the non-linear nature of our experiments.

The same phase dependence of the polariton distribution is observed on Fig. 4.12 (d-f) which correspond to downward scans of the pump power starting from the highest accessible value. However, due to the hysteretic behavior of the system, the transitions between bistability branches occur at lower power thresholds compared to Fig. 4.12 (a-c). In the vicinity of $\Delta\varphi = 0$, as the input power decreases, we observe that the soliton core initially spreading over three unit cells undergoes a non-linear cascade leading to the presence of a single soliton either on the left or right dimer depending on the sign of $\Delta\varphi$. Remarkably, a stable solution corresponding to having a soliton localized on the undriven dimer only is obtained in the downward scan only, for $\Delta\varphi \approx 0$ and $P \sim P_{\text{th}}$.

In the vicinity of $\Delta\varphi = \pm\pi$ a single stable branch is encountered as the power is scanned down which corresponds to the existence of a soliton at the location of both pump spots.

To better highlight the different stable solutions observed during these experiments, we can superimpose these individual diagrams. To do so we took advantage of the ternary nature of our data by associating each unit-cell to a given color of the RGB code. In this way, we generate false color images, where red color represents a soliton localized on the left dimer, blue color corresponds to a soliton localized on the right dimer, while green regions are related to a soliton localized on the center dimer. In the phase diagram, the color representing solitons localized on two or three dimers is obtained by simple additive color synthesis, as illustrated in Fig. 4.13. In this figure we binarized the images presented in Fig. 4.12 (a-c) and used each of them as a given color layer of the new image.

Figure 4.14 (a-b) present the obtained RGB images for the upward and downward power scans. Seven different solutions are observed over the two images. In particular, the blue and red regions are characteristic from the spatial symmetry breaking and correspond to the localization of a single soliton on one of the two pumped dimers. The schematic representation of the fluid density (white and gray circles) clearly highlights the chirality (left or right localization) of these two solutions which are enantiomorphs: they are mirror images of each other. In the downward scan (Fig. 4.14 (b)), we observe the presence of a green region, which corresponds to a single soliton localized on the undriven unit cell, whereas no green region is found in the upward scan (Fig. 4.14 (a)). This is a strong indication of the presence of multi-stability in the system. Note that an asymmetry is clearly observed *via* the presence of a cyan region associated to a soliton spreading on the two rightmost unit cells: one would expect to observe its mirror symmetric counterpart (a yellow

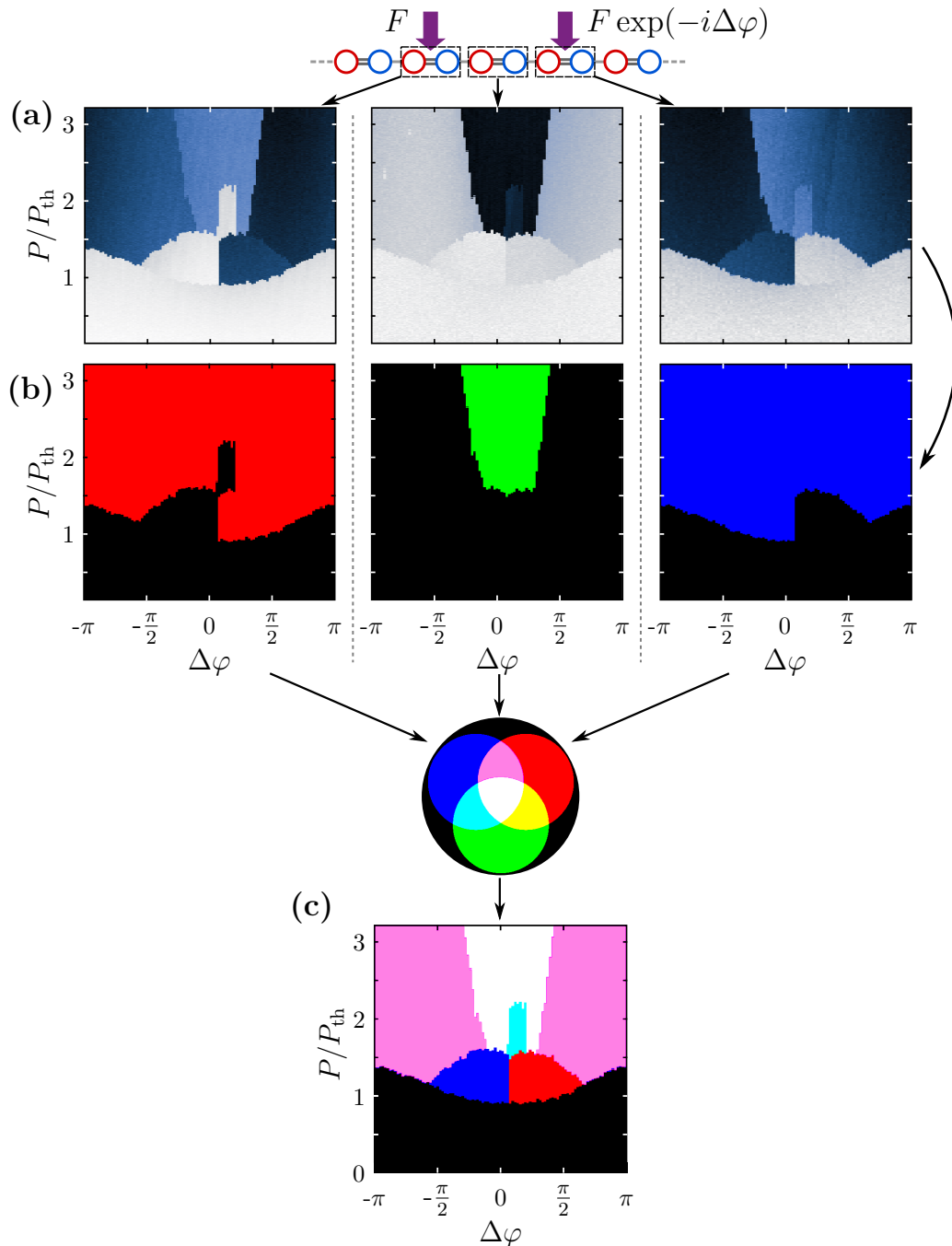


Figure 4.13: **a**, Phase-Power diagrams of the normalized polariton density presented in Fig. 4.12 (a-c). **b** Binarized diagram with red, green and blue areas indicating the Phase-Power regions where a soliton was present on the left, central (undriven) and right unit cell respectively. **c** RGB image obtained superimposition of the three binarized images presented in (b). The additive color synthesis scheme is displayed on top.

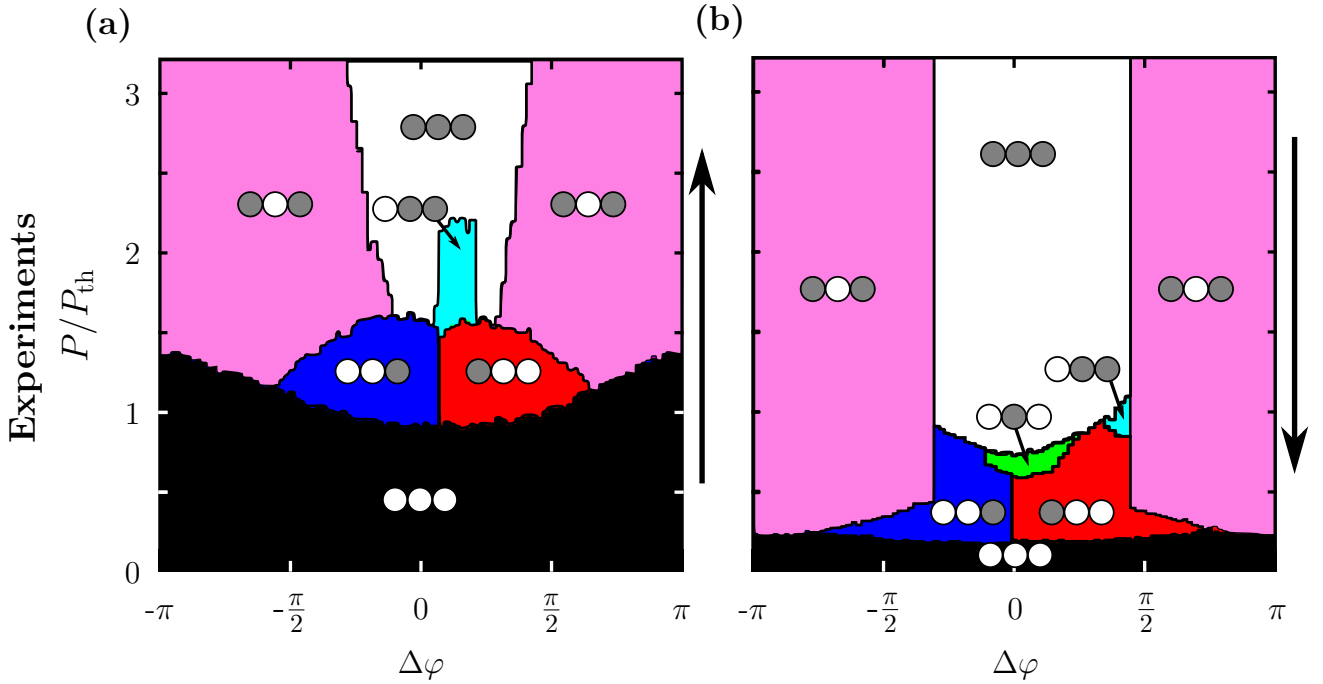


Figure 4.14: RGB images obtained by additive color synthesis of diagrams presented in Fig. 4.12 with (a): synthesis of the three upward scans and (b): synthesis of the three downward power scans. The power scan direction is indicated by an arrow at the right of each panel. Schematic representation of the polariton fluid density is represented in each colored region: a strong (weak) intensity in a dimer is represented by a gray (white) circle.

region) where the soliton would be located on the two leftmost unit cells.

4.3 Helical bistability

Due to the hysteretic behavior of the system, all trajectories between two points of the P - $\Delta\varphi$ phase space are not always equivalent. In this section we take profit of a knob which has rarely been considered in open systems: the possibility to implement continuous scans of the relative phase $\Delta\varphi$. Doing so, we demonstrate that the chiral symmetry of gap solitons has striking consequences on their interaction: we unveil a novel effect of phase multi-stability in the vicinity of the symmetry breaking. The helicity of the phase scan (clockwise or counterclockwise) will be shown to control the chirality of the solution (left or right localization of the soliton) encountered across the broken symmetry region. We compare these results to the case of the AB lattice and we demonstrate this effect to be specific to gap solitons presenting the chiral symmetry.

4.3.1 Scanning the phase to navigate through the stability diagram

We now turn to the exploration of the stability diagram of our system of coupled solitons by performing scans of $\Delta\varphi$ for fixed values of P . Note that due to the hysteretic behavior associated to the competition between non-linearity and dissipation, the clockwise and counterclockwise phase scans are different and we thus present

both in all figures. The RGB images associated to relative phase scans as a function of the input power are presented in Fig. 4.15. We here provided the phase scans in the case of upward and downward power scans. Note that, since the $\Delta\varphi$ scans are performed at fixed values of the power, the system does not “remember” the way the power is varied (increased or decreased) after each $\Delta\varphi$ scan. As a result, the only main difference between panels (a) and (b) ((c) and (d)) lies in the initialization of the system: the system remains empty (no soliton) up to $P/P_{\text{th}} \approx 0.7$ when increasing the power from $P/P_{\text{th}} = 0$ ((a) and (c)), while a soliton is observed down to $P/P_{\text{th}} \approx 0.35$ when decreasing the power from $P/P_{\text{th}} = 3.2$.

Let us start with a general description of the images.

- Firstly, as a result of the hysteretic tendency of the system, one can notice that the stability regions of most solutions extend in the scan direction of $\Delta\varphi$. Consequently, no mirror symmetry of the images is observed with respect to $\Delta\varphi = 0$. Exception made for the magenta area, the different solutions are observed on the leftmost (rightmost) part of the phase interval for clockwise (counterclockwise) scans of $\Delta\varphi$.
- Secondly, one can note that the asymmetry of the system is still observed through the presence of a cyan region while no yellow region is observed.
- Finally, three main different power ranges can be identified:
 - The high input power range ($P/P_{\text{th}} > 1.5$) where one observes a phase hysteresis between the magenta and white solutions. It corresponds to the presence of a soliton under each pump spot while a third soliton can be formed ($\Delta\varphi \rightarrow 0$) or extinguished ($\Delta\varphi \rightarrow \pm\pi$) in the central unit cell.
 - The low power range where no soliton can subsist in the system ($P/P_{\text{th}} < 0.35$).
 - The middle input power range ($0.35 < P/P_{\text{th}} < 1.5$) where different solutions are observed depending whether the phase is scanned in the clockwise or counterclockwise direction.

We will focus on the middle range of power and more precisely on the power range $0.35 < P/P_{\text{th}} < 1$ in the case of a downward scan of power. The corresponding zooms of Fig. 4.15 (b,d) are presented in Fig. 4.16. In this power range we observe two solutions which are spatially symmetric with respect to the central unit cell (magenta and green areas) and the two chiral solutions associated to the symmetry breaking (red and blue areas). Interestingly, while several solutions are encountered at a given power value above $P/P_{\text{th}} = 0.5$, only one of the two chiral solutions is encountered at every phase scan. Strikingly, one observes that the helicity of the scan of $\Delta\varphi$ (clockwise or counterclockwise) seems to be associated to a given chirality (left or right localization) of the system response. In the following sections we will separately discuss the three power ranges labeled “R1”, “R2” and “R3” in Fig. 4.16³. In those power ranges, the system exhibit different interesting behaviors:

³Note that in ranges R1 and R2, a non-linear steady state can only be reached by decreasing the power. Otherwise no soliton is formed in these power ranges.

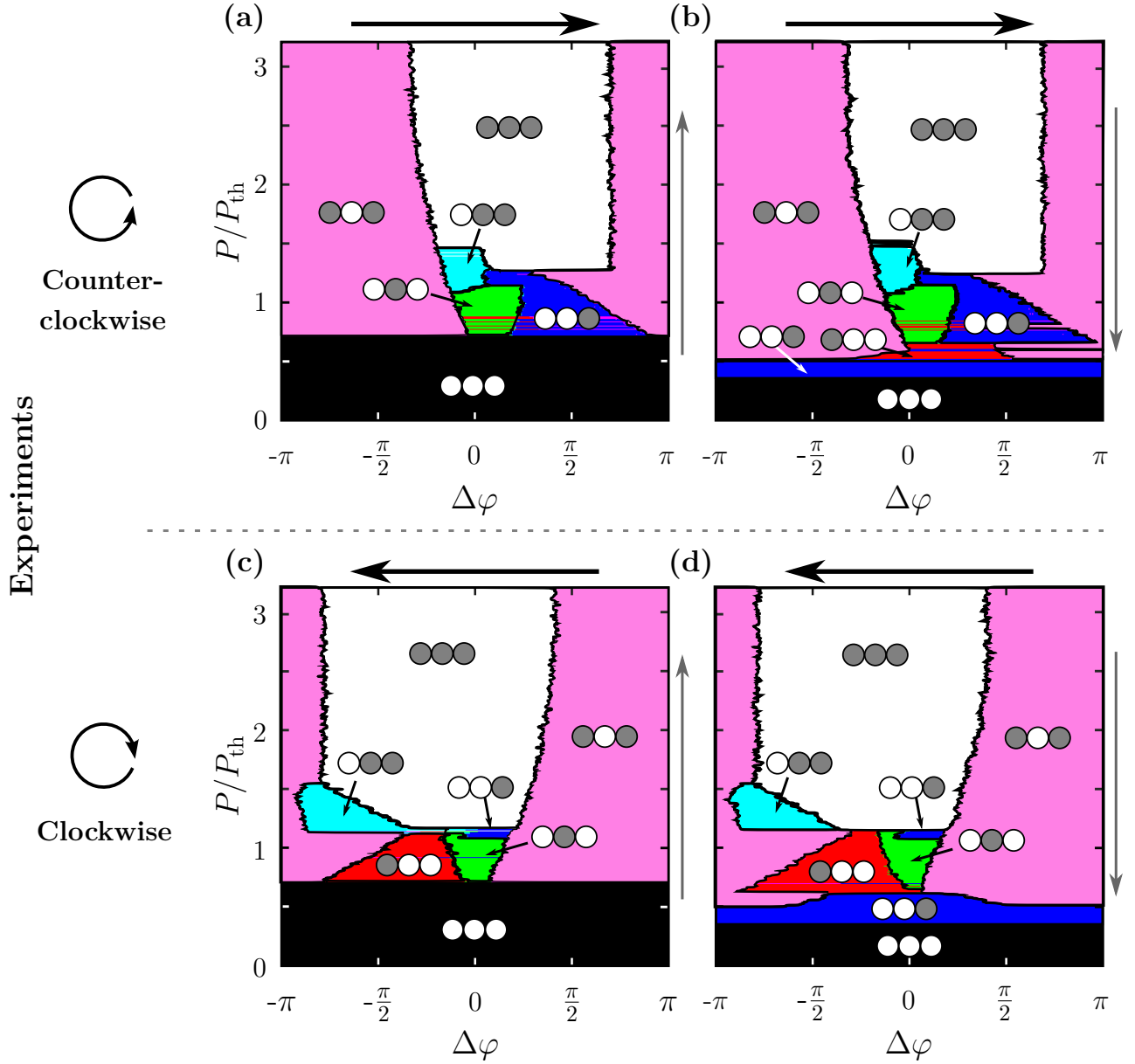


Figure 4.15: RGB images summarizing the results obtained by performing phase scans as a function of the input power. **a-b**, Counterclockwise scans of $\Delta\varphi$ ($\partial_t \Delta\varphi > 0$) for the upward and downward power scan respectively. **c-d**, Same as **(a-b)** for a clockwise scans of the phase difference ($\partial_t \Delta\varphi < 0$).

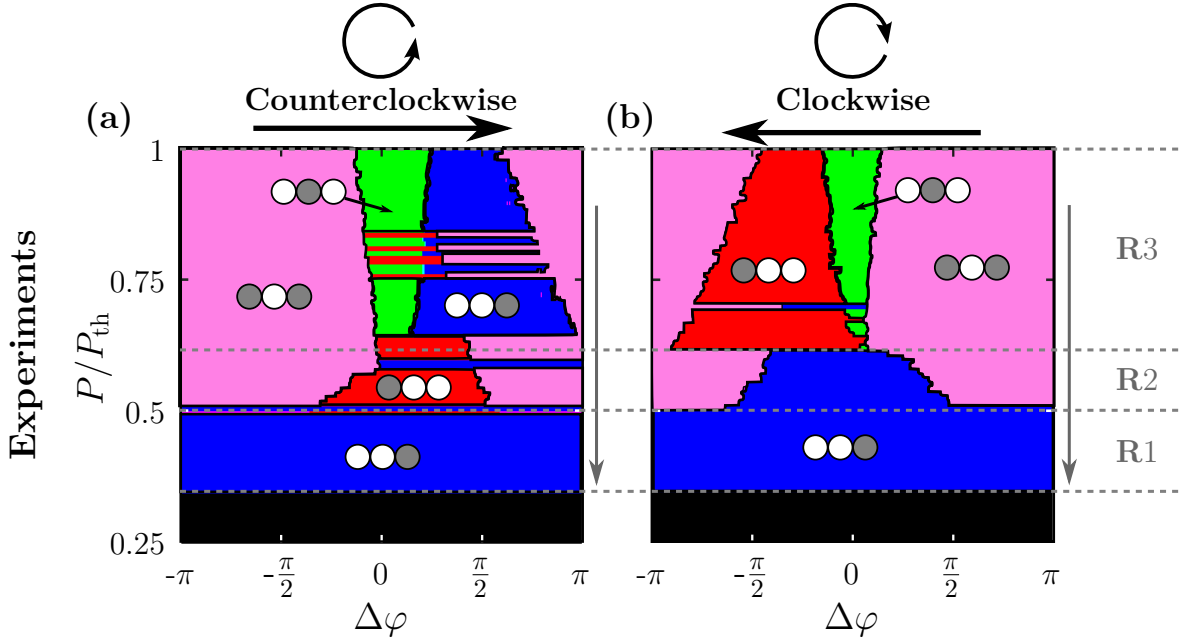


Figure 4.16: Zoom of Fig. 4.15 (b,d) in the power range $0.25 < P/P_{\text{th}} < 1$.

- **R2:** For $0.5 < P/P_{\text{th}} < 0.6$, the system mainly jumps between two possible solutions: a symmetric solution where a soliton is present under each pump spot (magenta) and one of the two chiral solutions where the soliton is localized under one of the two pumps (red or blue). The soliton localizes on the right for clockwise phase scans and on the left for counterclockwise ones.
- **R3:** For $0.6 < P/P_{\text{th}} < 1$, the system still switches between symmetric and one chiral solutions. However, before reaching the chiral solution, the system reaches the symmetric case where a single soliton is localized on the undriven unit cell (green area). Interestingly, when comparing to the system behavior in the range R2, we observe a change of the chirality of the system response with the phase gradient: the soliton localizes on the left (right) during the clockwise (counterclockwise) scan.
- **R1:** For $0.35 < P/P_{\text{th}} < 0.5$, a single solution is observed (blue region): the soliton is trapped in one of the two chiral solutions. Note that depending on the realization, the soliton can be localized either on the left or right unit cell.

4.3.2 Chiral response to the phase gradient

Let us first focus on the power range R2 where the system switches between the symmetric solution (magenta) and the two chiral solutions encountered through the symmetry breaking. To get a better insight on the state of the system we again monitor the polariton distribution using the CCD camera, the evolution of the density profile (integrated transversely to the lattice) of the polariton fluid as a function of the phase difference is presented in Fig. 4.17 for $P/P_{\text{th}} = 0.57$. We observe the behavior unveiled by photodiode measurements: the intensity profile switches between a symmetric and asymmetric distribution of the polariton density. In the vicinity of $\Delta\varphi = \pm\pi$ the polariton fluid is constituted of two solitons located under each of the pump spots. As $\Delta\varphi$ departs from $\pm\pi$ and reaches 0, the density tends

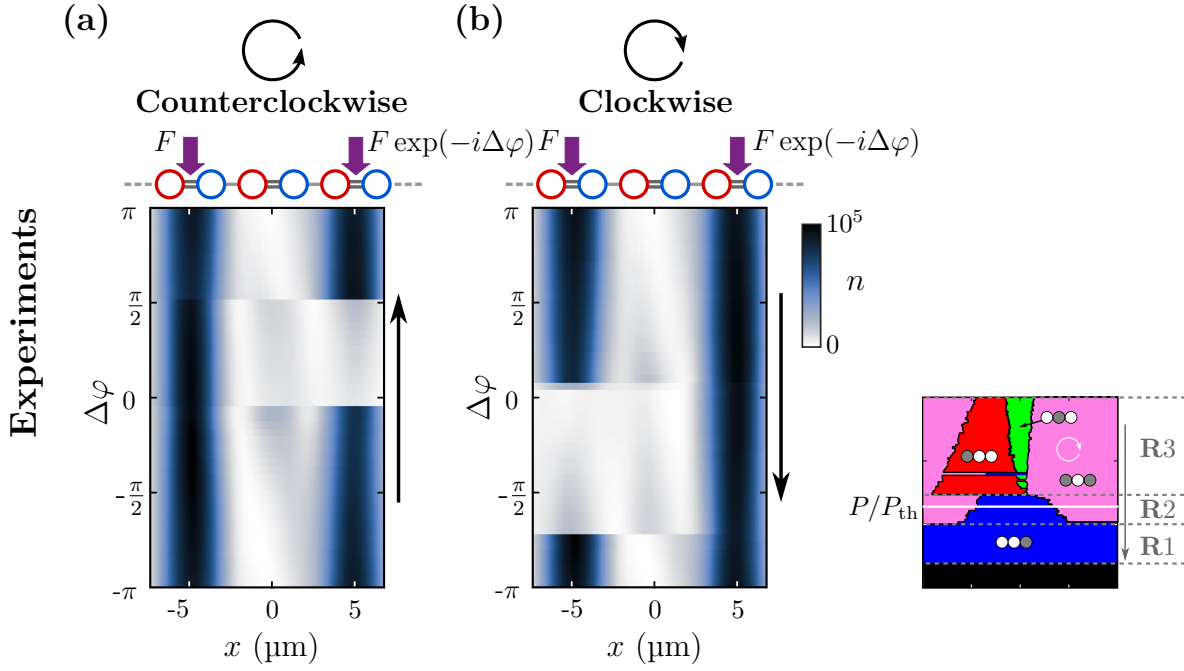


Figure 4.17: **a-b**, Evolution of the density profile of the polariton fluid as a function of the phase difference for $P/P_{\text{th}} = 0.57$ with **(a)** and **(b)** respectively corresponding to a counterclockwise and clockwise scan of $\Delta\varphi$. A sketch of the clockwise P - $\Delta\varphi$ diagram is displayed at bottom right of the figure. The horizontal white line indicates the input power considered in the experiment.

to spatially dissymetrize and we ultimately observe a transition to an asymmetric situation where a single soliton is present under one of the two pumps: in the case of the counterclockwise (clockwise) scan, the soliton localizes on the left (right) dimer. Due to the weak polariton density measured in the central unit cell for all values of $\Delta\varphi$, we can restrict our analysis to the left and right dimers and compute the density imbalance between these two by defining:

$$I_{\text{LR}} = \frac{n_L - n_R}{n_L + n_R} \quad (4.2)$$

with n_L (n_R) the number of polaritons in the left (right) unit cell. An imbalance close to $+1$ (-1) thus corresponds to a soliton localized on the left (right) dimer and the symmetric solution is associated to $I_{\text{LR}} \approx 0$. The results of such procedure is displayed in Fig. 4.18. One can observe the presence of three different branches⁴ associated to:

- The symmetric solution (magenta) with an imbalance $I_{\text{LR}} \approx 0$.
- Each of the two chiral solutions (red and blue) with an imbalance $I_{\text{LR}} \approx \pm 0.8$.

During the counterclockwise (clockwise) scan, the system only explores the upper (lower) half of the graph⁵. This representation highlights the relation between the helicity of the phase scan and the spatial imbalance of the system response:

$$\partial_t \Delta\varphi > 0 \implies I_{\text{LR}} > 0 \quad \text{and} \quad \partial_t \Delta\varphi < 0 \implies I_{\text{LR}} < 0 \quad (4.3)$$

⁴We here only consider solutions presenting at least one soliton on the lattice.

⁵Note that the location of the chiral solutions on the $\Delta\varphi$ axis matches with their position on the diagrams measured with power scans (see Fig. 4.14)

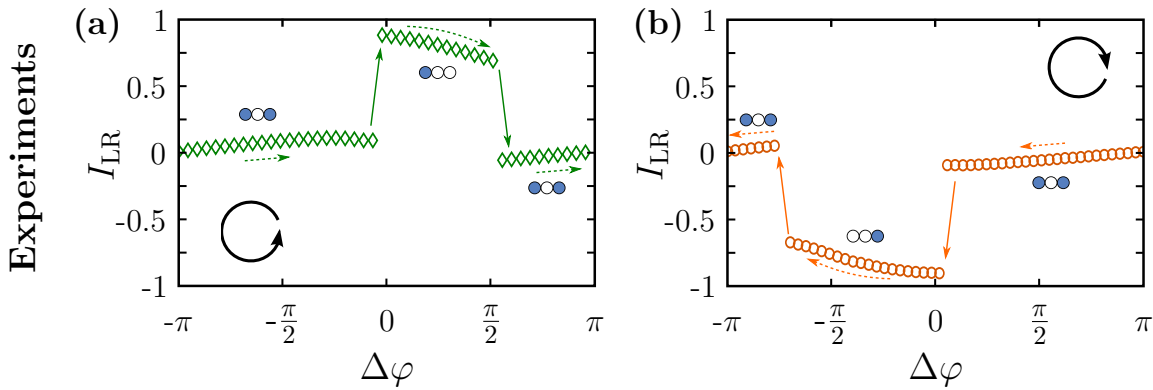


Figure 4.18: Evolution of the density imbalance between the two driven unit cells as a function of $\Delta\varphi$. Data for the counterclockwise (a) and clockwise (b) scans are represented by green diamonds and orange circles. Dashed and solid colored arrows indicate the direction of the scans and jumps. Sketches of the density distribution are depicted next to each stable branch.

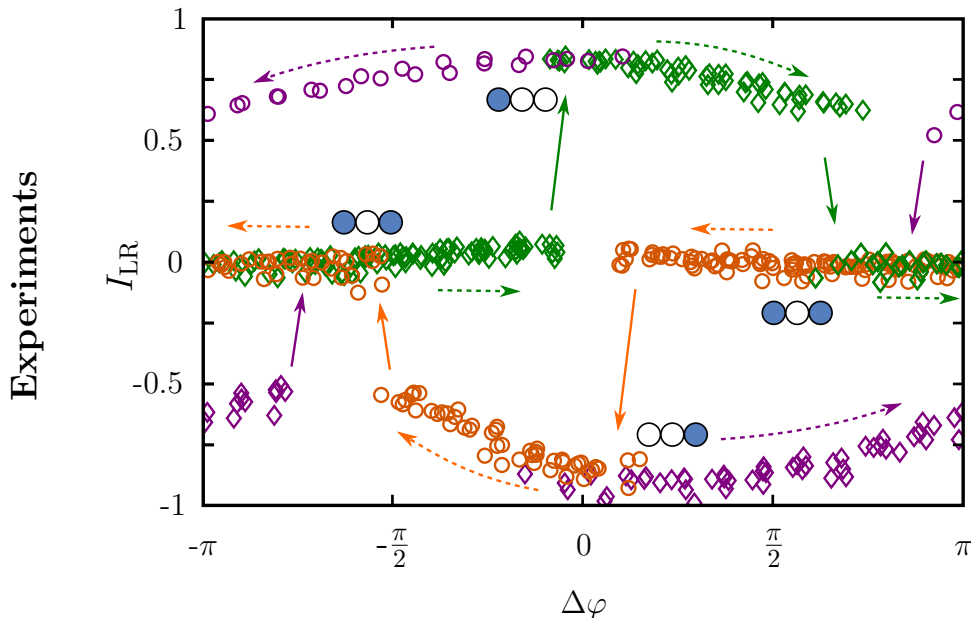


Figure 4.19: Evolution of the density imbalance between the two driven unit cells as a function of $\Delta\varphi$ for $P/P_{\text{th}} = 0.57 \in \text{R2}$. Data for counterclockwise and clockwise scans are represented by diamonds and circles. Green and orange symbols represent data points obtained for continuous counterclockwise and clockwise scans. Purple symbols show data points obtained by switching the direction of the scan when the system is in a chiral solution. Dashed and solid colored arrows indicate the direction of the scans and jumps.

We want to emphasize that this multi-stability diagram is particularly intriguing. The directionality the scan of $\Delta\varphi$ controls the symmetry of the solution encountered across the broken symmetry region. Even though $\Delta\varphi$ is bound to a compact, if one would perform continuous scan of $\Delta\varphi$ in a given direction, one of the two chiral solutions would never be observed.

To complete the exploration of the stability diagram of the system, we performed more elaborated scans of the relative phase and especially changed the direction of the phase scan when the system is in a chiral solution: in this way we probe the

whole stability range of each solution. The diagram obtained by performing such scans of $\Delta\varphi$ is presented in Fig. 4.19. One can notice that the two chiral solutions are stable on a very large range which almost covers the interval $[-\pi, \pi]$. Remarkably, no direct channel links these two solutions: the system has to be brought to the symmetric state to enable switching between the two stability branches associated to chiral solutions. In addition, the only way to access a chiral solution relies on scanning the phase difference across $\Delta\varphi = 0$, which is the symmetry breaking point unveiled with power scans. The chirality of the reached solution only depends on the way the driving field reaches $\Delta\varphi = 0$: a positive (negative) phase gradient leads to approaching the breaking point from $\Delta\varphi < 0$ ($\Delta\varphi > 0$) and results in a jump toward the $I_{LR} \approx +0.8$ ($I_{LR} \approx -0.8$) stability branch. Interestingly, this means that the state of the system contains information concerning the history of the phase scan.

The wide stability range of the two asymmetric solutions is counter-intuitive as a clear separation between the two red and blue areas was observed on the stability diagram built *via* scans of P (see Fig. 4.14). One could expect to observe a transition from one asymmetric solution to the other as the driving field crosses the axis $\Delta\varphi = 0$. Indeed, intuitively we could consider that imposing a phase difference $\Delta\varphi$ between the two pumps induces a flux of polariton from one driven unit cell to the other which would explain why particles tend to localize on one side of the pumped region. In this regard crossing the axis $\Delta\varphi = 0$ would be equivalent to reversing the phase gradient and thus the flux. We could therefore expect a transfer of polaritons on the other side of the pumped region. We observe that such transition does not exist and that the system is easily stabilized in any of these two chiral solutions regardless of the sign of $\Delta\varphi$ ⁶.

In this section we unveiled a new effect of multi-stability in the vicinity of a spatial symmetry breaking. We experimentally demonstrated that the helicity of the scan of $\Delta\varphi$ (its directionality) controls the chirality of the solution (left or right localization of the soliton) encountered across the broken symmetry region. As a consequence we decided to call this effect a "Helical bistability". In the vicinity of the spatial symmetry breaking, the state of the system contains information about the history of the phase scan.

⁶Note that the stability range of the upper branch (red solution) is centered on $\Delta\varphi < 0$ whereas this solution is only observed on the right side ($\Delta\varphi > 0$) of the symmetry breaking in diagrams obtained by scans of P (see Fig. 4.12, the same remark also applies to blue solution with mirror symmetry).

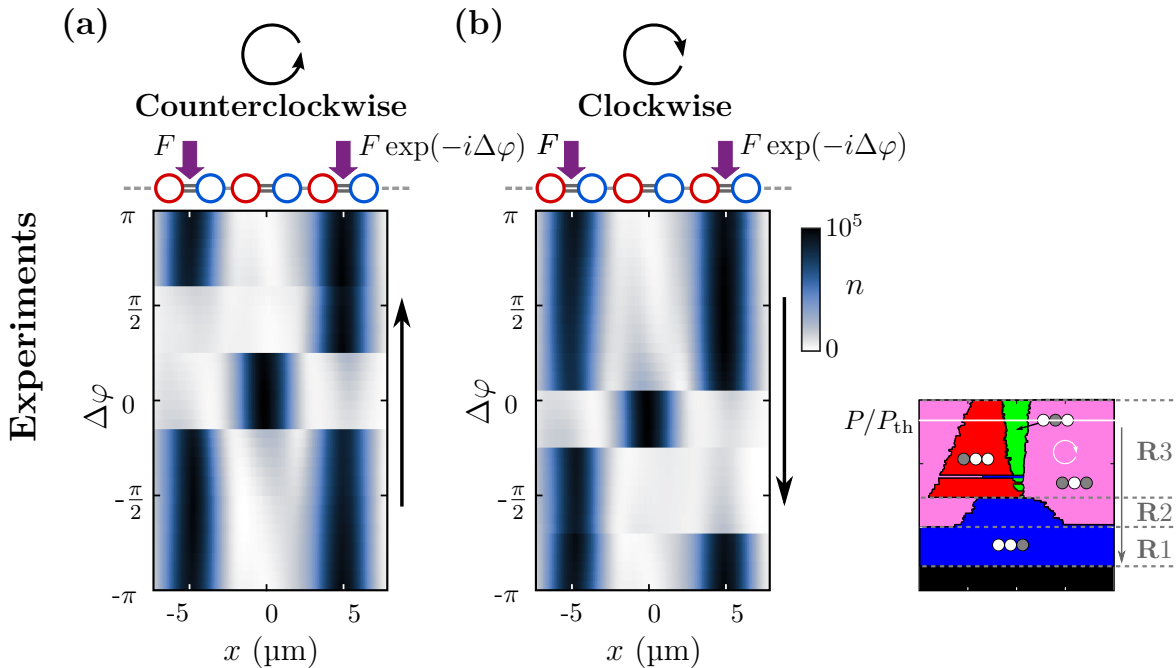


Figure 4.20: Evolution of the density profile of the polariton fluid as a function of the phase difference for $P/P_{\text{th}} = 0.92$ with (a): the counterclockwise and (b): the clockwise scans of $\Delta\varphi$. A sketch of the clockwise P - $\Delta\varphi$ diagram is displayed at bottom right of the figure. The horizontal white line indicates the input power considered in the experiment.

4.3.3 Power dependence of the helical bistability

We now turn to the description of the system of interacting solitons in the power range R3. In this range the system can be found in four different solutions: two symmetric solutions (magenta and green) and the two chiral solutions.

Similarly to what was observed at lower power, the system switches between mirror-symmetric and mirror-asymmetric solutions. Once again, only one of the two chiral solution is reached for a given direction of the phase scan. The evolution of the density profile of the polariton fluid as a function of the phase difference is presented in Fig. 4.20 (a-b) for unidirectional phase scans at $P/P_{\text{th}} = 0.92$. In the vicinity of $\Delta\varphi = \pm\pi$ two solitons are again observed, each under one of the two pump spots (magenta area). Before reaching $\Delta\varphi = 0$, the system jumps to another symmetric solution where a single soliton is localized on the undriven unit cell (green). Then, as the phase scan progresses, we observe a transition to a mirror-asymmetric situation where a single soliton is present on the left or right dimer: in the case of the counterclockwise (clockwise) scan the soliton localizes on the right (left) unit cell. Note that this relation between the sign of $\Delta\varphi$ and the position of the soliton is opposite to what we observed before, in the power range R2. Pursuing the analysis developed in Sec. 4.2.2, this change of directionality is associated to a change of the effective hopping between the two pumped unit cells and so to a reversion of the particle flux between driven unit-cells. A soliton has formed on the central unit cell, in this case the matrix M describing the system now reads

$$M(D = 2a) = \begin{pmatrix} 0 & -t & 0 \\ -t & \beta & -t \\ 0 & -t & 0 \end{pmatrix} \quad (4.4)$$

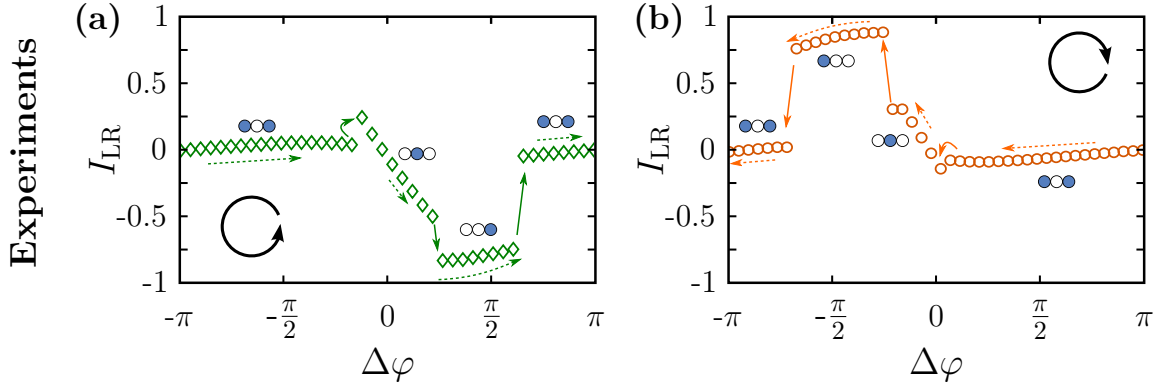


Figure 4.21: Evolution of the density imbalance between the two driven unit cells as a function of $\Delta\varphi$. Data for (a) the counterclockwise and (b) the clockwise scans are represented by green diamonds and orange circles. Dashed and solid colored arrows indicate the direction of the scans and jumps. Sketches of the density distribution are depicted next to each stable branch.

In the limit $\beta \gg t$ the effective coupling between the left and right dimers is now given by the symmetry of the two lowest eigenstates. The lowest eigenstate present a bonding symmetry while the middle energy one present an anti-bonding symmetry: the effective hopping is now positive, which coincides with the change of relationship between the localization of polaritons and the sign of $\Delta\varphi$.

In the continuity of the representation developed previously, we can again plot the density imbalance between the two driven dimers as a function of $\Delta\varphi$. The resulting curve is presented in Fig. 4.20 (c). One can observe the presence of four different branches⁷ associated to:

- The symmetric solution where a soliton is located on each pumped unit cell (magenta), with an imbalance $I_{LR} \approx 0$.
- The symmetric solution where a single soliton is located on the central unit cell (green). In this representation, the branch is oblique with an imbalance $I_{LR} < 0$ for $\Delta\varphi > 0$ and $I_{LR} > 0$ for $\Delta\varphi < 0$.
- Each of the two chiral solutions (red and blue) with an imbalance $I_{LR} \approx \pm 0.8$.

Those graphs exhibit a certain similarity with the ones presented in Fig. 4.18, exception made of the oblique central branch associated to the soliton localized in the undriven unit cell. Note that this single diagram does not represent a complete representation of the state of the system as it ignores variations of the polariton density in the central unit cell, which have now become significant.

To explore the whole stability diagram, we have then performed more elaborated scans of $\Delta\varphi$. The result of this procedure is presented in Fig. 4.22. We observe the same features noticed in the power range R2: no direct channel exists between the two chiral solutions and they can only be reached by selecting a specific direction of the phase scan. However, the directionality of the phase scan here only matters once the system as reached the central solution (corresponding to the green (VI) region on RGB diagrams). Changing the scan direction when reaching the central branch changes the asymmetric solution reached after the next jump: each of the

⁷We here only consider solutions presenting at least one soliton on the lattice.

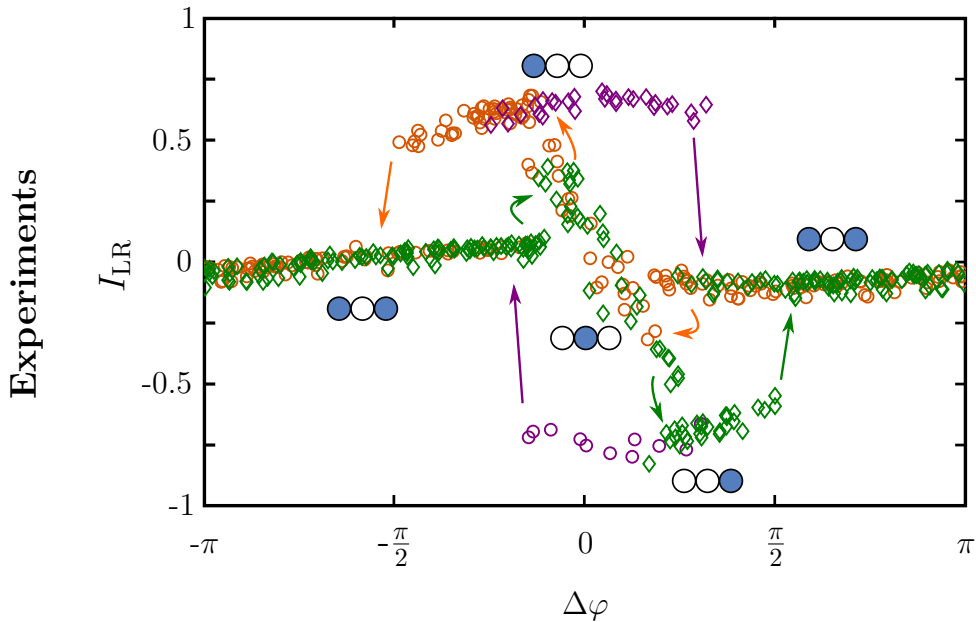


Figure 4.22: Evolution of the density imbalance between the two driven unit cells as a function of $\Delta\varphi$ at $P/P_{\text{th}} = 0.92 \in \text{R3}$. Data for counterclockwise and clockwise scans are represented by diamonds and circles. Green and orange symbols represent data points obtained for continuously counterclockwise and clockwise scans. Purple symbols show data points obtained by switching the scan direction when the system is in a chiral solution. Dashed and solid colored arrows indicate the direction of the scans and jumps.

asymmetric solution can be reached from the solution where a single soliton is localized on the central unit cell. Starting from $\Delta\varphi = \pm\pi$ and the case where a soliton is located under each pump spot (II), the same central branch will be reached for both scan directions and one can then tune $\Delta\varphi$ to reach the desired asymmetric solution. Note that no channel exists from the branch associated to the green region to the branch associated to the magenta region: the system needs to be brought to a chiral solution before going back to solution where two soliton are simultaneously localized on the left and right dimers. Finally, one can observe that the stability range of the two asymmetric solution is much smaller than at high power as one can also see in the shape of the red and blue regions on Fig. 4.14 (b).

In the power range R3, the multi-stability diagram of the system is very similar to the one measured in the range R2. We observe the presence of a helical bistability. Comparing to the observations made at low power, the effect presents an opposite relation between the sign of $\partial_t \Delta\varphi$ and the chirality of the system response. The transition between the two helical bistability effect is due the presence of a additional multi-stability branch at high power. This branch evidences the possibility to stabilize a single soliton in the central unit cell, which is facilitated by the increase of the input power. The presence of the soliton in the central unit cell can be interpreted as flipping the sign of the effective hopping between the pumped dimers which induces the aforementioned transition.

4.3.4 Soliton trapping

Let us finally discuss the lowest input power range R1. When decreasing the power from the range R2, only a single soliton can be observed in the system and no transition is possible towards any other solution. On the graphs presented up to now in Fig. 4.16, the system is shown to only exhibit a single soliton localized on the right dimer (blue area). However this solution is not the only one that can be observed in this power range as, from one realization to another, the soliton can indeed be localized on any of the driven dimers depending on the history of the phase scan. To highlight this particular regime, we performed a phase scan during which we changed the input power: when $P/P_{\text{th}} \in \text{R1}$, polaritons localize under one of the pump spots and remain trapped in this position. To displace the soliton, one has to increase the input power back to $P/P_{\text{th}} \in \text{R2}$. The result of such procedure is presented in Fig 4.23. The chronographs of $\Delta\varphi$ and P/P_{th} are presented in Fig 4.23 (a) and the evolution of the fluid profile is displayed in Fig 4.23 (a). The experiment starts with a soliton localized on the left dimer (here placed at the bottom of the image) for $P/P_{\text{th}} = 0.42 \in \text{R1}$ and $\Delta\varphi \approx \pi$. $\Delta\varphi$ was scanned over 4π in both directions: we observe that the soliton remains localized on the left dimer. The input power was then brought to $P/P_{\text{th}} = 0.58 \in \text{R2}$ and $\Delta\varphi$ was scanned in the clockwise direction: we use the helical bistability effect to localize a single soliton on the right dimer (at the top of the image). The power was then brought back to $P/P_{\text{th}} = 0.42 \in \text{R1}$ and scanning $\Delta\varphi$ in both directions demonstrated that the soliton was trapped on the right dimer.

Figure 4.24 presents the density imbalance between the two driven dimers as a function of $\Delta\varphi$ in the power range R1. Two cases are represented depending on the initial state of the system: the soliton is either localized on the left or right dimer. A single stability branch is observed in both cases with an imbalance $I_{\text{LR}} \approx \pm 0.8$. We observe an oscillation of the density imbalance between $I_{\text{LR}} = \pm 0.88$ for $\Delta\varphi = 0$ and $I_{\text{LR}} = \pm 0.62$ for $\Delta\varphi = \pm\pi$: as the phase difference approaches $\Delta\varphi = \pm\pi$, the polariton density in the empty driven unit cell (without soliton) tend to increase (see Fig 4.23 (b)).

In the range R1, the input power is enough to maintain a soliton in a single of the two driven unit cells. However, the blueshift induced by the weak polariton density in the second driven unit cell is not sufficient to bring the associated eigenmode in resonance with the laser. As a consequence the soliton remains in an energy gap whatever the value of $\Delta\varphi$ and the system response is bound to one of the two possible chiral solutions. Note that the trapping mechanism is similar to the self-trapping usually observed in coupled waveguides when the self-focusing interaction overcomes hopping constants: here the trapping of the soliton occurs when the maximum accessible blueshift on the second driven unit cell remains smaller than the detuning between the band and the laser (which is roughly given by the hopping J).

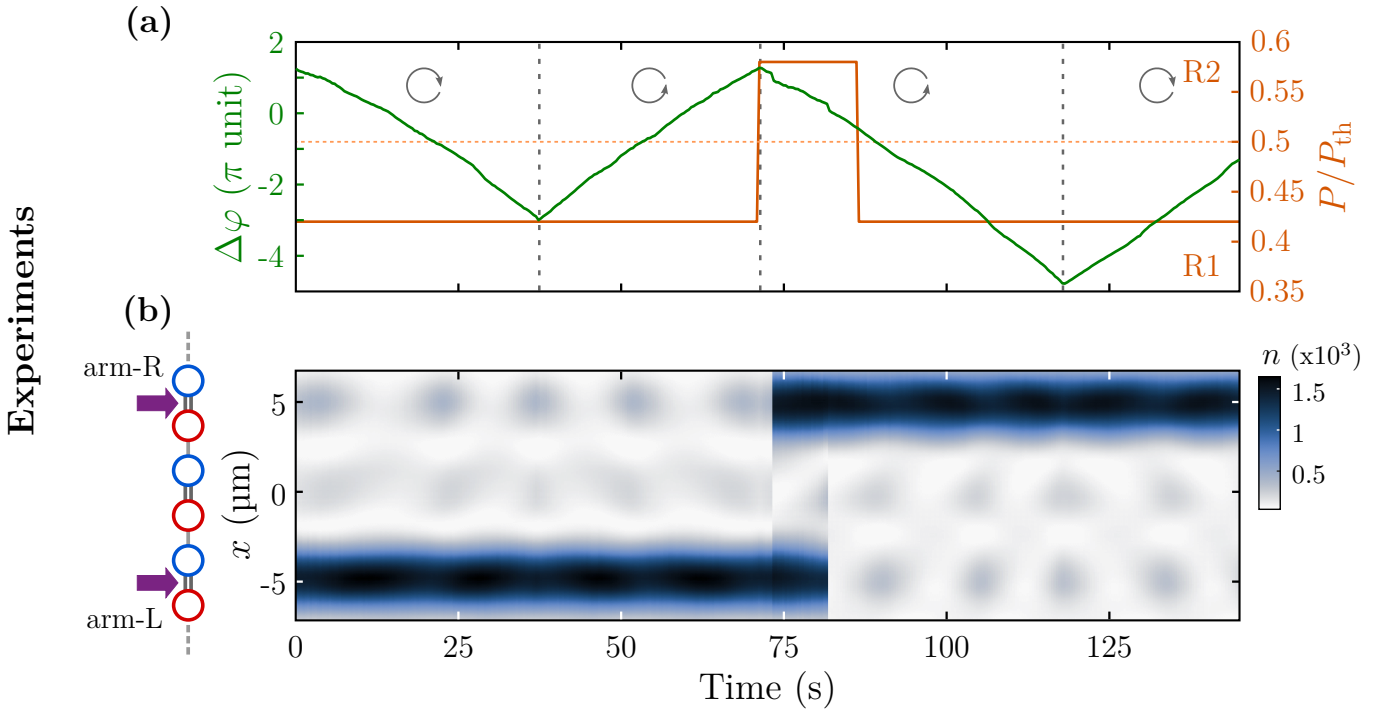


Figure 4.23: Demonstration of the on demand trapping of a soliton. **a**, Chronographs of the phase difference $\Delta\varphi$ (green) and of input power P/P_{th} (orange). Vertical dotted lines delimit the clockwise and counterclockwise intervals of the phase scan. The horizontal dotted line delimits the separation between the power ranges R1 and R2. **b**, Evolution of the density profile as a function of time. The left and right dimers are respectively displayed at the bottom and top of the image. A sketch of the lattice and drive architecture is displayed on the left.

In the power range R1, only two non-linear multi-stability branches are accessible to the system, which represent the two chiral solutions associated to the symmetry breaking. No channel allows switching from one solution to the other and as a consequence, both chiral solutions are robust to any perturbation on the phase of the drive: the system remains trapped in the state in which it is prepared.

In Fig. 4.25 we provide a sketch summarizing the power dependence of the system response observed through clockwise and counterclockwise phase scans.

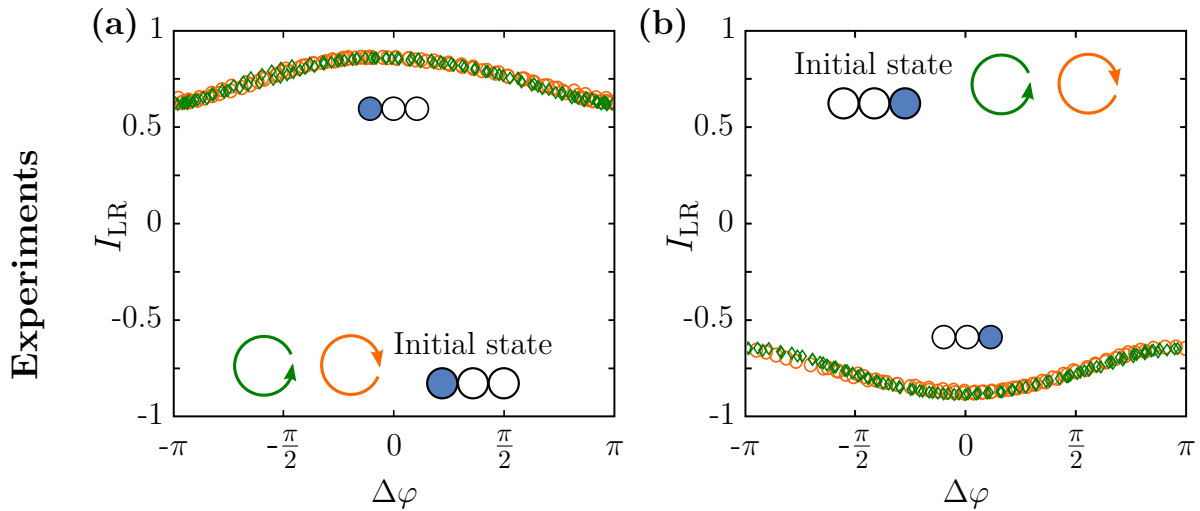


Figure 4.24: Evolution of the density profile of the polariton fluid as a function of the phase difference in the case of soliton trapped in the left dimer **(a)** and in the right dimer **(b)**. In both cases, the clockwise (counter-clockwise) scan is represented with orange (green) symbols.

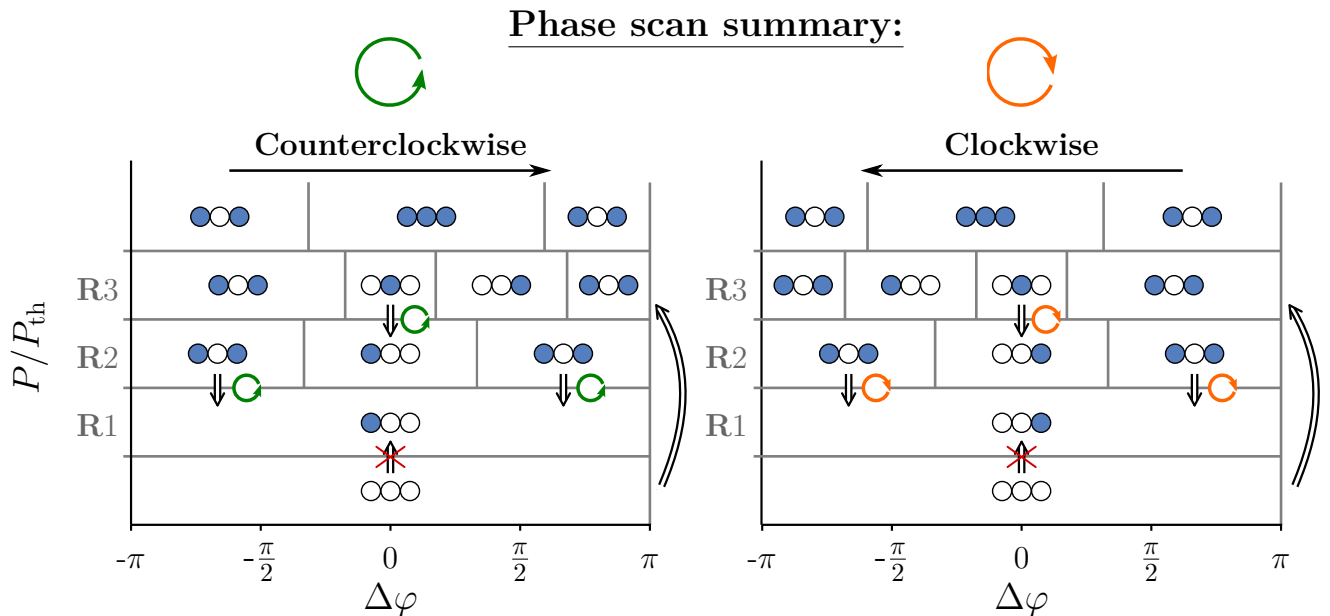


Figure 4.25: Power dependence of phase scans. Double arrows indicate one-way transitions.

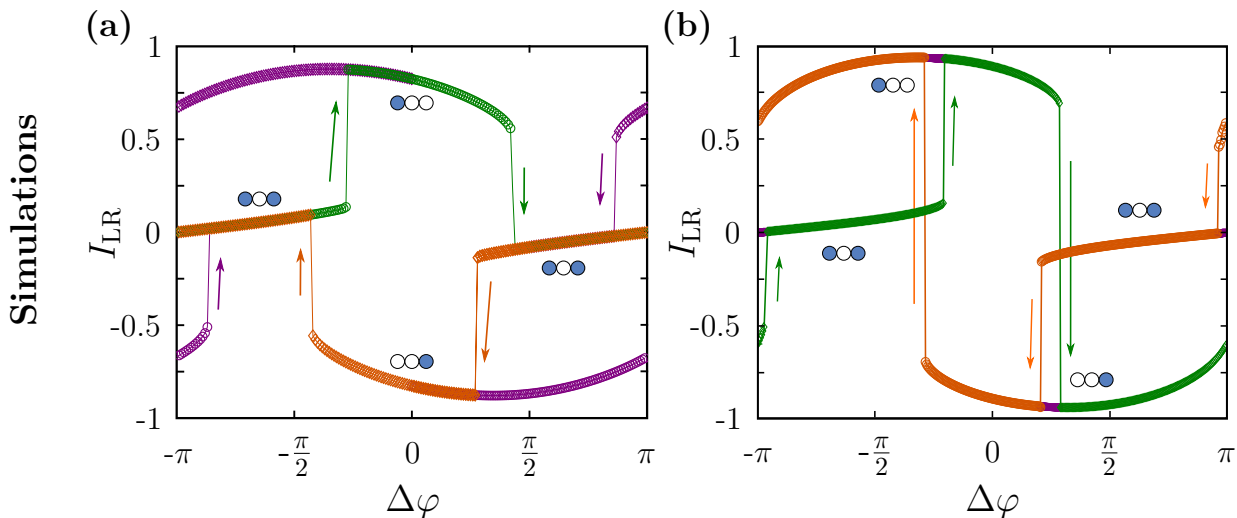


Figure 4.26: **a**, Evolution of the density imbalance between the two driven unit cells as a function of $\Delta\varphi$ for $P/P_{th} = 0.69$ in the case of the SSH model. **b**, Same as **(a)** for the AB model and $P/P_{th} = 0.59$. In both cases, green and orange symbols represent data points obtained for continuously counterclockwise and clockwise phase scans. Purple symbols show data points obtained by switching the direction of the scans. Colored arrows indicate the direction of the jumps.

4.3.5 The helical bistability: an effect specific from lattices with chiral symmetry

In this chapter we experimentally unveiled a phase multi-stability effect in which the system expresses a spatially chiral response to a helical driving protocol. We did not consider any system but the topological gap of the SSH lattice which is protected by the chiral symmetry. The observation of this chiral phenomenon raises an evident question: is it linked to the chiral symmetry of the SSH model? To answer this question, we propose to numerically study the case of a lattice with staggered onsite energies that we call the AB lattice and which do not possess the chiral symmetry.

A comparison between the SSH and AB models is presented in appendix A. We address the profile of solitons generated in the gap of the AB model and present the diagrams obtained *via* power and phase scans in the case of two pumps separated by $D = 2a$. We show that now clear discrepancies is observed between the two models when considering power scans. On the contrary, phase scans reveals that the helical bistability is not observed in the case of the AB model. To summarize the results of these numerical calculations, we here present the simulated multi-stability diagrams of the SSH and AB models. We performed elaborated scans of $\Delta\varphi$ to explore the stability range of each solutions. The results of this procedure is presented in Fig. 4.26.

In the case of the SSH model (see Fig. 4.26 (a)), we qualitatively retrieve the structure unveiled experimentally: the upper and lower branches associated to chiral solutions are only accessible from the symmetric solution and for a specific direction of the phase scan. The soliton localizes on the left (right) dimer during the counterclockwise (clockwise) phase scan and no direct channel exists between the two chiral solutions.

The result of simulation conducted in case of the AB lattice are presented in

Fig. 4.26 (b). One observes branches with a positioning and stability range comparable to the results obtained in the case of SSH gap solitons. However, the paths followed by the system as $\Delta\varphi$ is scanned in the clockwise or counterclockwise directions are clearly different from what we observed in Fig. 4.26 (a). In the case of the AB model, the two branches associated to chiral solution are linked by direct channels. When the soliton is localized on the left (right) dimer, scanning the phase in the counterclockwise (clockwise) direction leads to the transfer of the soliton on the right (left) dimer for $\Delta\varphi \approx \pi/3.5$ ($\Delta\varphi \approx -\pi/3.5$). Both chiral solutions are reached during a counterclockwise or clockwise scan of $\Delta\varphi$. As a result, the state of the system cannot be unequivocally related to the directionality of the phase scan: no information is kept about the history of the phase scan

We would like to stress on one particular observation. In the case of SSH, the system always jumps from a chiral solution to the symmetric one (magenta). On the contrary, in the AB case the system jumps from one chiral solution to the other one, even though the branch associated to the symmetric solution is stable at the position of the jumps (here $\Delta\varphi = \pm\pi/3.5$). Up to now we have not found an explanation to this phenomenon but the similarities between the two models lead us to believe that it originates from the unit cell distribution of the soliton wavefunctions. Interestingly, even though no evident relation exist between the different mirror operations involved in the effect (to our current knowledge), we notice that the helical bistability is only observed with the model presenting the chiral symmetry as defined for Hamiltonians.

4.4 Conclusion and perspectives

4.4.0.1 Summary

In this chapter we explored the interaction between gap solitons created in the topological gap of the SSH lattice. Our first results confirmed the results of previous works on soliton interaction: controlling the relative phase engineered in the drive between the two pumping spots enables to tune the effective interaction of two solitons. Numerical calculations demonstrated that engineering the band structure by tuning the sign of hopping constants enables to tailor the phase dependence of the interaction between two solitons. We then deepened the exploration of the case where the two pump spots are focused at the center of two dimers separated by one unit cell ($D = 2a$). Performing systematic ramps of the input power as a function of the phase difference imposed between the two pumps ($\Delta\varphi$), we demonstrated the existence of a symmetry breaking around $\Delta\varphi = 0$. This symmetry breaking leads to a chiral response of the system with the formation of a single soliton on either the left or right driven unit cell. Interestingly, performing systematic scans of $\Delta\varphi$ as a function of the input power, we unveiled a phase multi-stability effect occurring in the vicinity of the broken symmetry region. The chirality of the system response is directly related to the directionality of the phase scan: a given chiral solution is observed during the clockwise scan of $\Delta\varphi$ while its mirror-symmetric was reached during the counterclockwise scan. Finally, numerically comparing the case of the SSH model to the one of a lattice with staggered onsite energy (AB lattice), we evidenced an apparent relation between this helical bistability effect and the chiral symmetry of the SSH Hamiltonian.

4.4.0.2 Generalization of the Helical bistability and observation in higher dimensions

This work raises many questions. On the one hand it would be interesting to extend these ideas to solitons in higher dimensions, using 2D lattices exhibiting the chiral symmetry such as the honeycomb or 2D Lieb lattices. On the other hand it is stimulating to deepen our understanding of the effect. What are the minimal ingredients required to observe the "Helical bistability" and is it possible to develop a more analytical description of this effect? In particular, the role of the chiral symmetry of the Hamiltonian in the non-linear transitions undergone by the system remains to be explained. Finding a smaller system exhibiting the same behavior would help to get more insight on the underlying physics. In the next chapter, we demonstrate the helical bistability effect to be a general phenomenon which can be observed in a system of two coupled Kerr resonator.

Chapter 5

Chiral symmetry breaking at the heart of the Helical bistability

This last chapter is dedicated to a deeper exploration of the helical bistability effect described in chapter 4. The chiral symmetry of the SSH model (sub-lattice symmetry with respect to the σ_Z operator) was shown to play a particular role and we propose to study the simplest model exhibiting such symmetry. We here address the general case of two coupled Kerr resonators, which is sometimes called “Bose-Hubbard dimer” in the literature. We show that this simple system can be subjected to a chiral symmetry breaking and exhibit the helical bistability effect. We start by a general description based on two coupled driven-dissipative Gross-Pitaevskii equations, map this system to a classical pseudo-spin 1/2 and represent it using a Bloch sphere. Using this representation, we give an intuitive explanation of the effect. The helical bistability effect is thus found to be very general and we discuss different possibilities for its experimental observation. We report on the observation of the Helical bistability using solitons in two coupled dimers of the SSH lattice. Indeed, we show a complete equivalence of this configuration with a set of two coupled resonators.

5.1 Helical bistability in two coupled Kerr resonators

The helical bistability effect consists in inducing chirality in the response of a symmetric system using the external drive. Observing this effect thus presupposes the existence of symmetry broken phases in the system. In this section, we turn to the simplest system exhibiting a spontaneous symmetry breaking: two coupled driven-dissipative resonators with a Kerr non-linearity. We show that in the vicinity of this symmetry breaking, it is possible to observe the effect of helical bistability. The representation of the system response on the Bloch sphere is particularly insightful as it helps highlighting the self-trapping mechanism at the origin of the bistability effect.

5.1.1 Phase bistability of two coupled Kerr resonators

We consider a system of two coupled resonators that we label L and R with a repulsive onsite Kerr non-linearity ($g > 0$, similar results are obtained for $g < 0$). The system dynamics is described by the following set of non-linear equations:

$$\begin{aligned} i\hbar\partial_t\Psi_L &= \left(E_L - \hbar\omega_p - i\frac{\hbar\gamma}{2} + g|\Psi_L|^2\right)\Psi_L - J_{LR}\Psi_R + iF_L \\ i\hbar\partial_t\Psi_R &= \left(E_R - \hbar\omega_p - i\frac{\hbar\gamma}{2} + g|\Psi_R|^2\right)\Psi_R - J_{RL}\Psi_L + iF_R \end{aligned} \quad (5.1)$$

To observe a spontaneous symmetry breaking induced by the onsite interactions, the system has to be invariant by exchange of the two resonators: $J_{LR} = J_{RL} = J_0$ and $E_L = E_R = E_0$. Note that the system thus possess the chiral symmetry with respect to the σ_Z operator, which is precisely the operator involved in the chiral symmetry of the SSH model.

We address the case where the driving field has the same modulus in each resonator, $|\mathbf{F}\rangle = [F_L, F_R]^T$ with $F_L = F_0 e^{i\varphi_L}$ and $F_R = F_0 e^{i\varphi_R}$, such that the driving field does not break the system symmetry with respect to σ_Z ($\langle\mathbf{F}|\sigma_Z|\mathbf{F}\rangle = 0$). It yields:

$$\begin{aligned} i\hbar\partial_t\Psi_L &= \left(E_0 - \hbar\omega_p - i\frac{\hbar\gamma}{2} + g|\Psi_L|^2\right)\Psi_L - J_0\Psi_R + iF_0 \\ i\hbar\partial_t\Psi_R &= \left(E_0 - \hbar\omega_p - i\frac{\hbar\gamma}{2} + g|\Psi_R|^2\right)\Psi_R - J_0\Psi_L + iF_0 e^{-i\Delta\varphi} \end{aligned} \quad (5.2)$$

As seen in the previous chapter, observing a spontaneous symmetry breaking in a system of two coupled identical resonators requires the system to be driven with a phase pattern equivalent to the one of the system highest energy mode. Figure 5.1 presents the numerical simulation of this spontaneous symmetry breaking in the case $J_0 = 100 \mu\text{eV}$, $\hbar\gamma = J_0/3$ and $g = 0.1 \mu\text{eV}$ when the system is driven at an energy $\hbar\omega_p = E_0$ with an anti-symmetric drive pattern: $F_R = F_L \exp(i\pi)$ (see Fig. 5.1 (a)). Figure 5.1 (b) shows the two possible trajectories followed by the density in each resonator ($n_i = |\Psi_i|^2$) as a function of the input power in each resonator $|F_0|^2$. We

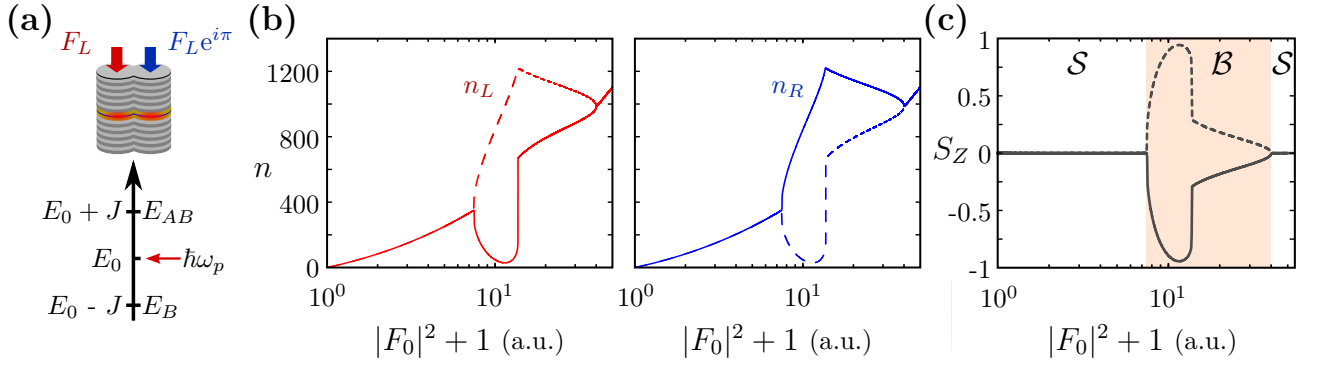


Figure 5.1: **a**, Schematic representation of the system. **b**, Evolution of the density in each resonator as a function of the input power. Two different solutions can be obtained which are represented with solid and dashed lines. Red (blue) color is associated to the left (right) resonator. **c**, Representation of the symmetry breaking using the pseudo-spin S_Z . The solid and dashed lines correspond to the two different solutions presented in panel **(b)**. The symmetric and broken-symmetry phases are respectively labeled \mathcal{S} and \mathcal{B} .

observe a symmetry breaking with two possible solutions associated to a localization of density on the left or right resonator. This feature is better highlighted by computing the density imbalance between the two resonators, which corresponds to the pseudo-spin S_Z associated to the Pauli matrix and chiral operator σ_Z :

$$S_Z = \frac{\langle \Psi | \sigma_Z | \Psi \rangle}{\langle \Psi | \Psi \rangle} = \frac{n_L - n_R}{n_L + n_R} \quad (5.3)$$

where $|\Psi\rangle = [\Psi_L, \Psi_R]^T$. The evolution of S_Z as a function of the input power is presented in Fig. 5.1 (c). In the broken symmetry phase (\mathcal{B}), one can observe that the pseudo-spin reaches values up to 0.95, which means that the field density is almost fully localized on a single resonator.

We then computed scans of the phase difference $\Delta\varphi = \varphi_L - \varphi_R$ for different values of the input power: these calculations evidence different regimes among which we find the helical bistability effect. Figure 5.2 presents the results of these calculations. At low power (range $\mathcal{Z}1$ and Fig. 5.2 (b)) a single solution is explored which exhibits a variation of S_Z with extrema around $\Delta\varphi = \pm\frac{\pi}{2}$. To understand this phenomenon, we recall that a phase gradient of the field $|\Psi\rangle$ is responsible for a net density flux in the gradient direction. Writing $\Psi_L = \sqrt{n_L} \exp(i\phi_L)$, $\Psi_R = \sqrt{n_R} \exp(i\phi_R)$ and $\Delta\phi = \phi_R - \phi_L$, we thus expect a flux from L to R (R to L) for $0 < \Delta\phi < \pi$ ($-\pi < \Delta\phi < 0$). In the present case, calculations show that the phase difference imposed by the driving field leads to $S_Z \propto \sin(\Delta\varphi)$ in the limit $|F_0|^2 \ll 1$. In the range $\mathcal{Z}2$, the resonators energies are renormalized by the interactions, and the linear branch splits. We observe the appearance of two discontinuities in the evolution of S_Z versus $\Delta\varphi$. We can distinguish two branches, the first one (①) showing a strong variation of S_Z around $\Delta\varphi = \pi$ and exhibiting an increased maximum value for $|S_Z|$ as compared to the one observed in Fig. 5.2 (b) (linear case). The second branch (②) shows less variation of S_Z and almost no spin polarization. This correspond to solutions having significant polariton densities in both resonator: it corresponds to the upper branch one can observe by performing a bistability experiment with the bonding mode of the system *via* input power ramps. For some values of $\Delta\varphi$, both solutions can be simultaneously stable, leading to a bistable behavior in phase.

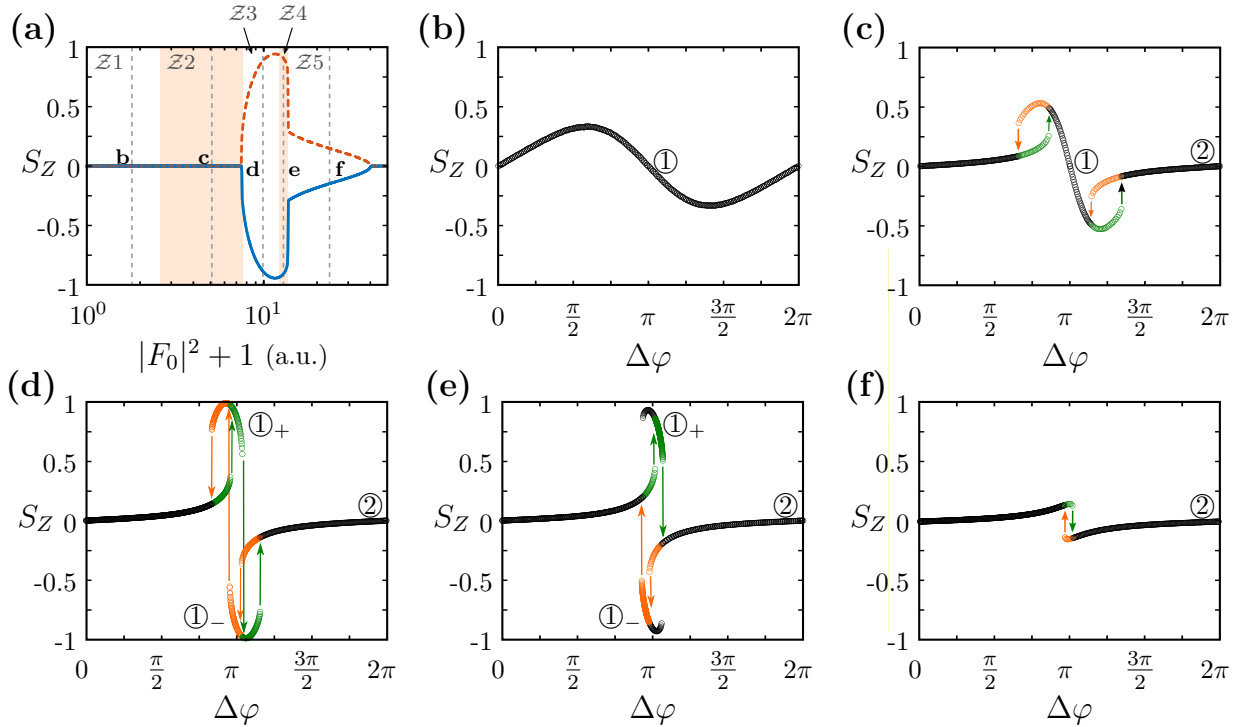


Figure 5.2: **a**, Reproduction of the symmetry breaking presented in Fig. 5.1 (c). The power ranges associated to different regimes are highlighted by white and orange patches. They are labeled Z_j with $1 \leq j \leq 5$. **b-f**, Evolution of S_Z as a function of $\Delta\varphi$ for different values of the input power which are marked with vertical dashed lines in **(a)**. Orange and green data points indicate bistability regions which are exclusively explored during the clockwise and counterclockwise phase scans. Colored arrows indicate the direction of the jumps. The power ranges associated to each regime are highlighted using light orange patches in **(a)**.

In the ranges Z_3 and Z_4 (Fig. 5.2 (d-e)), the highly spin-polarized branch splits into two separated branches with opposite spin $|S_Z| \approx \pm 1$, we thus labeled them $\textcircled{1}_+$ and $\textcircled{1}_-$. Interestingly, in the range Z_4 , only one of these branches is reached during the clockwise and counterclockwise scan of $\Delta\varphi$: during the counterclockwise scan, the system only explores the branch $\textcircled{1}_+$ while the branch $\textcircled{1}_-$ is explored during the clockwise scan of $\Delta\varphi$. This phenomenon is what we call the Helical bistability: the helicity of the drive protocol induces a given chirality in the system response (Fig. 5.2 (e)).

In the range Z_5 , only the branch $\textcircled{2}$ is observed with almost no variation of S_Z . In addition to these data, the evolution of the total density is presented in appendix B.1, which shows that above the range Z_1 , all stability branches are associated with a non-negligible interaction energy.

5.1.2 Representation on the Bloch Sphere

Interestingly, the elementary system we consider can be represented on a Bloch sphere: in addition to the pseudo-spin associated to the σ_z Pauli matrix, one can

compute the pseudo-spins associated to σ_X and σ_Y .

$$S_X = \frac{\langle \Psi | \sigma_X | \Psi \rangle}{\langle \Psi | \Psi \rangle} = \frac{2\sqrt{n_L n_R} \cos(\Delta\phi)}{n_L + n_R} \quad (5.4)$$

$$S_Y = \frac{\langle \Psi | \sigma_Y | \Psi \rangle}{\langle \Psi | \Psi \rangle} = \frac{2\sqrt{n_L n_R} \sin(\Delta\phi)}{n_L + n_R} \quad (5.5)$$

Similar mapping to a classical spin $\frac{1}{2}$ can be done when considering the driving field, writing $|F\rangle = [F_L, F_R]^T$ we define:

$$S_{X,P} = \frac{\langle F | \sigma_X | F \rangle}{\langle F | F \rangle} = \frac{2\sqrt{|F_L|^2 |F_R|^2} \cos(\Delta\varphi)}{|F_L|^2 + |F_R|^2} \quad (5.6)$$

$$S_{Y,P} = \frac{\langle F | \sigma_Y | F \rangle}{\langle F | F \rangle} = \frac{2\sqrt{|F_L|^2 |F_R|^2} \sin(-\Delta\varphi)}{|F_L|^2 + |F_R|^2} \quad (5.7)$$

$$S_{Z,P} = \frac{\langle F | \sigma_Z | F \rangle}{\langle F | F \rangle} = \frac{|F_L|^2 - |F_R|^2}{|F_L|^2 + |F_R|^2} \quad (5.8)$$

Figure 5.3 presents the result of this mapping to classical spins $\frac{1}{2}$. The scans protocols are summarized in Fig. 5.3 (a). We represent $\tilde{S}_{j,P} = S_{j,P} \log_{10}((|F_L|^2 + |F_R|^2)/2 + 1)$ for $j = \{X, Y, Z\}$ so that the norm of $\tilde{S}_P = [\tilde{S}_{X,P}, \tilde{S}_{Y,P}, \tilde{S}_{Z,P}]^T$ contains the information on $|F_0|^2$. As we restrict our two pumps to have the same constant modulus, the trajectories of the driving field are represented by concentric circles in the equator of the sphere. Figure 5.3 (b-f) directly corresponds to graphs presented in Fig. 5.2 (b-f).

In the linear regime ($\mathcal{Z}1$, see Fig. 5.3 (b)) the system describes a closed trajectory in a plan which is tilted with respect to the sphere equator. The linear trajectory can be derived from the set of equations 5.1 by neglecting non-linear terms. It yields:

$$S_X = \cos(\Delta\varphi), \quad S_Y = \sin(\Delta\varphi) \frac{J^2 - \gamma^2/4}{J^2 + \gamma^2/4}, \quad S_Z = \sin(\Delta\varphi) \frac{\gamma J}{J^2 + \gamma^2/4} \quad (5.9)$$

In the linear regime we note that the system response rotates in opposite direction with respect to the pump: $S_{Y,P} \propto \sin(-\Delta\varphi)$ while $S_Y \propto \sin(\Delta\varphi)$. If $\Delta\varphi$ is scanned in the clockwise direction, $\Delta\phi$ cycles in the counter-clockwise direction. On the contrary for $|F_0|^2 \rightarrow \infty$, we expect the system to follow the trajectory imposed by the pump: the steady state of the set of equations 5.1 is dominated by the non-linear terms and one can do the approximation $g|\Psi_j|^2\Psi_j \approx -iF_j$ with $j = \{L, R\}$. In that limit, the field in a resonator is fully determined by the driving field applied to this resonator: $\phi_j = \varphi_j - \frac{\pi}{2}$ and $|\Psi_j|^2 = (|F_j|/g)^{2/3}$. In the intermediate regimes $\mathcal{Z}2$ to $\mathcal{Z}4$, we observe a competition between the two effects (Fig. 5.3 (c-e)). The pump imposes the state of the system on the branch ② in the vicinity of $S=[S_X=1, S_Y=0, S_Z=0]$ with a range increasing with the input power. The other branches (① $_{\pm}$) correspond to a renormalization of the linear behavior presented in Fig. 5.2 (b) and this is particularly well observed in Fig. 5.2 (c): the branch crossing $S=[S_X=0, S_Y=-1, S_Z=0]$ is still relatively close to the trajectory followed in the linear regime. As the input power increases (Fig. 5.2 (d)), the renormalization of the branch pushes the system toward the north and south poles. This can be explained by the onsite nature of the considered Kerr interaction (contact polariton-polariton interaction): a large imbalance between the two resonators induces a spectral shift that tends to decouple the resonators and the interaction is thus responsible for self-trapping of field density inside one resonator (see Ref. [216]).

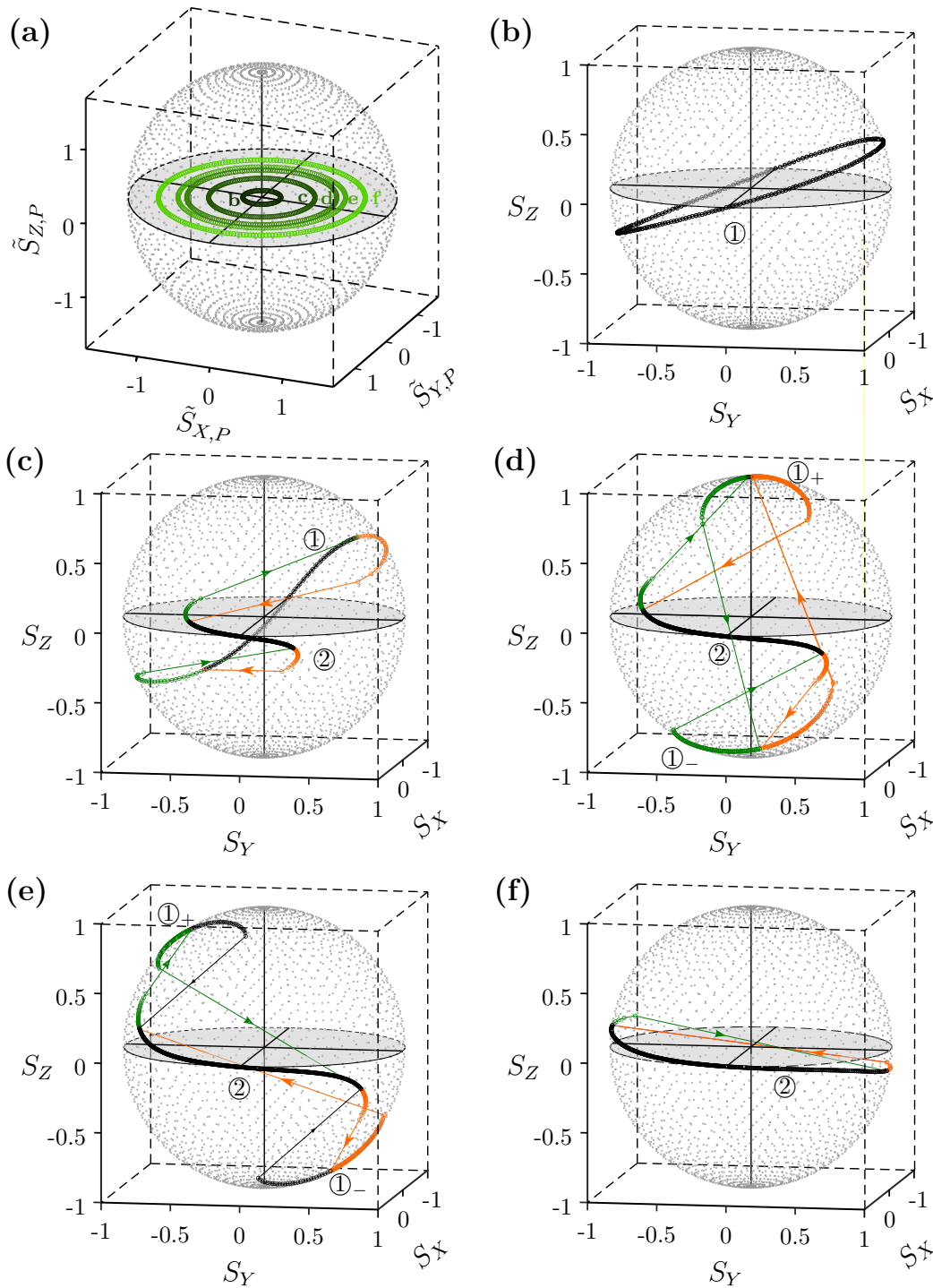


Figure 5.3: **a**, Representation of the phase scan protocols using decomposition of the driving field on Pauli matrices, the radius is chosen to represent the input power $|F_0|^2$ in logarithmic scale. **b-f**, Bloch sphere representation of the trajectories followed by the field inside the two coupled resonators for the five regimes evidenced in Fig. 5.2. Orange and green data points indicate bistability regions which are exclusively explored during the clockwise and counterclockwise phase scans. Colored arrows indicate the direction of the spin switches.

The helical bistability effect is clearly evidenced in Fig. 5.2 (e) as the system only explores the north (south) hemisphere during the counterclockwise (clockwise) scan of $\Delta\phi$. We interpret the helical bistability phenomenon as a competition between the self-trapping associated to the density and the flux induced by the phase difference $\Delta\phi$. The transition between the regimes presented in Fig. 5.2 (d-e) occurs when the self-trapping mechanism is sufficiently strong (high enough density) to prevent the density flux to reverse the density imbalance.

In this section we numerically demonstrated that the helical bistability effect can be predicted in the simplest system presenting a chiral symmetry breaking. We considered a set of two coupled identical resonators with an onsite Kerr non-linearity and showed that, in the vicinity of symmetry broken phase, there exists a power range for which the helicity of the phase scan is directly related to the chirality of the system response. Due to the two component structure of the system, we were able to represent the effect on the Bloch sphere. This representation better evidences the mechanism at the origin of the effect: a competition between the self trapping mechanism associated to onsite interactions and the density flux induced by the phase gradient.

5.2 Observation with gap solitons

To observe the helical bistability in its simplest form, we considered a set of two coupled pillars but due to technical limitations, principally heating of these small structures, we have not yet managed to observe the effect in such an elementary structure ¹. We here report on the observation of the helical bistability using gap solitons of the SSH model in the simplest possible configuration: the two pumps were placed on neighboring unit cells ².

5.2.1 The SSH unit cell as a single Kerr resonator

To experimentally reproduce our numerical results, we consider a SSH lattice and the excitation setup comprising two pump beams. The pump spots are focused onto the centers of two neighboring dimers and we here propose to show why this system can be mapped to two coupled Kerr resonators. We recall the set of Gross-Pitaevskii equations governing the temporal evolution of the polariton field at the middle of

¹Our understanding is that 0D structures do not thermalize efficiently compared to 1D structures.

²The results discussed here are very reminiscent of those presented in Chap. 4. In the previous chapter, we did not address this case as the interaction is not mediated by the chiral tails of the solitons. In addition, it is unclear whether this system completely falls under the description of two interacting solitons while it can be interpreted as a large single soliton (Truncated Bloch Wave).

the SSH gap:

$\forall m :$

$$\begin{aligned} i\hbar\partial_t\Psi_{A,m} &= -J\Psi_{B,m} - J'\Psi_{B,m-1} - (\Delta E + i\frac{\gamma_0}{2})\Psi_{A,m} + g|\Psi_{A,m}|^2\Psi_{A,m} + iF_{A,m} \\ i\hbar\partial_t\Psi_{B,m} &= -J\Psi_{A,m} - J'\Psi_{A,m+1} - (\Delta E + i\frac{\gamma_0}{2})\Psi_{B,m} + g|\Psi_{B,m}|^2\Psi_{B,m} + iF_{B,m} \end{aligned} \quad (5.10)$$

where the drive architecture can be summarized as $F_{A,m} = F_{B,m} = 0 \forall m \neq \{0, 1\}$, $F_{A,0} = F_{B,0} = F_0$ and $F_{A,1} = F_{B,1} = F_0 \exp(-i\Delta\varphi)$. We show that the system reduces to two coupled Kerr resonators, constituted by the bonding mode of each driven dimer:

1. Both dimers are blueshifted, they are thus decoupled from the rest of the lattice. From our study of SSH gap soliton, we know that undriven unit cells do not play a role in the system response for input power $P/P_{\text{th}} < 5$ ³ (see Chap. 3). In the present study, the input power will always remain far below this limit.
2. Each pump spot is positioned at the center of a dimer, consequently, there is no spatial overlap between the driving field and the anti-bonding mode.
3. The drive energy is set at the center of the SSH gap and is thus below the anti-bonding modes. As a result, the spectral overlap between the driving field and anti-bonding modes can only decrease due to the blueshift induced by interactions.

Only the bonding modes of the driven dimers are relevant to describe the system: it can be approximated to a set of two coupled Kerr resonators with onsite energies $E_L = E_R = \hbar\omega_p - J$ and coupled with a hopping strength J' (see Fig. 5.4).

5.2.2 Phase diagrams and symmetry breaking

To determine the power range corresponding to the symmetry broken phases (\mathcal{B}), we first perform power ramps various values of the phase difference between the two pumps collecting the emission of each driven unit cells on separated photo-detectors⁴. The result of the procedure is presented in Fig. 5.5 with color encoded images⁵. The diagrams of the normalized density associated to individual unit cells are provided in appendix B.2.1.

The two diagrams (upward and downward scan of P) reveal the existence of a region associated to a broken symmetry (red and blue patches) which is located in between the linear (black region) and non-linear regime (magenta). The interface between the red and blue regions is located in the vicinity of $\Delta\varphi = \pi$, signaling that

³We recall that P_{th} is the power threshold at which a single soliton is formed in presence of a single pump spot.

⁴We recall that the input power of each beam is balanced such that P_{th} is reached simultaneously for both resonators.

⁵These images were obtained following the procedure detailed in Chap. 4. We replaced the green layer of the RGB image by a blank matrix (Fig. 4.13).

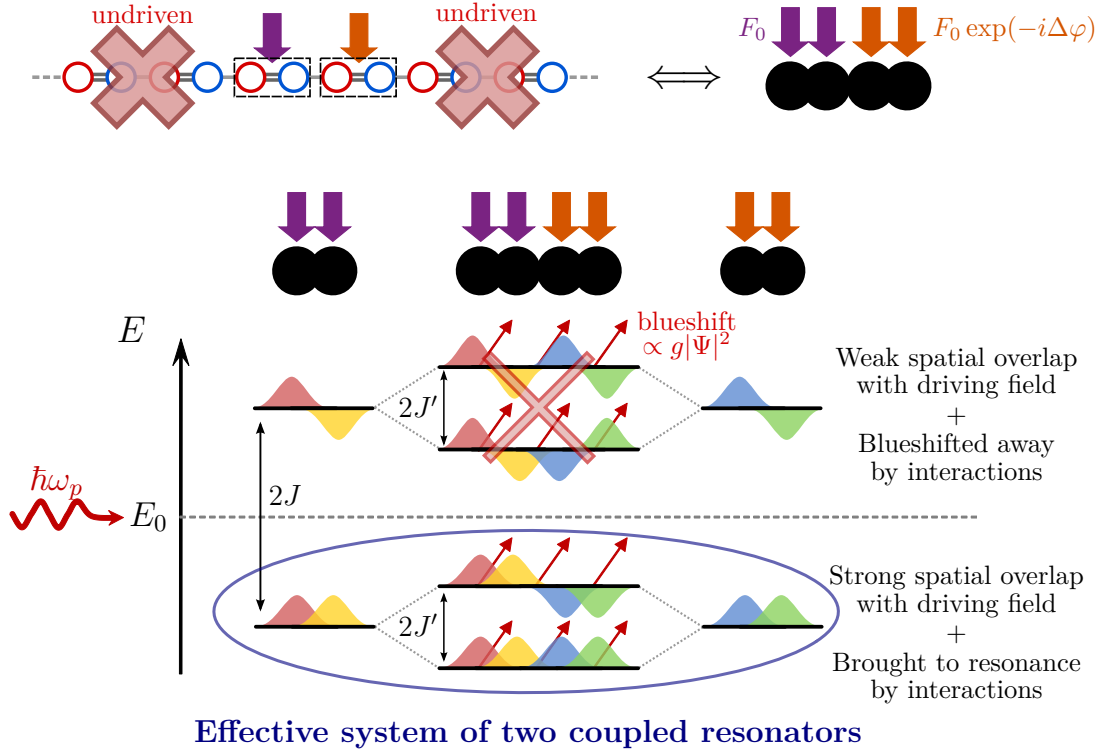


Figure 5.4: Scheme presenting how driving two unit cells of the SSH lattice can be mapped to two driven-dissipative coupled Kerr resonators.

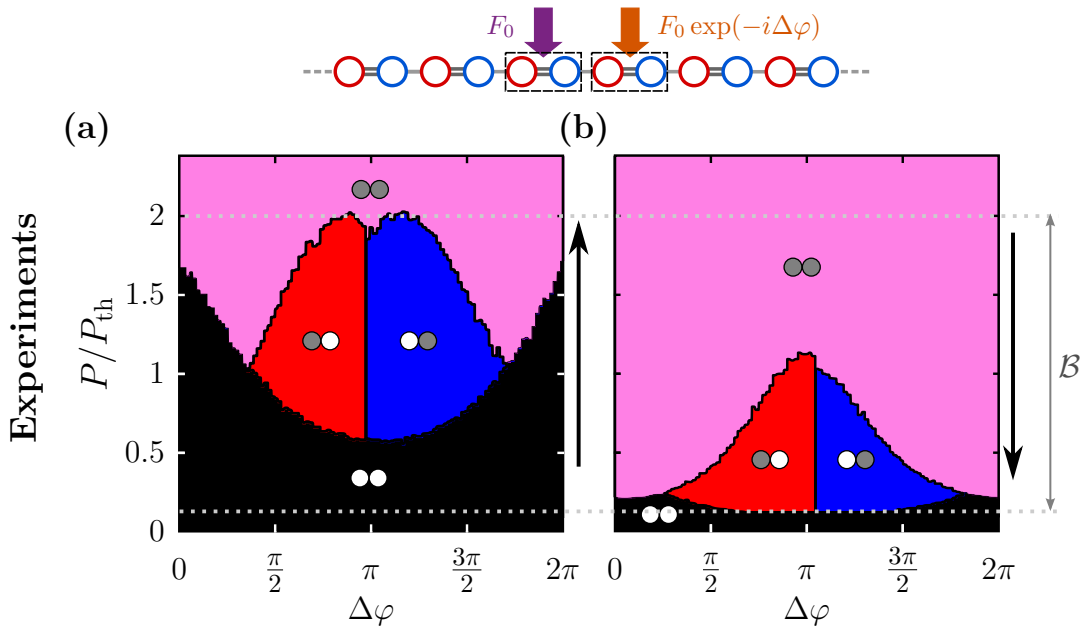


Figure 5.5: Phase diagrams of the non-linear solutions observed by performing power scans as a function $\Delta\varphi$. **a-b**, Upward and downward scans of the input power, the scan direction is indicated by an arrow at the right of each panel. A sketch of the lattice is displayed on top.

the effective coupling between driven unit cells is positive. Comparing these diagrams to the results presented in Chap. 4 where the effective coupling was negative, we observe the expected exchange between red and blue region with respect to the interface.

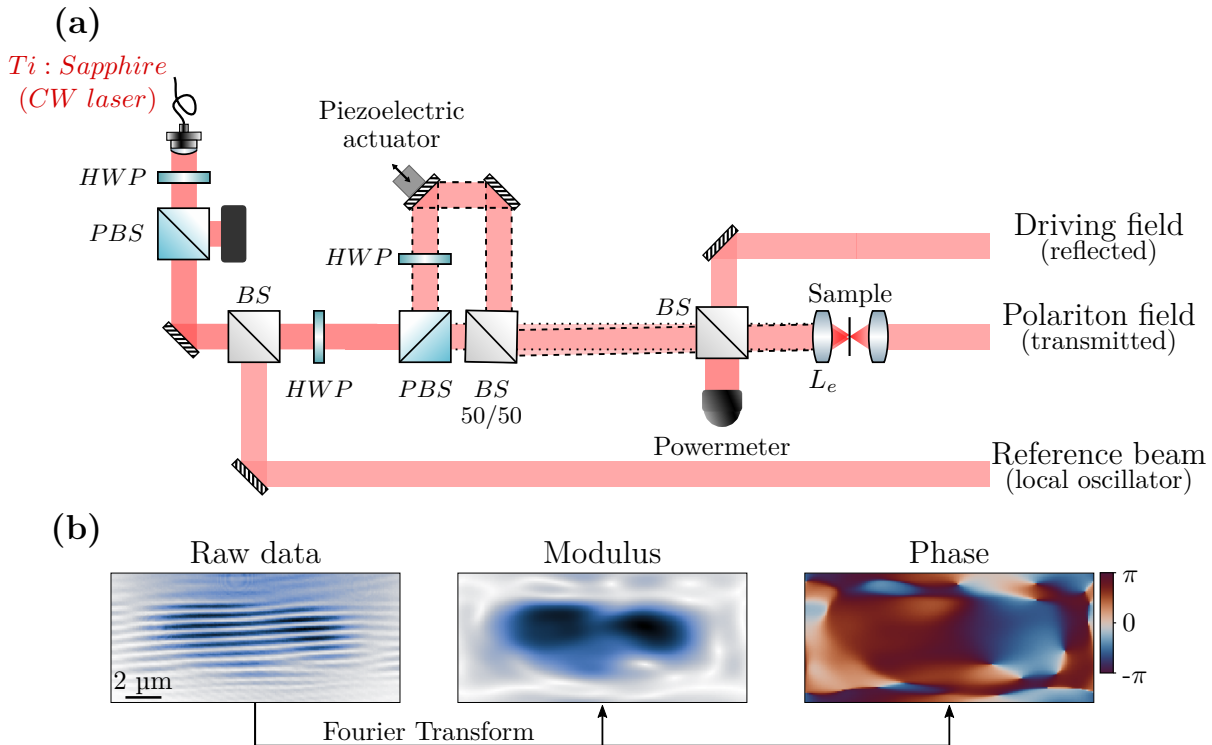


Figure 5.6: **a**, Experimental setup for performing the polariton field tomography. **b**, Left: Example of fringe pattern obtained by interfering the polariton field with the reference beam. Right: modulus and phase pattern of the polariton field extracted by Fourier analysis.

5.2.3 Experimental Helical bistability, representation on the Bloch sphere

We now turn to the exploration of the system response observed when performing scans of $\Delta\varphi$ for fixed input power. To enable full tomography of the spin state and represent the system response on the Bloch sphere, we need to measure the three components of S . We therefore perform the tomography of the polariton field: while performing scans of $\Delta\varphi$, we monitor the polariton density as well as the phase relation between the fields in each of the unit cells. To do so, we slightly modified the experimental setup (see Fig. 5.6 (a)) by adding two beam splitters: the first one allows to monitor the pump field by collecting photons reflected from the sample surface while the second one is placed before the delay line and is used as a phase reference to produce interference with the driving and polariton fields. The important parameters, n_L , n_R and $\Delta\phi$, are extracted by Fourier analysis of the measured interferograms. An example is provided in Fig. 5.6 (b).

We performed phase scans for various values of the input power and extracted the values of S_X , S_Y and S_Z associated to the polariton field. The representation of the polariton field evolution on the Bloch sphere is presented in Fig. 5.7. Experimental results are in very good agreement with numerical predictions. In the linear regime (Fig. 5.7 (a)) the system follows a closed trajectory tilted with respect to the equator while this trajectory is pushed toward the equator in the non-linear regime (Fig. 5.7 (d)). The intermediate regimes are also well captured (Fig. 5.7 (b-c)), the system can be brought to the north and south poles of the sphere in presence of

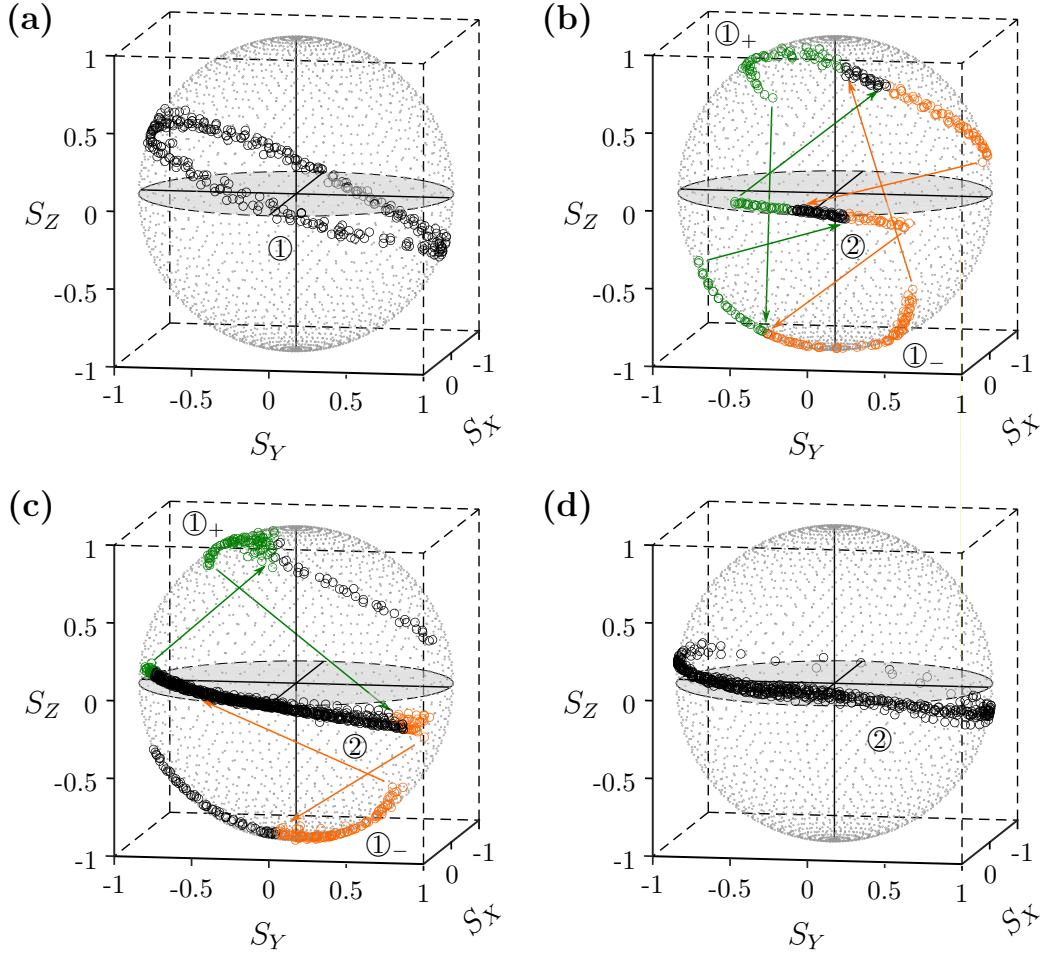


Figure 5.7: Bloch sphere representation of the stability branches covered during phase scans for fixed input power with **a:** $P/P_{\text{th}} \approx 0.1$, **b:** $P/P_{\text{th}} = 0.77$, **c:** $P/P_{\text{th}} = 0.94$ and **d:** $P/P_{\text{th}} = 1.85$. Orange and green data points indicate bistability regions which are exclusively explored during the clockwise and counterclockwise phase scans. Colored arrows indicate the direction of the jumps.

sufficient inter-particle interactions. For $P/P_{\text{th}} = 0.94$ (panel c), the system can only be brought to the north (south) pole by a counterclockwise (clockwise) scan of $\Delta\varphi$: this is the helical bistability phenomenon. The corresponding graphs of S_Z as a function of $\Delta\varphi$ are provided in appendix B.2.2.

To the best of our knowledge this is the first time such helical bistability is discussed and observed experimentally.

5.2.3.1 Side note

Note that we can use this representation on the Bloch sphere to revisit the experimental results presented in Chap. 4 where we studied the interaction of two gap solitons *via* their chiral tails. We perform similar tomography experiment for pump spots separated by $D = 2a$ (configuration considered in Chap. 4). In appendix B.2.3, we provide the Bloch sphere representations of two effects discussed in this configuration: the soliton trapping and the helical bistability unveiled at low input power. Due to a non negligible density in the central undriven unit cell at higher power,

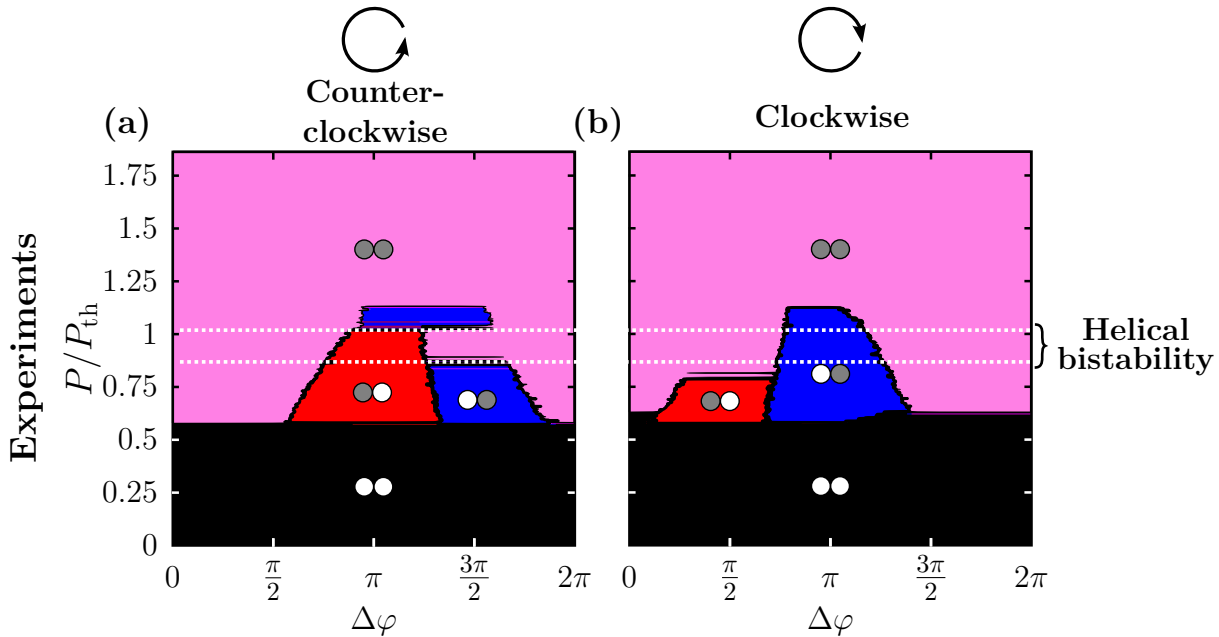


Figure 5.8: Phase diagrams of the non-linear solutions observed by performing phase scans for a fixed input power. **a-b**, Counterclockwise and clockwise scans of $\Delta\varphi$, the scan direction is indicated by an arrow at the top of each panel.

the system becomes three component and the representation on the Bloch sphere is not adequate.

5.2.4 Phase diagrams associated to phase scans

To complement our experimental investigations of the helical bistability effect, we realized systematic scans of $\Delta\varphi$ as a function of P/P_{th} while collecting the intensity signal using photo-detectors. In this way, we can identify the power ranges associated to each bistability regime. Figure. 5.8 presents the color encoded images summarizing the results. As no difference was observed between the two directions of the power scan, we only present phase scans obtained during the upward scan of the input power. The helical bistability is observed in the power range $0.9 < P/P_{\text{th}} < 1.0$ with the soliton localizing on the left (right) unit cell for a counterclockwise (clockwise) scan of $\Delta\varphi$. The regime associated to the numerical calculation presented in Fig. 5.2 (d) is observed in the range $0.6 < P/P_{\text{th}} < 0.8$: in the vicinity of $\Delta\varphi = \pi$ the soliton localizes on one of the two dimers and hops from this dimer to the other, which corresponds to a pseudo-spin switching from 1 to -1 (-1 to 1) during the counterclockwise (clockwise) scan of $\Delta\varphi$ ⁶. Note that an asymmetry is observed in the power range $1.0 < P/P_{\text{th}} < 1.12$, which we attribute to a slight asymmetry of the setup alignment.

⁶Note that the regime associated to the numerical calculation presented in Fig. 5.2 (c) is not observed experimentally, this discrepancy originates from the energy detuning between the laser and the eigenmodes. In simulations, tuning the pump energy to $\hbar\omega_p = E_0 + J$ allows reproducing experimental conditions.

5.3 Conclusion and perspectives

5.3.0.1 Summary

We have numerically revealed the helical bistability effect in its simplest form, considering solely two coupled Kerr resonators. We hereby demonstrated that this effect, inducing chirality in a symmetric system, is a very general phenomenon emerging in a set of two coupled non-linear Schrödinger equations. Thanks to the binary nature of the system, we were able to map it to a classical spin $\frac{1}{2}$ and to represent its trajectory on the Bloch sphere. The helical bistability is interpreted as a competition between the density flux and the self-trapping mechanism induced by repulsive interactions. We experimentally observe this novel non-linear effect by pumping two neighboring unit cells of a SSH lattice. Using interferometry, we realized the tomography of the polariton field while performing scans of $\Delta\varphi$ for fixed values of P/P_{th} . In this way we were able to experimentally follow the system trajectory on the Bloch sphere and to unambiguously reveal the different predicted regimes.

5.3.0.2 Generalizations of the model

Helical bistability occurs in any system described by the two coupled equations Eq. 5.2. Pivotal to this effect, the dominant interaction term must not couple the two equations, thus allowing for self-trapping. Since the polariton-polariton interaction is anisotropic ($V_{\sigma_+, \sigma_+} = V_{\sigma_-, \sigma_-} > V_{\sigma_+, \sigma_-} = V_{\sigma_-, \sigma_+}$), we can predict a helical bistability of polaritons in an elliptical or rectangular micro-pillar which would lead to emission of circularly polarized light. In a rectangular pillar, the cylindrical symmetry is broken which leads to a lift of polarization degeneracy between polariton states: the system presents two s modes at different energies with linear polarizations that we can label H and V . These two states can actually be described as resulting from the linear coupling between σ_+ and σ_- polarization states. Neglecting the cross-polarization interaction $V_{\sigma_+, \sigma_-} = V_{\sigma_-, \sigma_+}$, the set of equations describing the system is completely analogous to the one considered in this chapter:

$$\begin{aligned} i\hbar\partial_t\Psi_+ &= \left(E_0 - \hbar\omega_p - i\frac{\hbar\gamma}{2} + V_{\sigma_+, \sigma_+}|\Psi_+|^2 \right) \Psi_+ - J_\sigma\Psi_- + iF_+ \\ i\hbar\partial_t\Psi_- &= \left(E_0 - \hbar\omega_p - i\frac{\hbar\gamma}{2} + V_{\sigma_-, \sigma_-}|\Psi_-|^2 \right) \Psi_- - J_\sigma\Psi_+ + iF_- \end{aligned} \quad (5.11)$$

To scan the relative phase between F_+ and F_- simply corresponds to a rotation of a linearly polarized light: the driving field follows the equator of the Poincaré sphere. If the polarization direction is rotated in the counterclockwise (clockwise) direction, we expect to observe a strong emission of σ_+ (σ_-) polarized light.

Lattices with chiral symmetry are other natural candidates for Helical bistability as, by definition, they are constituted by two coupled sub-lattices. Pumping the two sub-lattice independently with a well define wavevector, we expect to observe Helical bistability for the pseudo-spin defined by the sub-lattice chiral operator.

The study of the helical bistability is an on going work. Important questions remain to be answered: what are the most general conditions a system must fulfill to exhibit helical bistability? How does the effect depend on the nature of the

inter-particle interaction ? (χ^2 versus χ^3 , amplitude of cross interactions between resonators, ...). We are discussing a possible interpretation of the helical bistability linked to the eventual presence of an exceptional point in the system. The reader can for example refer to Ref. [359–361].

Conclusion and outlook

In this thesis we investigated the non-linear physics of polaritons in chiral systems. We especially explored a one-dimensional lattice emulating a driven-dissipative version of a non-linear Su-Schrieffer-Heeger model. This lattice is a toy model to start the exploration of the interplay between non-linearities and topology in a driven-dissipative context. By engineering the drive phase profile, we discovered solutions that are specific to dissipative systems: we reported the discovery of novel solitons which are fully spin-polarized and a new non-linear effect that we name “Helical bistability”.

We explored the formation of solitons in the topological gap of the SSH lattice under quasi-resonant drive. A first family we found is similar to those already reported in conservative systems, in our experiments these solitons are obtained under coherent drive with a homogeneous phase profile. The analysis of their density profile revealed a pseudo-spin texture induced by the chiral symmetry: the core of topological gap solitons shows no sub-lattice polarization while their exponentially decaying tails are localized on one sub-lattice on the left and on the other one on the right. We optically created non-Hermitian defects and realized the first study of the robustness properties of these solitons. We demonstrated a robustness inherited from the chiral symmetry: topological gap solitons are unaffected by defects localized on the sub-lattice presenting a vanishing amplitude of their wavefunction. Taking advantage of the driven-dissipative nature of the lattice we engineered the phase profile of the drive and evidenced the existence of fully spin-polarized solitons. These novel solutions require to be stabilized by the driving field and are thus specific to open systems. We numerically analyzed the excitation spectrum of the system in presence of such a steady state and showed that a fully spin-polarized gap soliton induces a non-trivial interface for Bogolons: a spin-polarized edge state appears in the topological gap. These results show how non-linearities induced by gap solitons can modify the topology of the system.

We then focused on the interaction between two gap solitons with spin-polarized tails. As for the conservative case, the interaction between solitons depends on their relative phase difference and relative distance. Also, a spontaneous symmetry breaking is found for certain values of the phase difference. The novelty brought by the chiral symmetry is revealed when one performs scans of the relative phase difference between the driving fields. Such drive protocol allowed us to unravel a novel non-linear effect which links the helicity of the drive protocol to the chirality of the system response: the helical bistability. To better understand the effect we considered the simplest system presenting chiral symmetry that is two coupled non-linear resonators, and numerically demonstrated that it can exhibit the helical

bistability effect. We showed that the effect is linked to the presence of a chiral symmetry breaking induced by anisotropic interactions and that it can be mapped to a spin one-half particle. To experimentally validate these predictions, we considered the interactions of two solitons on neighboring unit cells of the SSH lattice and showed that such system can be mapped to a set of two coupled Kerr resonators. We performed the polariton field tomography and represented the system trajectory on the Bloch sphere. These latter results constitute an experimental observation of the simplest form of the helical bistability, a novel non-linear effect that to our knowledge had never been observed nor discussed so far. These results illustrate how chirality considerably enriches the physics in the driven-dissipative context and opens interesting perspectives that I would like to discuss briefly below.

In the near future, it will be interesting to consider the exploration of chiral lattices with higher dimensions. The proposition for 2D topological insulator based on polaritonic graphene [319] is particularly interesting. In this model, the addition of a Zeeman splitting and spin-orbit coupling enable to open a topological gap at the energy of the Dirac cones (see Fig. 5.9 (a)). This proposal has been implemented by S. Klemmt et al. in Ref. [182]. The exploration of non-linearities in such lattice promises the observation of novel phenomena induced by the non-trivial topology of the model. It would be particularly interesting to study the formation of gap solitons at the edge of the lattice [323, 325] where one can observe protected chiral edge states. In the bulk of such topological system the physics of solitons is interestingly linked to the topics covered in this manuscript: when generated close to the Dirac energy, solitons with a ring shape could present a sub-lattice localization [206].

In addition, the present work demonstrates the potential of the polariton platform to manipulate non-linear fluids in tailored lattice. The engineering of the drive offers a lot of possibilities that one could use to induce non-trivial topology in driven-dissipative platforms. Such proposals are theoretically discussed in the case of a static configuration of the driving field with the work of C. E. Bardyn in Ref. [8]. It would also be interesting to consider a periodic evolution of the driving field to induce a dynamic at a temporal scale given by the drive protocol. This effective time could be used as a synthetic dimension to study topological invariants of higher dimensions.

A possible application of Helical bistability is to realize quantized transport (or geometric pump) of a soliton using a periodic phase protocol of the drive. Preliminary numerical calculations show that the implementation of a periodic drive protocol in the one-dimensional SSH lattice allows to realize the quantized transport of gap solitons. A simplified scheme of the protocol and its result are presented in Fig. 5.9 (b). We first got inspired by the helical bistability effect and tried to develop a pump protocol based on periodic scans of the driving field phase: we pump the whole lattice with an homogeneous input power and apply a spatially and temporally periodic modulation of the phase. In this way, we can displace the soliton toward the left or the right by scanning the phase in the counterclockwise or clockwise direction: this is a geometric pump for solitons. We are trying to interpret this phenomenon using the Bogoliubov spectrum and to describe the periodic evolution of the excitation spectrum as a modification of a non-linear potential for the soliton.

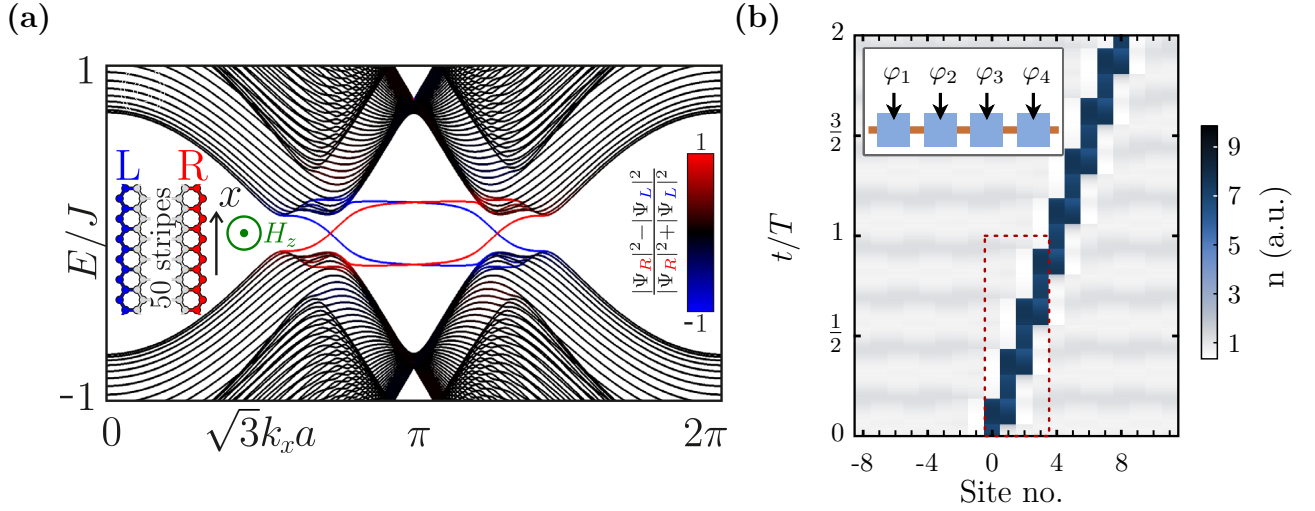


Figure 5.9: **a**, Numerical calculation of the polariton graphene band structure in presence of a magnetic field and TE-TM splitting. Topological edge states of the model are represented in red and blue. Image taken from Ref. [319]. **b**, Numerical simulation of a geometric pump for soliton based on the helical bistability effect. The effective unit cell contains four sites (see inset) which are driven by pump terms $F_j = F_0 \exp(i\varphi_j(t))$ with $\varphi_j(t)$ a periodic function of period T and $\varphi_j(t) = \varphi_1(t + \frac{j-1}{4} T)$. The period of the pump protocol is evidenced by a red dotted rectangle. After one temporal period, the soliton has been displaced by one unit cell (four sites).

We aim at going beyond this protocol and realize the equivalent of a nonlinear Thouless pump: a pump where the displacement of the soliton is associated to a non-zero topological invariant [322]. Interestingly, in conservative systems, recent results show that the motion of solitons can be explained from the band structure and topology of the underlying lattice [329, 330]. In the driven-dissipative context, the invariant would have to be measured in the Bogoliubov excitation spectrum calculated far from the soliton.

The Bogoliubov spectrum is a powerful tool to analyze and understand the behavior of non-linear fluids. This work demonstrated that interesting topology can emerge in the excitation spectrum thanks to drive engineering. It would be of great interest to probe this spectrum in tailored lattices. To do so, several configurations can be considered. The first one relies on incoherently populating all Bogoliubov modes by relaxation of particles from an exciton reservoir. We have performed such experiments and have very promising preliminary results. In presence of a fully spin-polarized soliton, we observed the appearance of a topological edge state in the gap of the SSH lattice. A second approach consists in using a weak resonant probe to coherently measure the transmission at the energy of Bogoliubov modes. Recent works by the group of A. Bramati report on the use of this pump and probe spectroscopy technique to observe the Bogoliubov branches associated to polariton fluid superfluidity in a planar cavity [127].

Finally, the possibilities offered by the polariton platform to engineer non-linear lattices opens the door to the observation of driven-dissipative solitons or vortices in models with symmetries other than the chiral symmetry. I would be particularly interested in exploring the structure and interaction of gap solitons generated in the fractal spectrum of quasi-crystalline lattices. For example, the solitons generated

in the gap of Fibonacci quasi-crystals are expected to present tails with a decay showing the self-similar profile characteristic from critically localized eigenstates. This could result in an intriguing spatial dependence of the interaction between two of these solitons. Moreover, one could explore the evolution of these properties through the transition toward critically theoretically discovered by O. Zilberberg and collaborators [362] and experimentally observed in our group [191].

Publications

- V. Goblot, A. Štrkalj, N. Pernet, J. L. Lado, C. Dorow, A. Lemaître, L. Le Gratiet, A. Harouri, I. Sagnes, S. Ravets, A. Amo, J. Bloch, and O. Zilberberg, “Emergence of criticality through a cascade of delocalization transitions in quasiperiodic chains”. *Nature Physics* **16** (8), 832-836 (2020).
- B. Real, O. Jamadi, M. Milićević, N. Pernet, P. St-Jean, T. Ozawa, G. Montambaux, I. Sagnes, A. Lemaître, L. Le Gratiet, A. Harouri, S. Ravets, J. Bloch, and A. Amo. “Semi-Dirac Transport and Anisotropic Localization in Polariton Honeycomb Lattices”, *Physical Review Letters* **125** (18), 186601 (2020).
- N. Pernet, P. St-Jean, D.D. Solnyshkov, G. Malpuech, N. Carlon Zambon, Q. Fontaine, B. Real, O. Jamadi, A. Lemaître, M. Morassi, L. Le Gratiet, T. Baptiste, A. Harouri, I. Sagnes, A. Amo, S. Ravets, and J. Bloch. “Gap solitons in a one-dimensional driven-dissipative topological lattice”, *Nature Physics* **18**, 678-684 (2022).
- O. Jamadi, B. Real, K. Sawicki, C. Hainaut, A. González-Tudela, N. Pernet, I. Sagnes, M. Morassi, A. Lemaître, L. Le Gratiet, A. Harouri, S. Ravets, J. Bloch and A. Amo. “Reconfigurable photon localization by coherent drive and dissipation in photonic lattices”, *Optica* **9** (7), 706-712 (2022).

Chapter A

Interaction between gap solitons: SSH versus AB lattice

A.1 The AB lattice: gap solitons in a trivial gap

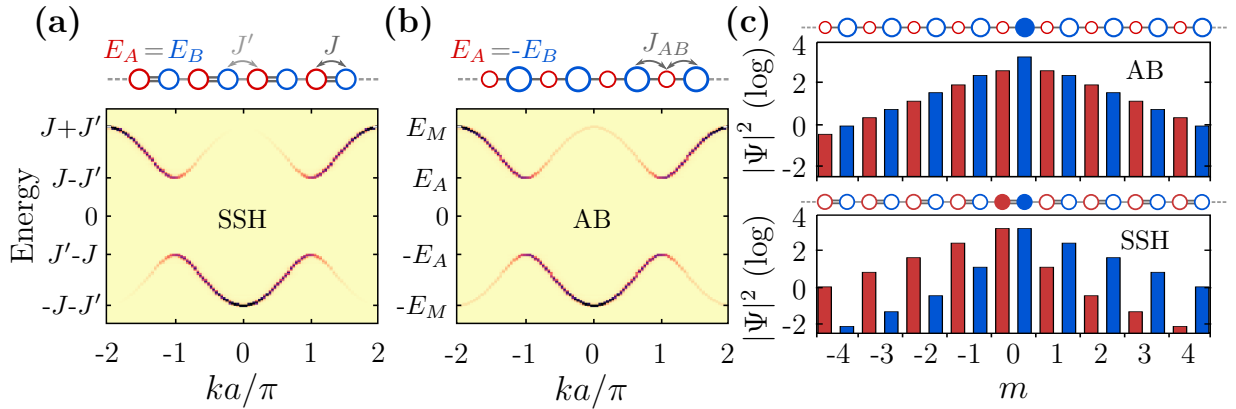


Figure A.1: **a**, Top: schematic representation of the SSH lattice. Bottom: Simulated momentum space dispersion of the SSH lattice. **b**, Same as **(a)** for the AB lattice with $E_M = \sqrt{E_A^2 + 4J_{AB}^2}$. Parameters were chosen for the dispersion to match the one presented in **(a)**. **c**, Top: Profile of a soliton generated in the center of the gap of the AB lattice. Bottom: Profile of a gap soliton of the SSH model generated in the same conditions. Red and blue bars respectively represent the soliton intensity on the A and B sub-lattice. Schemes on top of each panel depict the associated lattice. In both cases the soliton was injected in the unit cell $m = 0$ by driving the pillar(s) evidenced by a filled circle(s).

To compare the case of topological gap solitons of the SSH lattice to a trivial case, we simulated a binary lattice (AB) with staggered onsite energies. The AB chain is topologically trivial and no interface of the lattice can lead to the appearance of an edge state. However, the energy dispersion of the AB lattice can be made exactly similar to the SSH one. The Hamiltonian of the AB model reads:

$$\mathcal{H}_{AB} = \begin{bmatrix} E_A & -t \\ -t & E_B \end{bmatrix} \quad (\text{A.1})$$

Setting $E_A = -E_B = J - J'$ and $J_{A \rightarrow B} = J_{B \rightarrow A} = \sqrt{J * J'}$, the diagonalization of \mathcal{H}_{AB} yields the same eigenenergies obtain in the case of the SSH model with hopping

J and J' . Energy bands calculated in the case of tight-binding AB and SSH models are presented in Fig. A.1 (a-b). Note that the difference observed between the two panels originate from the distribution of eigenstate inside the unit cell.

The difference in the internal degree of freedom of the AB and SSH eigenstates is at the core of the comparison we propose. In the case of the AB model, the winding number (in the sense of the one describing SSH) is not defined as the decomposition of $\mathcal{H}_{\text{AB}}(k)$ on Pauli matrices has a non-zero component $d_z(k)$: $\mathcal{H}_{\text{AB}}(k)$ does not possess the Chiral symmetry associated to $\hat{\mathcal{C}} = \mathbb{1} \otimes \hat{\sigma}_z$. A quick calculation shows that an operator $\hat{\mathcal{C}}_{\text{AB}}$ anti-commuting with $\mathcal{H}_{\text{AB}}(k)$ has to be non-local: the diagonal elements of $\hat{\mathcal{C}}_{\text{AB}}$ depend on k . The AB lattice thus does not possess the chiral symmetry as defined for Hamiltonians in Chap. 3.1.4.

In this appendix, we will use the similarities between the energy dispersion of SSH and AB lattices to observe whether the interaction between gap solitons is modified or not by the chirality of their tails. By construction of the band structure, the energy detuning between the pump and the lower band is kept the same in both models as well as the amplitudes and curvature of the bands. As a consequence, the formation of solitons in the gap of the two different lattices occurs at comparable power thresholds, these solitons present similar peak densities and both types of solitons possess evanescent tails with the same exponential decay. The discrepancies between solitons of both model originate from the eigenstates distribution inside the unit cell: their tails differ in their sub-lattice distribution. The profiles of both types of solitons are presented in Fig. A.1 (c): the SSH gap soliton (bottom) presents sub-lattice localized tails while the AB gap soliton (top) present a regular exponential decay with no particular sub-lattice texture. Note that to respect the symmetry and efficiently couple to the lower band of the AB model, one need to only drive the B pillar of the pumped unit cell. Driving the two pillars of the unit cell $m = 0$ with equal pump amplitudes leads to the formation of two solitons localized on the B pillar of unit cells $m = 0$ and $m = -1$ (undriven).

A.2 Numerical comparison

A.2.1 Power scans

We start by the reproducing the phase diagrams obtained via power scans and presented in Sec. 4.2.3. The RGB images obtained by tight-binding simulations of the SSH lattice are displayed in Fig. A.2 (a-b). They exhibit a global mirror symmetry, with respect to $\Delta\varphi = 0$, which confirms the presence of a residual asymmetry in the experimental setup. The experimental data are relatively well reproduced by tight-binding simulations even though no fine tuning of the simulation parameters was realized. The structure associated to the symmetry breaking is observed around $\Delta\varphi = 0$ and the magenta and white regions are well captured by the simulation. Even the small cyan region observed on the downward scan around $\Delta\varphi = \pi/2$ is observed in the simulated images, with a mirror symmetric yellow region observed around $\Delta\varphi = -\pi/2$. Note that in the simulations, we observed parametric instabilities in the downward scan, which hinders the formation of a clear green region (soliton localized on the central dimer). Such instabilities were not observed experimentally.

We repeated these simulations in the case of the AB lattice. The obtained results are displayed in Fig. A.2 (c-d). We observe a striking similarity between those diagrams and the ones obtained in the context of the SSH lattice (Fig. A.2 (a-b)). Even though the shapes and positions of the different colored areas slightly differ from their counterpart in the SSH model, we recover the blue/red broken symmetry phase with a very similar power and phase distribution same goes for the magenta and white regions as well as for the small yellow/cyan areas. These results corroborate the intuitive picture consisting in treating each unit cell as a simple resonator.

Note that further exploration of these diagrams can be done by performing back and forth power ramps to explore the stability power range associated to each solution. Especially, doing so for the cyan and yellow regions reached during the downward scan, one observe (see Fig A.3) that these areas extend up to $P > 2 P_{\text{th}}$ in both cases (SSH and AB lattice). Similarly to the red and blue regions observed at low power, the cyan and yellow areas also represent asymmetric solutions. The main difference resides in the localization of light with respect to the sign of the phase difference: at low power (red and blue) the soliton is localized on the right for $\Delta\varphi < 0$ and left for $\Delta\varphi > 0$). On the contrary, at high power (cyan and yellow) we observe the opposite relationship, the soliton is localized on the left (right) for $\Delta\varphi < 0$ (> 0). A soliton has formed on the central unit cell and the effective coupling between the left and right dimer is now opposite to its value at lower power. It coincides with the change of relationship between the localization of polaritons and the sign of $\Delta\varphi$.

A.2.2 Phase scans

In both AB and SSH models, the diagrams of gap solitons formation obtained *via* power scans can be generally described approximating each unit cell to a single resonator: the notion of chiral symmetry (linked to the unit cell internal spin degree of freedom) does not play a crucial role in power dependence of solitons formation. We here show that this general description is not possible when addressing scans of $\Delta\varphi$ and that the unit cell internal degree of freedom plays a crucial role in the structure of the phase multi-stability diagram.

A.2.2.1 Phase scans in the SSH model

We first performed numerical simulations aiming at qualitatively reproducing the P - $\Delta\varphi$ diagrams obtained for the SSH model which were presented in Fig. 4.15. We only present the diagrams computed for a downward scan of input power as no relevant additional information is contained in the diagram of the upward power scan. The RGB images obtained *via* tight-binding simulations are displayed in Fig. A.4. We retrieve the general features unveiled experimentally with trapping of the soliton at low power in a range R1_S ($0.4 < P/P_{\text{th}} < 0.6$) and a phase bistability between white and magenta solutions at very large power ($P/P_{\text{th}} > 1.5$).

In the power range R2_S ($0.6 < P/P_{\text{th}} < 0.7$) we observe switching between the mirror-symmetric solution (magenta) and the two chiral solutions (red and blue regions). We numerically retrieve the helical bistability effect: the soliton localizes on

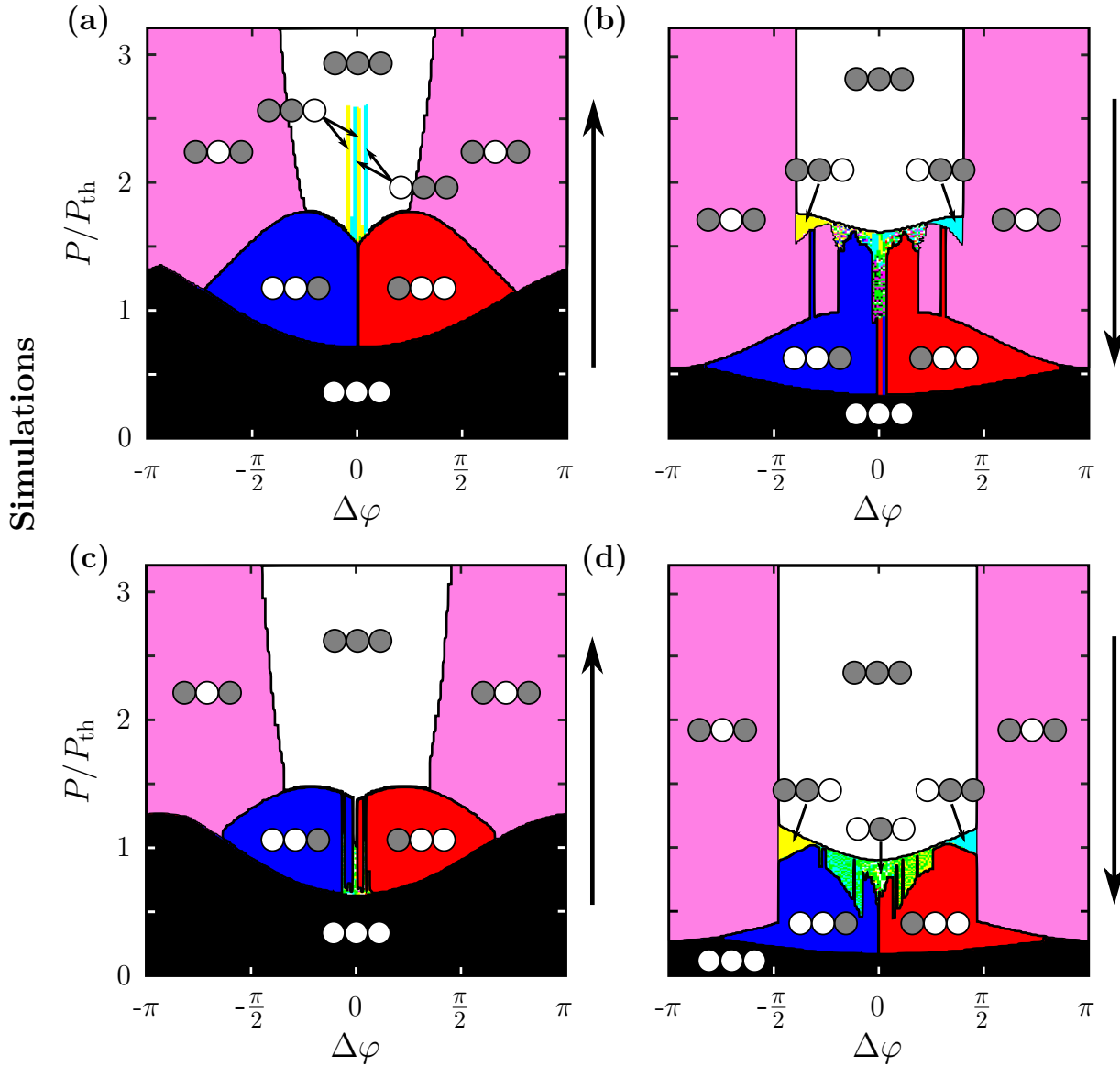


Figure A.2: **a-b**, Simulated RGB images obtained by additive color synthesis of upward and downward power scan diagrams associated to the polariton density in the three central unit cells of the SSH lattice for $D = 2a$. **c-d**, Same as **(a-b)** for the case of the AB lattice. The power scan direction is indicated by an arrow at the right of each panel. On all images, a schematic representation of the polariton fluid density is represented in each colored region: a strong (weak) intensity in a dimer is represented by a gray (white) circle.

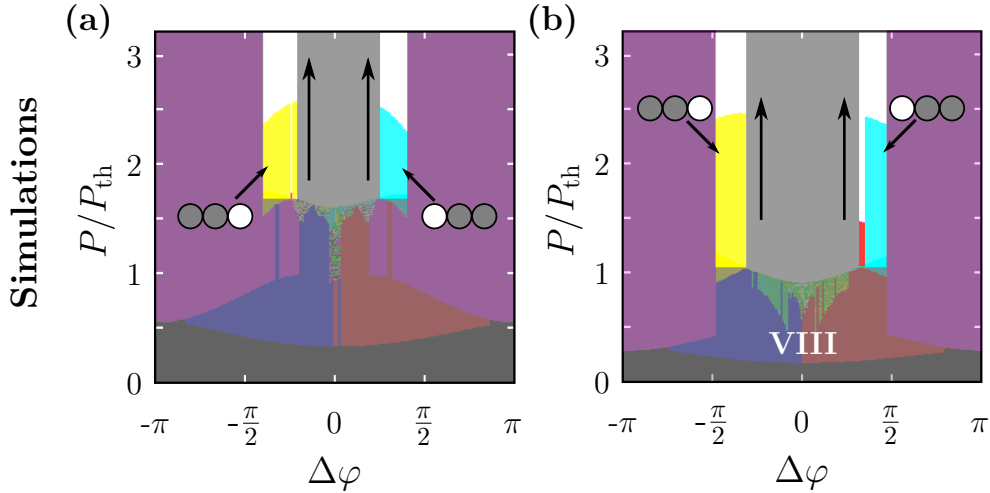


Figure A.3: **a-b**, Simulated RGB images obtained by additive color synthesis of upward and downward power scan diagrams associated to the polariton density in the three central unit cells of an AB lattice for $D = 2a$. Parameters of the lattice were tuned to match the dispersion of the simulated SSH lattice considered in Fig. A.2. The color code associated to the spatial distribution of polaritons is displayed on the right. **c**, Zoom of **(b)** around the region where parametric instabilities are observed. **d**, Upward scan starting from the cyan (III) and yellow (IV) regions of **(b)**. A darkened copy of **(b)** was superimposed to aid visualization.

the left dimer during counterclockwise scans of $\Delta\varphi$ and on the right dimer during clockwise phase scans. In the intermediate power range ($0.7 < P/P_{\text{th}} < 1.5$) we recognize the general shape of the experimental diagrams but, as in the case of simulated diagrams realized for power scans, the green region experimentally observed in the vicinity of $\Delta\varphi = 0$ is replaced by parametric instabilities. As a consequence, the simulated system does not always reach a chiral solution.

Note that reasonable efforts have been made to try to numerically suppress or at least damp these instabilities. We considered tuning each of the available parameters and tried to include phase noise to no avail. Diminishing the simulation time step or going to the next order of approximation in the split step method did not help damping the oscillations.

A.2.2.2 Phase scans in the AB model

We now turn to simulated phase scans in the case of the AB model. The diagrams obtained by counterclockwise and clockwise scans of $\Delta\varphi$ are presented in Fig. A.5. The only similarity between SSH and AB models lies in their behavior at high power ($P/P_{\text{th}} > 1.5$): we observe a phase bistability between white and magenta solutions.

In the case of the AB model, only one characteristic behavior is observed between the high power regime and the linear regime. The medium range $0.5 < P/P_{\text{th}} < 1$ exhibit a phase bistability between the symmetric solution (magenta) and the two chiral solutions (red and blue). Contrary to the case of SSH, both chiral solutions are reached in the clockwise or counterclockwise phase scans: the helical bistability effect is not observed in the AB model. The soliton localizes on the left dimer in a range centered on a value $\Delta\varphi < 0$ and on the right dimer for a phase range centered on a value $\Delta\varphi > 0$. In addition, no trapping of the soliton is observed at low power.

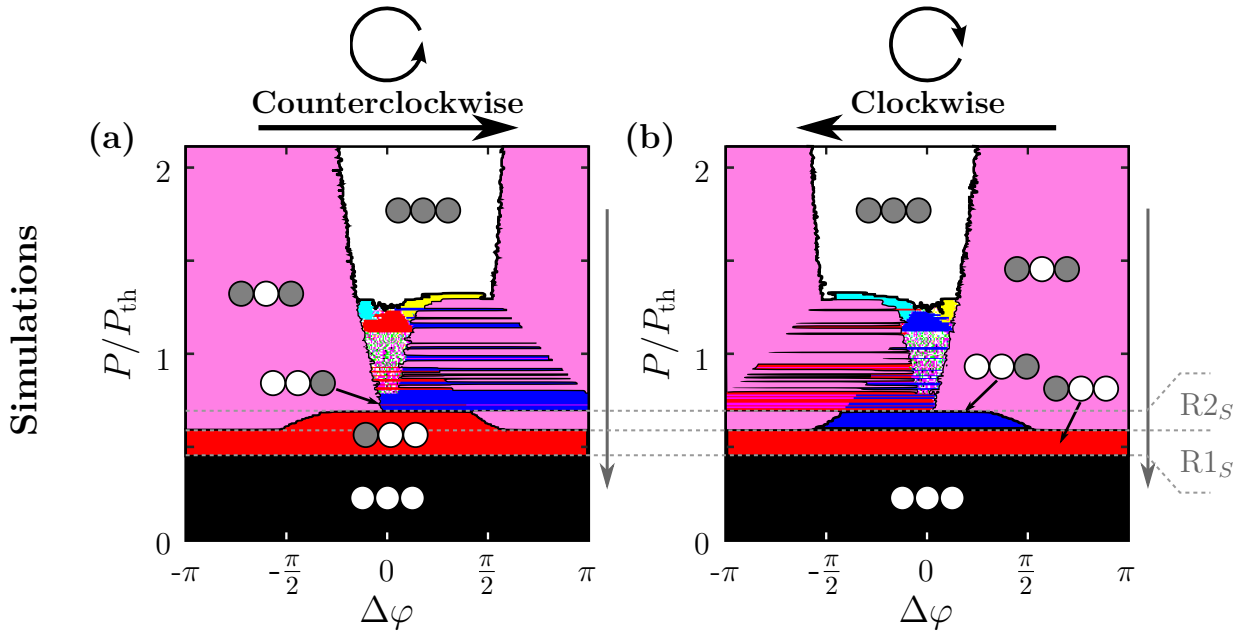


Figure A.4: a-b, RGB images of simulated counterclockwise and clockwise scans of $\Delta\varphi$ as a function of the input power P in the case of the SSH lattice. We here only show the downward scan of power. $R1_S$ and $R2_S$ correspond to the power ranges for which simulations reproduce the soliton trapping and the helical bistability.

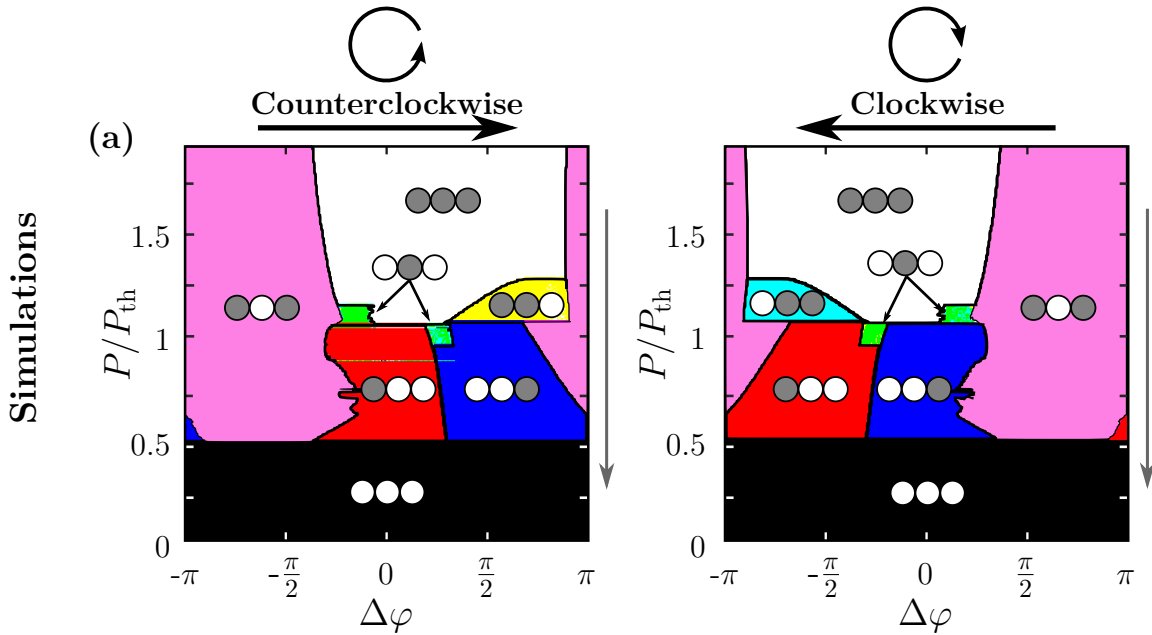


Figure A.5: a-b, RGB images of simulated counterclockwise and clockwise scans of $\Delta\varphi$ as a function of the input power P in the case of the AB lattice. We here only show the downward scan of power.

Chapter B

Helical bistability of two coupled Kerr resonators

B.1 Numerical results: particle density versus $\Delta\varphi$

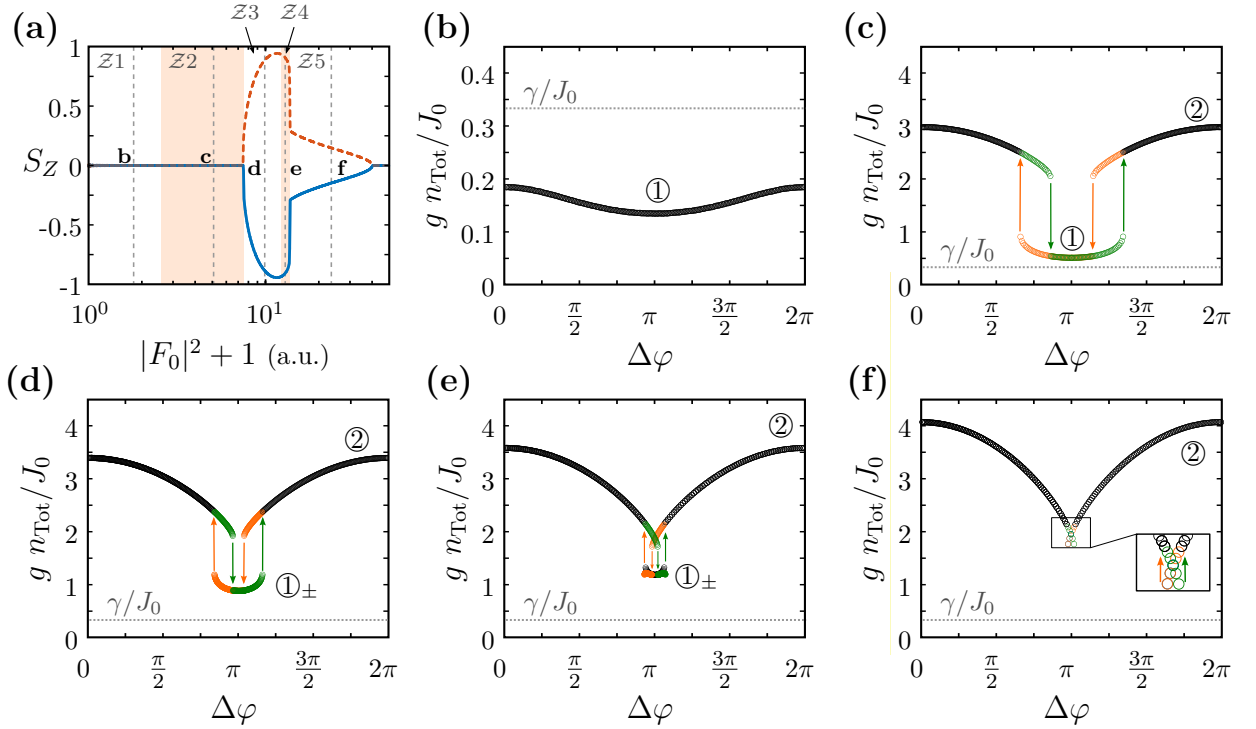


Figure B.1: **a**, Reproduction of the symmetry breaking presented in Fig. 5.1 (c). **b-f**, Evolution of the total density $g n_{\text{Tot}}/J_0$ as a function of $\Delta\varphi$ for different values of the input power which are marked with vertical dashed lines in (a). Orange and green data points indicate bistability regions which are exclusively explored during the clockwise and counterclockwise phase scans. Colored arrows indicate the direction of the jumps. The power ranges associated to each regime are highlighted using light orange patches in (a).

In Fig. B.1 we provide the graphs of the particle density $n_{\text{Tot}} = |\Psi_L|^2 + |\Psi_R|^2$ as a function of $\Delta\varphi$, corresponding to the graphs of S_Z presented in Fig. 5.2. To give more meaningful information, we present the evolution of $g n_{\text{Tot}}/J_0$: the interaction energy normalized to the hopping constant which represents the detuning between

the laser and the bonding state of the linear model. For reference, the value γ/J_0 is indicated by a horizontal dotted line. Above the range $\mathcal{Z}1$, all stability branches present densities associated to an interaction energy on the order of J_0 (significantly non-linear).

B.2 Experimental results

B.2.1 Density diagrams

In Fig. B.2 we provide the graphs of the normalized polariton density in each driven unit cells as a function of $\Delta\varphi$, corresponding to the color encoded images presented in Fig. 5.5 (a-b).

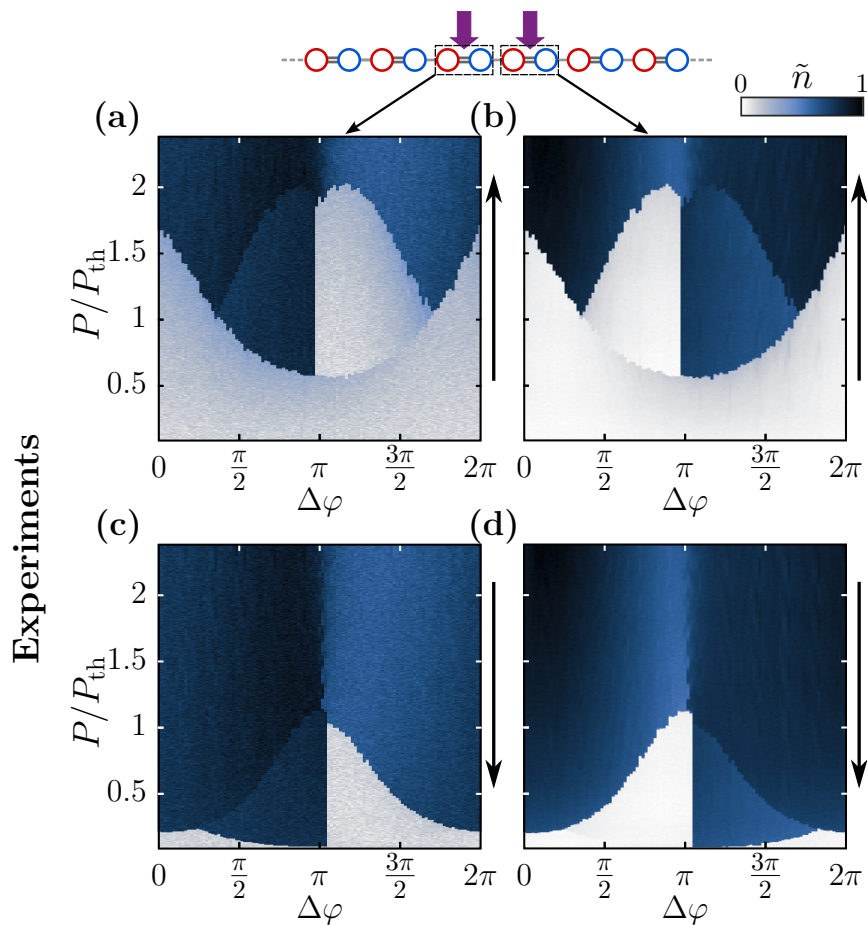


Figure B.2: Diagrams of the normalized density in the left and right driven unit cells for scans of input power as a function of $\Delta\varphi$ **a-b**, Diagrams corresponding to the upward scan of input power. **c-d**, Same as **(c-d)** for the downward scan of input power.

B.2.2 Evolution of S_Z versus $\Delta\varphi$

In Fig. B.3 we provide the graphs of S_Z as a function of $\Delta\varphi$ corresponding to the data presented as Bloch spheres in Fig. 5.7.

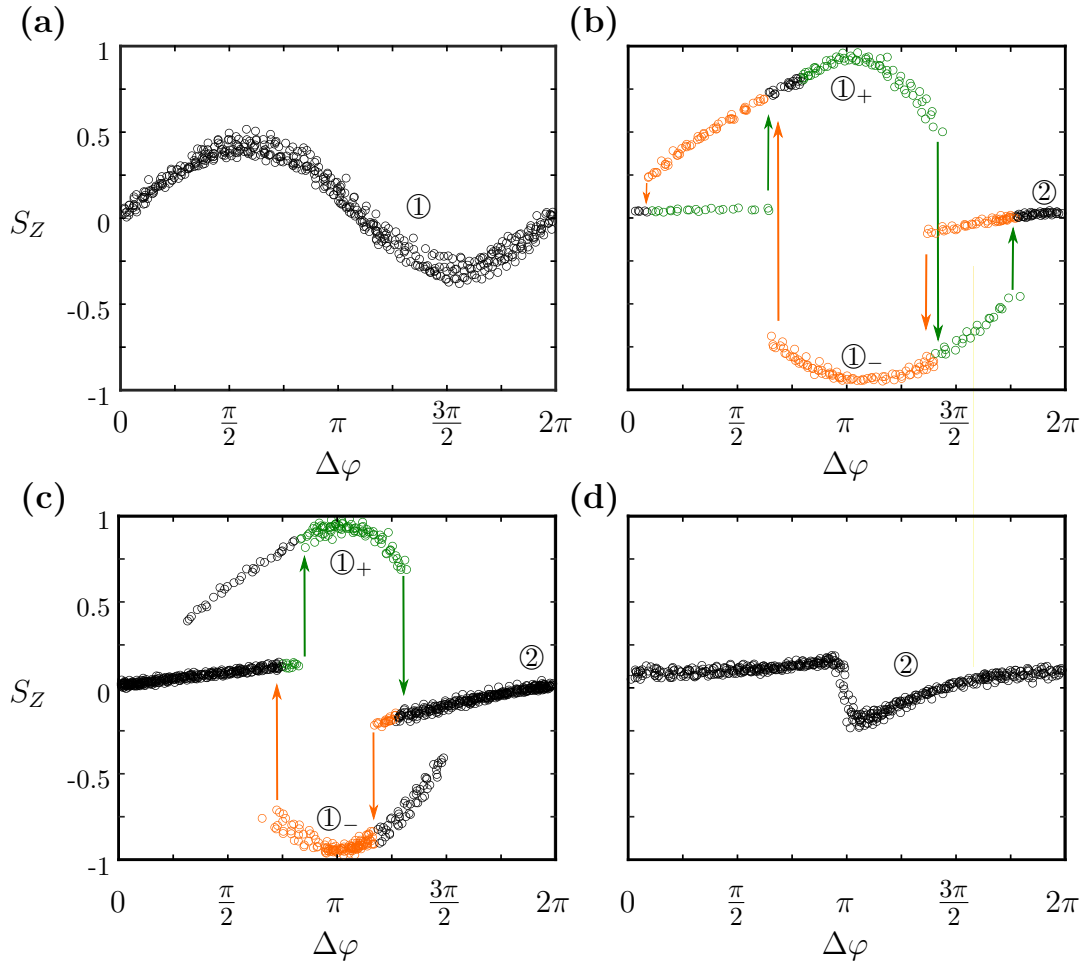


Figure B.3: Evolution of S_Z as a function of $\Delta\varphi$ for fixed input power with **a:** $P/P_{th} \approx 0.1$, **b:** $P/P_{th} = 0.77$, **c:** $P/P_{th} = 0.94$ and **d:** $P/P_{th} = 1.85$. Orange and green data points indicate bistability regions which are exclusively explored during the clockwise and counterclockwise phase scans. Colored arrows indicate the direction of the jumps.

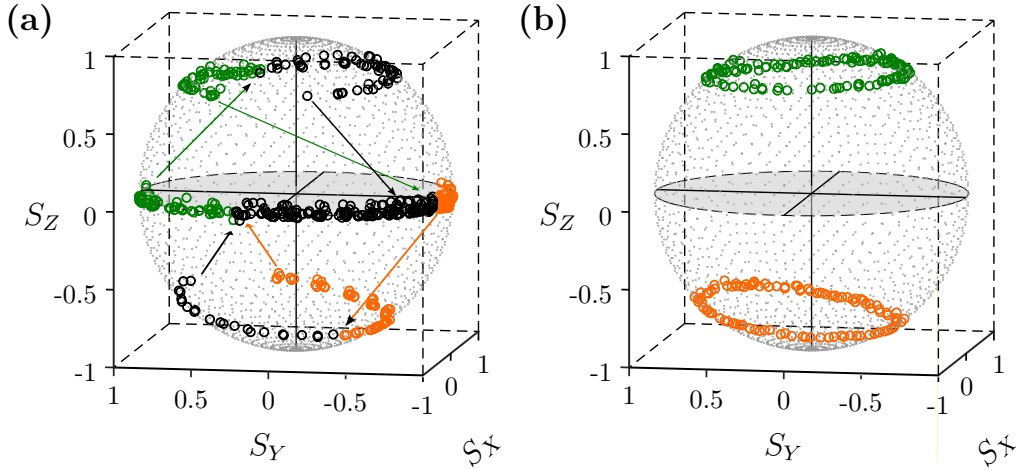


Figure B.4: Bloch sphere representation of the stability branches covered during phase scans for fixed input power in the case where the two pumps are separated by a distance $D = 2a$. **a:** Helical bistability between two gap solitons with chiral tails. Orange and green data points indicate bistability regions which are exclusively explored during the clockwise and counterclockwise phase scans. Colored arrows indicate the direction of the jumps. **b:** Trapping of a single soliton. Depending on the history of the drive, the soliton can either be locked to the north or south pole (green or orange data points).

B.2.3 Bloch sphere representation of the helical bistability and soliton trapping for solitons interacting *via* chiral tails

In Fig. B.4 we present the polariton field tomography in the case of phase scans where the two pumps are separated from $D = 2a$, this configuration was discussed in a major part of Chap. 4. Figure B.4 (a) corresponds to the regime of helical bistability unveiled for $0.6 < P/P_{\text{th}} < 1.0$: the north (south) hemisphere is only explored during the counterclockwise (clockwise) scan of $\Delta\varphi$. Figure B.4 (b) corresponds to the regime of soliton trapping unveiled for $0.35 < P/P_{\text{th}} < 0.5$: the system is locked to the north or south pole of the sphere depending on the history of the drive. Note that in the configuration $D = 2a$, the effective hopping between the two driven unit cells is negative. As a consequence we decided to change the orientation of the Bloch sphere with respect to the one chosen in Chap. 5 (the front bottom right corner corresponds to $S = \{-1, -1, -1\}$ while it used to be $S = \{1, 1, -1\}$).

Bibliography

- [1] Klitzing, K. v., Dorda, G. & Pepper, M. New Method for High-Accuracy Determination of the Fine-Structure Constant Based on Quantized Hall Resistance. *Phys. Rev. Lett.* **45**, 494–497 (1980). URL <https://link.aps.org/doi/10.1103/PhysRevLett.45.494>.
- [2] Thouless, D. J., Kohmoto, M., Nightingale, M. P. & den Nijs, M. Quantized Hall Conductance in a Two-Dimensional Periodic Potential. *Phys. Rev. Lett.* **49**, 405–408 (1982). URL <https://link.aps.org/doi/10.1103/PhysRevLett.49.405>.
- [3] Lu, L., Joannopoulos, J. D. & Soljačić, M. Topological photonics. *Nature Photonics* **8**, 821–829 (2014). URL <https://doi.org/10.1038/nphoton.2014.248>.
- [4] Ozawa, T. *et al.* Topological photonics. *Reviews of Modern Physics* **91**, 015006 (2019). [1802.04173](https://doi.org/10.1103/RevModPhys.91.015006).
- [5] Weimann, S. *et al.* Topologically protected bound states in photonic parity-time-symmetric crystals. *Nature Materials* **16**, 433–438 (2017). URL <https://doi.org/10.1038/nmat4811>.
- [6] Xia, S. *et al.* Nonlinear tuning of PT symmetry and non-Hermitian topological states. *Science* **372**, 72–76 (2021). URL <http://dx.doi.org/10.1126/science.abf6873>.
- [7] Smirnova, D., Leykam, D., Chong, Y. & Kivshar, Y. Nonlinear topological photonics. *Applied Physics Reviews* **7**, 021306 (2020). URL <https://doi.org/10.1063/1.5142397>. <https://doi.org/10.1063/1.5142397>.
- [8] Bardyn, C.-E., Karzig, T., Refael, G. & Liew, T. C. H. Chiral Bogoliubov excitations in nonlinear bosonic systems. *Phys. Rev. B* **93**, 020502 (2016). URL <https://link.aps.org/doi/10.1103/PhysRevB.93.020502>.
- [9] Bastard, G. Wave Mechanics Applied to Semiconductor Heterostructures. *Les éditions de physique, Les Ulis* (1988).
- [10] Bastard, G., Mendez, E. E., Chang, L. L. & Esaki, L. Exciton binding energy in quantum wells. *Phys. Rev. B* **26**, 1974–1979 (1982). URL <https://link.aps.org/doi/10.1103/PhysRevB.26.1974>.

- [11] Claudio Andreani, L. Optical Transitions, Excitons, and Polaritons in Bulk and Low-Dimensional Semiconductor Structures. *Confined Electrons and Photons: News Physics and Applications* **340**, 57–112 (1995). URL https://doi.org/10.1007/978-1-4615-1963-8_3.
- [12] Ismail, N., Calil Kores, C., Geskus, D. & Pollnau, M. Fabry-Pérot resonator: spectral line shapes, generic and related Airy distributions, linewidths, finesses, and performance at low or frequency-dependent reflectivity. *Opt. Express* **24**, 16366–16389 (2016). URL <http://www.opticsexpress.org/abstract.cfm?URI=oe-24-15-16366>.
- [13] Born, M. *et al.* *Principles of Optics: Electromagnetic Theory of Propagation, Interference and Diffraction of Light* (Cambridge University Press, 1999), 7 edn.
- [14] Hadley, G. R. Effective index model for vertical-cavity surface-emitting lasers. *Opt. Lett.* **20**, 1483–1485 (1995). URL <http://ol.osa.org/abstract.cfm?URI=ol-20-13-1483>.
- [15] Panzarini, G. *et al.* Cavity-polariton dispersion and polarization splitting in single and coupled semiconductor microcavities. *Physics of the Solid State* **41**, 1223–1238 (1999). URL <https://doi.org/10.1134/1.1130973>.
- [16] Savona, V., Andreani, L., Schwendimann, P. & Quattropani, A. Quantum well excitons in semiconductor microcavities: Unified treatment of weak and strong coupling regimes. *Solid State Communications* **93**, 733–739 (1995). URL <https://www.sciencedirect.com/science/article/pii/0038109894008655>.
- [17] Hopfield, J. J. Theory of the Contribution of Excitons to the Complex Dielectric Constant of Crystals. *Phys. Rev.* **112**, 1555–1567 (1958). URL <https://link.aps.org/doi/10.1103/PhysRev.112.1555>.
- [18] Weisbuch, C., Nishioka, M., Ishikawa, A. & Arakawa, Y. Observation of the coupled exciton-photon mode splitting in a semiconductor quantum microcavity. *Phys. Rev. Lett.* **69**, 3314–3317 (1992). URL <https://link.aps.org/doi/10.1103/PhysRevLett.69.3314>.
- [19] Wertz, E. *et al.* Propagation and Amplification Dynamics of 1D Polariton Condensates. *Phys. Rev. Lett.* **109**, 216404 (2012). URL <https://link.aps.org/doi/10.1103/PhysRevLett.109.216404>.
- [20] Houdré, R., Stanley, R. P. & Ilegems, M. Vacuum-field Rabi splitting in the presence of inhomogeneous broadening: Resolution of a homogeneous linewidth in an inhomogeneously broadened system. *Phys. Rev. A* **53**, 2711–2715 (1996). URL <https://link.aps.org/doi/10.1103/PhysRevA.53.2711>.
- [21] Houdré, R. *et al.* Measurement of Cavity-Polariton Dispersion Curve from Angle-Resolved Photoluminescence Experiments. *Phys. Rev. Lett.* **73**, 2043–2046 (1994). URL <https://link.aps.org/doi/10.1103/PhysRevLett.73.2043>.

- [22] Kavokin, A., Malpuech, G. & Glazov, M. Optical Spin Hall Effect. *Phys. Rev. Lett.* **95**, 136601 (2005). URL <https://link.aps.org/doi/10.1103/PhysRevLett.95.136601>.
- [23] Leyder, C. *et al.* Observation of the optical spin Hall effect. *Nature Physics* **3**, 628–631 (2007). URL <https://doi.org/10.1038/nphys676>.
- [24] Maragkou, M. *et al.* Optical analogue of the spin Hall effect in a photonic cavity. *Opt. Lett.* **36**, 1095–1097 (2011). URL <http://www.osapublishing.org/ol/abstract.cfm?URI=ol-36-7-1095>.
- [25] Cilibrizzi, P. *et al.* Half-skyrmion spin textures in polariton microcavities. *Phys. Rev. B* **94**, 045315 (2016). URL <https://link.aps.org/doi/10.1103/PhysRevB.94.045315>.
- [26] Carusotto, I. & Ciuti, C. Quantum fluids of light. *Rev. Mod. Phys.* **85**, 299–366 (2013). URL <https://link.aps.org/doi/10.1103/RevModPhys.85.299>.
- [27] Schmitt-Rink, S., Chemla, D. S. & Miller, D. A. B. Theory of transient excitonic optical nonlinearities in semiconductor quantum-well structures. *Phys. Rev. B* **32**, 6601–6609 (1985). URL <https://link.aps.org/doi/10.1103/PhysRevB.32.6601>.
- [28] Rochat, G. *et al.* Excitonic Bloch equations for a two-dimensional system of interacting excitons. *Phys. Rev. B* **61**, 13856–13862 (2000). URL <https://link.aps.org/doi/10.1103/PhysRevB.61.13856>.
- [29] Combescot, M. & Tanguy, C. New criteria for bosonic behavior of excitons. *Europhysics Letters (EPL)* **55**, 390–396 (2001). URL <https://doi.org/10.1209/epl/i2001-00427-7>.
- [30] Kappei, L., Szczytko, J., Morier-Genoud, F. & Deveaud, B. Direct Observation of the Mott Transition in an Optically Excited Semiconductor Quantum Well. *Phys. Rev. Lett.* **94**, 147403 (2005). URL <https://link.aps.org/doi/10.1103/PhysRevLett.94.147403>.
- [31] Ciuti, C., Savona, V., Piermarocchi, C., Quattropani, A. & Schwendimann, P. Role of the exchange of carriers in elastic exciton-exciton scattering in quantum wells. *Phys. Rev. B* **58**, 7926–7933 (1998). URL <https://link.aps.org/doi/10.1103/PhysRevB.58.7926>.
- [32] Tassone, F. & Yamamoto, Y. Exciton-exciton scattering dynamics in a semiconductor microcavity and stimulated scattering into polaritons. *Phys. Rev. B* **59**, 10830–10842 (1999). URL <https://link.aps.org/doi/10.1103/PhysRevB.59.10830>.
- [33] Combescot, M., Dupertuis, M. A. & Betbeder-Matibet, O. Polariton-polariton scattering: Exact results through a novel approach. *Europhysics Letters (EPL)* **79**, 17001 (2007). URL <https://doi.org/10.1209/0295-5075/79/17001>.
- [34] Glazov, M. M. *et al.* Polariton-polariton scattering in microcavities: A microscopic theory. *Phys. Rev. B* **80**, 155306 (2009). URL <https://link.aps.org/doi/10.1103/PhysRevB.80.155306>.

- [35] Vladimirova, M. *et al.* Polariton-polariton interaction constants in microcavities. *Phys. Rev. B* **82**, 075301 (2010). URL <https://link.aps.org/doi/10.1103/PhysRevB.82.075301>.
- [36] Ferrier, L. *et al.* Interactions in Confined Polariton Condensates. *Phys. Rev. Lett.* **106**, 126401 (2011). URL <https://link.aps.org/doi/10.1103/PhysRevLett.106.126401>.
- [37] Sun, Y. *et al.* Direct measurement of polariton-polariton interaction strength. *Nature Physics* **13**, 870–875 (2017). URL <https://doi.org/10.1038/nphys4148>.
- [38] Pieczarka, M. *et al.* Effect of optically induced potential on the energy of trapped exciton polaritons below the condensation threshold. *Phys. Rev. B* **100**, 085301 (2019). URL <https://link.aps.org/doi/10.1103/PhysRevB.100.085301>.
- [39] Walker, P. M. *et al.* Ultra-low-power hybrid light-matter solitons. *Nature Communications* **6**, 8317 (2015). URL <https://doi.org/10.1038/ncomms9317>.
- [40] Delteil, A. *et al.* Towards polariton blockade of confined exciton-polaritons. *Nature Materials* **18**, 219–222 (2019). URL <https://doi.org/10.1038/s41563-019-0282-y>.
- [41] Estrecho, E. *et al.* Direct measurement of polariton-polariton interaction strength in the Thomas-Fermi regime of exciton-polariton condensation. *Phys. Rev. B* **100**, 035306 (2019). URL <https://link.aps.org/doi/10.1103/PhysRevB.100.035306>.
- [42] Muñoz-Matutano, G. *et al.* Emergence of quantum correlations from interacting fibre-cavity polaritons. *Nature Materials* **18**, 213–218 (2019). URL <https://doi.org/10.1038/s41563-019-0281-z>.
- [43] Verger, A., Ciuti, C. & Carusotto, I. Polariton quantum blockade in a photonic dot. *Phys. Rev. B* **73**, 193306 (2006). URL <https://link.aps.org/doi/10.1103/PhysRevB.73.193306>.
- [44] Gross, E. P. Structure of a quantized vortex in boson systems. *Il Nuovo Cimento (1955-1965)* **20**, 454–477 (1961). URL <https://doi.org/10.1007/BF02731494>.
- [45] Pitaevskii, L. P. Vortex lines in an imperfect Bose gas. *Sov. Phys. JETP* **13**, 451–454 (1961).
- [46] Ciuti, C., Schwendimann, P. & Quattropani, A. Theory of polariton parametric interactions in semiconductor microcavities. *Semiconductor Science and Technology* **18**, S279–S293 (2003). URL <https://doi.org/10.1088/0268-1242/18/10/301>.
- [47] Carusotto, I. & Ciuti, C. Probing Microcavity Polariton Superfluidity through Resonant Rayleigh Scattering. *Phys. Rev. Lett.* **93**, 166401 (2004). URL <https://link.aps.org/doi/10.1103/PhysRevLett.93.166401>.

- [48] Wouters, M. & Carusotto, I. Excitations in a Nonequilibrium Bose-Einstein Condensate of Exciton Polaritons. *Phys. Rev. Lett.* **99**, 140402 (2007). URL <https://link.aps.org/doi/10.1103/PhysRevLett.99.140402>.
- [49] Kasprzak, J. *et al.* Bose-Einstein condensation of exciton polaritons. *Nature* **443**, 409–414 (2006). URL <https://doi.org/10.1038/nature05131>.
- [50] Lagoudakis, K. G. *et al.* Quantized vortices in an exciton–polariton condensate. *Nature Physics* **4**, 706–710 (2008). URL <https://doi.org/10.1038/nphys1051>.
- [51] Imamoglu, A., Ram, R. J., Pau, S. & Yamamoto, Y. Nonequilibrium condensates and lasers without inversion: Exciton-polariton lasers. *Phys. Rev. A* **53**, 4250–4253 (1996). URL <https://link.aps.org/doi/10.1103/PhysRevA.53.4250>.
- [52] Kasprzak, J., Solnyshkov, D. D., André, R., Dang, L. S. & Malpuech, G. Formation of an Exciton Polariton Condensate: Thermodynamic versus Kinetic Regimes. *Phys. Rev. Lett.* **101**, 146404 (2008). URL <https://link.aps.org/doi/10.1103/PhysRevLett.101.146404>.
- [53] Sun, Y. *et al.* Bose-Einstein Condensation of Long-Lifetime Polaritons in Thermal Equilibrium. *Phys. Rev. Lett.* **118**, 016602 (2017). URL <https://link.aps.org/doi/10.1103/PhysRevLett.118.016602>.
- [54] Deng, H., Haug, H. & Yamamoto, Y. Exciton-polariton Bose-Einstein condensation. *Rev. Mod. Phys.* **82**, 1489–1537 (2010). URL <https://link.aps.org/doi/10.1103/RevModPhys.82.1489>.
- [55] Byrnes, T., Kim, N. Y. & Yamamoto, Y. Exciton-polariton condensates. *Nature Physics* **10**, 803–813 (2014). URL <https://doi.org/10.1038/nphys3143>.
- [56] Lai, C. W. *et al.* Coherent zero-state and π -state in an exciton-polariton condensate array. *Nature* **450**, 529–532 (2007). URL <https://doi.org/10.1038/nature06334>.
- [57] Baboux, F. *et al.* Unstable and stable regimes of polariton condensation. *Optica* **5**, 1163–1170 (2018). URL <http://www.osapublishing.org/optica/abstract.cfm?URI=optica-5-10-1163>.
- [58] Rubo, Y. G. Half Vortices in Exciton Polariton Condensates. *Phys. Rev. Lett.* **99**, 106401 (2007). URL <https://link.aps.org/doi/10.1103/PhysRevLett.99.106401>.
- [59] Lagoudakis, K. G. *et al.* Observation of Half-Quantum Vortices in an Exciton-Polariton Condensate. *Science* **326**, 974–976 (2009). URL <https://science.sciencemag.org/content/326/5955/974>. <https://science.sciencemag.org/content/326/5955/974.full.pdf>.
- [60] Manni, F., Lagoudakis, K. G., Liew, T. C. H., André, R. & Deveaud-Plédran, B. Spontaneous Pattern Formation in a Polariton Condensate. *Phys. Rev. Lett.* **107**, 106401 (2011). URL <https://link.aps.org/doi/10.1103/PhysRevLett.107.106401>.

- [61] Baas, A. *et al.* Synchronized and Desynchronized Phases of Exciton-Polariton Condensates in the Presence of Disorder. *Phys. Rev. Lett.* **100**, 170401 (2008). URL <https://link.aps.org/doi/10.1103/PhysRevLett.100.170401>.
- [62] Berloff, N. G. *et al.* Realizing the classical XY Hamiltonian in polariton simulators. *Nature Materials* **16**, 1120–1126 (2017). URL <https://doi.org/10.1038/nmat4971>.
- [63] Dall, R. *et al.* Creation of Orbital Angular Momentum States with Chiral Polaritonic Lenses. *Phys. Rev. Lett.* **113**, 200404 (2014). URL <https://link.aps.org/doi/10.1103/PhysRevLett.113.200404>.
- [64] Kwon, M.-S. *et al.* Direct Transfer of Light’s Orbital Angular Momentum onto a Nonresonantly Excited Polariton Superfluid. *Phys. Rev. Lett.* **122**, 045302 (2019). URL <https://link.aps.org/doi/10.1103/PhysRevLett.122.045302>.
- [65] Berger, B. *et al.* Formation dynamics of exciton-polariton vortices created by nonresonant annular pumping. *Phys. Rev. B* **101**, 245309 (2020). URL <https://link.aps.org/doi/10.1103/PhysRevB.101.245309>.
- [66] Ma, X. *et al.* Realization of all-optical vortex switching in exciton-polariton condensates. *Nature Communications* **11**, 897 (2020). URL <https://doi.org/10.1038/s41467-020-14702-5>.
- [67] Tosi, G. *et al.* Geometrically locked vortex lattices in semiconductor quantum fluids. *Nature Communications* **3**, 1243 (2012). URL <https://doi.org/10.1038/ncomms2255>.
- [68] Cookson, T. *et al.* Geometric frustration in polygons of polariton condensates creating vortices of varying topological charge. *Nature Communications* **12**, 2120 (2021). URL <https://doi.org/10.1038/s41467-021-22121-3>.
- [69] Christopoulos, S. *et al.* Room-Temperature Polariton Lasing in Semiconductor Microcavities. *Phys. Rev. Lett.* **98**, 126405 (2007). URL <https://link.aps.org/doi/10.1103/PhysRevLett.98.126405>.
- [70] Christmann, G., Butté, R., Feltin, E., Carlin, J.-F. & Grandjean, N. Room temperature polariton lasing in a GaN/AlGaIn multiple quantum well microcavity. *Applied Physics Letters* **93**, 051102 (2008). URL <https://doi.org/10.1063/1.2966369>. <https://doi.org/10.1063/1.2966369>.
- [71] Lu, T.-C. *et al.* Room temperature polariton lasing vs. photon lasing in a ZnO-based hybrid microcavity. *Opt. Express* **20**, 5530–5537 (2012). URL <http://www.osapublishing.org/oe/abstract.cfm?URI=oe-20-5-5530>.
- [72] Li, F. *et al.* From Excitonic to Photonic Polariton Condensate in a ZnO-Based Microcavity. *Phys. Rev. Lett.* **110**, 196406 (2013). URL <https://link.aps.org/doi/10.1103/PhysRevLett.110.196406>.
- [73] Kéna-Cohen, S. & Forrest, S. R. Room-temperature polariton lasing in an organic single-crystal microcavity. *Nature Photonics* **4**, 371–375 (2010). URL <https://doi.org/10.1038/nphoton.2010.86>.

- [74] Plumhof, J. D., Stöferle, T., Mai, L., Scherf, U. & Mahrt, R. F. Room-temperature Bose-Einstein condensation of cavity exciton-polaritons in a polymer. *Nature Materials* **13**, 247–252 (2014). URL <https://doi.org/10.1038/nmat3825>.
- [75] Anton-Solanas, C. *et al.* Bosonic condensation of exciton-polaritons in an atomically thin crystal. *Nature Materials* **20**, 1233–1239 (2021). URL <https://doi.org/10.1038/s41563-021-01000-8>.
- [76] Zhao, J. *et al.* Ultralow Threshold Polariton Condensate in a Monolayer Semiconductor Microcavity at Room Temperature. *Nano Letters* **21**, 3331–3339 (2021). URL <https://doi.org/10.1021/acs.nanolett.1c01162>.
- [77] Su, R. *et al.* Room-Temperature Polariton Lasing in All-Inorganic Perovskite Nanoplatelets. *Nano Letters* **17**, 3982–3988 (2017). URL <https://doi.org/10.1021/acs.nanolett.7b01956>.
- [78] Su, R. *et al.* Observation of exciton polariton condensation in a perovskite lattice at room temperature. *Nature Physics* **16**, 301–306 (2020). URL <https://doi.org/10.1038/s41567-019-0764-5>.
- [79] Su, R. *et al.* Perovskite semiconductors for room-temperature exciton-polaritonics. *Nature Materials* **20**, 1315–1324 (2021). URL <https://doi.org/10.1038/s41563-021-01035-x>.
- [80] Butté, R., Skolnick, M. S., Whittaker, D. M., Bajoni, D. & Roberts, J. S. Dependence of stimulated scattering in semiconductor microcavities on pump power, angle, and energy. *Phys. Rev. B* **68**, 115325 (2003). URL <https://link.aps.org/doi/10.1103/PhysRevB.68.115325>.
- [81] Deng, H., Weihs, G., Snoke, D., Bloch, J. & Yamamoto, Y. Polariton lasing vs. photon lasing in a semiconductor microcavity. *Proceedings of the National Academy of Sciences* **100**, 15318–15323 (2003). URL <https://www.pnas.org/content/100/26/15318>. <https://www.pnas.org/content/100/26/15318.full.pdf>.
- [82] Bajoni, D. *et al.* Polariton Laser Using Single Micropillar GaAs–GaAlAs Semiconductor Cavities. *Phys. Rev. Lett.* **100**, 047401 (2008). URL <https://link.aps.org/doi/10.1103/PhysRevLett.100.047401>.
- [83] Schneider, C. *et al.* An electrically pumped polariton laser. *Nature* **497**, 348–352 (2013). URL <https://doi.org/10.1038/nature12036>.
- [84] Fischer, J. *et al.* Anomalies of a Nonequilibrium Spinor Polariton Condensate in a Magnetic Field. *Phys. Rev. Lett.* **112**, 093902 (2014). URL <https://link.aps.org/doi/10.1103/PhysRevLett.112.093902>.
- [85] Carlon Zambon, N. *et al.* Optically controlling the emission chirality of microlasers. *Nature Photonics* **13**, 283–288 (2019). URL <https://doi.org/10.1038/s41566-019-0380-z>.

- [86] Shelykh, I. A., Kavokin, A. V., Rubo, Y. G., Liew, T. C. H. & Malpuech, G. Polariton polarization-sensitive phenomena in planar semiconductor microcavities. *Semiconductor Science and Technology* **25**, 013001 (2009). URL <https://doi.org/10.1088/0268-1242/25/1/013001>.
- [87] Gippius, N. A. *et al.* Polarization Multistability of Cavity Polaritons. *Phys. Rev. Lett.* **98**, 236401 (2007). URL <https://link.aps.org/doi/10.1103/PhysRevLett.98.236401>.
- [88] Flayac, H., Solnyshkov, D. D. & Malpuech, G. Oblique half-solitons and their generation in exciton-polariton condensates. *Phys. Rev. B* **83**, 193305 (2011). URL <https://link.aps.org/doi/10.1103/PhysRevB.83.193305>.
- [89] Flayac, H., Solnyshkov, D. D. & Malpuech, G. Separation and acceleration of magnetic monopole analogs in semiconductor microcavities. *New Journal of Physics* **14**, 085018 (2012). URL <https://doi.org/10.1088/1367-2630/14/8/085018>.
- [90] Solnyshkov, D. D., Flayac, H. & Malpuech, G. Stable magnetic monopoles in spinor polariton condensates. *Phys. Rev. B* **85**, 073105 (2012). URL <https://link.aps.org/doi/10.1103/PhysRevB.85.073105>.
- [91] Flayac, H., Solnyshkov, D. D., Shelykh, I. A. & Malpuech, G. Transmutation of Skyrmions to Half-Solitons Driven by the Nonlinear Optical Spin Hall Effect. *Phys. Rev. Lett.* **110**, 016404 (2013). URL <https://link.aps.org/doi/10.1103/PhysRevLett.110.016404>.
- [92] Gippius, N. A. & Tikhodeev, S. G. Multiple-polariton scattering in a semiconductor microcavity. *Journal of Physics: Condensed Matter* **16**, S3653–S3664 (2004). URL <https://doi.org/10.1088/0953-8984/16/35/007>.
- [93] Pitaevskii, L. & Stringari, S. *Bose-Einstein Condensation and Superfluidity*. International Series of Monographs on Physics (OUP Oxford, 2016). URL <https://books.google.fr/books?id=yHByCwAAQBAJ>.
- [94] Savvidis, P. G. *et al.* Angle-Resonant Stimulated Polariton Amplifier. *Phys. Rev. Lett.* **84**, 1547–1550 (2000). URL <https://link.aps.org/doi/10.1103/PhysRevLett.84.1547>.
- [95] Baas, A., Karr, J. P., Eleuch, H. & Giacobino, E. Optical bistability in semiconductor microcavities. *Phys. Rev. A* **69**, 023809 (2004). URL <https://link.aps.org/doi/10.1103/PhysRevA.69.023809>.
- [96] Stevenson, R. M. *et al.* Continuous Wave Observation of Massive Polariton Redistribution by Stimulated Scattering in Semiconductor Microcavities. *Phys. Rev. Lett.* **85**, 3680–3683 (2000). URL <https://link.aps.org/doi/10.1103/PhysRevLett.85.3680>.
- [97] Baumberg, J. J. *et al.* Parametric oscillation in a vertical microcavity: A polariton condensate or micro-optical parametric oscillation. *Phys. Rev. B* **62**, R16247–R16250 (2000). URL <https://link.aps.org/doi/10.1103/PhysRevB.62.R16247>.

- [98] Saba, M. *et al.* High-temperature ultrafast polariton parametric amplification in semiconductor microcavities. *Nature* **414**, 731–735 (2001). URL <https://doi.org/10.1038/414731a>.
- [99] Ballarini, D. *et al.* Observation of Long-Lived Polariton States in Semiconductor Microcavities across the Parametric Threshold. *Phys. Rev. Lett.* **102**, 056402 (2009). URL <https://link.aps.org/doi/10.1103/PhysRevLett.102.056402>.
- [100] Diederichs, C. *et al.* Parametric oscillation in vertical triple microcavities. *Nature* **440**, 904–907 (2006). URL <https://doi.org/10.1038/nature04602>.
- [101] Romanelli, M., Leyder, C., Karr, J. P., Giacobino, E. & Bramati, A. Four Wave Mixing Oscillation in a Semiconductor Microcavity: Generation of Two Correlated Polariton Populations. *Phys. Rev. Lett.* **98**, 106401 (2007). URL <https://link.aps.org/doi/10.1103/PhysRevLett.98.106401>.
- [102] Fox, A. M., Baumberg, J. J., Dabbicco, M., Huttner, B. & Ryan, J. F. Squeezed Light Generation in Semiconductors. *Phys. Rev. Lett.* **74**, 1728–1731 (1995). URL <https://link.aps.org/doi/10.1103/PhysRevLett.74.1728>.
- [103] Liew, T. C. H. & Savona, V. Quantum entanglement in nanocavity arrays. *Phys. Rev. A* **85**, 050301 (2012). URL <https://link.aps.org/doi/10.1103/PhysRevA.85.050301>.
- [104] Karr, J. P., Baas, A., Houdré, R. & Giacobino, E. Squeezing in semiconductor microcavities in the strong-coupling regime. *Phys. Rev. A* **69**, 031802 (2004). URL <https://link.aps.org/doi/10.1103/PhysRevA.69.031802>.
- [105] Larionova, Y., Stolz, W. & Weiss, C. O. Optical bistability and spatial resonator solitons based on exciton-polariton nonlinearity. *Opt. Lett.* **33**, 321–323 (2008). URL <http://ol.osa.org/abstract.cfm?URI=ol-33-4-321>.
- [106] Gavrilov, S. S. *et al.* Spin multistability of cavity polaritons in a magnetic field. *Phys. Rev. B* **87**, 201303 (2013). URL <https://link.aps.org/doi/10.1103/PhysRevB.87.201303>.
- [107] Gavrilov, S. S. *et al.* Polariton multistability and fast linear-to-circular polarization conversion in planar microcavities with lowered symmetry. *Applied Physics Letters* **102**, 011104 (2013). URL <https://doi.org/10.1063/1.4773523>. <https://doi.org/10.1063/1.4773523>.
- [108] Sarkar, D. *et al.* Polarization Bistability and Resultant Spin Rings in Semiconductor Microcavities. *Phys. Rev. Lett.* **105**, 216402 (2010). URL <https://link.aps.org/doi/10.1103/PhysRevLett.105.216402>.
- [109] Amo, A. *et al.* Exciton-polariton spin switches. *Nature Photonics* **4**, 361–366 (2010). URL <https://doi.org/10.1038/nphoton.2010.79>.
- [110] Takemura, N., Trebaol, S., Wouters, M., Portella-Oberli, M. T. & Deveaud, B. Polaritonic Feshbach resonance. *Nature Physics* **10**, 500–504 (2014). URL <https://doi.org/10.1038/nphys2999>.

- [111] Deveaud, B. Polariton interactions in semiconductor microcavities. *Comptes Rendus Physique* **17**, 874–892 (2016). URL <https://www.sciencedirect.com/science/article/pii/S1631070516300329>. Polariton physics / Physique des polaritons.
- [112] Amo, A. *et al.* Superfluidity of polaritons in semiconductor microcavities. *Nature Physics* **5**, 805–810 (2009). URL <https://doi.org/10.1038/nphys1364>.
- [113] Sanvitto, D. *et al.* Persistent currents and quantized vortices in a polariton superfluid. *Nature Physics* **6**, 527–533 (2010). URL <https://doi.org/10.1038/nphys1668>.
- [114] Keeling, J. & Berloff, N. G. Going with the flow. *Nature* **457**, 273–274 (2009). URL <https://doi.org/10.1038/457273a>.
- [115] Lerario, G. *et al.* Room-temperature superfluidity in a polariton condensate. *Nature Physics* **13**, 837–841 (2017). URL <https://doi.org/10.1038/nphys4147>.
- [116] Nardin, G. *et al.* Hydrodynamic nucleation of quantized vortex pairs in a polariton quantum fluid. *Nature Physics* **7**, 635–641 (2011). URL <https://doi.org/10.1038/nphys1959>.
- [117] Grosso, G., Nardin, G., Morier-Genoud, F., Léger, Y. & Deveaud-Plédran, B. Soliton Instabilities and Vortex Street Formation in a Polariton Quantum Fluid. *Phys. Rev. Lett.* **107**, 245301 (2011). URL <https://link.aps.org/doi/10.1103/PhysRevLett.107.245301>.
- [118] Sanvitto, D. *et al.* All-optical control of the quantum flow of a polariton condensate. *Nature Photonics* **5**, 610–614 (2011). URL <https://doi.org/10.1038/nphoton.2011.211>.
- [119] Dominici, L. *et al.* Interactions and scattering of quantum vortices in a polariton fluid. *Nature Communications* **9**, 1467 (2018). URL <https://doi.org/10.1038/s41467-018-03736-5>.
- [120] Boulrier, T. *et al.* Vortex Chain in a Resonantly Pumped Polariton Superfluid. *Scientific Reports* **5**, 9230 (2015). URL <https://doi.org/10.1038/srep09230>.
- [121] Boulrier, T. *et al.* Injection of Orbital Angular Momentum and Storage of Quantized Vortices in Polariton Superfluids. *Phys. Rev. Lett.* **116**, 116402 (2016). URL <https://link.aps.org/doi/10.1103/PhysRevLett.116.116402>.
- [122] Pigeon, S. & Bramati, A. Sustained propagation and control of topological excitations in polariton superfluid. *New Journal of Physics* **19**, 095004 (2017). URL <https://doi.org/10.1088/1367-2630/aa849c>.
- [123] Lerario, G. *et al.* Vortex-stream generation and enhanced propagation in a polariton superfluid. *Phys. Rev. Research* **2**, 023049 (2020). URL <https://link.aps.org/doi/10.1103/PhysRevResearch.2.023049>.

- [124] Utsunomiya, S. *et al.* Observation of Bogoliubov excitations in exciton-polariton condensates. *Nature Physics* **4**, 700–705 (2008). URL <https://doi.org/10.1038/nphys1034>.
- [125] Kohnle, V. *et al.* From Single Particle to Superfluid Excitations in a Dissipative Polariton Gas. *Phys. Rev. Lett.* **106**, 255302 (2011). URL <https://link.aps.org/doi/10.1103/PhysRevLett.106.255302>.
- [126] Stepanov, P. *et al.* Dispersion relation of the collective excitations in a resonantly driven polariton fluid. *Nature Communications* **10**, 3869 (2019). URL <https://doi.org/10.1038/s41467-019-11886-3>.
- [127] Claude, F. *et al.* High-resolution coherent probe spectroscopy of a polariton quantum fluid (2021). [2112.09903](https://arxiv.org/abs/2112.09903).
- [128] Solnyshkov, D. D., Flayac, H. & Malpuech, G. Black holes and wormholes in spinor polariton condensates. *Phys. Rev. B* **84**, 233405 (2011). URL <https://link.aps.org/doi/10.1103/PhysRevB.84.233405>.
- [129] Gerace, D. & Carusotto, I. Analog Hawking radiation from an acoustic black hole in a flowing polariton superfluid. *Phys. Rev. B* **86**, 144505 (2012). URL <https://link.aps.org/doi/10.1103/PhysRevB.86.144505>.
- [130] Nguyen, H. S. *et al.* Acoustic Black Hole in a Stationary Hydrodynamic Flow of Microcavity Polaritons. *Phys. Rev. Lett.* **114**, 036402 (2015). URL <https://link.aps.org/doi/10.1103/PhysRevLett.114.036402>.
- [131] Solnyshkov, D. D., Leblanc, C., Koniakhin, S. V., Bleu, O. & Malpuech, G. Quantum analogue of a Kerr black hole and the Penrose effect in a Bose-Einstein condensate. *Phys. Rev. B* **99**, 214511 (2019). URL <https://link.aps.org/doi/10.1103/PhysRevB.99.214511>.
- [132] Jacquet, M. J. *et al.* Polariton fluids for analogue gravity physics. *Philosophical Transactions of the Royal Society A: Mathematical, Physical and Engineering Sciences* **378**, 20190225 (2020). URL <http://dx.doi.org/10.1098/rsta.2019.0225>.
- [133] Russell, J. S. Report on waves. *Report of the 14th Meeting of the British Association for the Advancement of Science, Plates XLVII-LVII, 90-311* (1844).
- [134] Boussinesq, J. Théorie des ondes et des remous qui se propagent le long d'un canal rectangulaire horizontal, en communiquant au liquide contenu dans ce canal des vitesses sensiblement pareilles de la surface au fond. *Journal de Mathématiques Pures et Appliquées* 55–108 (1872). URL <http://eudml.org/doc/234248>.
- [135] Fermi, E., Pasta, P., Ulam, S. & Tsingou, M. STUDIES OF THE NONLINEAR PROBLEMS. *Technical Report Los Alamos National Lab* (1955). URL <https://www.osti.gov/biblio/4376203>.
- [136] Kivshar, Y. S. & Malomed, B. A. Dynamics of solitons in nearly integrable systems. *Rev. Mod. Phys.* **61**, 763–915 (1989). URL <https://link.aps.org/doi/10.1103/RevModPhys.61.763>.

- [137] Zabusky, N. J. & Kruskal, M. D. Interaction of "Solitons" in a Collisionless Plasma and the Recurrence of Initial States. *Phys. Rev. Lett.* **15**, 240–243 (1965). URL <https://link.aps.org/doi/10.1103/PhysRevLett.15.240>.
- [138] Haus, H. A. & Wong, W. S. Solitons in optical communications. *Rev. Mod. Phys.* **68**, 423–444 (1996). URL <https://link.aps.org/doi/10.1103/RevModPhys.68.423>.
- [139] Hasegawa, A. An historical review of application of optical solitons for high speed communications. *Chaos: An Interdisciplinary Journal of Nonlinear Science* **10**, 475–485 (2000). URL <https://doi.org/10.1063/1.1286914>. <https://doi.org/10.1063/1.1286914>.
- [140] Kartashov, Y. V., Malomed, B. A. & Torner, L. Solitons in nonlinear lattices. *Rev. Mod. Phys.* **83**, 247–305 (2011). URL <https://link.aps.org/doi/10.1103/RevModPhys.83.247>.
- [141] Kivshar, Y. & Agrawal, G. *Optical Solitons* (Elsevier Science, 2003). URL <https://www.elsevier.com/books/optical-solitons/kivshar/978-0-12-410590-4>.
- [142] Claude, F. *et al.* Taming the snake instabilities in a polariton superfluid. *Optica* **7**, 1660–1665 (2020). URL <http://www.osapublishing.org/optica/abstract.cfm?URI=optica-7-12-1660>.
- [143] Sich, M. *et al.* Observation of bright polariton solitons in a semiconductor microcavity. *Nature Photonics* **6**, 50–55 (2012). URL <https://doi.org/10.1038/nphoton.2011.267>.
- [144] Yulin, A. V., Egorov, O. A., Lederer, F. & Skryabin, D. V. Dark polariton solitons in semiconductor microcavities. *Phys. Rev. A* **78**, 061801 (2008). URL <https://link.aps.org/doi/10.1103/PhysRevA.78.061801>.
- [145] Kamchatnov, A. M. & Korneev, S. V. Oblique solitons generated by the flow of a polariton condensate past an obstacle. *Journal of Experimental and Theoretical Physics* **115**, 579–585 (2012). URL <https://doi.org/10.1134/S1063776112080080>.
- [146] Amo, A. *et al.* Polariton Superfluids Reveal Quantum Hydrodynamic Solitons. *Science* **332**, 1167–1170 (2011). URL <https://science.sciencemag.org/content/332/6034/1167>. <https://science.sciencemag.org/content/332/6034/1167.full.pdf>.
- [147] Hivet, R. *et al.* Half-solitons in a polariton quantum fluid behave like magnetic monopoles. *Nature Physics* **8**, 724–728 (2012). URL <https://doi.org/10.1038/nphys2406>.
- [148] Lerario, G. *et al.* Parallel dark-soliton pair in a bistable two-dimensional exciton-polariton superfluid. *Phys. Rev. Research* **2**, 042041 (2020). URL <https://link.aps.org/doi/10.1103/PhysRevResearch.2.042041>.
- [149] Walker, P. M. *et al.* Dark Solitons in High Velocity Waveguide Polariton Fluids. *Phys. Rev. Lett.* **119**, 097403 (2017). URL <https://link.aps.org/doi/10.1103/PhysRevLett.119.097403>.

- [150] Maître, A. *et al.* Dark-Soliton Molecules in an Exciton-Polariton Superfluid. *Phys. Rev. X* **10**, 041028 (2020). URL <https://link.aps.org/doi/10.1103/PhysRevX.10.041028>.
- [151] Koniakhin, S. V. *et al.* Stationary Quantum Vortex Street in a Driven-Dissipative Quantum Fluid of Light. *Phys. Rev. Lett.* **123**, 215301 (2019). URL <https://link.aps.org/doi/10.1103/PhysRevLett.123.215301>.
- [152] Kartashov, Y. V. & Skryabin, D. V. Temporal dark polariton solitons. *Opt. Lett.* **41**, 1760–1763 (2016). URL <http://www.osapublishing.org/ol/abstract.cfm?URI=ol-41-8-1760>.
- [153] Opala, A., Pieczarka, M., Bobrovska, N. & Matuszewski, M. Dynamics of defect-induced dark solitons in an exciton-polariton condensate. *Phys. Rev. B* **97**, 155304 (2018). URL <https://link.aps.org/doi/10.1103/PhysRevB.97.155304>.
- [154] Amo, A. *et al.* Collective fluid dynamics of a polariton condensate in a semiconductor microcavity. *Nature* **457**, 291–295 (2009). URL <https://doi.org/10.1038/nature07640>.
- [155] Chana, J. K. *et al.* Spatial Patterns of Dissipative Polariton Solitons in Semiconductor Microcavities. *Phys. Rev. Lett.* **115**, 256401 (2015). URL <https://link.aps.org/doi/10.1103/PhysRevLett.115.256401>.
- [156] Schneider, C. *et al.* Exciton-polariton trapping and potential landscape engineering. *Reports on Progress in Physics* **80**, 016503 (2016). URL <https://doi.org/10.1088/0034-4885/80/1/016503>.
- [157] Balili, R., Hartwell, V., Snoke, D., Pfeiffer, L. & West, K. Bose-Einstein Condensation of Microcavity Polaritons in a Trap. *Science* **316**, 1007–1010 (2007). URL <https://science.sciencemag.org/content/316/5827/1007>. <https://science.sciencemag.org/content/316/5827/1007.full.pdf>.
- [158] Cerda-Méndez, E. A., Krizhanovskii, D. N., Skolnick, M. S. & Santos, P. V. Quantum fluids of light in acoustic lattices. *Journal of Physics D: Applied Physics* **51**, 033001 (2017). URL <https://doi.org/10.1088/1361-6463/aa9ec7>.
- [159] Amo, A. *et al.* Light engineering of the polariton landscape in semiconductor microcavities. *Phys. Rev. B* **82**, 081301 (2010). URL <https://link.aps.org/doi/10.1103/PhysRevB.82.081301>.
- [160] Cerda-Méndez, E. A. *et al.* Polariton Condensation in Dynamic Acoustic Lattices. *Phys. Rev. Lett.* **105**, 116402 (2010). URL <https://link.aps.org/doi/10.1103/PhysRevLett.105.116402>.
- [161] Cerda-Méndez, E. A. *et al.* Exciton-Polariton Gap Solitons in Two-Dimensional Lattices. *Phys. Rev. Lett.* **111**, 146401 (2013). URL <https://link.aps.org/doi/10.1103/PhysRevLett.111.146401>.
- [162] Wertz, E. *et al.* Spontaneous formation and optical manipulation of extended polariton condensates. *Nature Physics* **6**, 860–864 (2010). URL <https://doi.org/10.1038/nphys1750>.

- [163] Askitopoulos, A. *et al.* Polariton condensation in an optically induced two-dimensional potential. *Phys. Rev. B* **88**, 041308 (2013). URL <https://link.aps.org/doi/10.1103/PhysRevB.88.041308>.
- [164] Ohadi, H. *et al.* Synchronization crossover of polariton condensates in weakly disordered lattices. *Phys. Rev. B* **97**, 195109 (2018). URL <https://link.aps.org/doi/10.1103/PhysRevB.97.195109>.
- [165] Kim, N. Y. *et al.* Dynamical d-wave condensation of exciton-polaritons in a two-dimensional square-lattice potential. *Nature Physics* **7**, 681–686 (2011). URL <https://doi.org/10.1038/nphys2012>.
- [166] Masumoto, N. *et al.* Exciton–polariton condensates with flat bands in a two-dimensional kagome lattice. *New Journal of Physics* **14**, 065002 (2012). URL <https://doi.org/10.1088/1367-2630/14/6/065002>.
- [167] Kim, N. Y. *et al.* Exciton–polariton condensates near the Dirac point in a triangular lattice. *New Journal of Physics* **15**, 035032 (2013). URL <https://doi.org/10.1088/1367-2630/15/3/035032>.
- [168] Cerna, R. *et al.* Coherent optical control of the wave function of zero-dimensional exciton polaritons. *Phys. Rev. B* **80**, 121309 (2009). URL <https://link.aps.org/doi/10.1103/PhysRevB.80.121309>.
- [169] Bayer, M. *et al.* Optical Demonstration of a Crystal Band Structure Formation. *Phys. Rev. Lett.* **83**, 5374–5377 (1999). URL <https://link.aps.org/doi/10.1103/PhysRevLett.83.5374>.
- [170] Kaitouni, R. I. *et al.* Engineering the spatial confinement of exciton polaritons in semiconductors. *Phys. Rev. B* **74**, 155311 (2006). URL <https://link.aps.org/doi/10.1103/PhysRevB.74.155311>.
- [171] El Daïf, O. *et al.* Polariton quantum boxes in semiconductor microcavities. *Applied Physics Letters* **88**, 061105 (2006). URL <https://doi.org/10.1063/1.2172409>. <https://doi.org/10.1063/1.2172409>.
- [172] Winkler, K. *et al.* A polariton condensate in a photonic crystal potential landscape. *New Journal of Physics* **17**, 023001 (2015). URL <https://doi.org/10.1088/1367-2630/17/2/023001>.
- [173] Harder, T. H. *et al.* Exciton-polaritons in flatland: Controlling flatband properties in a Lieb lattice. *Phys. Rev. B* **102**, 121302 (2020). URL <https://link.aps.org/doi/10.1103/PhysRevB.102.121302>.
- [174] Harder, T. H. *et al.* Kagome Flatbands for Coherent Exciton-Polariton Lasing. *ACS Photonics* **8**, 3193–3200 (2021). URL <https://doi.org/10.1021/acsp Photonics.1c00950>.
- [175] Bloch, J. *et al.* Strong-coupling regime in pillar semiconductor microcavities. *Superlattices and Microstructures* **22**, 371–374 (1997). URL <https://www.sciencedirect.com/science/article/pii/S0749603696903171>.

- [176] Gutbrod, T. *et al.* Weak and strong coupling of photons and excitons in photonic dots. *Phys. Rev. B* **57**, 9950–9956 (1998). URL <https://link.aps.org/doi/10.1103/PhysRevB.57.9950>.
- [177] Kuther, A. *et al.* Confined optical modes in photonic wires. *Phys. Rev. B* **58**, 15744–15748 (1998). URL <https://link.aps.org/doi/10.1103/PhysRevB.58.15744>.
- [178] Fischer, J. *et al.* Spatial Coherence Properties of One Dimensional Exciton-Polariton Condensates. *Phys. Rev. Lett.* **113**, 203902 (2014). URL <https://link.aps.org/doi/10.1103/PhysRevLett.113.203902>.
- [179] Skryabin, D. V. *et al.* Backward Cherenkov radiation emitted by polariton solitons in a microcavity wire. *Nature Communications* **8**, 1554 (2017). URL <https://doi.org/10.1038/s41467-017-01751-6>.
- [180] Klemmt, S. *et al.* Polariton condensation in S- and P-flatbands in a two-dimensional Lieb lattice. *Applied Physics Letters* **111**, 231102 (2017). URL <https://doi.org/10.1063/1.4995385>. <https://doi.org/10.1063/1.4995385>.
- [181] Whittaker, C. E. *et al.* Exciton Polaritons in a Two-Dimensional Lieb Lattice with Spin-Orbit Coupling. *Phys. Rev. Lett.* **120**, 097401 (2018). URL <https://link.aps.org/doi/10.1103/PhysRevLett.120.097401>.
- [182] Klemmt, S. *et al.* Exciton-polariton topological insulator. *Nature* **562**, 552–556 (2018). URL <https://doi.org/10.1038/s41586-018-0601-5>.
- [183] Whittaker, C. E. *et al.* Optical and magnetic control of orbital flat bands in a polariton Lieb lattice. *Phys. Rev. A* **104**, 063505 (2021). URL <https://link.aps.org/doi/10.1103/PhysRevA.104.063505>.
- [184] Zhang, B. *et al.* Zero-dimensional polariton laser in a subwavelength grating-based vertical microcavity. *Light: Science & Applications* **3**, e135–e135 (2014). URL <https://doi.org/10.1038/lsa.2014.16>.
- [185] Kim, S. *et al.* Coherent Polariton Laser. *Phys. Rev. X* **6**, 011026 (2016). URL <https://link.aps.org/doi/10.1103/PhysRevX.6.011026>.
- [186] Besga, B. *et al.* Polariton Boxes in a Tunable Fiber Cavity. *Phys. Rev. Applied* **3**, 014008 (2015). URL <https://link.aps.org/doi/10.1103/PhysRevApplied.3.014008>.
- [187] Dufferwiel, S. *et al.* Tunable polaritonic molecules in an open microcavity system. *Applied Physics Letters* **107**, 201106 (2015). URL <https://doi.org/10.1063/1.4936092>. <https://doi.org/10.1063/1.4936092>.
- [188] Nguyen, H. S. *et al.* Realization of a Double-Barrier Resonant Tunneling Diode for Cavity Polaritons. *Phys. Rev. Lett.* **110**, 236601 (2013). URL <https://link.aps.org/doi/10.1103/PhysRevLett.110.236601>.
- [189] Tanese, D. *et al.* Polariton condensation in solitonic gap states in a one-dimensional periodic potential. *Nature Communications* **4**, 1749 (2013). URL <https://doi.org/10.1038/ncomms2760>.

- [190] Sturm, C. *et al.* All-optical phase modulation in a cavity-polariton Mach-Zehnder interferometer. *Nature Communications* **5**, 3278 (2014). URL <https://doi.org/10.1038/ncomms4278>.
- [191] Goblot, V. *et al.* Emergence of criticality through a cascade of delocalization transitions in quasiperiodic chains. *Nature Physics* **16**, 832–836 (2020). URL <https://doi.org/10.1038/s41567-020-0908-7>.
- [192] Tanese, D. *et al.* Fractal Energy Spectrum of a Polariton Gas in a Fibonacci Quasiperiodic Potential. *Phys. Rev. Lett.* **112**, 146404 (2014). URL <https://link.aps.org/doi/10.1103/PhysRevLett.112.146404>.
- [193] Michaelis de Vasconcellos, S. *et al.* Spatial, spectral, and polarization properties of coupled micropillar cavities. *Applied Physics Letters* **99**, 101103 (2011). URL <https://doi.org/10.1063/1.3632111>. <https://doi.org/10.1063/1.3632111>.
- [194] Mangussi, F. *et al.* Multi-orbital tight binding model for cavity-polariton lattices. *Journal of Physics: Condensed Matter* **32**, 315402 (2020). URL <https://doi.org/10.1088/1361-648x/ab8524>.
- [195] Sala, V. G. *et al.* Spin-Orbit Coupling for Photons and Polaritons in Microstructures. *Phys. Rev. X* **5**, 011034 (2015). URL <https://link.aps.org/doi/10.1103/PhysRevX.5.011034>.
- [196] Zambon, N. C. *et al.* Orbital angular momentum bistability in a microlaser. *Opt. Lett.* **44**, 4531–4534 (2019). URL <http://ol.osa.org/abstract.cfm?URI=ol-44-18-4531>.
- [197] St-Jean, P. *et al.* Lasing in topological edge states of a one-dimensional lattice. *Nature Photonics* **11**, 651–656 (2017). URL <https://doi.org/10.1038/s41566-017-0006-2>.
- [198] Jacqumin, T. *et al.* Direct Observation of Dirac Cones and a Flatband in a Honeycomb Lattice for Polaritons. *Phys. Rev. Lett.* **112**, 116402 (2014). URL <https://link.aps.org/doi/10.1103/PhysRevLett.112.116402>.
- [199] Milićević, M. *et al.* Type-III and Tilted Dirac Cones Emerging from Flat Bands in Photonic Orbital Graphene. *Phys. Rev. X* **9**, 031010 (2019). URL <https://link.aps.org/doi/10.1103/PhysRevX.9.031010>.
- [200] Anderson, B. M., Ma, R., Owens, C., Schuster, D. I. & Simon, J. Engineering Topological Many-Body Materials in Microwave Cavity Arrays. *Phys. Rev. X* **6**, 041043 (2016). URL <https://link.aps.org/doi/10.1103/PhysRevX.6.041043>.
- [201] Owens, C. *et al.* Quarter-flux Hofstadter lattice in a qubit-compatible microwave cavity array. *Phys. Rev. A* **97**, 013818 (2018). URL <https://link.aps.org/doi/10.1103/PhysRevA.97.013818>.
- [202] Solnyshkov, D. D., Bleu, O., Teklu, B. & Malpuech, G. Chirality of Topological Gap Solitons in Bosonic Dimer Chains. *Physical Review Letters* **118**, 023901 (2017). URL <https://journals.aps.org/prl/abstract/10.1103/PhysRevLett.118.023901>. 1607.01805.

- [203] Smirnova, D. A., Smirnov, L. A., Leykam, D. & Kivshar, Y. S. Topological Edge States and Gap Solitons in the Nonlinear Dirac Model. *Laser & Photonics Reviews* **13**, 1900223 (2019). URL <https://onlinelibrary.wiley.com/doi/abs/10.1002/lpor.201900223>. <https://onlinelibrary.wiley.com/doi/pdf/10.1002/lpor.201900223>.
- [204] Kartashov, Y. V., Malomed, B. A., Vysloukh, V. A. & Torner, L. Two-dimensional solitons in nonlinear lattices. *Opt. Lett.* **34**, 770–772 (2009). URL <http://www.osapublishing.org/ol/abstract.cfm?URI=ol-34-6-770>.
- [205] Gulevich, D. R., Yudin, D., Skryabin, D. V., Iorsh, I. V. & Shelykh, I. A. Exploring nonlinear topological states of matter with exciton-polaritons: Edge solitons in kagome lattice. *Scientific Reports* **7**, 1780 (2017). URL <https://doi.org/10.1038/s41598-017-01646-y>.
- [206] Poddubny, A. N. & Smirnova, D. A. Ring Dirac solitons in nonlinear topological systems. *Phys. Rev. A* **98**, 013827 (2018). URL <https://link.aps.org/doi/10.1103/PhysRevA.98.013827>.
- [207] Di Liberto, M., Mukherjee, S. & Goldman, N. Nonlinear dynamics of Aharonov-Bohm cages. *Phys. Rev. A* **100**, 043829 (2019). URL <https://link.aps.org/doi/10.1103/PhysRevA.100.043829>.
- [208] Ouellet-Plamondon, C. *et al.* Spatial multistability induced by cross interactions of confined polariton modes. *Phys. Rev. B* **93**, 085313 (2016). URL <https://link.aps.org/doi/10.1103/PhysRevB.93.085313>.
- [209] Paraíso, T. K., Wouters, M., Léger, Y., Morier-Genoud, F. & Deveaud-Plédran, B. Multistability of a coherent spin ensemble in a semiconductor microcavity. *Nature Materials* **9**, 655–660 (2010). URL <https://doi.org/10.1038/nmat2787>.
- [210] Real, B. *et al.* Chiral emission induced by optical Zeeman effect in polariton micropillars (2021). [2107.11131](https://doi.org/10.1103/PhysRevLett.117.217401).
- [211] Ferrier, L. *et al.* Polariton parametric oscillation in a single micropillar cavity. *Applied Physics Letters* **97**, 031105 (2010). URL <https://doi.org/10.1063/1.3466902>. <https://doi.org/10.1063/1.3466902>.
- [212] Boulier, T. *et al.* Polariton-generated intensity squeezing in semiconductor micropillars. *Nature Communications* **5**, 3260 (2014). URL <https://doi.org/10.1038/ncomms4260>.
- [213] Rodriguez, S. R. K. *et al.* Probing a Dissipative Phase Transition via Dynamical Optical Hysteresis. *Phys. Rev. Lett.* **118**, 247402 (2017). URL <https://link.aps.org/doi/10.1103/PhysRevLett.118.247402>.
- [214] Carlon Zambon, N. *et al.* Parametric instability in coupled nonlinear microcavities. *Phys. Rev. A* **102**, 023526 (2020). URL <https://link.aps.org/doi/10.1103/PhysRevA.102.023526>.
- [215] Goblot, V. *et al.* Phase-Controlled Bistability of a Dark Soliton Train in a Polariton Fluid. *Phys. Rev. Lett.* **117**, 217401 (2016). URL <https://link.aps.org/doi/10.1103/PhysRevLett.117.217401>.

- [216] Abbarchi, M. *et al.* Macroscopic quantum self-trapping and Josephson oscillations of exciton polaritons. *Nature Physics* **9**, 275–279 (2013). URL <https://doi.org/10.1038/nphys2609>.
- [217] Rodriguez, S. R. K. *et al.* Interaction-induced hopping phase in driven-dissipative coupled photonic microcavities. *Nature Communications* **7**, 11887 (2016). URL <https://doi.org/10.1038/ncomms11887>.
- [218] Petrov, M. Y. & Kavokin, A. V. Polariton transport in one-dimensional channels. *Phys. Rev. B* **88**, 035308 (2013). URL <https://link.aps.org/doi/10.1103/PhysRevB.88.035308>.
- [219] Goblot, V. *et al.* Nonlinear Polariton Fluids in a Flatband Reveal Discrete Gap Solitons. *Phys. Rev. Lett.* **123**, 113901 (2019). URL <https://link.aps.org/doi/10.1103/PhysRevLett.123.113901>.
- [220] Rosenau, P. & Hyman, J. M. Compactons: Solitons with finite wavelength. *Phys. Rev. Lett.* **70**, 564–567 (1993). URL <https://link.aps.org/doi/10.1103/PhysRevLett.70.564>.
- [221] Vicencio, R. A. & Johansson, M. Discrete flat-band solitons in the kagome lattice. *Phys. Rev. A* **87**, 061803 (2013). URL <https://link.aps.org/doi/10.1103/PhysRevA.87.061803>.
- [222] Alexander, T. J., Ostrovskaya, E. A. & Kivshar, Y. S. Self-Trapped Nonlinear Matter Waves in Periodic Potentials. *Phys. Rev. Lett.* **96**, 040401 (2006). URL <https://link.aps.org/doi/10.1103/PhysRevLett.96.040401>.
- [223] Bersch, C., Onishchukov, G. & Peschel, U. Optical Gap solitons and Truncated Nonlinear Bloch Waves in Temporal Lattices. *Phys. Rev. Lett.* **109**, 093903 (2012). URL <https://link.aps.org/doi/10.1103/PhysRevLett.109.093903>.
- [224] Alexander, T. J. & Kivshar, Y. S. Soliton complexes and flat-top nonlinear modes in optical lattices. *Applied Physics B* **82**, 203–206 (2006). URL <https://doi.org/10.1007/s00340-005-2071-3>.
- [225] Wang, J., Yang, J., Alexander, T. J. & Kivshar, Y. S. Truncated-Bloch-wave solitons in optical lattices. *Phys. Rev. A* **79**, 043610 (2009). URL <https://link.aps.org/doi/10.1103/PhysRevA.79.043610>.
- [226] Anker, T. *et al.* Nonlinear Self-Trapping of Matter Waves in Periodic Potentials. *Phys. Rev. Lett.* **94**, 020403 (2005). URL <https://link.aps.org/doi/10.1103/PhysRevLett.94.020403>.
- [227] Bennet, F. H. *et al.* Observation of Nonlinear Self-Trapping of Broad Beams in Defocusing Waveguide Arrays. *Phys. Rev. Lett.* **106**, 093901 (2011). URL <https://link.aps.org/doi/10.1103/PhysRevLett.106.093901>.
- [228] Bogolyubov, N. N. On the theory of superfluidity. *J. Phys. (USSR)* **11**, 23–32 (1947).
- [229] Bogolyubov, N. N. On a New method in the theory of superconductivity. *Nuovo Cim.* **7**, 794–805 (1958).

- [230] Hasan, M. Z. & Kane, C. L. Colloquium: Topological insulators. *Rev. Mod. Phys.* **82**, 3045–3067 (2010). URL <https://link.aps.org/doi/10.1103/RevModPhys.82.3045>.
- [231] Qi, X.-L. & Zhang, S.-C. Topological insulators and superconductors. *Rev. Mod. Phys.* **83**, 1057–1110 (2011). URL <https://link.aps.org/doi/10.1103/RevModPhys.83.1057>.
- [222] Xiao-Gang, W. Topological orders and edge excitations in fractional quantum Hall states. *Advances in Physics* **44**, 405–473 (1995). URL <https://doi.org/10.1080/00018739500101566>. <https://doi.org/10.1080/00018739500101566>.
- [233] Tsui, D. C., Stormer, H. L. & Gossard, A. C. Two-Dimensional Magnetotransport in the Extreme Quantum Limit. *Phys. Rev. Lett.* **48**, 1559–1562 (1982). URL <https://link.aps.org/doi/10.1103/PhysRevLett.48.1559>.
- [234] Laughlin, R. B. Anomalous Quantum Hall Effect: An Incompressible Quantum Fluid with Fractionally Charged Excitations. *Phys. Rev. Lett.* **50**, 1395–1398 (1983). URL <https://link.aps.org/doi/10.1103/PhysRevLett.50.1395>.
- [235] Rechtsman, M. C. *et al.* Photonic Floquet topological insulators. *Nature* **496**, 196–200 (2013). URL <https://doi.org/10.1038/nature12066>.
- [236] Zilberberg, O. *et al.* Photonic topological boundary pumping as a probe of 4D quantum Hall physics. *Nature* **553**, 59–62 (2018). URL <https://doi.org/10.1038/nature25011>.
- [237] Vaughan, H. Rectangles and simple closed curves. *Lecture, Univ. of Ill. at Urbana* (1977).
- [238] Meyerson, M. D. Balancing acts. *Topology Proceedings* **6**, 59–75 (1981).
- [239] Blevins, A. S. & Bassett, D. S. *Topology in Biology*, 1–23 (Springer International Publishing, Cham, 2020). URL https://doi.org/10.1007/978-3-319-70658-0_87-1.
- [240] Thom, R. Topological models in biology. *Topology* **8**, 313–335 (1969). URL <https://www.sciencedirect.com/science/article/pii/0040938369900184>.
- [241] Dokholyan, N. V., Li, L., Ding, F. & Shakhnovich, E. I. Topological determinants of protein folding. *Proceedings of the National Academy of Sciences* **99**, 8637–8641 (2002). URL <https://www.pnas.org/content/99/13/8637>. <https://www.pnas.org/content/99/13/8637.full.pdf>.
- [242] Mucherino, A. *et al.* Understanding the role of the topology in protein folding by computational inverse folding experiments. *Computational Biology and Chemistry* **32**, 233–239 (2008). URL <https://www.sciencedirect.com/science/article/pii/S1476927108000297>.

- [243] Flapan, E., He, A. & Wong, H. Topological descriptions of protein folding. *Proceedings of the National Academy of Sciences* **116**, 9360–9369 (2019). URL <https://www.pnas.org/content/116/19/9360>. <https://www.pnas.org/content/116/19/9360.full.pdf>.
- [244] Haldane, F. D. M. Model for a Quantum Hall Effect without Landau Levels: Condensed-Matter Realization of the "Parity Anomaly". *Phys. Rev. Lett.* **61**, 2015–2018 (1988). URL <https://link.aps.org/doi/10.1103/PhysRevLett.61.2015>.
- [245] Kane, C. L. & Mele, E. J. Quantum Spin Hall Effect in Graphene. *Phys. Rev. Lett.* **95**, 226801 (2005). URL <https://link.aps.org/doi/10.1103/PhysRevLett.95.226801>.
- [246] Kane, C. L. & Mele, E. J. Z_2 Topological Order and the Quantum Spin Hall Effect. *Phys. Rev. Lett.* **95**, 146802 (2005). URL <https://link.aps.org/doi/10.1103/PhysRevLett.95.146802>.
- [247] König, M. *et al.* Quantum Spin Hall Insulator State in HgTe Quantum Wells. *Science* **318**, 766–770 (2007). URL <http://dx.doi.org/10.1126/science.1148047>.
- [248] Schnyder, A. P., Ryu, S., Furusaki, A. & Ludwig, A. W. W. Classification of topological insulators and superconductors in three spatial dimensions. *Phys. Rev. B* **78**, 195125 (2008). URL <https://link.aps.org/doi/10.1103/PhysRevB.78.195125>.
- [249] Kitaev, A. Periodic table for topological insulators and superconductors. *AIP Conference Proceedings* **1134**, 22–30 (2009). URL <https://aip.scitation.org/doi/abs/10.1063/1.3149495>. <https://aip.scitation.org/doi/pdf/10.1063/1.3149495>.
- [250] Schnyder, A. P. *et al.* Classification of Topological Insulators and Superconductors. *AIP Conference Proceedings* (2009). URL <http://dx.doi.org/10.1063/1.3149481>.
- [251] Berry, M. V. Quantal phase factors accompanying adiabatic changes. *Proceedings of the Royal Society of London. A. Mathematical and Physical Sciences* **392**, 45–57 (1984). URL <https://royalsocietypublishing.org/doi/abs/10.1098/rspa.1984.0023>. <https://royalsocietypublishing.org/doi/pdf/10.1098/rspa.1984.0023>.
- [252] Pancharatnam, S. Generalized theory of interference and its applications. *Proceedings of the Indian Academy of Sciences - Section A* **44**, 398–417 (1956). URL <https://doi.org/10.1007/BF03046095>.
- [253] Jackiw, R. & Rebbi, C. Solitons with fermion number $\frac{1}{2}$. *Phys. Rev. D* **13**, 3398–3409 (1976). URL <https://link.aps.org/doi/10.1103/PhysRevD.13.3398>.
- [254] Hatsugai, Y. Chern number and edge states in the integer quantum Hall effect. *Phys. Rev. Lett.* **71**, 3697–3700 (1993). URL <https://link.aps.org/doi/10.1103/PhysRevLett.71.3697>.

- [255] Qi, X.-L., Wu, Y.-S. & Zhang, S.-C. General theorem relating the bulk topological number to edge states in two-dimensional insulators. *Phys. Rev. B* **74**, 045125 (2006). URL <https://link.aps.org/doi/10.1103/PhysRevB.74.045125>.
- [256] Novoselov, K. S. *et al.* Room-Temperature Quantum Hall Effect in Graphene. *Science* **315**, 1379–1379 (2007). URL <http://dx.doi.org/10.1126/science.1137201>.
- [257] Chiu, C.-K., Teo, J. C. Y., Schnyder, A. P. & Ryu, S. Classification of topological quantum matter with symmetries. *Rev. Mod. Phys.* **88**, 035005 (2016). URL <https://link.aps.org/doi/10.1103/RevModPhys.88.035005>.
- [258] Tokura, Y., Yasuda, K. & Tsukazaki, A. Magnetic topological insulators. *Nature Reviews Physics* **1**, 126–143 (2019). URL <https://doi.org/10.1038/s42254-018-0011-5>.
- [259] Wu, S. *et al.* Observation of the quantum spin Hall effect up to 100 kelvin in a monolayer crystal. *Science* **359**, 76–79 (2018). URL <http://dx.doi.org/10.1126/science.aan6003>.
- [260] Wang, Z., Chong, Y., Joannopoulos, J. D. & Soljačić, M. Observation of unidirectional backscattering-immune topological electromagnetic states. *Nature* **461**, 772–775 (2009). URL <https://doi.org/10.1038/nature08293>.
- [261] Hafezi, M., Mittal, S., Fan, J., Migdall, A. & Taylor, J. M. Imaging topological edge states in silicon photonics. *Nature Photonics* **7**, 1001–1005 (2013). URL <https://doi.org/10.1038/nphoton.2013.274>.
- [262] Chen, W.-J. *et al.* Experimental realization of photonic topological insulator in a uniaxial metacrystal waveguide. *Nature Communications* **5**, 5782 (2014). URL <https://doi.org/10.1038/ncomms6782>.
- [263] Ningyuan, J., Owens, C., Sommer, A., Schuster, D. & Simon, J. Time- and Site-Resolved Dynamics in a Topological Circuit. *Phys. Rev. X* **5**, 021031 (2015). URL <https://link.aps.org/doi/10.1103/PhysRevX.5.021031>.
- [264] Schine, N., Ryou, A., Gromov, A., Sommer, A. & Simon, J. Synthetic Landau levels for photons. *Nature* **534**, 671–675 (2016). URL <https://doi.org/10.1038/nature17943>.
- [265] Hofstadter, D. R. Energy levels and wave functions of Bloch electrons in rational and irrational magnetic fields. *Phys. Rev. B* **14**, 2239–2249 (1976). URL <https://link.aps.org/doi/10.1103/PhysRevB.14.2239>.
- [266] Maczewsky, L. J., Zeuner, J. M., Nolte, S. & Szameit, A. Observation of photonic anomalous Floquet topological insulators. *Nature Communications* **8**, 13756 (2017). URL <https://doi.org/10.1038/ncomms13756>.
- [267] Mukherjee, S. *et al.* Experimental observation of anomalous topological edge modes in a slowly driven photonic lattice. *Nature Communications* **8**, 13918 (2017). URL <https://doi.org/10.1038/ncomms13918>.

- [268] Wimmer, M., Price, H. M., Carusotto, I. & Peschel, U. Experimental measurement of the Berry curvature from anomalous transport. *Nature Physics* **13**, 545–550 (2017). URL <https://doi.org/10.1038/nphys4050>.
- [269] Hu, W. *et al.* Measurement of a Topological Edge Invariant in a Microwave Network. *Phys. Rev. X* **5**, 011012 (2015). URL <https://link.aps.org/doi/10.1103/PhysRevX.5.011012>.
- [270] Bellec, M., Kuhl, U., Montambaux, G. & Mortessagne, F. Manipulation of edge states in microwave artificial graphene. *New Journal of Physics* **16**, 113023 (2014). URL <https://doi.org/10.1088/1367-2630/16/11/113023>.
- [271] Plotnik, Y. *et al.* Observation of unconventional edge states in ‘photonic graphene’. *Nature Materials* **13**, 57–62 (2014). URL <https://doi.org/10.1038/nmat3783>.
- [272] Milićević, M. *et al.* Edge states in polariton honeycomb lattices. *2D Materials* **2**, 034012 (2015). URL <https://doi.org/10.1088/2053-1583/2/3/034012>.
- [273] St-Jean, P. *et al.* Measuring Topological Invariants in a Polaritonic Analog of Graphene. *Phys. Rev. Lett.* **126**, 127403 (2021). URL <https://link.aps.org/doi/10.1103/PhysRevLett.126.127403>.
- [274] Li, M. *et al.* Higher-order topological states in photonic kagome crystals with long-range interactions. *Nature Photonics* **14**, 89–94 (2020). URL <https://doi.org/10.1038/s41566-019-0561-9>.
- [275] Lu, L. *et al.* Experimental observation of Weyl points. *Science* **349**, 622–624 (2015). URL <http://dx.doi.org/10.1126/science.aaa9273>.
- [276] Lu, L., Gao, H. & Wang, Z. Topological one-way fiber of second Chern number. *Nature Communications* **9**, 5384 (2018). URL <https://doi.org/10.1038/s41467-018-07817-3>.
- [277] Yang, Y. *et al.* Realization of a three-dimensional photonic topological insulator. *Nature* **565**, 622–626 (2019). URL <https://doi.org/10.1038/s41586-018-0829-0>.
- [278] Kraus, Y. E., Lahini, Y., Ringel, Z., Verbin, M. & Zilberberg, O. Topological States and Adiabatic Pumping in Quasicrystals. *Phys. Rev. Lett.* **109**, 106402 (2012). URL <https://link.aps.org/doi/10.1103/PhysRevLett.109.106402>.
- [279] Baboux, F. *et al.* Measuring topological invariants from generalized edge states in polaritonic quasicrystals. *Physical Review B* **95** (2017). URL <http://dx.doi.org/10.1103/PhysRevB.95.161114>.
- [280] Verbin, M., Zilberberg, O., Lahini, Y., Kraus, Y. E. & Silberberg, Y. Topological pumping over a photonic Fibonacci quasicrystal. *Phys. Rev. B* **91**, 064201 (2015). URL <https://link.aps.org/doi/10.1103/PhysRevB.91.064201>.
- [281] Su, W. P., Schrieffer, J. R. & Heeger, A. J. Solitons in Polyacetylene. *Phys. Rev. Lett.* **42**, 1698–1701 (1979). URL <https://link.aps.org/doi/10.1103/PhysRevLett.42.1698>.

- [282] Asbóth, J. K., Oroszlány, L. & Pályi, A. A Short Course on Topological Insulators. *Lecture Notes in Physics* (2016). URL <http://dx.doi.org/10.1007/978-3-319-25607-8>.
- [283] Lieb, E. H. Two theorems on the Hubbard model. *Phys. Rev. Lett.* **62**, 1201–1204 (1989). URL <https://link.aps.org/doi/10.1103/PhysRevLett.62.1201>.
- [284] Zak, J. Berry’s phase for energy bands in solids. *Phys. Rev. Lett.* **62**, 2747–2750 (1989). URL <https://link.aps.org/doi/10.1103/PhysRevLett.62.2747>.
- [285] Li, L., Xu, Z. & Chen, S. Topological phases of generalized Su-Schrieffer-Heeger models. *Phys. Rev. B* **89**, 085111 (2014). URL <https://link.aps.org/doi/10.1103/PhysRevB.89.085111>.
- [286] Pérez-González, B., Bello, M., Gómez-León, A. & Platero, G. SSH model with long-range hoppings: topology, driving and disorder (2018). [1802.03973](https://arxiv.org/abs/1802.03973).
- [287] Pérez-González, B., Bello, M., Gómez-León, A. & Platero, G. Interplay between long-range hopping and disorder in topological systems. *Phys. Rev. B* **99**, 035146 (2019). URL <https://link.aps.org/doi/10.1103/PhysRevB.99.035146>.
- [288] Chen, B.-H. & Chiou, D.-W. An elementary rigorous proof of bulk-boundary correspondence in the generalized Su-Schrieffer-Heeger model. *Physics Letters A* **384**, 126168 (2020). URL <https://www.sciencedirect.com/science/article/pii/S0375960119311028>.
- [289] Malkova, N., Hromada, I., Wang, X., Bryant, G. & Chen, Z. Observation of optical Shockley-like surface states in photonic superlattices. *Opt. Lett.* **34**, 1633–1635 (2009). URL <http://ol.osa.org/abstract.cfm?URI=ol-34-11-1633>.
- [290] Martínez Alvarez, V. M., Barrios Vargas, J. E., Berdakin, M. & Foa Torres, L. E. F. Topological states of non-Hermitian systems. *The European Physical Journal Special Topics* **227**, 1295–1308 (2018). URL <https://doi.org/10.1140/epjst/e2018-800091-5>.
- [291] Zeuner, J. M. *et al.* Observation of a Topological Transition in the Bulk of a Non-Hermitian System. *Phys. Rev. Lett.* **115**, 040402 (2015). URL <https://link.aps.org/doi/10.1103/PhysRevLett.115.040402>.
- [292] Song, W. *et al.* Breakup and Recovery of Topological Zero Modes in Finite Non-Hermitian Optical Lattices. *Phys. Rev. Lett.* **123**, 165701 (2019). URL <https://link.aps.org/doi/10.1103/PhysRevLett.123.165701>.
- [293] Liu, J. & Fu, L. B. Berry phase in nonlinear systems. *Phys. Rev. A* **81**, 052112 (2010). URL <https://link.aps.org/doi/10.1103/PhysRevA.81.052112>.
- [294] Bomantara, R. W., Zhao, W., Zhou, L. & Gong, J. Nonlinear Dirac cones. *Phys. Rev. B* **96**, 121406 (2017). URL <https://link.aps.org/doi/10.1103/PhysRevB.96.121406>.

- [295] Smirnova, D., Leykam, D., Chong, Y. & Kivshar, Y. Nonlinear topological photonics. *Applied Physics Reviews* **7**, 021306 (2020). URL <https://doi.org/10.1063/1.5142397>. <https://doi.org/10.1063/1.5142397>.
- [296] Ikeda, K. & Akimoto, O. Instability Leading to Periodic and Chaotic Self-Pulsations in a Bistable Optical Cavity. *Phys. Rev. Lett.* **48**, 617–620 (1982). URL <https://link.aps.org/doi/10.1103/PhysRevLett.48.617>.
- [297] Haus, H. Mode-locking of lasers. *IEEE Journal of Selected Topics in Quantum Electronics* **6**, 1173–1185 (2000).
- [298] Bahari, B. *et al.* Nonreciprocal lasing in topological cavities of arbitrary geometries. *Science* **358**, 636–640 (2017). URL <https://science.sciencemag.org/content/358/6363/636><https://science.sciencemag.org/content/358/6363/636.abstract>.
- [299] Harder, T. H. *et al.* Coherent Topological Polariton Laser. *ACS Photonics* **8**, 1377–1384 (2021). URL <https://doi.org/10.1021/acsp Photonics.0c01958>.
- [300] Parto, M. *et al.* Edge-Mode Lasing in 1D Topological Active Arrays. *Phys. Rev. Lett.* **120**, 113901 (2018). URL <https://link.aps.org/doi/10.1103/PhysRevLett.120.113901>.
- [301] Zhao, H. *et al.* Topological hybrid silicon microlasers. *Nature Communications* **9**, 981 (2018). URL <https://doi.org/10.1038/s41467-018-03434-2>.
- [302] Ota, Y., Katsumi, R., Watanabe, K., Iwamoto, S. & Arakawa, Y. Topological photonic crystal nanocavity laser. *Communications Physics* **1**, 86 (2018). URL <https://doi.org/10.1038/s42005-018-0083-7>.
- [303] Dikopoltsev, A. *et al.* Topological insulator vertical-cavity laser array. *Science* **373**, 1514–1517 (2021). URL <https://www.science.org/doi/abs/10.1126/science.abj2232>. <https://www.science.org/doi/pdf/10.1126/science.abj2232>.
- [304] Dusel, M. *et al.* Room-Temperature Topological Polariton Laser in an Organic Lattice. *Nano Letters* **21**, 6398–6405 (2021). URL <https://doi.org/10.1021/acs.nanolett.1c00661>.
- [305] Harari, G. *et al.* Topological insulator laser: Theory. *Science* **359**, eaar4003 (2018).
- [306] Bandres, M. A. *et al.* Topological insulator laser: Experiments. *Science* **359**, eaar4005 (2018). URL <http://science.sciencemag.org/>.
- [307] Smirnova, D. *et al.* Room-temperature lasing from nanophotonic topological cavities. *Light: Science & Applications* **9**, 127 (2020). URL <https://doi.org/10.1038/s41377-020-00350-3>.
- [308] Suchomel, H. *et al.* Platform for Electrically Pumped Polariton Simulators and Topological Lasers. *Phys. Rev. Lett.* **121**, 257402 (2018). URL <https://link.aps.org/doi/10.1103/PhysRevLett.121.257402>.

- [309] Amelio, I. & Carusotto, I. Theory of the Coherence of Topological Lasers. *Phys. Rev. X* **10**, 041060 (2020). URL <https://link.aps.org/doi/10.1103/PhysRevX.10.041060>.
- [310] Mittal, S., Goldschmidt, E. A. & Hafezi, M. A topological source of quantum light. *Nature* **561**, 502–506 (2018). URL <https://doi.org/10.1038/s41586-018-0478-3>. 1709.09984.
- [311] Kruk, S. *et al.* Nonlinear light generation in topological nanostructures. *Nature Nanotechnology* **14**, 126–130 (2019). URL <https://doi.org/10.1038/s41565-018-0324-7>.
- [312] De Léséleuc, S. *et al.* Observation of a symmetry-protected topological phase of interacting bosons with Rydberg atoms. *Science* **365**, 775–780 (2019).
- [313] Clark, L. W., Schine, N., Baum, C., Jia, N. & Simon, J. Observation of Laughlin states made of light. *Nature* **582**, 41–45 (2020). URL <http://dx.doi.org/10.1038/s41586-020-2318-5>.
- [314] Dobrykh, D. A., Yulin, A. V., Slobozhanyuk, A. P., Poddubny, A. N. & Kivshar, Y. S. Nonlinear Control of Electromagnetic Topological Edge States. *Phys. Rev. Lett.* **121**, 163901 (2018). URL <https://link.aps.org/doi/10.1103/PhysRevLett.121.163901>.
- [315] Hadad, Y., Khanikaev, A. B. & Alù, A. Self-induced topological transitions and edge states supported by nonlinear staggered potentials. *Phys. Rev. B* **93**, 155112 (2016). URL <https://link.aps.org/doi/10.1103/PhysRevB.93.155112>.
- [316] Zhou, X., Wang, Y., Leykam, D. & Chong, Y. D. Optical isolation with nonlinear topological photonics. *New Journal of Physics* **19**, 095002 (2017). URL <https://doi.org/10.1088/1367-2630/aa7cb5>.
- [317] Maczewsky, L. J. *et al.* Nonlinearity-induced photonic topological insulator. *Science* **370**, 701–704 (2020). URL <http://dx.doi.org/10.1126/science.abd2033>.
- [318] Bleu, O., Solnyshkov, D. D. & Malpuech, G. Interacting quantum fluid in a polariton Chern insulator. *Phys. Rev. B* **93**, 085438 (2016). URL <https://link.aps.org/doi/10.1103/PhysRevB.93.085438>.
- [319] Nalitov, A. V., Solnyshkov, D. D. & Malpuech, G. Polariton \mathbb{Z} Topological Insulator. *Phys. Rev. Lett.* **114**, 116401 (2015). URL <https://link.aps.org/doi/10.1103/PhysRevLett.114.116401>.
- [320] Mukherjee, S. & Rechtsman, M. C. Observation of Floquet solitons in a topological bandgap. *Science* **368**, 856–859 (2020). URL <http://dx.doi.org/10.1126/science.aba8725>.
- [321] Mukherjee, S. & Rechtsman, M. C. Observation of Unidirectional Soliton-like Edge States in Nonlinear Floquet Topological Insulators. *Phys. Rev. X* **11**, 041057 (2021). URL <https://link.aps.org/doi/10.1103/PhysRevX.11.041057>.

- [322] Jürgensen, M., Mukherjee, S. & Rechtsman, M. C. Quantized nonlinear Thouless pumping. *Nature* **596**, 63–67 (2021). URL <https://doi.org/10.1038/s41586-021-03688-9>.
- [323] Lumer, Y., Plotnik, Y., Rechtsman, M. C. & Segev, M. Self-Localized States in Photonic Topological Insulators. *Phys. Rev. Lett.* **111**, 243905 (2013). URL <https://link.aps.org/doi/10.1103/PhysRevLett.111.243905>.
- [324] Ablowitz, M. J., Curtis, C. W. & Ma, Y.-P. Linear and nonlinear traveling edge waves in optical honeycomb lattices. *Phys. Rev. A* **90**, 023813 (2014). URL <https://link.aps.org/doi/10.1103/PhysRevA.90.023813>.
- [325] Leykam, D. & Chong, Y. D. Edge Solitons in Nonlinear-Photonic Topological Insulators. *Phys. Rev. Lett.* **117**, 143901 (2016). URL <https://link.aps.org/doi/10.1103/PhysRevLett.117.143901>.
- [326] Ivanov, S. K. *et al.* Topological dipole Floquet solitons. *Phys. Rev. A* **103**, 053507 (2021). URL <https://link.aps.org/doi/10.1103/PhysRevA.103.053507>.
- [327] Ivanov, S. K., Kartashov, Y. V., Szameit, A., Torner, L. & Konotop, V. V. Floquet Edge Multicolor Solitons (2021). [2111.01291](https://arxiv.org/abs/2111.01291).
- [328] Zhang, W., Chen, X., Kartashov, Y. V., Konotop, V. V. & Ye, F. Coupling of Edge States and Topological Bragg Solitons. *Phys. Rev. Lett.* **123**, 254103 (2019). URL <https://link.aps.org/doi/10.1103/PhysRevLett.123.254103>.
- [329] Jürgensen, M. & Rechtsman, M. C. Chern Number Governs Soliton Motion in Nonlinear Thouless Pumps. *Phys. Rev. Lett.* **128**, 113901 (2022). URL <https://link.aps.org/doi/10.1103/PhysRevLett.128.113901>.
- [330] Mostaan, N., Grusdt, F. & Goldman, N. Quantized transport of solitons in nonlinear Thouless pumps: From Wannier drags to ultracold topological mixtures (2022). [2110.13075](https://arxiv.org/abs/2110.13075).
- [331] Bongiovanni, D. *et al.* Dynamically Emerging Topological Phase Transitions in Nonlinear Interacting Soliton Lattices. *Phys. Rev. Lett.* **127**, 184101 (2021). URL <https://link.aps.org/doi/10.1103/PhysRevLett.127.184101>.
- [332] Pernet, N. *et al.* Topological gap solitons in a 1D non-Hermitian lattice (2021). [2101.01038](https://arxiv.org/abs/2101.01038).
- [333] Sipe, J. E. *Gap Solitons*, 305–318 (Springer Netherlands, Dordrecht, 1992). URL https://doi.org/10.1007/978-94-011-2536-9_17.
- [334] Campbell, D. K., Flach, S. & Kivshar, Y. S. Localizing Energy Through Nonlinearity and Discreteness. *Physics Today* **57**, 43–49 (2004). URL <https://doi.org/10.1063/1.1650069>. <https://doi.org/10.1063/1.1650069>.
- [335] Stegeman, G. I. & Segev, M. Optical Spatial Solitons and Their Interactions: Universality and Diversity. *Science* **286**, 1518–1523 (1999). URL <https://www.science.org/doi/abs/10.1126/science.286.5444.1518>. <https://www.science.org/doi/pdf/10.1126/science.286.5444.1518>.

- [336] Dabrowska, B. J., Ostrovskaya, E. A. & Kivshar, Y. S. Interaction of matter-wave gap solitons in optical lattices. *Journal of Optics B: Quantum and Semiclassical Optics* **6**, 423–427 (2004). URL <https://doi.org/10.1088/1464-4266/6/10/007>.
- [337] Soto-Crespo, J. M., Akhmediev, N. & Ankiewicz, A. Pulsating, Creeping, and Erupting Solitons in Dissipative Systems. *Phys. Rev. Lett.* **85**, 2937–2940 (2000). URL <https://link.aps.org/doi/10.1103/PhysRevLett.85.2937>.
- [338] Peng, J. & Zeng, H. Soliton collision induced explosions in a mode-locked fibre laser. *Communications Physics* **2**, 34 (2019). URL <https://doi.org/10.1038/s42005-019-0134-8>.
- [339] Aitchison, J. S. *et al.* Experimental observation of spatial soliton interactions. *Opt. Lett.* **16**, 15–17 (1991). URL <http://www.osapublishing.org/ol/abstract.cfm?URI=ol-16-1-15>.
- [340] Mitschke, F. M. & Mollenauer, L. F. Experimental observation of interaction forces between solitons in optical fibers. *Opt. Lett.* **12**, 355–357 (1987). URL <http://www.osapublishing.org/ol/abstract.cfm?URI=ol-12-5-355>.
- [341] Zakharov, V. E. & Shabat, A. B. Exact Theory of Two-dimensional Self-focusing and One-dimensional Self-modulation of Waves in Nonlinear Media. *Soviet Journal of Experimental and Theoretical Physics* **34**, 62–69 (1972).
- [342] Karpman, V. I. Breather decay into fluxon-antifluxon pair and its transformation into bunched fluxons in a long Josephson junction. *Physics Letters A* **88**, 207–210 (1982). URL <https://www.sciencedirect.com/science/article/pii/0375960182905655>.
- [343] Gordon, J. P. Interaction forces among solitons in optical fibers. *Opt. Lett.* **8**, 596–598 (1983). URL <http://www.osapublishing.org/ol/abstract.cfm?URI=ol-8-11-596>.
- [344] Barthélémy, A. & Reynaud, F. Optically Controlled Interaction Between Two Fundamental Soliton Beams. *EPL - Europhysics Letters* **12**, 401–405 (1990). URL <https://hal.archives-ouvertes.fr/hal-02098407>.
- [345] Lou, C., Wang, X., Xu, J., Chen, Z. & Yang, J. Nonlinear Spectrum Reshaping and Gap-Soliton-Train Trapping in Optically Induced Photonic Structures. *Phys. Rev. Lett.* **98**, 213903 (2007). URL <https://link.aps.org/doi/10.1103/PhysRevLett.98.213903>.
- [346] Fa-Jun, X., Peng, Z., Sheng, L. & Jian-Lin, Z. Coherent and Incoherent Interactions between Discrete-Soliton Trains in Two-Dimensional Light-Induced Photonic Lattices. *Chinese Physics Letters* **24**, 3435–3438 (2007). URL <https://doi.org/10.1088/0256-307x/24/12/040>.
- [347] Sheng, L., Peng, Z., Fa-Jun, X., Xue-Tao, G. & Jian-Lin, Z. The interaction of in-band and in-gap lattice soliton trains in optically induced two-dimensional photonic lattices. *Chinese Physics B* **19**, 065203 (2010). URL <https://doi.org/10.1088/1674-1056/19/6/065203>.

- [348] Meier, J., Stegeman, G. I., Silberberg, Y., Morandotti, R. & Aitchison, J. S. Nonlinear Optical Beam Interactions in Waveguide Arrays. *Phys. Rev. Lett.* **93**, 093903 (2004). URL <https://link.aps.org/doi/10.1103/PhysRevLett.93.093903>.
- [349] Stepić, M. *et al.* Beam interactions in one-dimensional saturable waveguide arrays. *Phys. Rev. E* **74**, 046614 (2006). URL <https://link.aps.org/doi/10.1103/PhysRevE.74.046614>.
- [350] Szameit, A. *et al.* Quasi-incoherent propagation in waveguide arrays. *Applied Physics Letters* **90**, 241113 (2007). URL <https://doi.org/10.1063/1.2735953>. <https://doi.org/10.1063/1.2735953>.
- [351] Xiao, F., Zhang, P., Liu, S. & Zhao, J. Tunable oscillation of discrete solitons triggered by coherent interactions. *Journal of Optics* **13**, 105101 (2011). URL <https://doi.org/10.1088/2040-8978/13/10/105101>.
- [352] Liu, S. *et al.* Anomalous interactions of spatial gap solitons in optically induced photonic lattices. *Opt. Lett.* **36**, 1167–1169 (2011). URL <http://www.osapublishing.org/ol/abstract.cfm?URI=ol-36-7-1167>.
- [353] Chen, Y., Cui, H., Luo, A., Luo, Z. & Zheng, C. Influence of lattice defects on the coherent interaction of photovoltaic lattice solitons. *Journal of Optics* **17**, 105902 (2015). URL <https://doi.org/10.1088/2040-8978/17/10/105902>.
- [354] Shi, Z., Xue, J., Zhu, X., Xiang, Y. & Li, H. Interaction of Airy-Gaussian beams in photonic lattices with defects. *Phys. Rev. E* **95**, 042209 (2017). URL <https://link.aps.org/doi/10.1103/PhysRevE.95.042209>.
- [355] Beličev, P. P. *et al.* Dynamics of gap solitons in one-dimensional binary lattices with saturable self-defocusing nonlinearity and alternating spacing. *Phys. Rev. A* **86**, 033835 (2012). URL <https://link.aps.org/doi/10.1103/PhysRevA.86.033835>.
- [356] Hamel, P. *et al.* Spontaneous mirror-symmetry breaking in coupled photonic-crystal nanolasers. *Nature Photonics* **9**, 311–315 (2015). URL <https://doi.org/10.1038/nphoton.2015.65>.
- [357] Garbin, B. *et al.* Spontaneous Symmetry Breaking in a Coherently Driven Nanophotonic Bose-Hubbard Dimer (2022). URL <https://link.aps.org/doi/10.1103/PhysRevLett.128.053901>.
- [358] Casteels, W. & Ciuti, C. Quantum entanglement in the spatial-symmetry-breaking phase transition of a driven-dissipative Bose-Hubbard dimer. *Phys. Rev. A* **95**, 013812 (2017). URL <https://link.aps.org/doi/10.1103/PhysRevA.95.013812>.
- [359] Brandstetter, M. *et al.* Reversing the pump dependence of a laser at an exceptional point. *Nature Communications* **5**, 4034 (2014). URL <https://doi.org/10.1038/ncomms5034>.
- [360] Doppler, J. *et al.* Dynamically encircling an exceptional point for asymmetric mode switching. *Nature* **537**, 76–79 (2016). URL <https://doi.org/10.1038/nature18605>.

- [361] Schumer, A. *et al.* Topological modes in a laser cavity through exceptional state transfer. *Science* **375**, 884–888 (2022). URL <https://www.science.org/doi/abs/10.1126/science.abl6571>. <https://www.science.org/doi/pdf/10.1126/science.abl6571>.
- [362] Kraus, Y. E. & Zilberberg, O. Topological Equivalence between the Fibonacci Quasicrystal and the Harper Model. *Phys. Rev. Lett.* **109**, 116404 (2012). URL <https://link.aps.org/doi/10.1103/PhysRevLett.109.116404>.

